Holographic Recording in Polymeric Materials with Applications

Thesis by

Gregory J. Steckman

In Partial Fulfillment of the Requirements

for the Degree of

Doctor of Philosophy

California Institute of Technology

Pasadena, California

2001

(Defended November 20, 2000)

Acknowledgments

Although only my name appears on the cover, I couldn't have completed this thesis and the past five years of research without the help of many people. First, I would like to thank my wife, Alicia, for her years of patience and understanding while I was off working long hours in the labs of Caltech. Also, my family for their continued encouragement through all the years of my education.

I owe my gratitude to Professor Demetri Psaltis for his support of my research as well as expert guidance on the direction and goals of my research. Undoubtedly, none of the results in this thesis would have been possible without his guidance and support. I owe a big "thank you" to Lucinda Acosta for her enthusiastically assisting with administrative matters that I preferred not to deal with. Even though Caltech is a relatively small place, it still has its bureaucracy, and without her efforts in shielding me from it I would have gone mad long ago. In the course of experimental research, few things are as important as reliable equipment. I would like to thank Ya-Yun Liu for her work on maintaining the many lasers I've had the privilege to use, as well as other assorted lab equipment.

Iouri Solomatine has been irreplaceable with his dexterity in fabricating all sorts of polymer materials. He was instrumental in my ability to work efficiently with many polymer samples. He literally made hundreds if not over a thousand material samples for me to use and abuse. I'd like to thank Vladimir Shelkovnikov and his team of chemists for the design and synthesis of chromophores for the NQ:PMMA material described in Chapter 3. Thanks to Dr. Gan Zhou for many conversations leading to insight into how to tackle some of the problems encountered with PQ:PMMA. Thanks also to Klaus Meerholz and Reinhard Bittner for bringing their photorefractive polymer materials from Germany and showing me the inside scoop on how to use them. I'd also like to thank Professor Ares Rosakis and Dr. David Owen for introducing me to the world of high-speed cameras, the inspiration for the sixth chapter.

I'd like to thank all of the Psaltis group members, past and present, for helping to create a professional and stimulating research environment. These include Dr. Xin An, Dr. George Barbastathis, Greg Billock, Dr. Geoff Burr, Dr. Ernest Chuang, Dr. Jean-Jacques

Drolet, Wenhai Liu, Zhiwen Liu, Irena Maravic, Dr. David Marx, Chris Moser, Jose Mumbru, George Panotopoulos, Dimitris Sakellariou, Dr. Xu Wang, Yunping Yang, and anyone else I might have unintentionally missed. Special thanks go to Dr. Allen Pu for showing me many of his tricks in the lab. Dr. Michael Levene was instrumental in formulation of the theoretical treatment of the adjustable shift-selectivity correlators in the fifth chapter. Thanks to Dr. Ali Adibi for many interesting conversations and for always finding the cheapest places to stay during conferences.

Finally, I would like to thank those additional organizations which have provided some form of financial support over the years. They are: Virginia Steele Scott for a one year fellowship, the Intel Foundation for a fellowship plus the donation of a computer which was extremely useful, and the Walker von Brimer Foundation for a generous grant.

Abstract

This thesis presents the results of research in volume holographic recording in several polymeric recording materials and their use in selected applications. The first chapter discusses the key properties of holographic recording materials. The second chapter develops a technique for calculating exposure schedules for photorefractive polymers which do not exhibit mono-exponential recording dynamics. It is determined that these materials require performance improvements before they can be successfully applied to many interesting applications of volume holography, such as holographic data storage and optical correlators which are described in later chapters.

The third chapter investigates recording in diffusion amplification based polymer materials. This class of materials overcomes many limitations of other polymer types, such as limited thicknesses and volume shrinkage. A new material based on the diffusion amplification principle is developed with the goal of increasing dynamic range. The new material, a naphtoquinone and PMMA based co-polymer, is demonstrated in holographic recording experiments.

In the fourth chapter, holographic data storage experiments are performed and a storage density of 7 bits/μm^2 is achieved. A holographic data storage system which utilizes shift multiplexing is modeled and simulated to determine optimal system parameters and material characteristics. It is discovered that the dynamic range of the material used, phenanthrenequinone doped poly(methyl methacrylate), is insufficient to provide very high data storage densities.

In the fifth chapter attention is focused on the development and characterization of an optical holographic correlator system using the DuPont HRF-150 photopolymer. The system is used for image recognition and tracking. The performance of the system is characterized with multiple 2-d and 3-d objects with respect to camera resolution, magnification, rotation, and other transformations. The system is demonstrated to be capable of simultaneously recognizing and tracking multiple targets, even in the presence of extraneous objects and partial obscuring of the targets.

The final chapter describes the development of a high-speed holographic movie camera. Utilizing a Q-switched Nd:YAG pulse laser and Aprilis ULSH500-7A recording material, multi-frame holographic exposures with a 80 MHz frame rate are recorded.

Table of Contents

CHAPTER 5 Optical Holographic Correlators

CHAPTER 6 The High Frame-rate Holographic Movie Camera

List of Figures

CHAPTER 5 Optical Holographic Correlators

1 Introduction

Holographic recording in polymeric materials is not new, and in fact one of the oldest and most widely used holographic recording materials, dichromated gelatin, is a polymer-based material. However, it is not suitable for many volume holographic applications due to its limited thickness of a few tens of microns and the severe shrinkage that occurs during exposure.[1-1] For many volume holography applications, the quality of the recording material is the most significant factor which limits performance. This thesis presents the basic characterization of several new polymeric recording materials in the context of their use in high-performance applications, such as high-density data storage. Furthermore, the large dynamic range, sensitivity, and durability of certain new materials have enabled applications to be realized which were not possible before. One example is the high frame-rate holographic movie system discussed in Chapter 6.

The development of new materials is driven primarily by the lure of a variety of applications of volume holography. The Bragg-effect[1-2] makes these applications possible, providing selectivity not possible with thin materials. With greater selectivity, a higher multiplexing density can be achieved. A single spot of material can be made to record and retrieve more holograms with less crosstalk, which is utilized in holographic memories. Nonspatial filters can also be constructed[1-3] to filter laser beams. However, there are many other properties of a recording material that influence the performance of a holographic system, which are outlined here:

•**Volume shrinkage and swelling.** Typically shrinkage is a problem in photopolymerizable materials because the process of creating the index modulation, polymerization, also causes an increase in density in the material, resulting in shrinkage. This causes distortion in the reconstruction of high-bandwidth images due to Bragg-mismatch of some grating components. For a data storage system, the effect is a loss of quality in the reconstructed data page. If swelling were to occur, it would cause similar problems to the quality of the recorded holograms.

•**Sensitivity.** High sensitivity is desirable so that shorter recording times can be used. There are two reasons why a short recording time is desirable. First, during recording the optical setup must be very stable. Any vibrations or unequal phase shifts between recording beams will cause the interference pattern to shift, decreasing the hologram quality. With a shorter recording time these problems are minimized, and the hologram quality will be better. The second reason is related to the multiplexing of many holograms in a single material. If a holographic memory is to be built and one-million holograms need to be recorded, then a 1 second exposure time per hologram would require about 11 days of recording. With higher sensitivity, this time can be reduced.

•**Dynamic range.** For holographic multiplexing, the maximum index change that can be induced in the material affects how many holograms can be stored at one location of material. For higher data densities at a given diffraction efficiency, a larger dynamic range would be needed.

•**Modulation transfer function.** The modulation transfer function (MTF) of a material determines how well it can record gratings of different frequencies. When recording high-bandwidth images, gratings covering a large bandwidth will be recorded. If the MTF of the material is not the same over the whole range, then essentially image filtering will occur upon readout, where the filtering depends on the shape of the MTF. Also, if the MTF extends over a large range, then many different angles between signal and reference beams can be used for holographic recording. The MTF can also impact system design because, for example, some materials cannot record reflection holograms which have a large grating vector.

•**Non-destructive readout.** For many applications, it is desirable to be able to readout holograms without causing them to erase. Many polymeric recording materials are write-once and non-destructive at the recording wavelength due to irreversible chemical reactions that take place during recording. The most notable exception are photorefractive polymer materials, discussed in Chapter 2.

•**Absorption.** As the recording beams propagate through the recording material, they are absorbed and exponentially decrease in strength, resulting in an uneven grating strength through the material. This causes broadening of the Bragg-selectivity. A low absorption is needed in order to minimize this problem; however, it often conflicts with the goal of high sensitivity.

•**Bulk optical quality.** For applications that perform imaging through the recording material, such as data storage, good optical quality is essential. Scatter is a major contributor to noise, and should be low.

•**Shape and thickness.** As discussed previously, thicker materials have better Bragg-selectivity. Depending on the application, a material should be able to be made in a large range of thicknesses as well as geometries, such as disks, cubes, etc., to fit the needs of a larger range of applications

•**Stability, durability, and weight.** Many applications require long-term stability of the recorded holograms. The material should be able to be heated and cooled by reasonable amounts without causing a significant degradation of hologram quality. For disk applications the less weight the better, enabling higher spin rates, lower cost motors, and lower power consumption.

For holographic data storage applications, the thickness of the material has a direct impact on storage densities due to selectivity. The most common type of materials used for this application are photorefractive crystals,[1-4]-[1-6] which can be made in very large thicknesses and used in the 90-degree geometry.[1-7] Due to their ability to be erased and re-used, as well as the extensive understanding of the photorefractive effect in crystals,[1-8] photorefractive polymers are an intense area of research, in which it is sought to duplicate the photorefractive effect in polymer based materials. Due to the great variability of polymer materials which can be chosen based on their performance characteristics, they have a level of compositional flexibility that is unmatched by inorganic crystals. Chapter two reviews the main types of photorefractive polymers that have been investigated in the past, and presents experimental results of holographic recording in a new type of photorefractive polymer. The performance of the material is studied with respect to its use in a read-write, multiple hologram system, and for this purpose a new exposure schedule is determined to enable the recording of multiple holograms of equal strength. It is shown that certain prop-

erties and the performance of the current generation of materials make them insufficient for holographic data storage applications, compared to the latest inorganic photorefractive materials.

Chapter 3 investigates holographic recording in materials exhibiting diffusion amplification. These polymers are not as limited in form-factor as many other photopolymers, and have been made into 3-mm thick disks, as well as 1 cm cubes. One such material, phenanthrenquinone doped poly(methyl methacrylate), is used for a holographic storage system capable of recording with a surface density of 7 bits/μm^2, described in Chapter 4. A new material was developed, based on the recording principles of diffusion amplification, with the goal of increasing the dynamic range. The experimental results of its recording behavior are also reported in Chapter 3.

Previously, storage densities as high as 10 bits/μm^2 have been achieved[1-9] using a 100 micron thick photopolymer made by DuPont, which, unlike photorefractive materials, is a write-once material. For certain applications, such as content distribution, a write-once permanent storage material is preferred, and it is for this application that photopolymers look most promising. Chapter 4 discusses holographic data storage with photopolymers that exhibit heating assisted diffusion amplification of the recorded holograms. Furthermore in Chapter 4, a model of holographic data storage systems is developed to enable the prediction of bit-densities based on properties of the recording material and optical system. It was determined through simulations that the material thickness is not the key limiting factor as was previously thought, but rather the dynamic range of the material is chiefly responsible for limiting the storage density.

Applications besides holographic data storage are also possible with volume holographic recording materials. In Chapter 5, the development of an optical holographic correlator system for image recognition and tracking is described. The performance of the system is characterized with multiple 2-d and 3-d objects with respect to camera resolution, magnification, rotation, and other transformations. The system is demonstrated to be capable of simultaneously recognizing and tracking multiple targets, even in the presence of extraneous objects and partial obscuring of the targets. This system utilized DuPont HRF150 as the recording material. Theory and experiments for a simple technique of adjusting the shift-selectivity of holographic correlator systems is also presented.

Holography has been used as a diagnostic tool for many years. Chapter 6 describes the development of a system capable of taking holographic movies of high-speed events with a frame rate in excess of 80 MHz. First, the characterization of a photopolymer capable of recording holograms with both CW and pulsed lasers is described. Then the design and operation of the optical system is described. Finally the recording of 5 holograms within 54 ns is demonstrated. Methods of improving the current system are discussed.

References

1-1 R. J. Collier, C. B. Burckhardt, L. H. Lin, *Optical Holography*, Academic Press, New York, 1971, Chapter 10.

1-2 H. Kogelnik, "Coupled wave theory for thick hologram gratings," Bell Sys. Tech. J. 48, 2909-2945 (1969).

1-3 J. E. Ludman, J. R. Riccobono, N. O. Reinhand, I. V. Semenova, Y. L. Korzinin, S. M. Shahriar, H. J. Caulfield, J-M Fournier, and P. Hemmer, "Very thick holographic non-spatial filtering of laser beams," Opt. Eng. **36**, 1700-1705 (1997).

1-4 G.W. Burr and I. Leyva, "Multiplexed phase-conjugate holographic data storage with a buffer hologram," Opt. Lett. **25**, 499-501 (2000).

1-5 L. Hesselink, S. S. Orlov, A. Liu, A. Akella, D. Lande, and R. R. Neurgaonkar, "Photorefractive materials for nonvolatile volume holographic data storage," Science **282**, 1089-1094 (1998).

1-6 J. Imbrock, D. Kip, E. Kratzig, "Nonvolatile holographic storage in iron-doped lithium tantalate with continuous-wave laser light," Opt. Lett. **24**, 1302-1304 (1999).

1-7 G. Burr, *Volume holographic storage using the 90-degree geometry*, Ph.D. thesis, California Institute of Technology, 1997.

1-8 Yeh, *Introduction to Photorefractive Nonlinear Optics* (Wiley, New York, 1993).

1-9 A. Pu and D. Psaltis, "High-density recording in photopolymer-based holographic three-dimensional disks," Appl. Opt. 35, 2389-2398, (1996).

2 Holographic Multiplexing with Photorefractive Polymers

2.1 Introduction

With the advent of the orientational enhancement effect, [2-1] photorefractive polymer materials have undergone tremendous improvements in their performance as measured by the maximum achievable refractive index modulation and two-beam coupling gain.[2-2]-[2-4] While these figures of merit may be useful for some applications, they are not sufficient for characterizing a material's capabilities when it comes to multiplexing holograms, which is essential for holographic data storage, as well as many other interesting applications. It is important, therefore, that measurements concerning the ability to record multiple overlapping holograms be performed in order to understand the capabilities and limitations of these materials. Such an understanding will lend itself to the further development and improvement of the material. Furthermore, the characteristics of a recording medium must be well understood before it can be successfully used in a holographic system.

Photorefractive polymers are a complicated class of holographic materials. Because of the variability and complexity of the materials and the unique nature of the photorefractive effect, a brief introduction to photorefractivity and photorefractive polymers will be first given. The remainder of the chapter is devoted to describing experiments performed on a single type of photorefractive polymer and a slight variation of it. The goal of the

experiments is to characterize and understand the material for use in holographic data storage applications. In order to be useful for holographic data storage, a material must be capable of achieving a high M/# [2-5], a property dependent on both the recording and erasure dynamics of the stored holograms. Experiments performed to measure the dynamic behavior of the material are described in Section 2.2. The photorefractive polymer that was used behaves differently than previously studied photorefractive materials and therefore a new scheme for deriving a holographic multiplexing recording schedule was needed. Section 2.3 describes the derivation of the new recording schedule based on experimental measurements, and Section 2.4 describes multiplexing experiments using this schedule. During the course of working with the photorefractive polymer material it was discovered that in the dark the holograms would decay with time. Section 2.5 describes experiments to measure this dark decay, and the effect it has when multiple holograms are stored in the material.

2.1.1 Photorefractivity

Photorefractive polymers are designed with the goal of duplicating the photorefractive effect that occurs in many inorganic crystals. Therefore, before getting into the details of photorefractive polymers, it is necessary to first look at the principles of photorefractivity. In the broadest meaning of the word, photorefractivity is any change in the refractive index of a material as a result of being illuminated. However, its common usage is to refer to the "photorefractive effect" of certain types of inorganic crystals such as $LiNbO_3$, $BaTiO_3$, SBN, and many others. In these materials, a spatial modulation of the index of refraction occurs only through the build-up of a space-charge field within the material. This process is inherently delocalized, requiring the photo-generation of charges, charge trans-

port, and trapping. Consequently, the term "photorefractive" is almost exclusively applied to the process of grating formation through non-local effects as occurs in traditional inorganic crystals. By comparison, many polymer materials and popular silver halide recording films are not thought of as photorefractive due to the local nature of the grating formation. Photorefractive polymers differ from most polymers in their approach to hologram formation. Their design approach is to mimic the hologram creation process of the inorganic crystals in order to take advantage of some of their useful properties, such as the ability to be recorded and erased multiple times, but with the added flexibility in tailoring performance that polymers provide over inorganic crystals.

Figure 2-1 illustrates the steps involved in photorefractive hologram formation. Two coherent laser beams interfere to form a spatially modulated intensity pattern throughout the photorefractive material. This results in an inhomogeneous generation of charges. In photorefractive polymers hole generation occurs, while in inorganic crystals, electrons are typically generated. Furthermore, the classical description of the photorefractive effect[2-6] involves the concept of a conduction band and a valence band resulting from the crystalline nature of inorganic materials. The material can be effectively thought of as consisting of two energy levels, the conduction and valence band, with impurities doped at more or less discrete levels between these two. Polymers, on the other hand, are not ordered materials, which makes it impossible to describe things in terms of energy levels and a conduction band.

Free charges can be redistributed through two mechanisms, drift and diffusion. Some inorganic crystals, such as $LiNbO_3$, have a "built-in" electric field which causes drift. For optimal performance, photorefractive polymers require an applied electric field, and

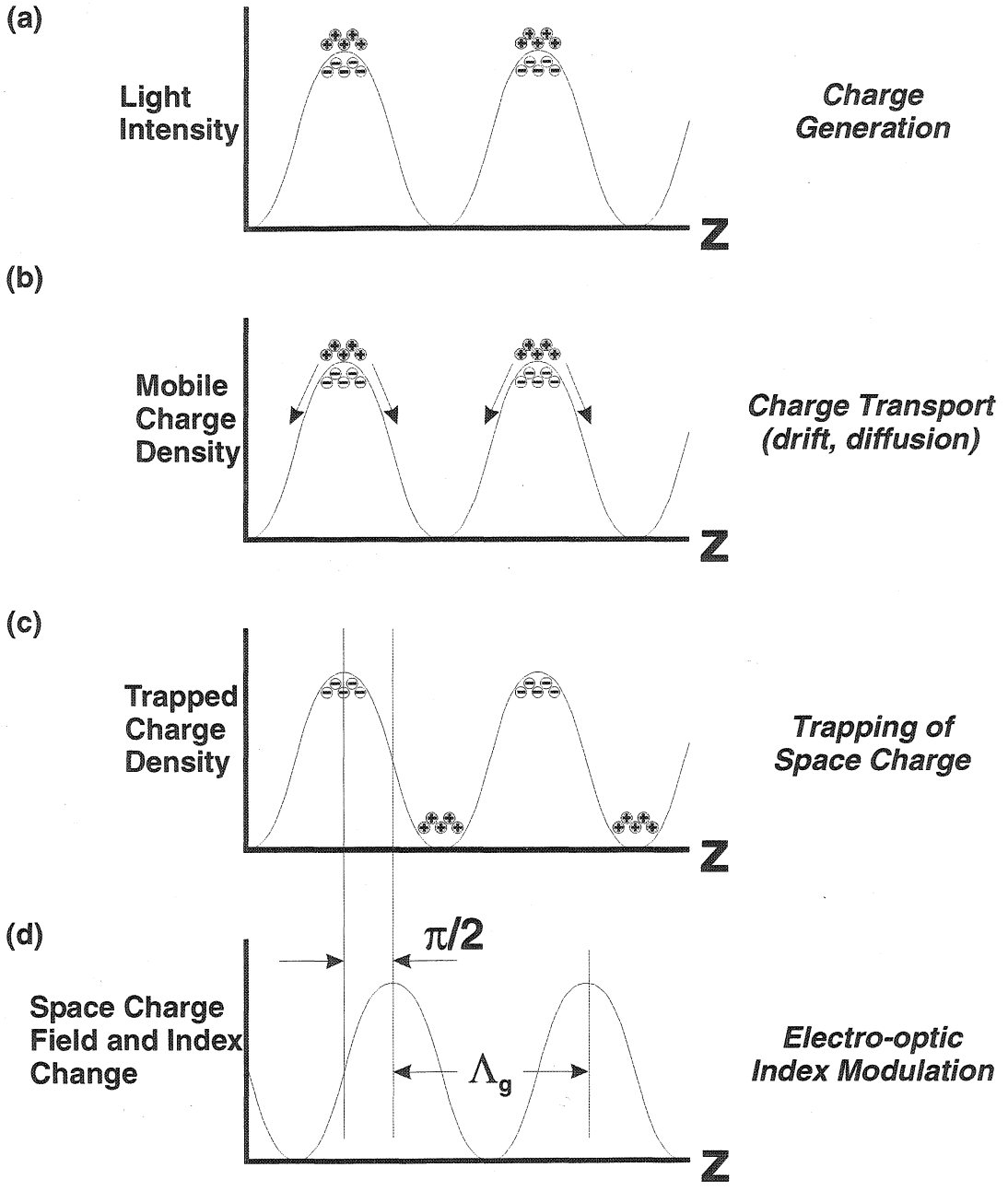

Fig. 2-1. Illustration of photorefractive grating formation (a) charge generation, (b) transport, (c) charge trapping, and (d) refractive index grating resulting from a space-charge field.

this will also cause drift. Eventually the free charges will become trapped as depicted in Figure 2-1(c). Because of drift, the phase of the distribution of charges will be shifted relative to the incident illumination. The sinusoidal distribution of charges gives rise to an

electric field, called the space-charge field, which is 90-degrees out of phase with respect to the charge distribution. In a photorefractive material the space-charge field induces a modulation of the index of refraction through the electro-optic effect. The phase shift between the illumination intensity and the grating is a key indication of the presence of the photorefractive effect and leads to beam-coupling and gain, the measurement of which can be used to confirm the existence of the photorefractive effect in a material.[2-7]

2.1.2 Photorefractive polymers

Several classes of photorefractive polymer materials can be identified, distinguished more or less by the amount of functionalization of the polymer backbone.[2-7] As discussed previously, a photorefractive material requires charge generation, transport, trapping, and an electro-optic response. How these properties are incorporated into the material is the basis for dividing photorefractive polymers into classes. The properties can be incorporated into the polymer itself, produced by the doping of guest molecules into the polymer, or a combination of the two. These three possibilities are schematically shown in Figure 2-2. In the first case, the polymer is responsible for the nonlinear behavior of the material, while dopants provide the required functionality of charge generation, charge transport, and trapping. In the second case, Figure 2-2(b), the polymer chain itself is responsible for charge transport, while dopants provide the nonlinear, generation, and trapping behaviors. In the final case, referred to as fully functionalized polymers, all functionality is provided by functional groups attached to the polymer backbone. The review papers[2-7]-[2-9] should be consulted for a more thorough description of these three schemes as well as a review of photorefractive polymers of each type.

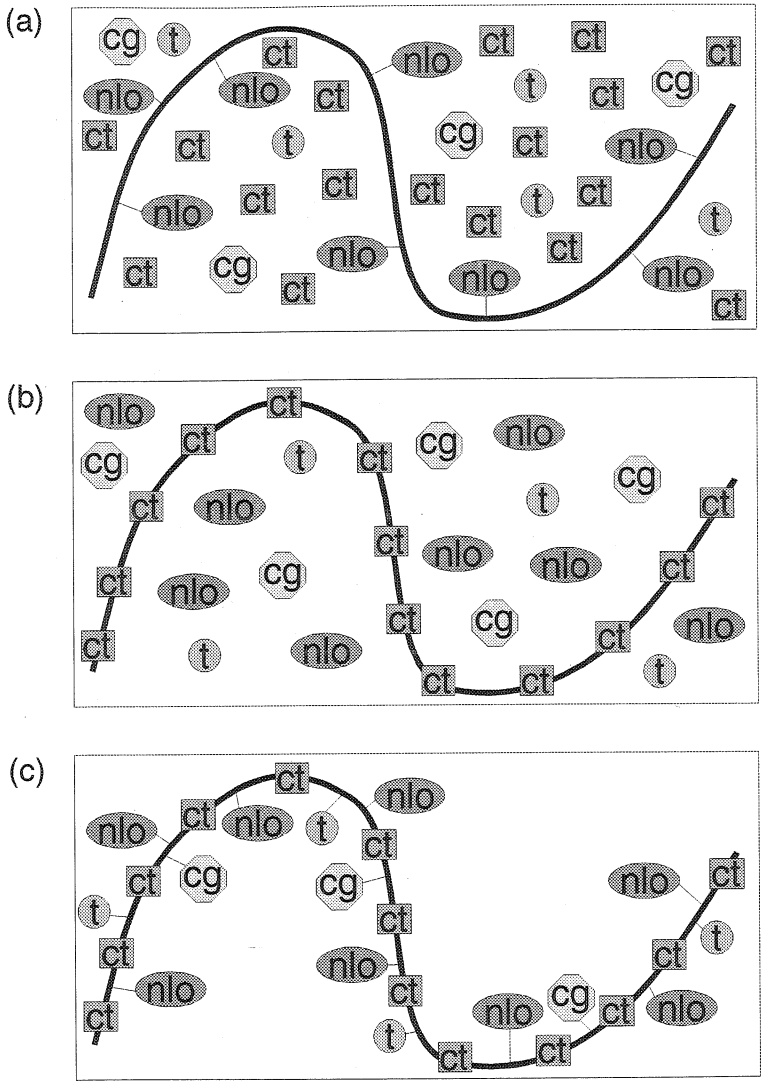

Fig. 2-2. Three approaches to creating a photorefractive polymeric material. (a) The nonlinear optical property (NLO) is incorporated directly into the polymer while dopants are responsible for charge generation (CG), transport (CT), and trapping (T). (b) The polymer chain is responsible only for charge transport. (c) All properties are provided by functional groups attached to the polymer.

The polymers used for the experiments described in this chapter are of the type depicted in Figure 2-2(b). It is very similar to a photorefractive polymer which has achieved 80% diffraction efficiency and is capable of image storage.[2-10] The material is based on the photoconductive polymer poly (N-vinylcarbazole) (PVK), shown in Figure 2-3. Photosensitivity to visible light is obtained by doping with a small amount of 2,4,7-trinitrofluo-

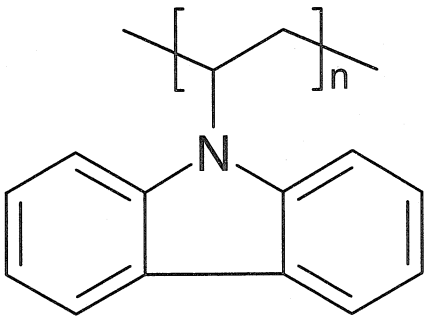

Fig. 2-3. Photoconductive polymer poly (N-vinylcarbazole) (PVK) which forms the basis for the photorefractive polymer used in experiments.

renone (TNF), shown in Figure 2-4, which forms a charge-transfer complex with PVK.[2-10] The electro-optic properties are provided by doping with the azo dyes 2,5-dim-

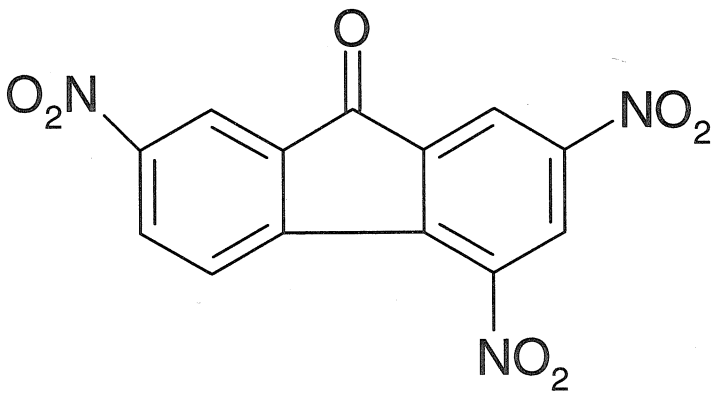

Fig. 2-4. 2,4,7-trinitrofluorenone (TNF) provides photosensitivity for the photorefractive polymer.

ethyl-4,4'-nitrophenylazoanisole (DMNPAA) and 3-methoxy-4,4'-nitrophenylazoanisole (MNPAA), shown in Figure 2-5. The final component, added to allow adjustment of the glass transition temperature of the composition, is N-ethylcarbazole (ECZ), shown in Figure 2-6. The glass transition temperature of the material impacts the speed and amount of reorientation possible with the azo dyes MNPAA and DMNPAA, which are the key contributors to holographic grating formation.

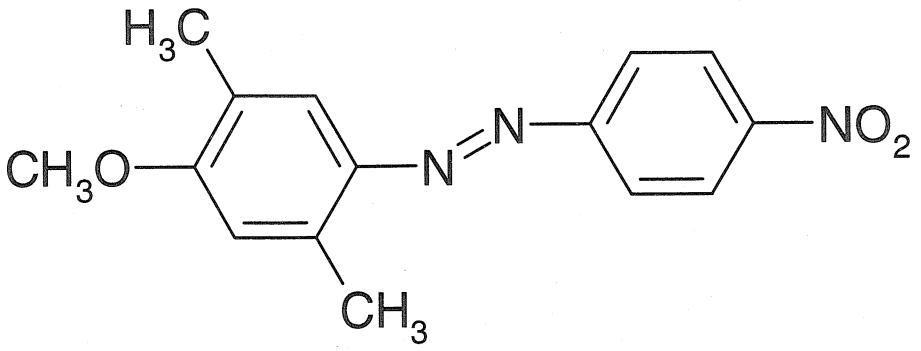

(a)

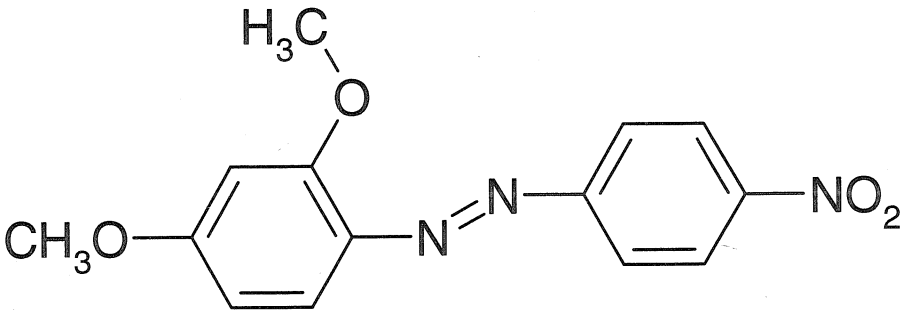

(b)

Fig. 2-5. Azo dyes (a) 2,5-dimethyl-4,4'-nitrophenylazoanisole (DMNPAA) and (b) 3-methoxy-4,4'-nitrophenylazoanisole.

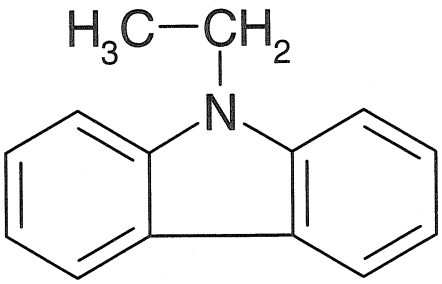

Fig. 2-6. N-ethylcarbazole (ECZ) is a plasticizer added to the photorefractive polymer.

To record a hologram with photorefractive polymers a tilted recording geometry must be used, as depicted in Figure 2-7. The bisector of the two recording beams is at an

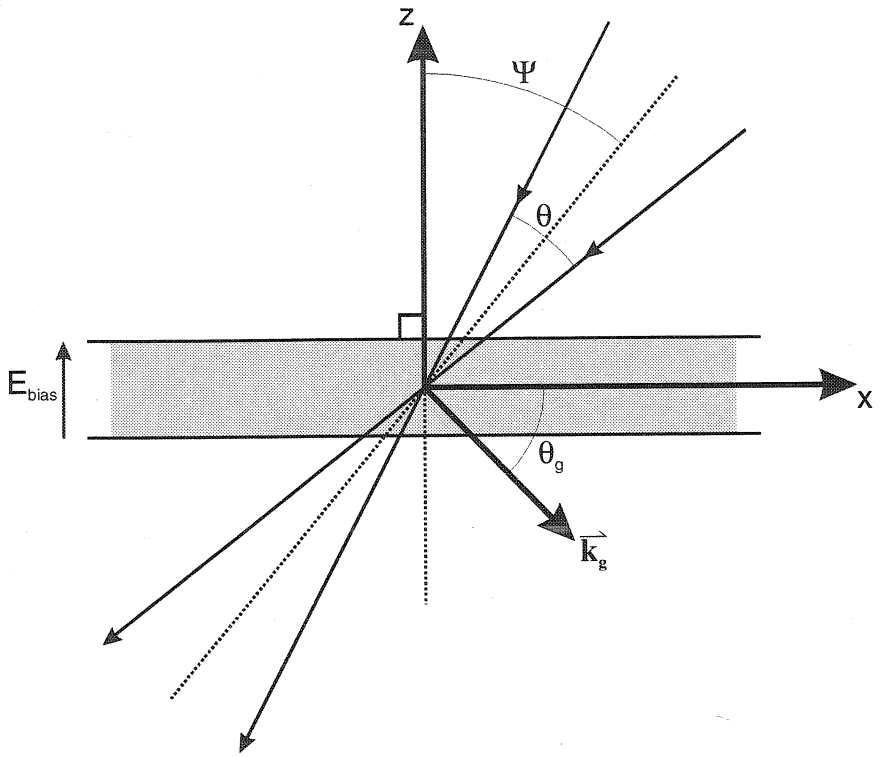

Fig. 2-7. Geometry used for holographic recording in photorefractive polymers.

angle Ψ relative to the surface normal of the material, with the recording beams separated by an angle θ. Writing the incident recording fields as

$$E_1 = e^{j\frac{2\pi}{\lambda}\left[-\sin\left(\Psi-\frac{\theta}{2}\right)\cdot x + \cos\left(\Psi-\frac{\theta}{2}\right)\cdot z\right]} \tag{2-1}$$

and

$$E_2 = e^{j\frac{2\pi}{\lambda}\left[-\sin\left(\Psi+\frac{\theta}{2}\right)\cdot x + \cos\left(\Psi+\frac{\theta}{2}\right)\cdot z\right]} \tag{2-2}$$

allows the holographic grating vector to be expressed as

$$\vec{k_g} = \frac{4\pi}{\lambda}\sin\left(\frac{\theta}{2}\right)\langle\cos(\Psi),\ \sin(\Psi)\rangle\,. \tag{2-3}$$

The space-charge field that results from the generation, transport, and trapping of charges during holographic recording depends on the grating as

$$\vec{E}_{sc} = E_0 \cos(\hat{k}_g \cdot \hat{r}) \langle \cos(\Psi), \sin(\Psi) \rangle . \quad (2\text{-}4)$$

The modulation of the birefringence of the polymer, the primary source of index modulation,[2-1] is proportional to the square of the total electric (polling) field E_p,

$$\vec{E}_p = \langle E_0 \cos(\hat{k}_g \cdot \hat{r}) \cos(\Psi), E_{bias} + E_0 \cos(\hat{k}_g \cdot \hat{r}) \sin(\Psi) \rangle . \quad (2\text{-}5)$$

Due to the presence of the bias a first order grating is produced, as well as higher order gratings, which are typically of no consequence since they are not Bragg-matched upon readout of the hologram.

The reasons for choosing the slanted recording geometry can now be explained. If the grating vector were normal to the bias field, there would be no drift current, the primary mechanism acting to transport charges. The corresponding space charge field would be very weak and consequently so would the hologram. Additionally, since the induced birefringence modulation depends on the square of E_p, without a component of the grating in the direction of the bias field, there would be no cross term $2E_{bias}(E_0 \cos(\hat{k}_g \cdot \hat{r}) \sin(\Psi))$ producing a first order grating. In practice, the maximum tilt angle Ψ that can be achieved is extremely limited by the index of refraction of the recording material, and based on the known dependence of the hologram strength on tilt angle,[2-1] the largest possible angles outside of the material should be used if no index matching techniques are utilized.

2.2 Dynamic behavior

In order to use a photorefractive material for holographic data storage it is necessary to have a complete understanding of the dynamic behavior of the recording characteristics. After a hologram is recorded in a photorefractive material subsequent illumination at the recording wavelength will cause the hologram to decay. If multiple holograms are to be recorded in the material, a suitable exposure schedule must be used. Furthermore, in order to get an idea of the capacity that is possible with the material, the M/# is measured.

2.2.1 Experimental system

The experimental optical system that was used is shown in Figure 2-8. The recording light source was a Helium-Neon laser operating at 633 nm. The raw laser beam was spatially filtered and collimated. A beamsplitter, which was actually a thick piece of glass, was used to provide a low intensity probe beam. A polarizer was used to polarize this beam in the plane of the recording beams, whose polarization was out-of-plane. In this way, the probe beam would not cause holograms to be recorded between it and the recording beams. Furthermore, the direction of polarization was chosen to coincide with the orientation of the birefringence modulation of the material in order to maximize the diffraction efficiency. After the first beamsplitter is a mirror mounted on a galvanometer. A galvanometer is an electro-mechanical device with an axle that rotates by an amount determined by the applied current. By connecting it to a power supply which could be switched by a computer, the mirror could be moved in or out of the beam path. This mirror was used to provide an erasing beam, which was necessary for measuring the erasure dynamics of the material. It was important to erase the holograms with a beam that was not Bragg-matched to the recorded hologram or else during erasure a new hologram would be recorded between the erasing

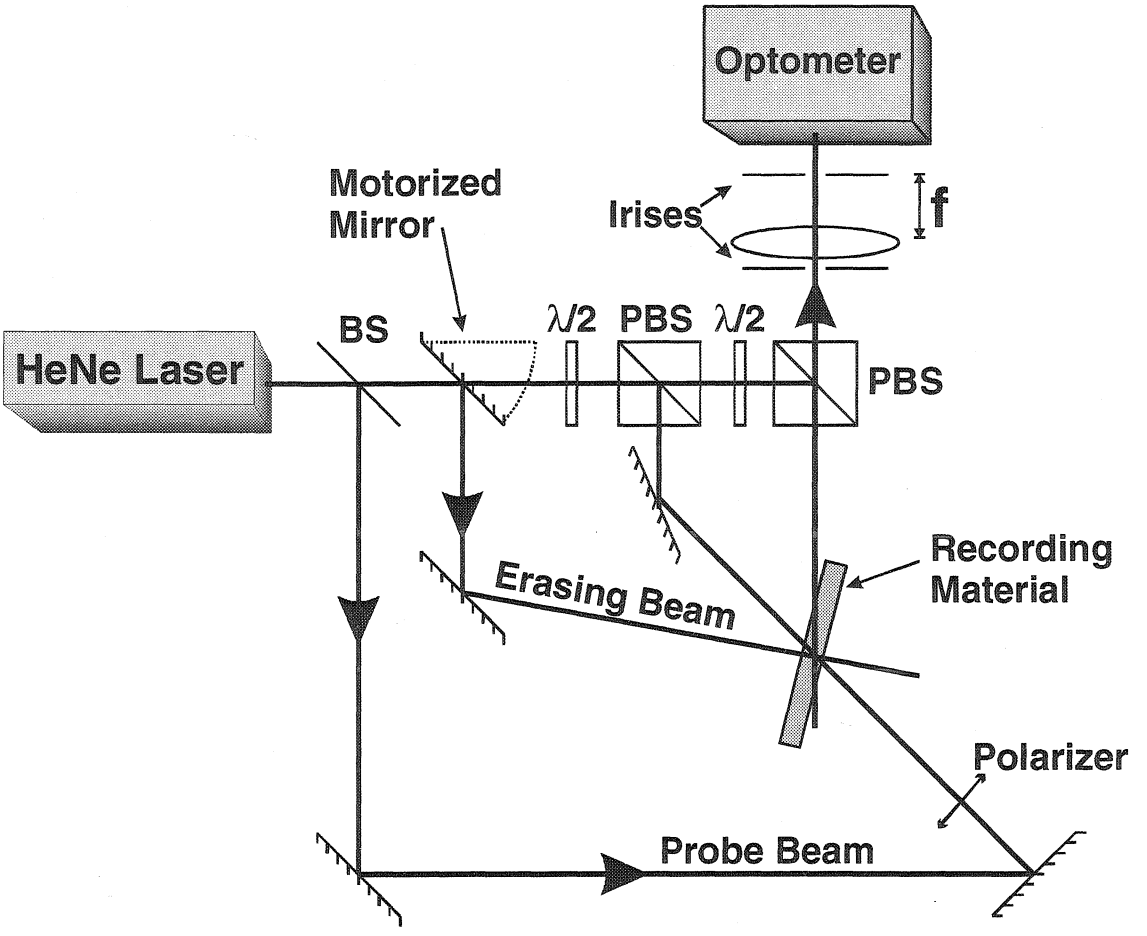

Fig. 2-8. Optical setup used for testing the photorefractive polymer materials. BS: beamsplitter, PBS: polarizing beamsplitter, λ/2: half-wave plate.

beam and the beam diffracted by the hologram. Also, the mirror used in the path of the erasing beam was actually a circular variable attenuator that used partial reflection and transmission to operate. With this device, the amount of power that reached the material could be easily set by rotating the attenuator.

After the erasure-beam pick-off mirror is a set of half-wave plates and polarizing beam splitters. The first half-wave plate is used to adjust the power ratio of the beams that are reflected and transmitted by the subsequent polarizing beam splitter. Since a polarizing beam splitter transmits light with a polarization orthogonal to the reflected beam, the

second half-wave plate is needed to rotate the beam transmitted from the first polarizing beam splitter such that the necessary optical power will be reflected by the second polarizing beam splitter. With this configuration two beams, polarized normal to the plane that contains them, were generated with a large amount of flexibility in their relative intensities.

When the hologram is read out with the probe beam, the diffracted wave will counterpropagate through the same path as the right most recording beam since it was aligned with the left most recording beam in a phase conjugate manner. Since the probe beam was polarized in the plane of interaction, it will pass through the subsequent polarizing beam splitter relatively unattenuated. A set of two irises and a lens are used to block scattered light so that a better signal to noise ratio could be obtained in reading the power of the diffracted beam. With a very slight misalignment of the polarizing beam splitter, reflections from the recording beam could be completely blocked by the second iris, which was placed at the back focal plane of the lens.

The recording beams corresponded to angles of Ψ=60 degrees and θ=20 degrees, outside the material, each with an intensity of 500 $\mu W/cm^2$ at the surface of the material. The erasure beam was normally incident on the material. The intensity of the readout beam was 1 μW after passing through the material. In order to simulate the erasure of a hologram by the subsequent recording of additional holograms, the erasure beam was used with an intensity approximately equal to the sum of the recording beams.

2.2.2 Hologram recording and erasure experiments

Using a photorefractive polymer with (by weight) 42% PVK, 7% ECZ, 25% each of the non-linear chromophores DMNPAA and MNPAA, and 1% TNF, the recording and

non-bragg matched erasure dynamics were measured. Figure 2-9 shows the results of the

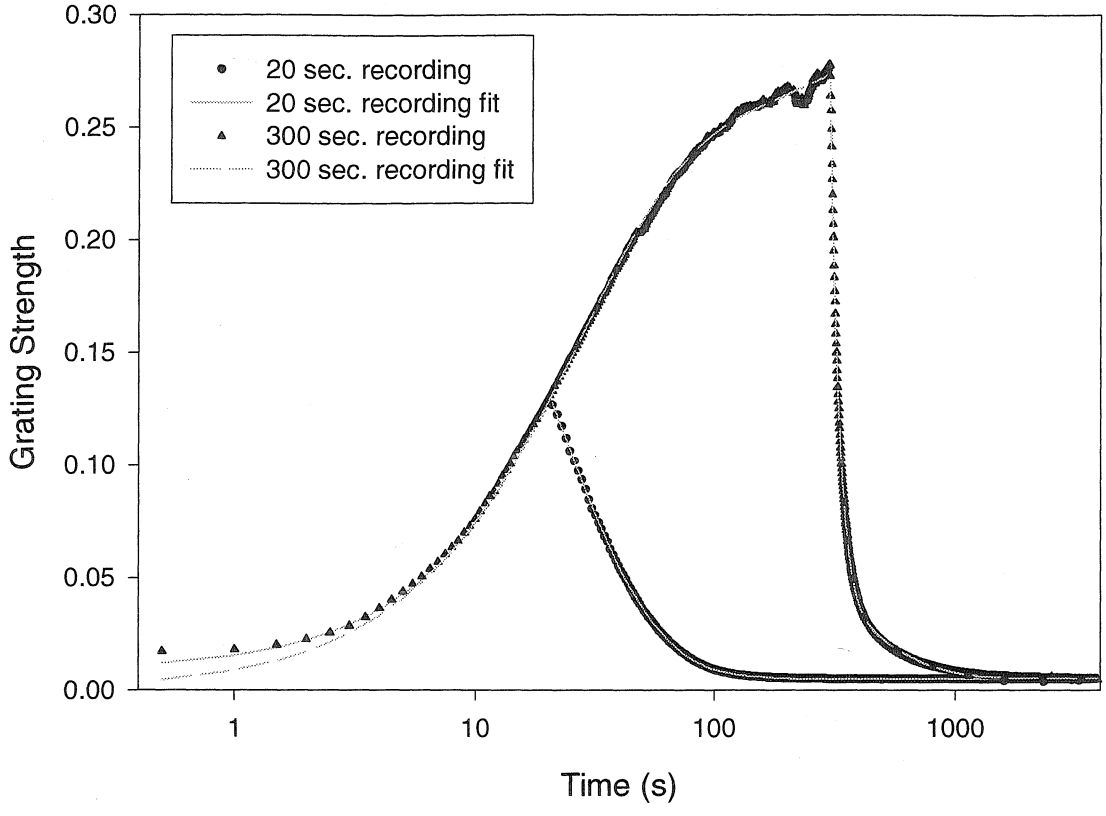

Fig. 2-9. Holographic recording and erasure curves for the photorefractive polymer.

measurements with two different recording times and an applied voltage of 7.7 kV across a 125 micron thick sample. Unlike conventional inorganic photorefractives, the recording and erasure curves could not be fit adequately with mono-exponential functions, but rather bi-exponential functions of the form $A = A_1 \exp(-t/\tau_1) + A_2 \exp(-t/\tau_2)$ were needed.

Another interesting result of this measurement is that different erasure time constants were observed for the two different recording times used. Because of the multi-exponential behavior, it becomes difficult to compare the erasure time constants between the multiple holograms which were recorded for different times. The time it takes the grating strength to decay to 1/e of its maximum value was chosen as a simple way to compare the

erasure behavior of different holograms. The alternatives are to individually compare the two time constants and their associated weighting factors directly, or to use some type of logarithmic averaging of the time constants that takes into account their associated weights. For multiple hologram recording times, Figure 2-10 shows the variation of the 1/e points

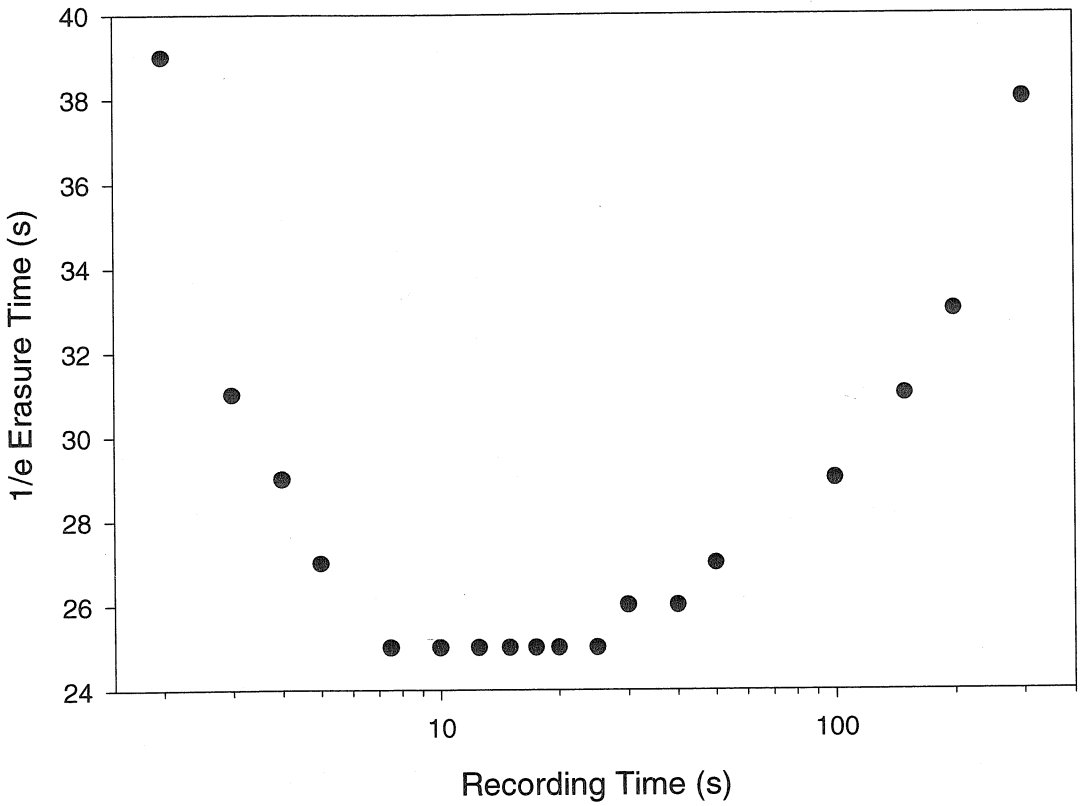

Fig. 2-10. Variation of the erasure rates with recording time.

during erasure. From this plot it is easily seen that the exposure time has an effect on the hologram's erasure behavior. In these experiments the diffraction efficiency was measured in increments of 1 second, which explains the lack of variation at some points and the incremental jumps at others. This large variability in the erasure time scales becomes important

when multiple holograms are to be stored in a single sample of material and a recording schedule needs to be derived, which is the topic of the next section.

Another factor influencing the recording and erasure times is the voltage applied to the sample. The applied field affects the amount of polling that occurs in the material as well as the charge generation and drift processes. Figure 2-11 and Figure 2-12 show the

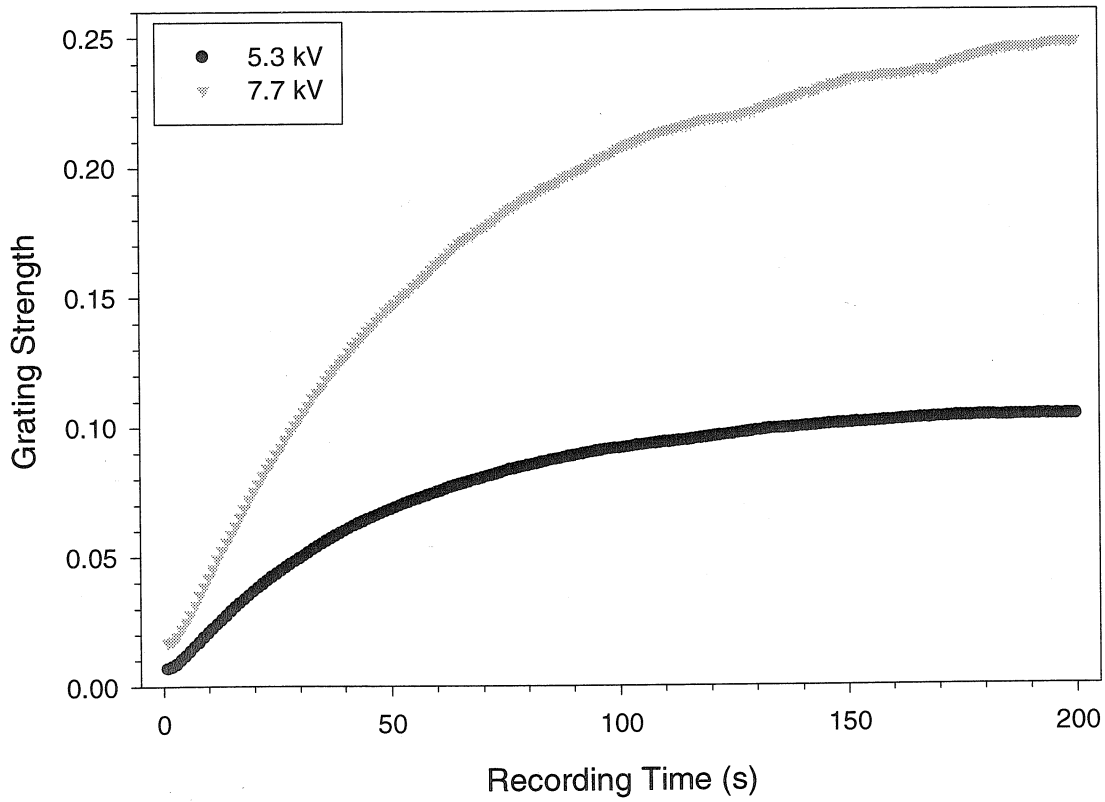

Fig. 2-11. Effect of applied voltage on the recording behavior of the photorefractive polymer.

holographic recording and erasure curves for two different applied fields. The time constants are faster at higher fields for both recording and erasure. Furthermore a higher peak diffraction efficiency can be achieved with a higher applied voltage. Because of these

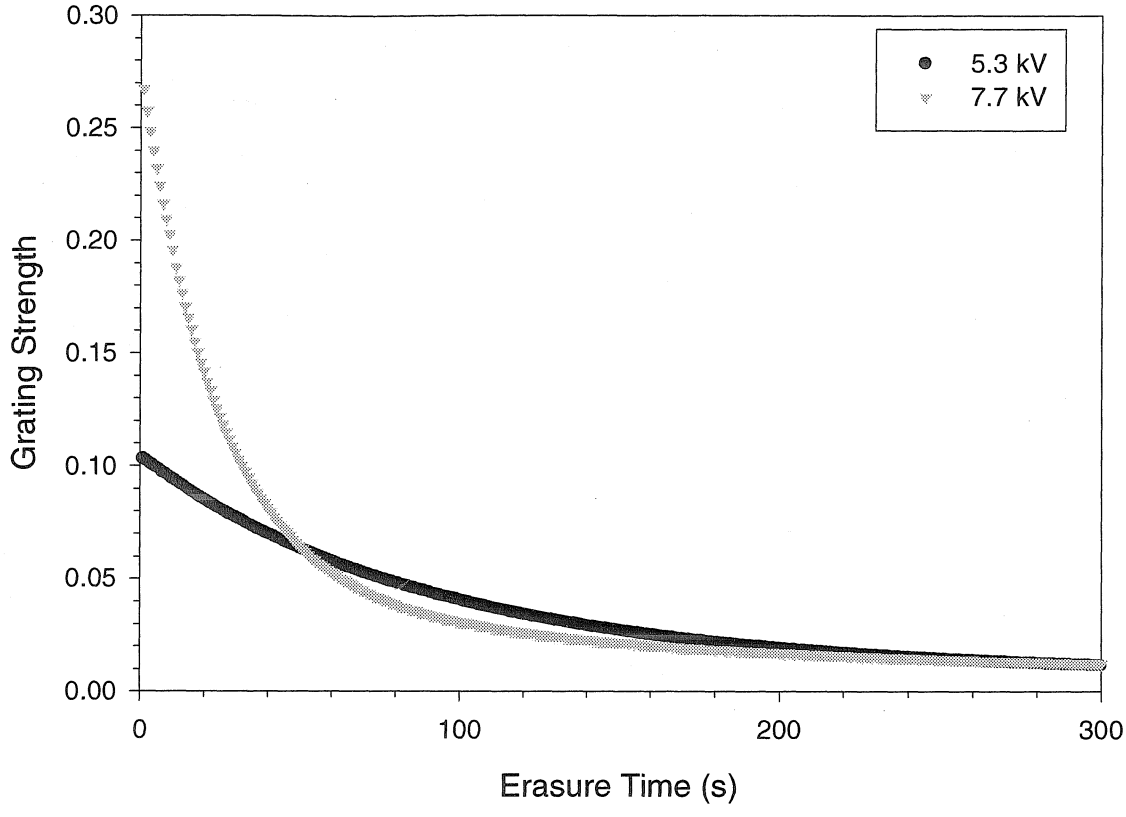

Fig. 2-12. Effect of applied voltage on the erasure behavior of the photorefractive polymer.

effects on the recording behavior of the material, the applied voltage will influence the recording schedule as well as the final M/#.

2.3 Deriving a recording schedule

In order to record multiple holograms of equal strength, a suitable exposure schedule must be used. With conventional inorganic photorefractive materials, mono-exponential recording and erasure dynamics are observed, allowing the exposure schedule and M/# to be calculated by measuring the initial slope of the recording curve and the single hologram erasure time constant. The hologram growth function can be written as

$$A = A_0\left(1 - e^{-\frac{t}{\tau_r}}\right) \tag{2-6}$$

and the hologram erasure can be expressed as

$$A = A_0 e^{-\frac{t}{\tau_e}}, \tag{2-7}$$

where A is the grating strength at time t with a saturation value of A_0, in the case of recording, and an initial strength of A_0, for case of erasing. τ_r and τ_e are the time constants for recording and erasing, respectively.

When M holograms are to be recorded the strength of the m^{th} hologram is given by[2-12]

$$A_m = A_0[1 - \exp(-t_m/\tau_r)]\exp\left(-\sum_{m'=m+1}^{M} t_{m'}/\tau_e\right). \tag{2-8}$$

The m^{th} hologram is recorded for t_m seconds, and then subsequently erased for a time equal to the sum of the recording times for all of the subsequently recorded holograms. To have equal strength holograms requires $A_m=A_{m+1}$, which after assuming $t_m \ll \tau_r, \tau_e$ and linearizing the exponentials yields the exposure schedule

$$1/t_{m+1} = 1/t_m + 1/\tau_e. \tag{2-9}$$

If the first hologram is recorded for $t_1=\tau_e$, then after application of the recording schedule all holograms will have an equal strength of

$$\eta = \left[\frac{A_0}{\tau_r}\frac{\tau_e}{M}\right]^2. \tag{2-10}$$

From the definition of M/#[2-5],

$$\eta = \left(\frac{M/\#}{M}\right)^2, \tag{2-11}$$

the M/# for inorganic photorefractives can be determined from measurement of the initial hologram recording slope and the erasure time constants as

$$M/\# = \left(\frac{A_0}{\tau_r}\right)\tau_e. \tag{2-12}$$

Since photorefractive polymers do not exhibit mono-exponential recording dynamics the M/# cannot be calculated in the standard way. An alternative method for measuring the M/# consists of recording multiple holograms of equal strength and then summing the grating strength of the recorded holograms.[2-11] To record multiple holograms at a single location of material the setup shown in Figure 2-8 was used with the material mounted on a rotation stage to enable the use of peristrophic multiplexing.[2-13] The beam angles, intensities, and polarizations are the same as those described previously for the setup to record a single hologram, and the applied voltage was 7.7 kV. The material was rotated 3 degrees between holograms. After some trials with various erasure time constants, 20 holograms were recording using the above schedule with a time constant of 75 seconds and an initial hologram recording time of 20 seconds. Figure 2-13 shows the strength of the 20 recorded holograms read-out immediately after recording. Obviously, there is significant deviation in the strengths of these holograms, making it difficult to deduce a value for the M/# from this experiment.

The primary factor for the inability of the standard, mono-exponential based, recording schedule to yield equal-strength holograms is the fact that the recording dynamics of the photorefractive polymer are inherently not mono-exponential. Furthermore, it has

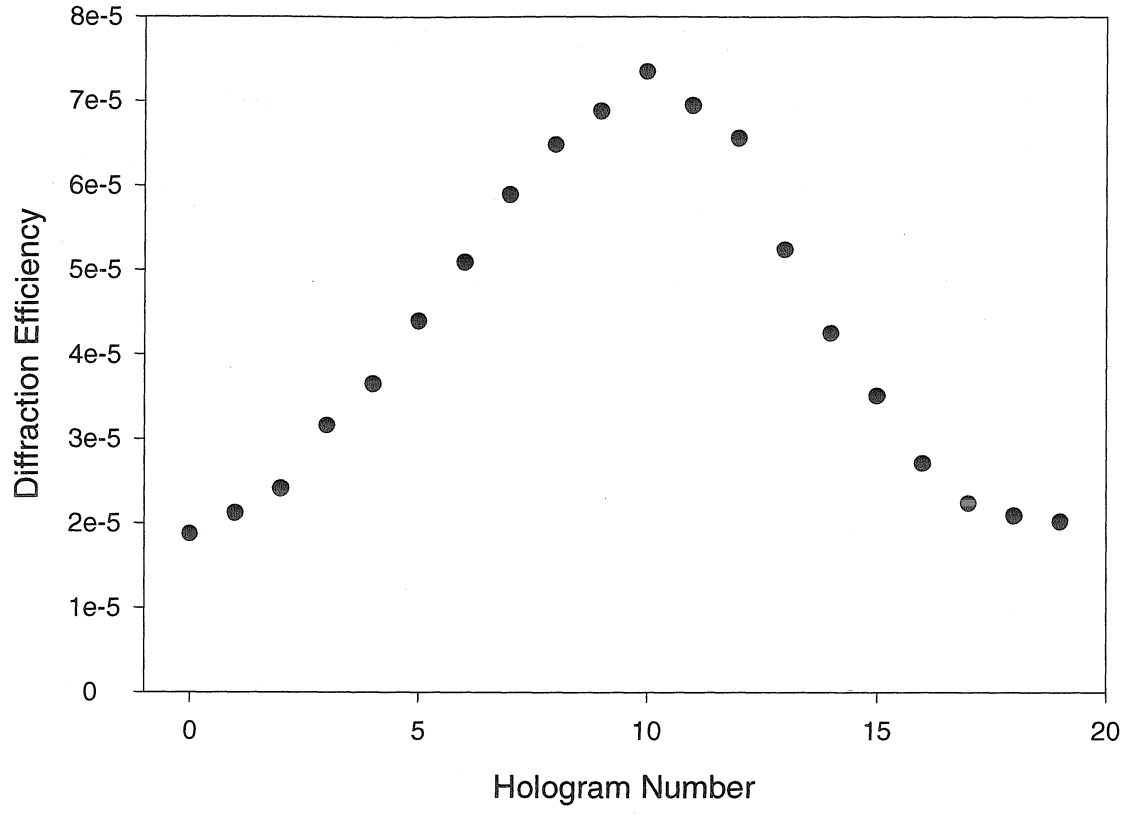

Fig. 2-13. 20 multiplexed holograms recorded using the standard recording schedule.

been experimentally shown that the erasure time constants vary depending on the initial strength of the recorded hologram. For the purpose of finding a holographic recording schedule that equalizes the strength of all the multiplexed holograms, the experimentally measured erasure curves were fit by a series of decaying exponentials. In this case, the strength of the m^{th} hologram after being erased for t_e seconds was:

$$w_m = w(t_m, t_e) = A_{e1}(t_m)e^{-t_e/\tau_{e1}(t_m)} + A_{e2}(t_m)e^{-t_e/\tau_{e2}(t_m)} + \ldots, \qquad (2\text{-}13)$$

where t_m is the time for which the m^{th} hologram was recorded, and the coefficients, A_{ei}, as well as the time constants, τ_{ei}, are determined experimentally by fitting the erasure measurements. To find the time constants and coefficients for various values of t_m, multiple

measurements were performed where the hologram was recorded for a certain time, and then erased. A set of time constants and coefficients were then generated, each applicable to a different recording time t_m. Given the time to record the last, M^{th}, hologram, t_M, the strength of the last hologram is $w_M = w(t_M, 0)$. The recording time required for the M-1 hologram can be computed by numerically solving for t_{M-1} from the relation $w(t_{M-1}, t_M) = w_M$, since the second to last hologram will be erased during the recording of the last hologram. In this way, the times necessary for recording all holograms can be numerically solved for, in backwards order, with the relation

$$w\left(t_m, \sum_{m' = m+1}^{M} t_{m'}\right) = w_M. \tag{2-14}$$

In general when finding numerical solutions the hologram strength function *w* must be known for some recording times t_m which were not experimentally measured. In this case the coefficients and time constants were linearly interpolated from the measured values for the nearest recording times. With this method, by recording and measuring the erasure curves of enough holograms, sufficiently accurate erasure curves can be generated by interpolating the parameters in Equation (2-13).

When using this method for computing the recording schedule, the time for recording the last hologram must be chosen carefully depending on the dynamics of the material and the total number of holograms to be recorded. In some instances, a solution cannot be found. A simple explanation of this is to consider what would happen if the last hologram were picked to be recorded long enough that it reached saturation. Then in this case, no matter how long the second to last hologram is recorded, it cannot reach a value large

enough such that after erasure during the recording of the last hologram they are both of equal strength. Also, if the time for recording the last hologram is chosen too small a solution will be found; however, the strength of all the holograms will be smaller than they would have been if a slightly larger recording time for the last hologram were used. In order to find the recording schedule that would give the strongest holograms possible, a numerical function maximization was used, where the parameter to maximize over was the time to record the last hologram. In order to still be able to interpolate erasure curves as discussed previously, the longest possible hologram recording time allowed was the maximum recording time for which experimental values were obtained.

2.4 Multiplexing experiments

In order to derive a proper recording schedule as discussed previously, erasure curves were measured for 18 different recording times varying between 2 seconds and 5 minutes. A schedule was then made for 11 holograms, but only the last 10 recording times were used to multiplex 10 holograms. Typically the exposure time for the first hologram is an order of magnitude longer than the rest, and by skipping it a lot of time can be saved, with only sacrificing one hologram. The diffraction efficiencies of the ten holograms are shown in Figure 2-14, where it can be seen that although the schedule is better than the conventional multiplexing schedule used in the previous section, the last few holograms are decreasing in strength. One reason for this is the dark decay that occurs in the photorefractive polymer materials. However, the effect of dark decay was not taken into account when deriving the recording schedule. Because of the delay in reading out the holograms, about 0.5 seconds each, the later holograms experience more decay than the holograms read-out

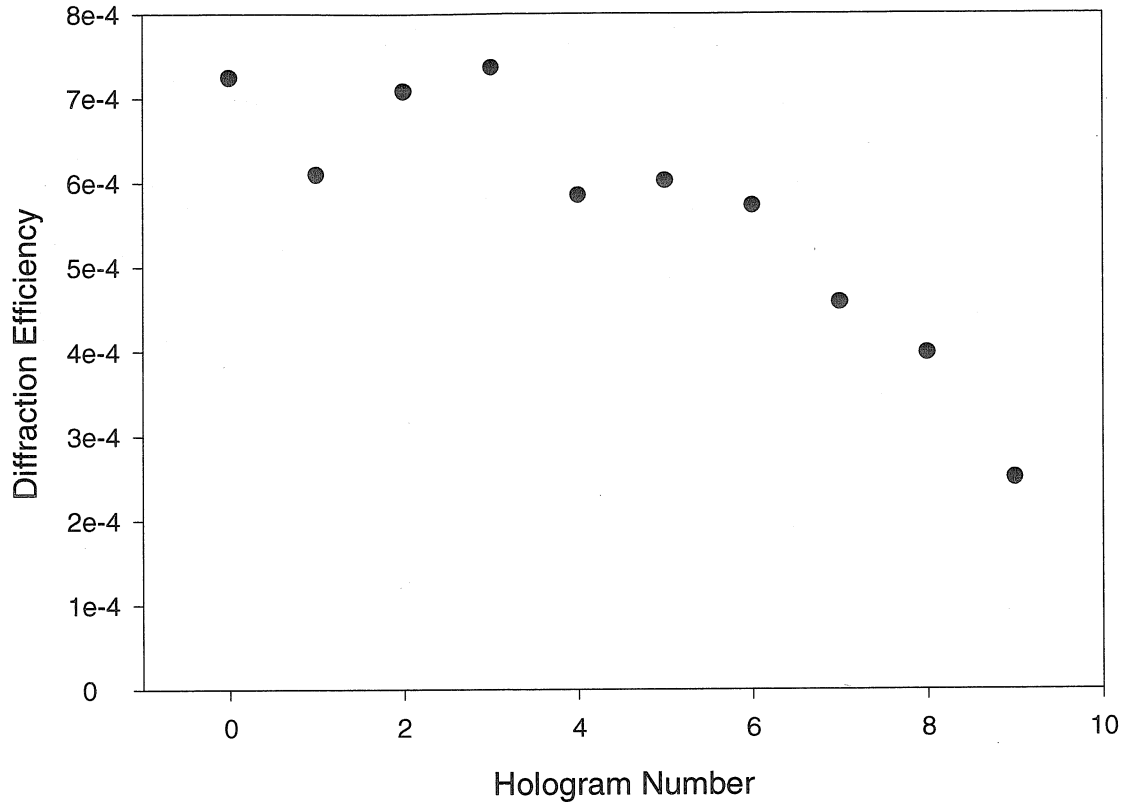

Fig. 2-14. 10 multiplexed holograms recorded using the new exposure schedule

earlier. To compensate for this, the recording schedule was modified by adding 1 second to each recording time, resulting in more even holograms as seen in Figure 2-15. The M-numbers, measured in each case by summing the square root of the diffraction efficiencies, were 0.24 and 0.26. Adding 1 second to each hologram in the second case helps because the holograms recorded first are for relatively long times, and 1 extra second is a negligible increase. However, for the holograms recorded near the end an extra second gives them an extra boost which compensates for the additional dark decay they experience during read-out.

Only 10 holograms were recorded because a schedule for recording more than 12 holograms could not be found with this material due to the fast erasure time constants. In

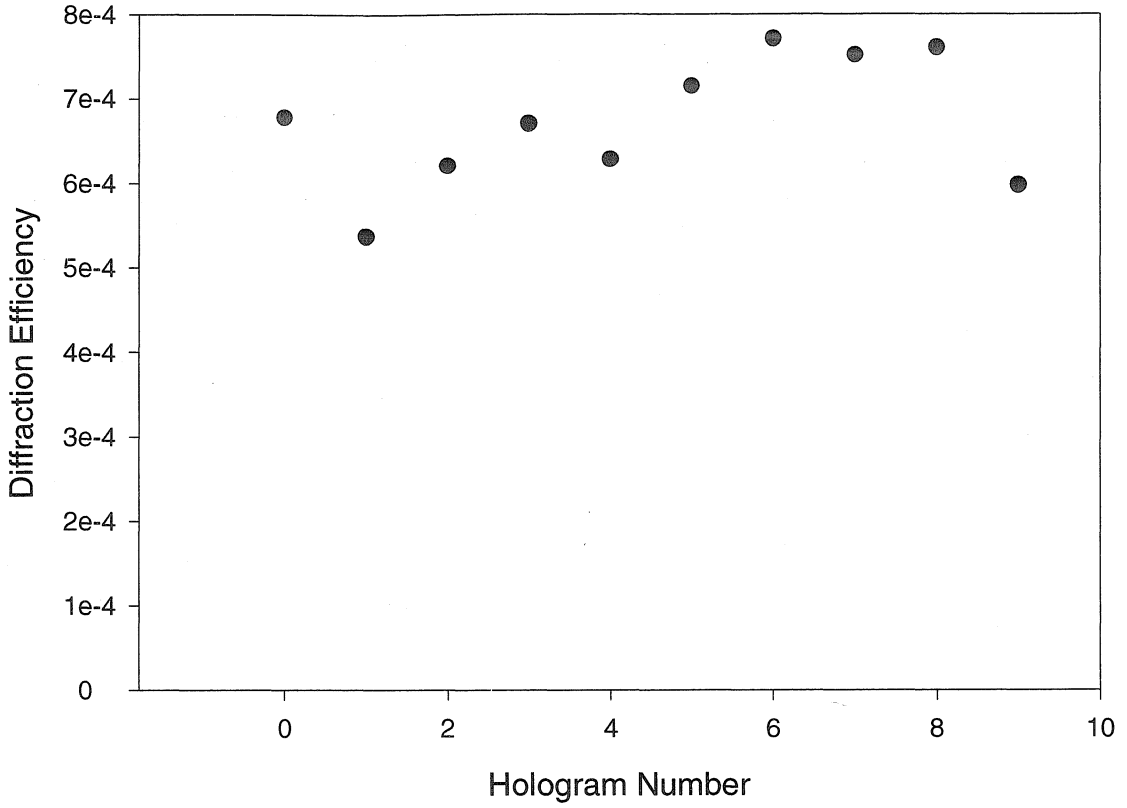

Fig. 2-15. Holograms recorded with the new schedule plus one second each.

an attempt to modify the dynamics of the material, a new composition was created consisting of the same components used previously, but with the addition of N,N,N',N'-Tetraphenylbenzidine (TPD), shown in Figure 2-16. This extra component acts as a deep trap for the

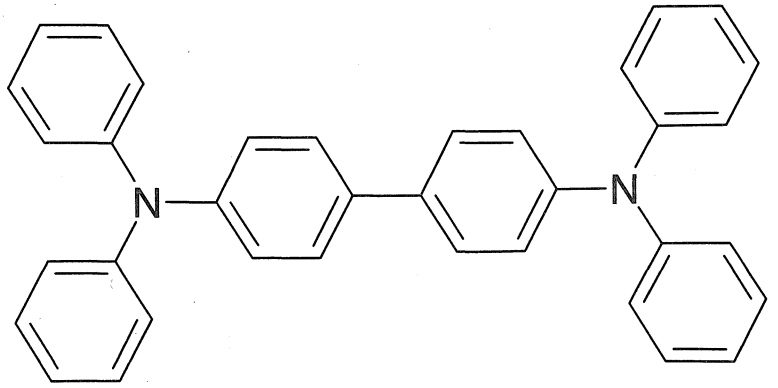

Fig. 2-16. N,N,N',N'-Tetraphenylbenzidine (TPD).

holes and was added to increase the erasure time constant.[2-14] When performing initial measurements of the recording and erasure time constants it was discovered that, for small recording times, after recording the hologram subsequent erasure would actually cause further development of the hologram, which would reach a maximum value and then begin to decay. Figure 2-17 contains plots of recording and erasure curves for several different

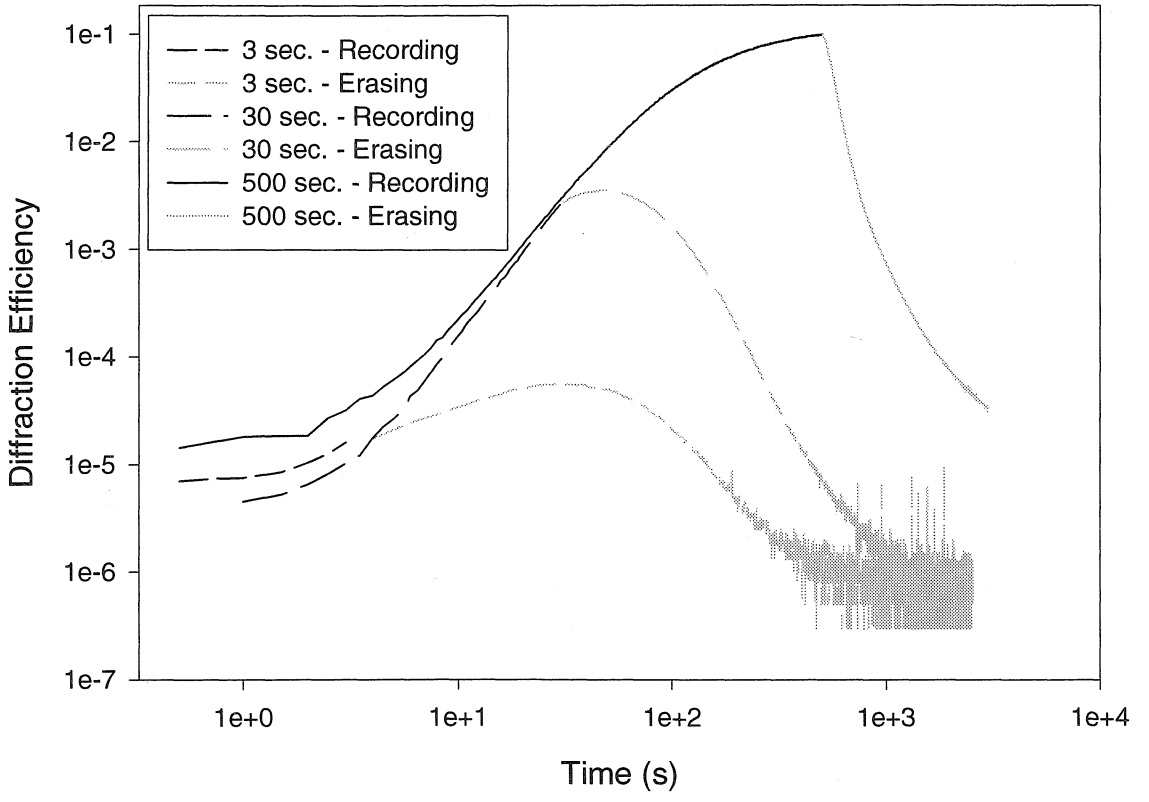

Fig. 2-17. Plot of recording and erasure curves for the TPD material.

recording times for the basic material with an additional 0.82% by weight of TPD, with the application of 5400 V.

In order to choose a concentration of TPD which would provide optimum performance, recording and erasure curve measurements were conducted on samples with 0.82,

1.64, 3, 4.9, and 10% by weight of TPD added to the basic composition. For all samples the behavior was similar to that shown in Figure 2-17, where the growth during erasure effect is larger for small recording times and vanishes for the longest recording times. The recording and erasure curve data was processed to extract key features of the hologram dynamics to allow easier comparisons to be made. Figure 2-18 shows the maximum diffraction effi-

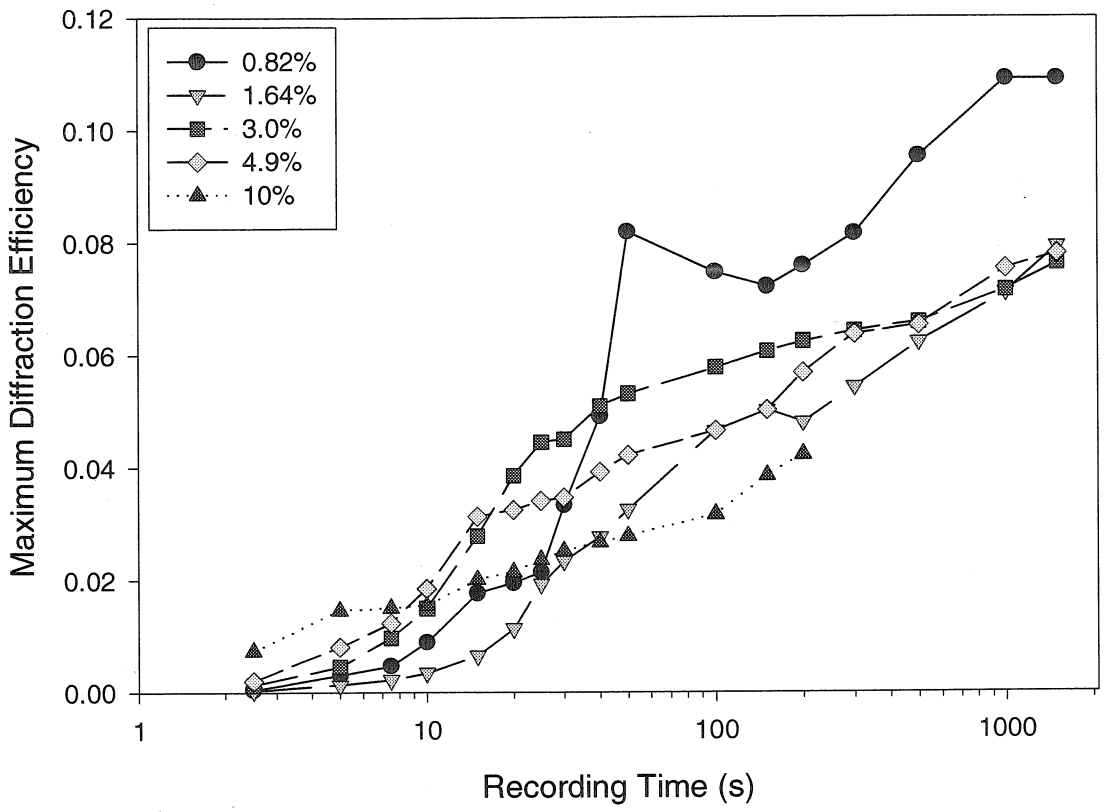

Fig. 2-18. Maximum diffraction efficiency obtained for materials with varying concentrations of TPD and recording time.

ciency achieved with various recording times for all of the samples. The maximum diffraction efficiency that is plotted is not necessarily that achieved during recording due to the growth that is seen during erasure. For the most part the maximum diffraction efficiencies do not vary much between materials for a given recording time. The most notable excep-

tions are for the 10% and 0.82% TPD material. The 10% material had higher efficiencies for low recording times, but then had the lowest efficiencies for long recording times. Roughly the opposite is true with the 0.82% material. The general trend is for the lower concentration TPD materials to have lower diffraction efficiencies with short recording times, yet higher diffraction efficiencies with longer recording times.

Another important aspect of the material's behavior is the decay time. To compare the decay rates, the time taken for the diffraction efficiency to reach 1/e of its value at the end of recording was extracted from the measurements. This means the 1/e erasure time includes the time it takes for the hologram to grow and then start to decay during erasure. Figure 2-19 shows the effects of TPD concentration on the decay rates of the materials. It

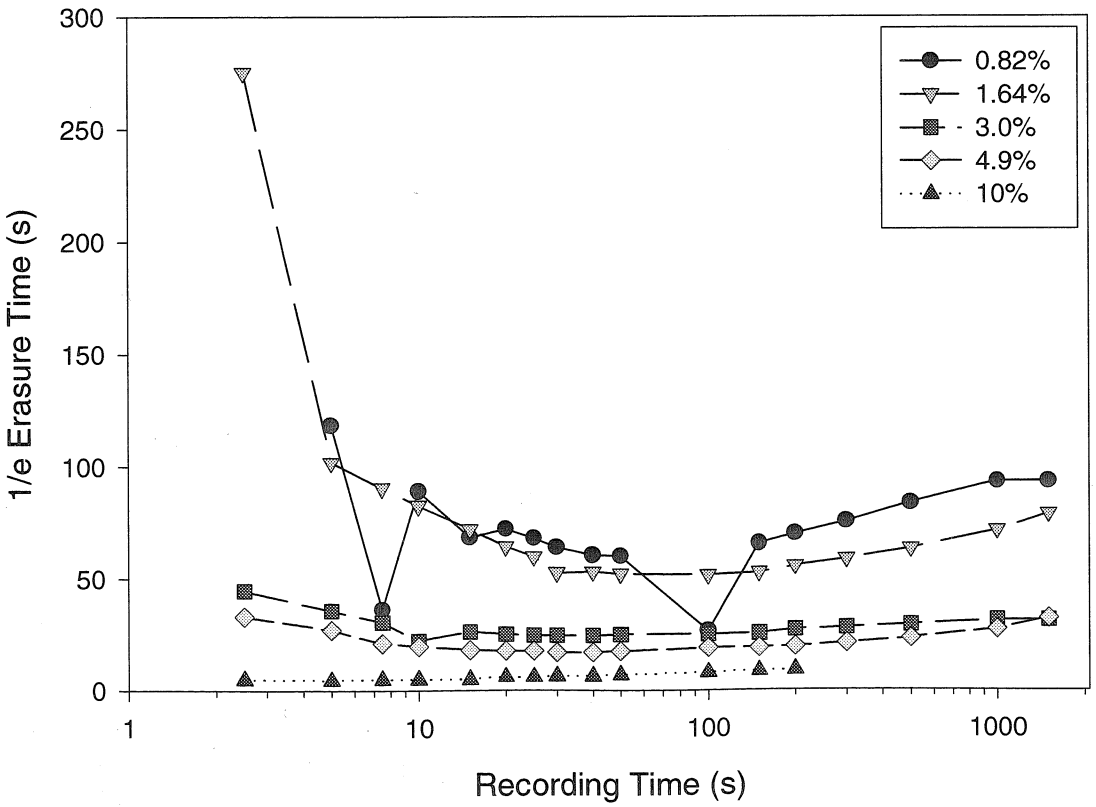

Fig. 2-19. Effect of the TPD concentration on erasure speed of holograms recorded for various exposure times.

is clearly seen that lower concentrations increase the erasure time regardless of the recording time that was used. This plot clearly shows the advantage the addition of TPD brings. From experiments with the basic material, the fast erasure time constants prohibited many holograms from being multiplexed. By increasing the effective erasure time, it is possible to multiplex additional holograms in the modified material.

The most peculiar property of the TPD doped materials is the growth of the hologram during erasure. This can be characterized by the amount of amplification that occurs after recording. Figure 2-20 is a plot of amplification that occurs in all the materials with

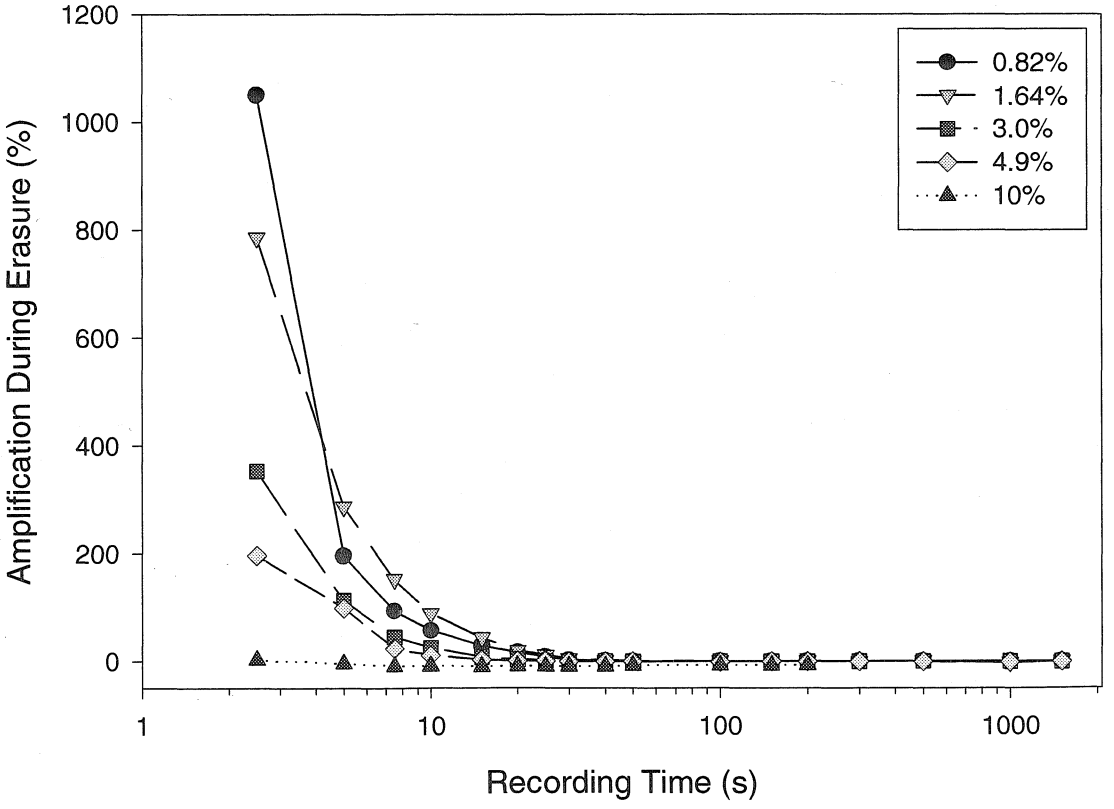

Fig. 2-20. Growth of holograms during erasure for various recording times and TPD concentrations.

different recording times. Roughly speaking, lower concentrations of TPD yield higher amplifications. Because of the higher amplification and longer effective erasure time of the materials with low TPD concentration, a material with 0.82% was chosen to be used for multiplexing experiments.

In order to calculate a multiplexing schedule with this material, the erasure curves were fit with a tri-exponential function where one of the coefficients is negative to account for the growth during erasure. The growth-during-erasure behavior results in exposure schedules whose recording times are not monotonically decreasing with hologram number, as is the case with conventional photorefractive materials. Figure 2-21 is an illustration of

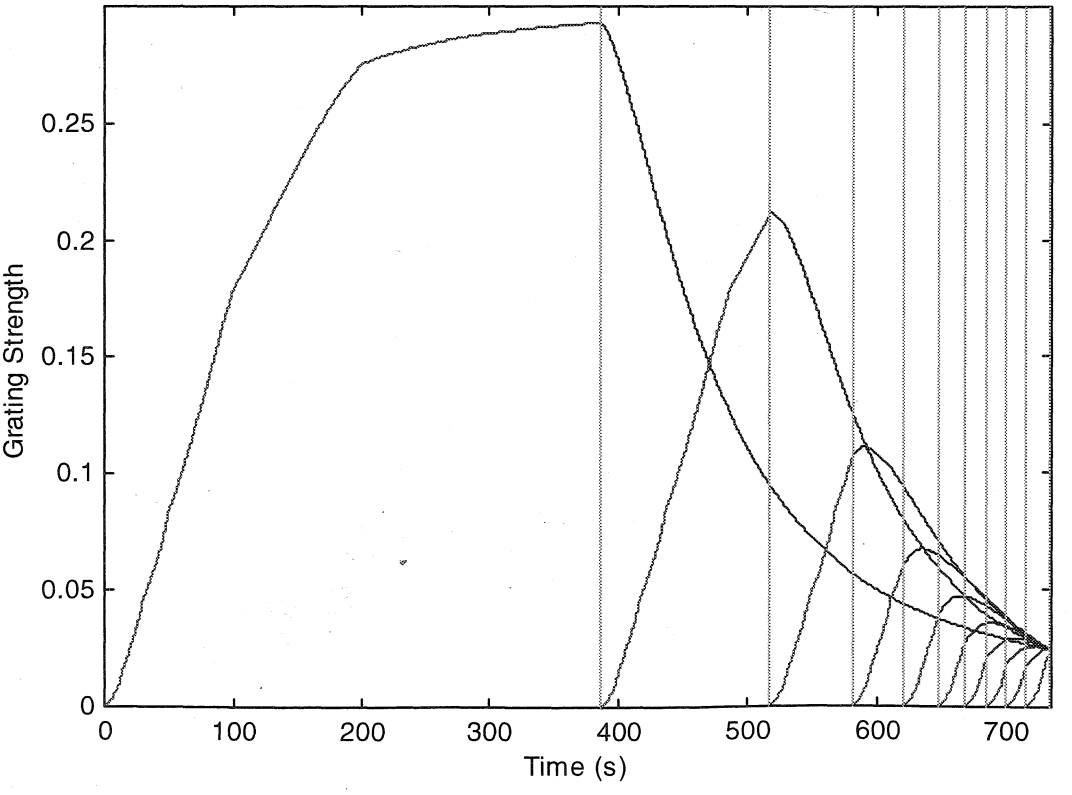

Fig. 2-21. Hologram strengths during recording with an exposure schedule for recording 10 holograms in the material with the TPD. The vertical dashed lines mark the end of recording for one hologram and the start of recording for another.

hologram development during the recording of 10 holograms with this material. The first hologram is recorded to saturation. Due to the erasure time constants decreasing with shorter exposures when the exposure times are relatively long, subsequent holograms must be recorded beyond the decay of the previous holograms, so that after their erasure they will become equalized. Furthermore, those holograms with shorter recording times experience growth during erasure, allowing in some cases their initial strengths to be less than what they will be at the end of recording. Finally, after the last hologram is recorded, all holograms have either grown or erased so that they have equal strengths.

Multiplexing experiments were performed with this material to record 20 and 30 holograms. First, schedules were calculated for recording 21 and 31 holograms. Because the first hologram requires much more time for recording than the subsequent holograms, the first recording time was skipped, resulting in 20 and 30 holograms being recorded. Figure 2-22 and Figure 2-23 show the results of these multiplexing experiments. Overall the uniformity of the recorded holograms is very good with the major deviations existing only at the boundaries. For the case with 20 holograms the M/# is 0.3, and for the case with 30 holograms it is 0.23. The M/# decreased for the case of 30 holograms because of the increased time required for read-out. During this time, dark decay caused erasure of the holograms more so than would have occurred with only 20 holograms. Furthermore, dark decay is partially responsible for any inequality between hologram strengths because each individual hologram will decay with a different time constant after recording has been completed.

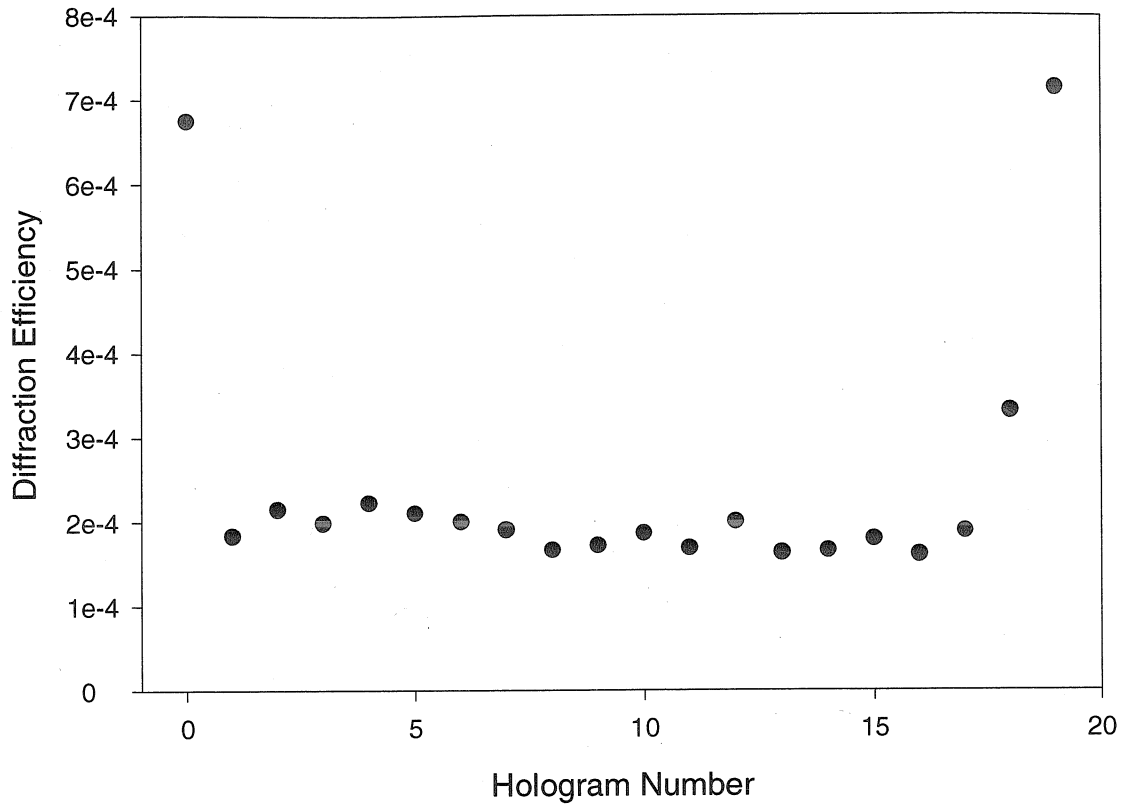

Fig. 2-22. 20 holograms multiplexed in the TPD material.

2.5 Effect of dark decay on hologram strength

To see the effects of dark decay on the measurement of multiplexed holograms, an experiment was performed where the holograms were measured after waiting a predetermined amount of time after the completion of recording. For this experiment 20 holograms were recorded, measured after a delay, and then erased with the erasure beam. Each subsequent M/# measurement is the result of re-recording the 20 holograms and then waiting a different length of time before measuring them. From Figure 2-24 the effects of dark decay are clear. It reduces the measured M/# since all holograms decay with time. More interesting is the plot in Figure 2-25 where we see the measured hologram's strengths for various delay times. The holograms are most equal for the case with no delay. However, after just

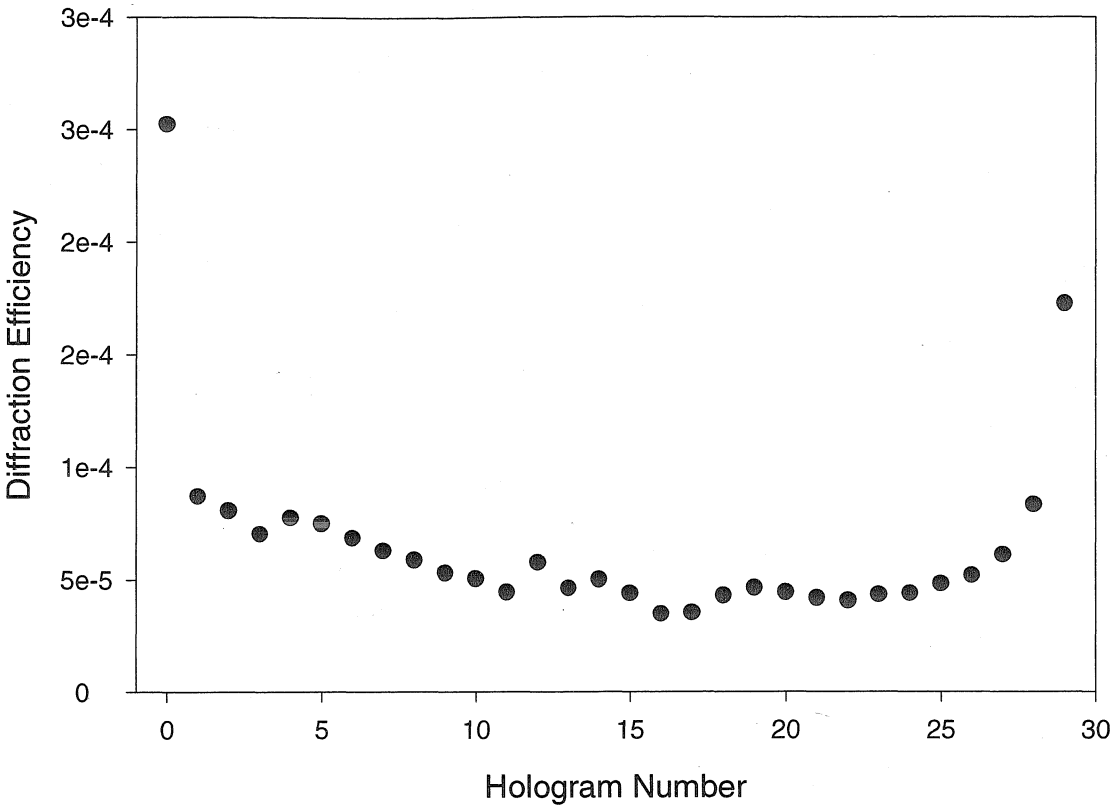

Fig. 2-23. 30 holograms multiplexed in the TPD material.

10 minutes in the dark, the holograms have decayed such that the earlier holograms show an exponential decay with hologram number, demonstrating the fact that each hologram has a different dark erasure time constant based on its recording time and where it was recorded in the sequence.

2.6 Conclusion

Since photorefractive polymers are a relatively new holographic recording material, it was not known what type of dynamic behavior could be expected. Initial assumptions were that they would behave similarly to $LiNbO_3$ or other inorganic photorefractive materials. However, because of the increased complexity of these materials, that was not the

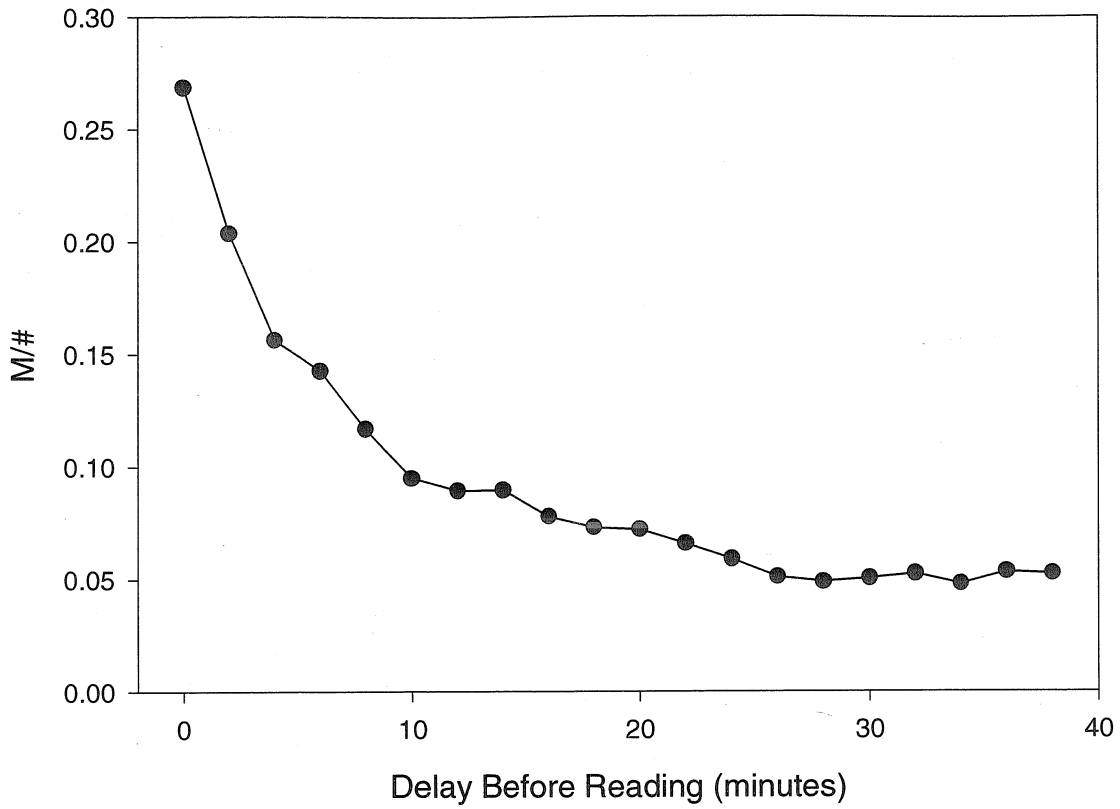

Fig. 2-24. Effect of dark decay on the measurement of M/#. Each point is the M/# calculated, after a delay, from the measured strengths of 20 holograms.

case. Because they did not exhibit mono-exponential recording and erasure dynamics, a new system had to be developed for deriving a recording schedule for these materials. This new system depended on the experimental measurement of the material's dynamics and subsequent numerical analysis of the dynamics to determine a suitable recording schedule. The schedule was shown to give improved multiple-hologram recording results compared to the original schedule for inorganics. However, the photorefractive polymer's performance was insufficient for multiplexing more than 10 holograms.

In an attempt to improve the performance of the photorefractive polymer, a dopant TPD was added to act as additional traps for the holes. The M/# was measured experimentally as 0.3. With this modified material a maximum of 30 holograms could be recorded.

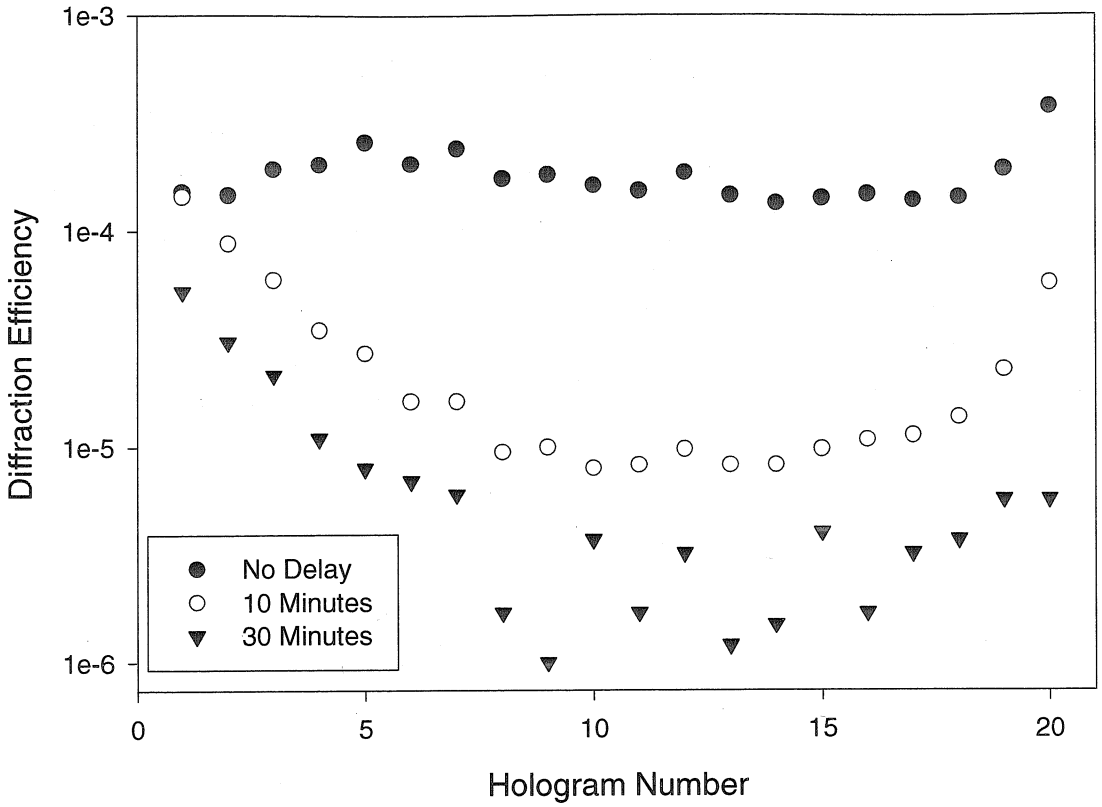

Fig. 2-25. Relative hologram strengths for measurement delays of 0, 10, and 20 minutes.

While photorefractive polymers are capable of achieving very large single hologram diffraction efficiencies, several problems remain to be solved before they are ready to be applied to applications requiring the multiplexing of holograms, such as holographic data storage and holographic correlators. The dependence of the erasure time constant on the initial hologram strength causes the holograms to lose their equality shortly after recording is complete. Furthermore, the fast dark decay times pose serious problems if persistent data storage is to be achieved. Finally, there is no gating mechanism involved as is the case in some inorganic materials such as doubly doped lithium niobate[2-15] and reduced near-stoichiometric lithium niobate.[2-16] Consequently, it is not possible to achieve non-destructive readout of holograms recorded in this material.

References

[2-1] W. E. Moerner, S. M. Silence, F. Hache, and G. C. Bjorklund, "Orientationally enhanced photorefractive effect in polymers," J. Opt. Soc. Am. B **11**(2), 320-330 (1994).

[2-2] K. Meerholz, B. L. Volodin, Sandalphon, B. Kippelen, and N. Peyghambarian, "A photorefractive polymer with high optical gain and diffraction efficiency near 100%," Nature **371**, 497-500 (1994).

[2-3] A. Grunnet-Jepson, C. L. Thompson, R. J. Twieg, and W. E. Moerner, "High performance photorefractive polymer with improved stability," Appl. Phys. Lett. **70**, 1515-1517 (1997).

[2-4] K. Meerholz, B. Kippelen, and N. Peyghambarian, "Non-Crystalline Organic Photorefractive Materials: Chemistry, Physics, and applications" in *Electrical and Optical Polymer Systems*, D.L. Wise, G.E. Wenk, D.J. Trantolo, J.D. Gresser, and T.M. Cooper, Eds. (World Scientific, 1998).

[2-5] F. H. Mok, G. W. Burr, and D. Psaltis, "System metric for holographic memory systems," Opt. Lett. **21,** 896 (1996).

[2-6] Introduction to Photorefractive Nonlinear Optics, Pochi Yeh, 1993 NY, NY. John Wiley & Sons, Inc.

[2-7] W. E. Moerner, A. Grunnet-Jepson, and C. L. Thompson, "Photorefractive polymers," Annu. Rev. Mater. Sci. **27**, 585-623 (1997).

[2-8] W. E. Moerner and S. M. Silence, "Polymeric photorefractive materials," Chem. Rev. **94**, 127-155 (1994).

[2-9] B. Kippelen, Sandalphon, B. L. Volodin, K. Meerholz, and N. Peyghambarian, "Organic polymers for photorefractive applications," in Photonic and Optoelectronic Polymers, American Chemical Society, 1997.

[2-10] B. L. Volodin, Sandalphon, K. Meerholz, B. Kippelen, N. V. Kukhtarev, and N. Peyghambarian, "Highly efficient photorefractive polymers for dynamic holography," Opt. Eng. **34**, 2213-2223 (1995).

[2-11] A. Pu, K. Curtis, and D. Psaltis, "Exposure schedule for multiplexing holograms in photopolymer films," Opt. Eng. **35**, 2824-2829 (1996).

[2-12] D. Psaltis, D. Brady, and K. Wagner, "Adaptive optical networks using photorefractive crystals," Appl. Opt. **27**, 1752-1759 (1988).

[2-13] K. Curtis, A. Pu, and D. Psaltis, "Method for holographic storage using peristrophic multiplexing," Opt. Lett. **19**, 993-994 (1994).

[2-14] Y. Zhang, R. Burzynski, S. Ghosal, and M. K. Casstevens, "Photorefractive polymers and composites," Adv. Mat. **8**, 111-125 (1996).

[2-15] K. Buse, A. Adibi, and D. Psaltis, "Non-volatile holographic storage in doubly doped lithium niobate crystals," Nature **393**, 665 (1998).

[2-16] H. Guenther, R. Macfarlane, Y. Furukawa, K. Kitamura, and R. Neurgaonkar, "Two-color holography in reduced near-stoichiometric lithium niobate," Appl. Opt. **37**, 7611 (1998).

3 Diffusion Amplified Photopolymers

3.1 Introduction

The primary factor limiting the performance of many holographic applications is the recording material itself. This chapter describes holographic recording with materials displaying hologram amplification through diffusion. While the photorefractive polymer materials of the previous chapter were capable of being recorded and erased, these materials are write-once, and permanent. Section 3.2 describes experiments characterizing the recording behavior of phenanthrenequinone-doped poly(methyl methacrylate) (PQ:PMMA). Since this material was limited in performance by the maximum achievable doping level, a new material system was desired to overcome this limitation. The initial development of the new material, also based on the diffusion amplification principle, is described in Section 3.3. Experiments show the fundamental behavior of the material agrees with what is expected of the diffusion amplification process.

3.2 Phenanthrenequinone-doped PMMA

Phenanthrenequinone-doped poly(methyl methacrylate) (PQ:PMMA) is a photopolymer holographic recording material that can be made in large thicknesses and does not exhibit any shrinkage.[3-1][3-2] Holograms are made permanent by a post-recording diffusion amplification process. PQ:PMMA thus exhibits many properties which make it a candidate for use in many volume holography applications.

This section presents experimental results concerning the holographic recording characteristics of this material. First, single hologram recording experiments are described. The observed behavior is understood with a model of the recording mechanisms which take place. Section 3.2.4 then describes experiments with multiplexing holograms in this material. The M/# is measured with various exposure energies to find the optimal. Finally, the measurements of optically induced birefringence are discussed in Section 3.2.5.

3.2.1 Sample preparation

The material consists of the polymer host matrix with added PQ molecules as photosensitive dopant. Sample preparation consists of dissolving 9,10-phenanthrenequinone, shown in Figure 3-1, in the monomer methyl methacrylate (MMA) together with the free-

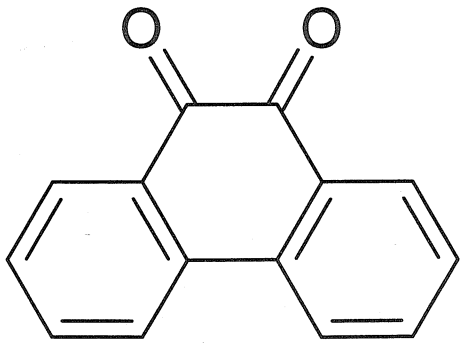

Fig. 3-1. 9,10-Phenanthrenequinone.

radical initiator 2,2-Azobisisobutyronitrile (AIBN). This solution is then poured into molds and polymerized in an argon atmosphere at an elevated temperature for 2 days. A concentration of 0.7% by weight of PQ relative to MMA is used, which is the solubility limit at room temperature.

The molding process allows samples to be fabricated in a variety of geometries. Samples of this material have been fabricated with high optical quality and variable thick-

nesses, up to 5 mm, and in a variety of shapes, as seen in Figure 3-2. Disks ranging between

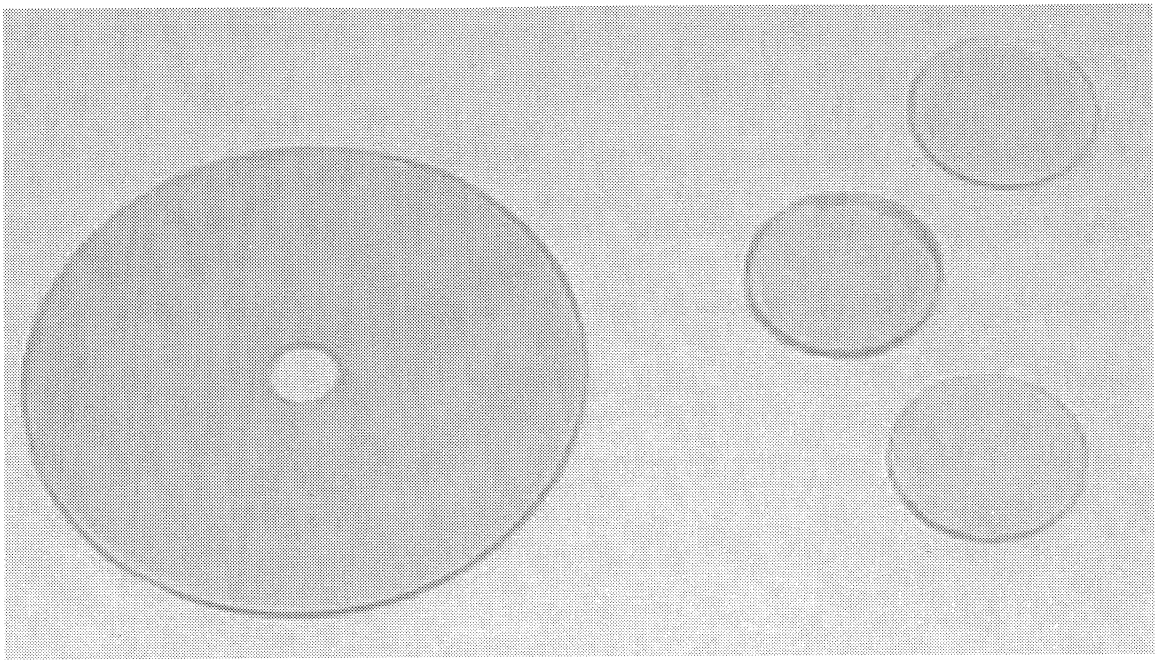

Fig. 3-2. Phenanthrenequinone-doped PMMA samples.

2.5 cm to 10 cm in diameter with 1 to 5 mm thicknesses have been made utilizing molds constructed from pairs of glass optical flats. Furthermore, bi-convex lenses have been made with this material by using two plano-concave lenses as molds. An alternative method which has been tested is to compression mold after partial polymerization. With this technique, the material is mixed and polymerization is begun as usual. However, before polymerization is complete the material will not be completely hardened. At this stage the material is placed into a steel compression mold and pressed. It will then take the shape of the mold, and because it has been partially polymerized, is structurally capable of maintaining the shape after being removed from the mold. Polymerization is then completed and the sample hardens. This technique has been used to create 1 3/8" diameter disks however, it is more appropriate for making shapes, such as cubes, that require multiple adjacent faces with good optical quality.

3.2.2 Basic material properties

3.2.2.1 Absorption spectra

In order to record holograms a material must be capable of absorbing light at some wavelength and then somehow create an index or absorption change in response to the illumination. From the Kramers-Kronig relations it can be shown that a measured change in absorption can be related to changes in index of refraction[3-3]. The absorption spectra have been measured for samples of PMMA (Figure 3-3) and PMMA doped with PQ before,

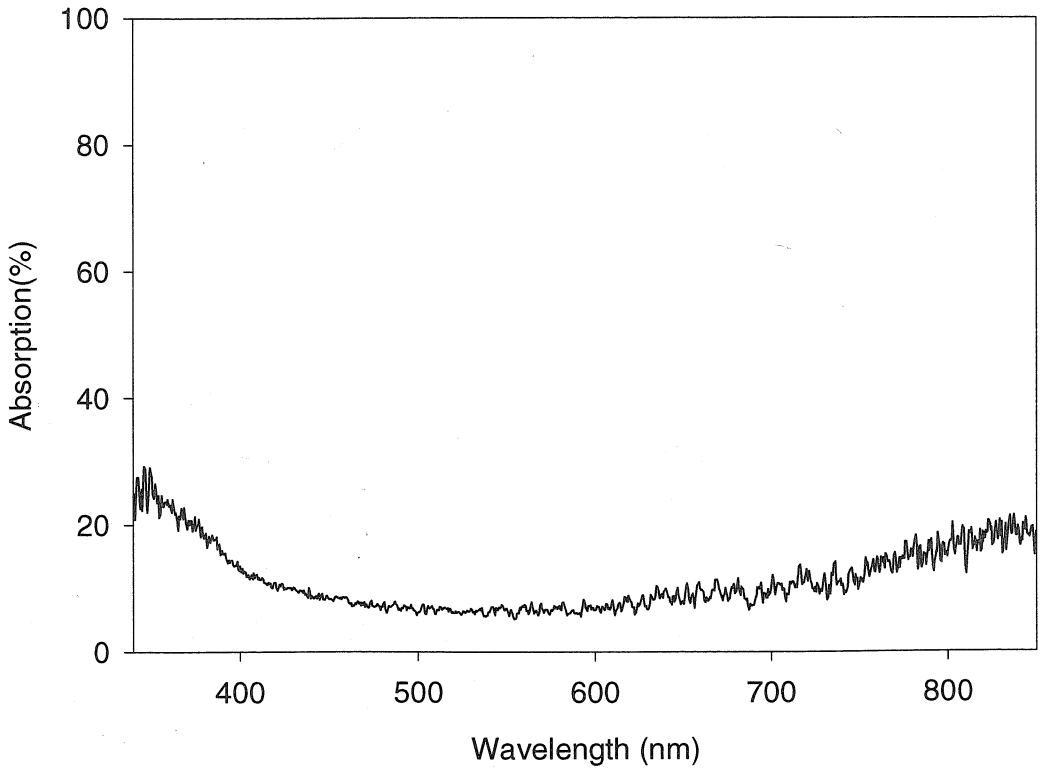

Fig. 3-3. Absorption of a 1-mm thick sample of PMMA.

Figure 3-4, and after, Figure 3-5, exposure. As can be seen from the absorption spectra, PQ has virtually no absorption above the mid-500 nm region. Holograms have been recorded in this material with 532 nm, 514 nm, and 488 nm wavelength laser light. For the experi-

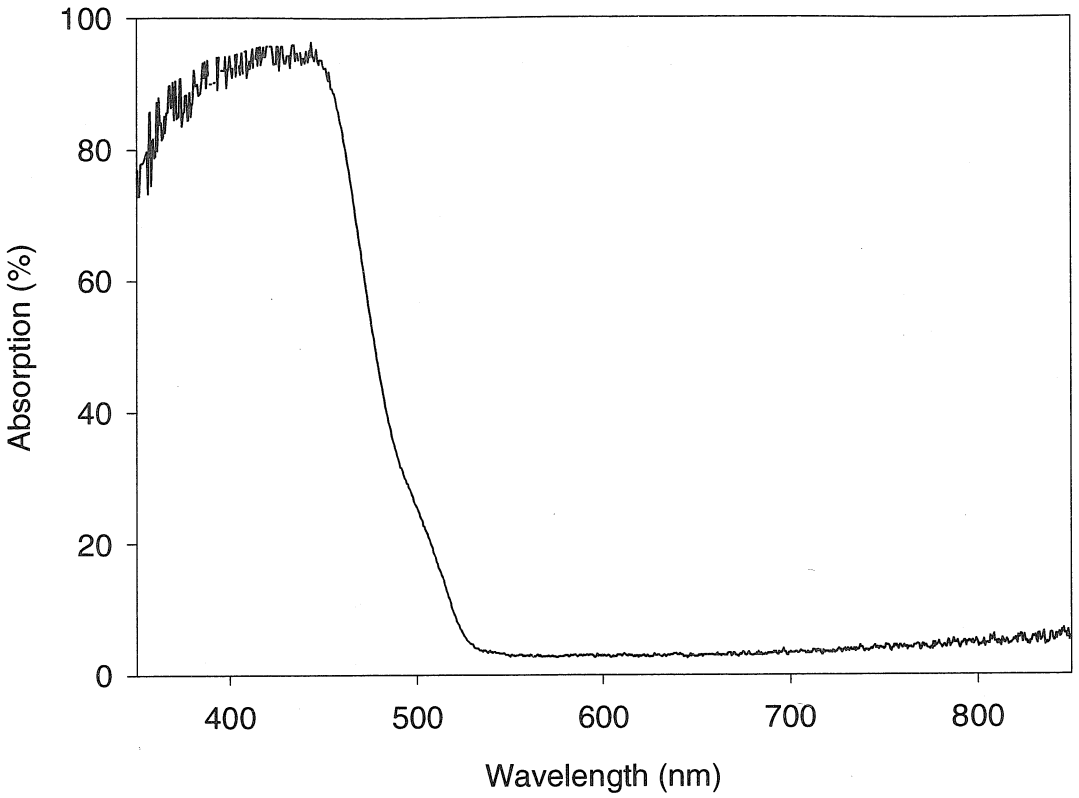

Fig. 3-4. Absorption of a 1-mm thick sample of unexposed PQ:PMMA.

ments described in this chapter 488 nm light from an Argon-ion laser was used because of the higher sensitivity of the material to this wavelength.

3.2.2.2 Single hologram recording and destruction dynamics

A hologram was recorded by a pair of 488 nm beams, each incident upon the material at an outside angle of 21.5°. The growth of the hologram was monitored during recording by probing the sample with a Bragg-matched He-Ne (633 nm) laser beam. Figure 3-6 shows the diffraction efficiency (diffracted power divided by the incident power) during recording in a 1-mm thick sample. The diffraction efficiency reached a maximum of 4.3% for an exposure energy of 3 J/cm^2. If exposure were allowed to continue, the diffraction efficiency began to drop. After 20 J/cm^2 of exposure with a single beam, the hologram has

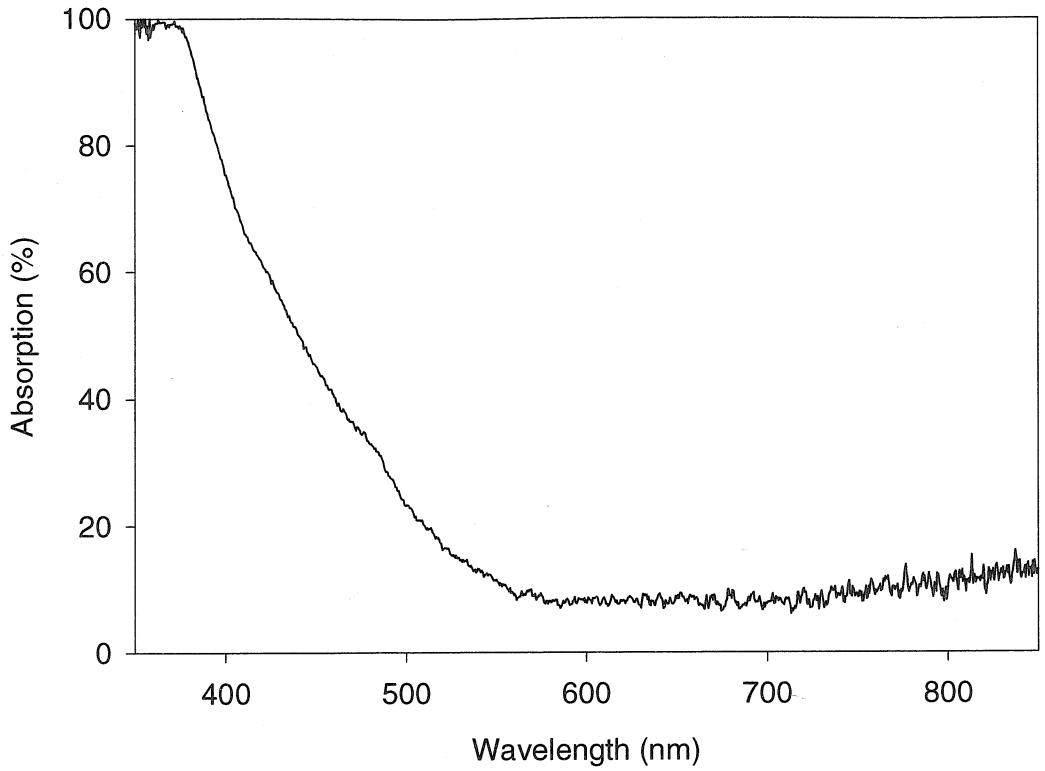

Fig. 3-5. Absorption of a 1mm thick sample of exposed PQ:PMMA.

decayed to approximately 0.1%. At this point the material was completely exposed and no more holograms could be recorded.

Permanent holograms that do not decay with subsequent illumination are recorded by stopping the exposure before saturation is reached and then baking the sample. Figure 3-7 shows the strength of a hologram as a function of baking time at a temperature of 55° centigrade. The diffraction efficiency reaches a maximum after 12 days and remains steady with continued baking.

Figure 3-8 shows the selectivity curves for a weak and a strong hologram (2% and 35% diffraction efficiency). The 2% hologram has the sinc-squared selectivity curve as expected for a 1 mm thick hologram. The stronger hologram on the other hand has a selec-

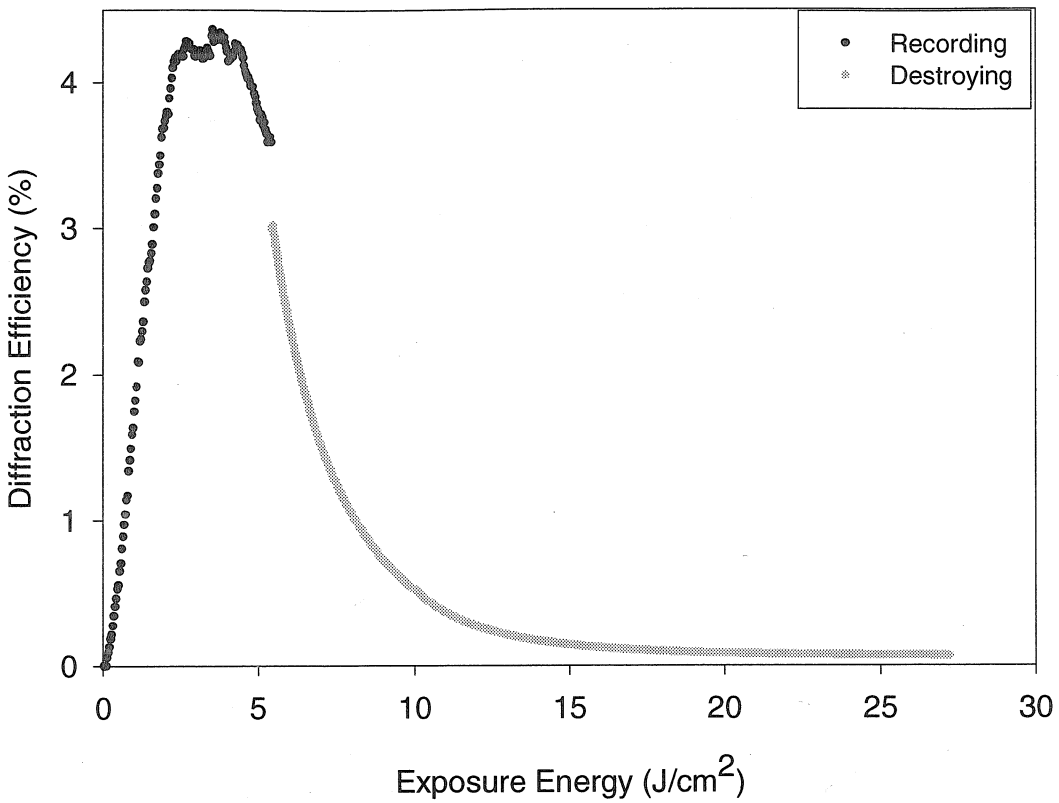

Fig. 3-6. Holographic recording and destruction curve.

tivity curve which is distorted and shifted. This distortion for strong holograms is believed to be due to stresses in the material that build up during hologram formation and are released during baking by reorientation of the PMMA chains. For a holographic memory the diffraction efficiency is relatively small because many holograms are multiplexed. Therefore, this effect is not going to be observed in practice. For characterization purposes, the diffraction efficiencies used are calculated as the peak of the ideal Bragg selectivity curve with the same area as that of the measured curve. The slight shift of the weak hologram is due to a re-positioning error arising from the removal of the material from the optical setup for baking. Shrinkage is not a suspect because of the ability to completely reconstruct high-bandwidth holograms.

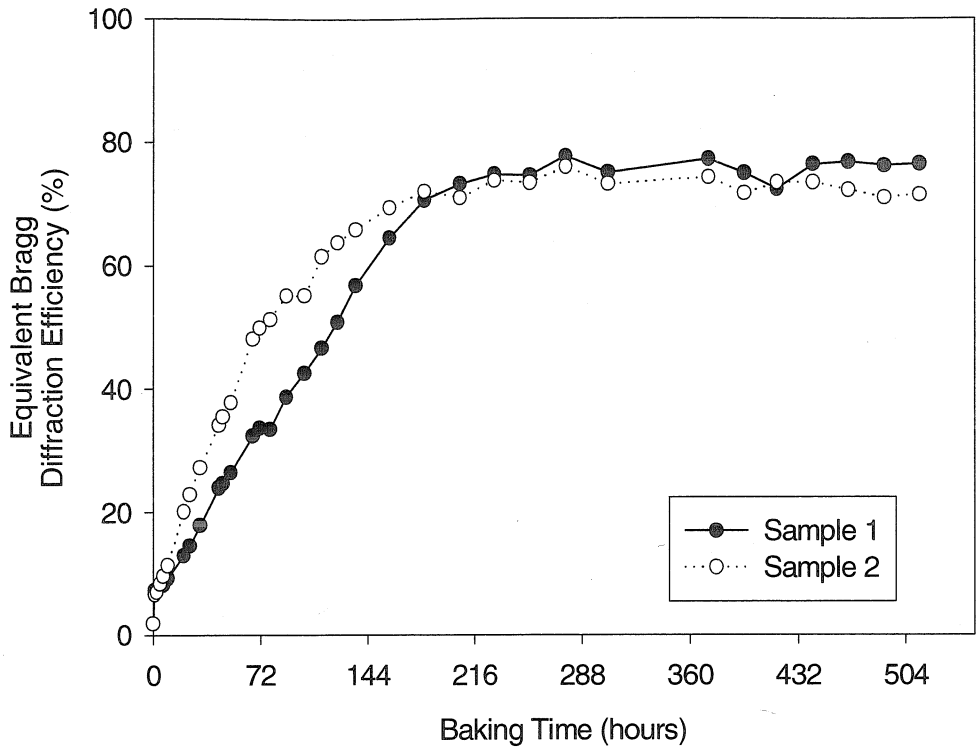

Fig. 3-7. Diffraction efficiency versus baking time for a hologram exposed to 1 J/cm^2 of energy.

The recording sensitivity has been measured for 1 mm and 3 mm thick samples as a function of exposure energy and is shown in Figure 3-9. For each exposure energy two holograms were recorded, each in a different sample of recording material, and then baked for 48 hours at 55° centigrade to partially reveal the holograms. Plotted is the average of the equivalent diffraction efficiencies of the two trials with their standard deviation used as the error. For 1 mm thick samples the maximum diffraction efficiency was achieved at 0.9 J/cm^2. For 3 mm thick samples the recording saturated after only 0.4 J/cm^2. The holographic sensitivity, defined as

$$S = \frac{1}{L \times I} \frac{\partial \sqrt{\eta}}{\partial t}, \tag{3-1}$$

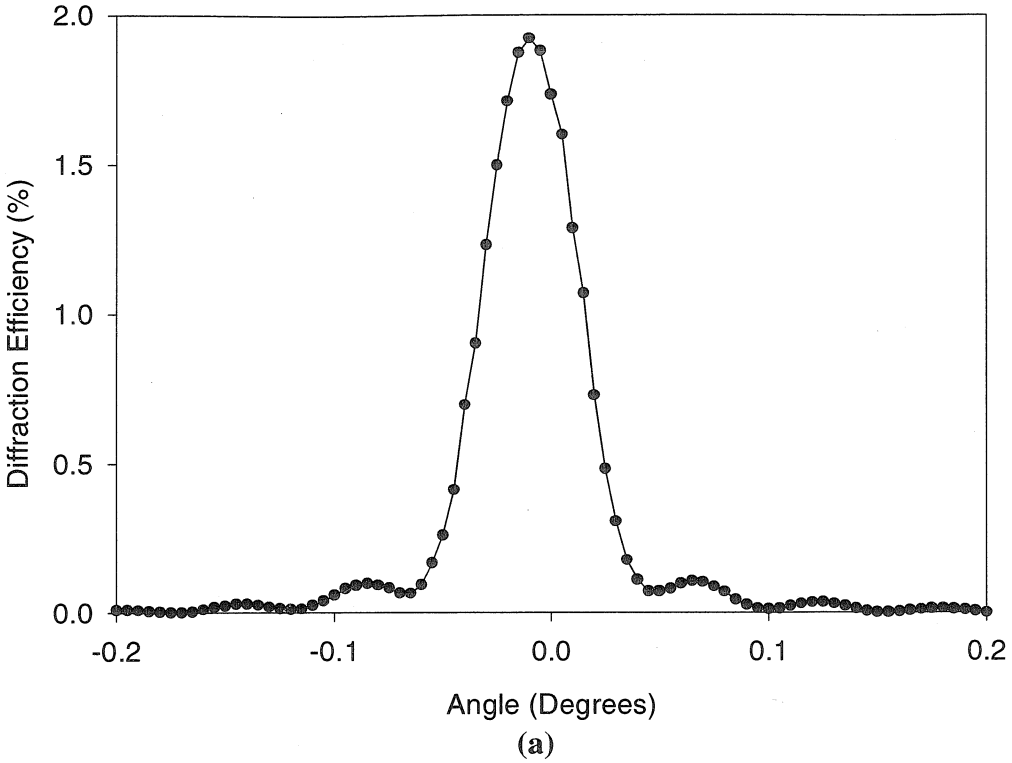

(a)

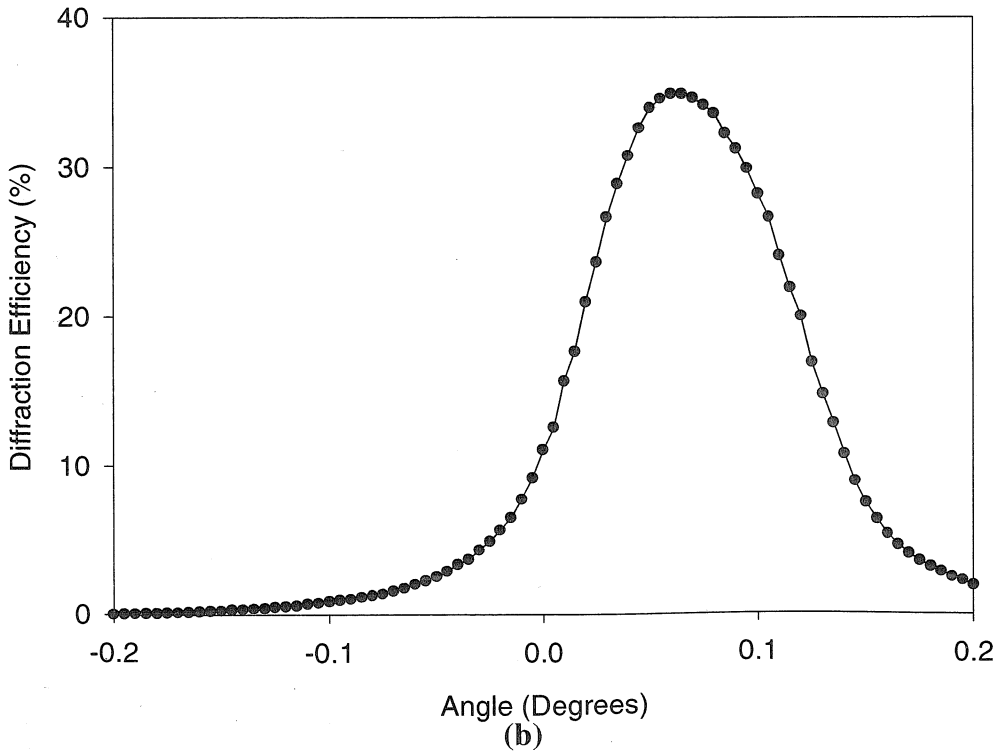

(b)

Fig. 3-8. Selectivity curves for a 1 mm thick sample for a (a) weak and (b) strong hologram.

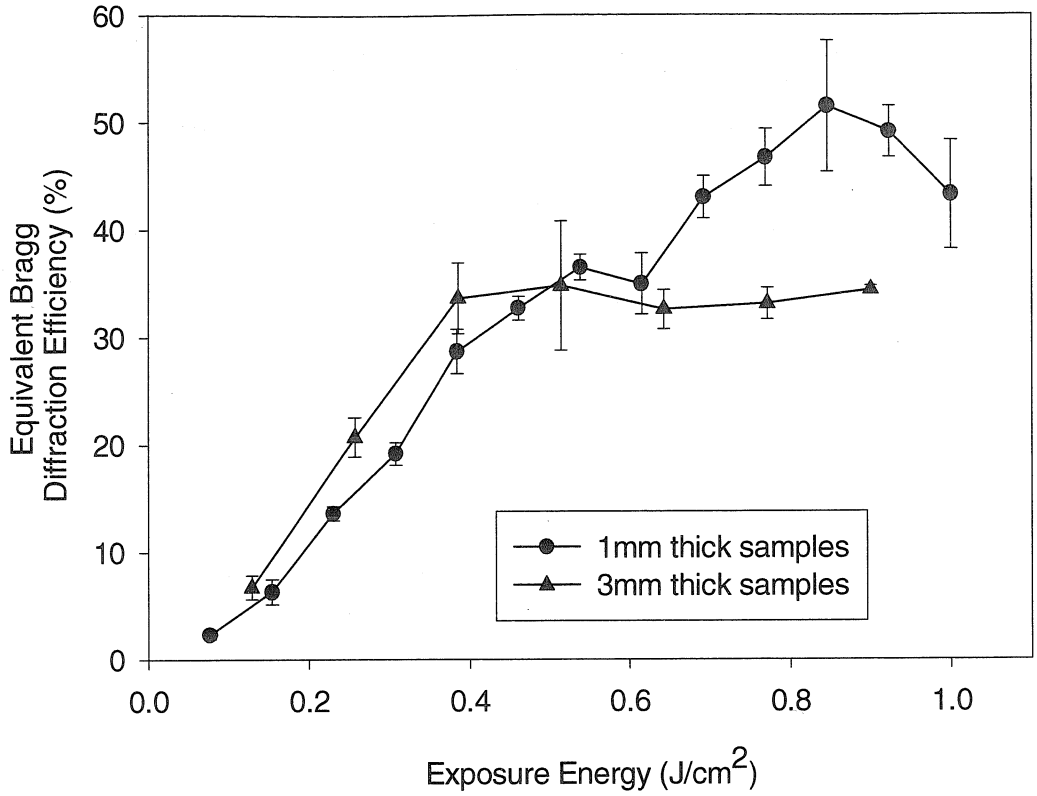

Fig. 3-9. Exposure sensitivity of 1-mm and 3-mm thick samples of PQ:PMMA.

where L is the material thickness, I is the intensity of the recording beams, and η is the diffraction efficiency, is 197 cm/J for the 1 mm sample and 67 cm/J for the 3 mm sample. Since the sensitivity measure is normalized to the thickness, it should be the same for both 1-mm and 3 mm samples. However, it isn't, and the primary reason is that because of the high absorption, for the 3 mm thick material the hologram was not recorded through the whole volume of the material for very small recording energies, which effectively causes the hologram to actually be thinner than 3 mm. If it is assumed that the effective hologram thickness is only 1 mm, then the 3 mm samples yield a sensitivity of 189, comparable to the measurement for actual 1 mm thick samples.

In a separate experiment, several holograms were recorded with different beam intensities while keeping the exposure energy constant at 0.04 J/cm^2 by varying the recording time. For each exposure time, holograms were recorded in two 1 mm thick samples and then baked for 72 hours. After baking they were flood illuminated for 1 day by a 500 W Halogen lamp. The diffraction efficiencies were measured and averaged among samples with the same exposure energy to help compensate for variances between samples. Figure 3-10 plots the resultant diffraction efficiencies as a function of exposure intensity.

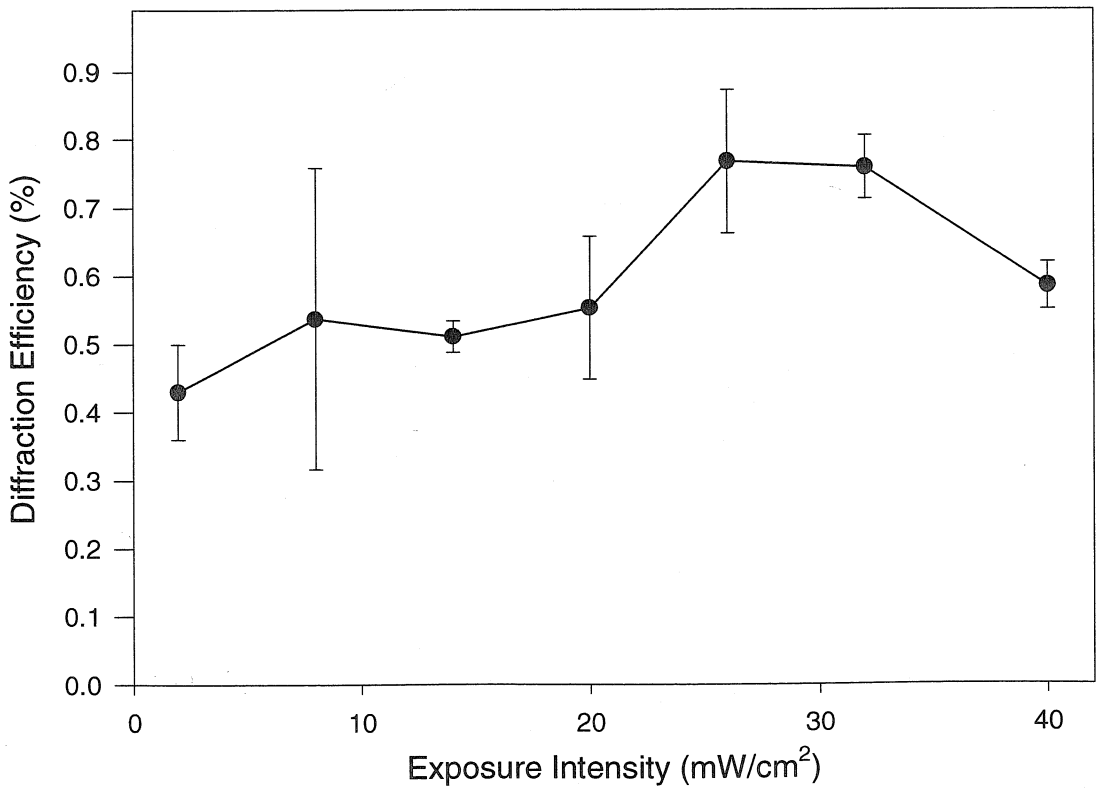

Fig. 3-10. Effect of laser intensity on the hologram diffraction efficiency while keeping the overall exposure energy constant.

Over the range of 2 to 40 mW/cm^2 the material's recording sensitivity is not strongly dependent on the intensities of the recording beams. A slight decrease in diffraction efficiency is seen for lower intensities however, with lower intensities longer exposure times

were used, making the recording setup more susceptible to variations in vibrations and other disturbances which can lower the achievable diffraction efficiency.

3.2.3 Description of recording mechanisms

As seen in the previous section, exposure subsequent to recording causes erasure of the previously recorded holograms as in photorefractives. However, continued exposure also causes the material to saturate as in many other photopolymers, thus not allowing record-erase-record cycles to be performed. In order to design a strategy for recording multiple holograms in this material the physical mechanism involved must be understood. Figure 3-11 schematically illustrates the holographic recording process in this material. Initially the PQ molecules are uniformly distributed throughout the bulk PMMA sample. Upon illumination the PQ molecules are photo-excited and bond to the host PMMA matrix. When illuminated with two interfering beams, this bonding occurs primarily in regions of constructive interference. If the sample is illuminated with a sinusoidally varying intensity pattern, $I = I_0[1 + \cos(2\pi x/\Lambda)]$, at time 0 immediately after exposure the concentration of the two species is

$$\begin{aligned} c_A(x, 0) &= c_0\left[1 + \cos\left(\frac{2\pi x}{\Lambda}\right)\right] \\ c_B(x, 0) &= c - c_0\left[1 + \cos\left(\frac{2\pi x}{\Lambda}\right)\right] \end{aligned}, \qquad (3\text{-}2)$$

where c_A is the concentration of the attached PQ molecules, c_B is the concentration of the unattached molecules, and c is the initial concentration of PQ. c_0 is the modulation depth of the concentration and depends on the initial concentration as well as the exposure energy of the recording and the conversion efficiency of the process of attaching the PQ molecules to the polymer matrix. Note that with this formulation the maximum value c_0 can attain is

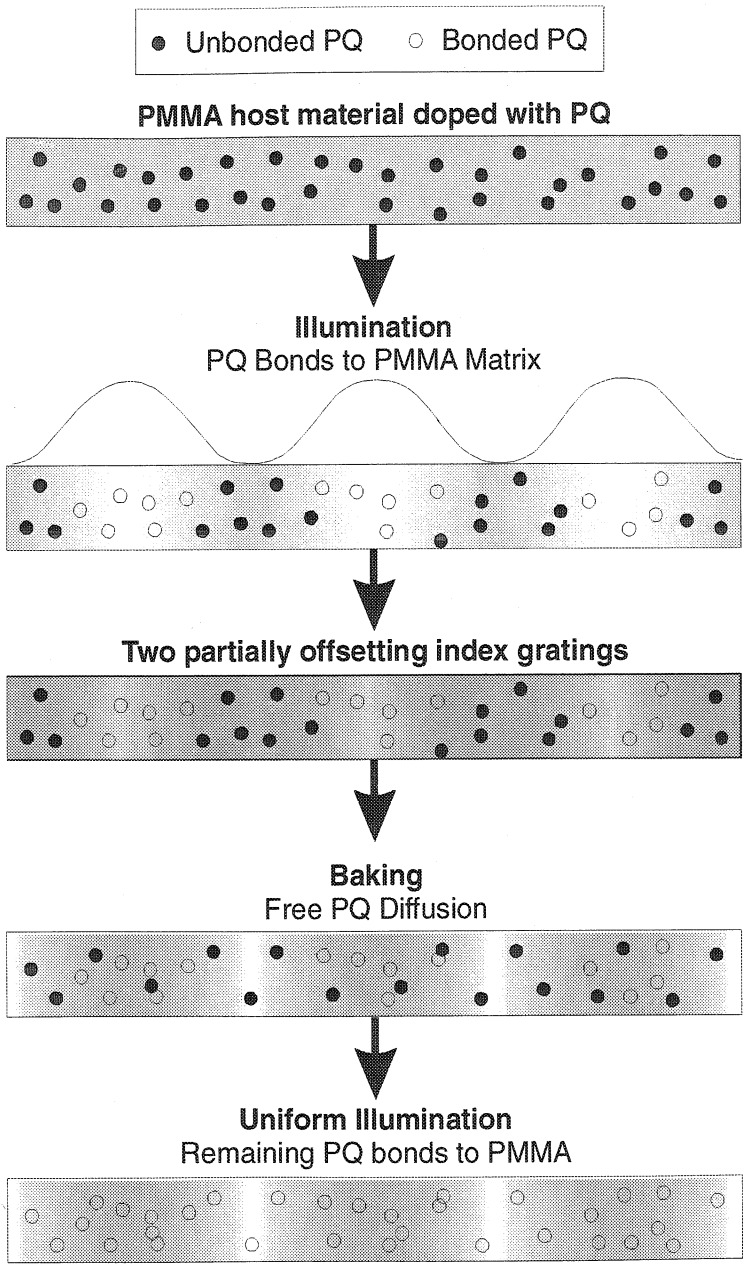

Fig. 3-11. The hologram recording process in PQ:PMMA.

half that of c. Through this process two partially offsetting gratings are created, one consisting of regions of photo-excited PQ molecules that have bonded to the host polymer and the other of PQ molecules that are not bonded to the host polymer. At this stage a small diffraction efficiency can be observed.

At room temperature there is minimal diffusion of the PQ molecules through the polymer matrix. During heating, the free PQ molecules diffuse and distribute evenly, revealing the hologram. In general, the space-time variation of the concentrations of the molecules follow the diffusion equations

$$\begin{aligned} \frac{\partial}{\partial t}c_A(x,t) &= 0 \\ \frac{\partial}{\partial t}c_B(x,t) &= D_B\frac{\partial^2}{\partial x^2}c_B(x,t) \end{aligned} . \tag{3-3}$$

The attached PQ molecules are assumed not to diffuse at all due to the large size of the PMMA chains. From Equation 3-3 and the boundary conditions in Equation 3-2 the time varying concentration of detached molecules is found to be

$$c_B(x,t) = c - c_0\left[1 + e^{-\frac{4\pi D_B t}{\Lambda^2}}\cos\left(\frac{2\pi x}{\Lambda}\right)\right]. \tag{3-4}$$

The diffusion time depends both on the grating frequency and, through the coefficient D_B, the temperature.[3-4]

The index of refraction of the material can be thought of as consisting of components from the bulk PMMA, the attached PQ molecules, and the detached molecules, and can be written as

$$n(x,t) = n_0 + c_A(x,t)\alpha_A + c_B(x,t)\alpha_B . \tag{3-5}$$

Here the contribution of the bulk material is n_0, while the concentrations of each form of the PQ molecules are weighted by constants α relating their molecular polarizabilities to their contribution to the index of refraction of the material. By combining Equation 3-5 with 3-4 and 3-2, the index modulation as a function of time can be expressed as

$$\Delta n(t) = c_0\left[\alpha_A - \alpha_B e^{-\frac{4\pi D_B t}{\Lambda^2}}\right]. \quad (3\text{-}6)$$

From this equation it is easy to see the effect of diffusion on the hologram strength. Initially the index modulation will be $c_0(\alpha_A-\alpha_B)$ however, after complete diffusion it will be $c_0\alpha_A$, for an amplification factor of

$$A = \alpha_A/(\alpha_A - \alpha_B). \quad (3\text{-}7)$$

After recording and baking, a final uniform exposure is used to cause all of the remaining free PQ molecules to bond to the PMMA matrix, thereby preventing any further holographic recording from taking place in the material.

3.2.4 Multiple hologram recording

For many interesting holographic applications, including holographic data storage, the recording material must be capable of recording multiple holograms overlapping at a single location. To characterize the material's ability to record multiple holograms, the following procedure was followed. First, 50 plane wave holograms were recorded with equal exposure energy at a single location of 3 mm thick samples using peristrophic multiplexing.[3-5] The square root of the measured diffraction efficiencies is then summed to form the cumulative grating strength[3-6] defined as $C = \sum_{i=1}^{M}\sqrt{\eta_i}$. The cumulative exposure energy was then varied by increasing the exposure time of the individual holograms. Figure 3-12 shows the strengths of 50 holograms recorded in a single sample. The cumulative grating strength with the 50 holograms recorded to different total exposure energies for different samples is shown in Figure 3-13. The saturation value of the cumulative grating strength is approximately equal to the M/# of the material.[3-7] The M/# reaches a maxi-

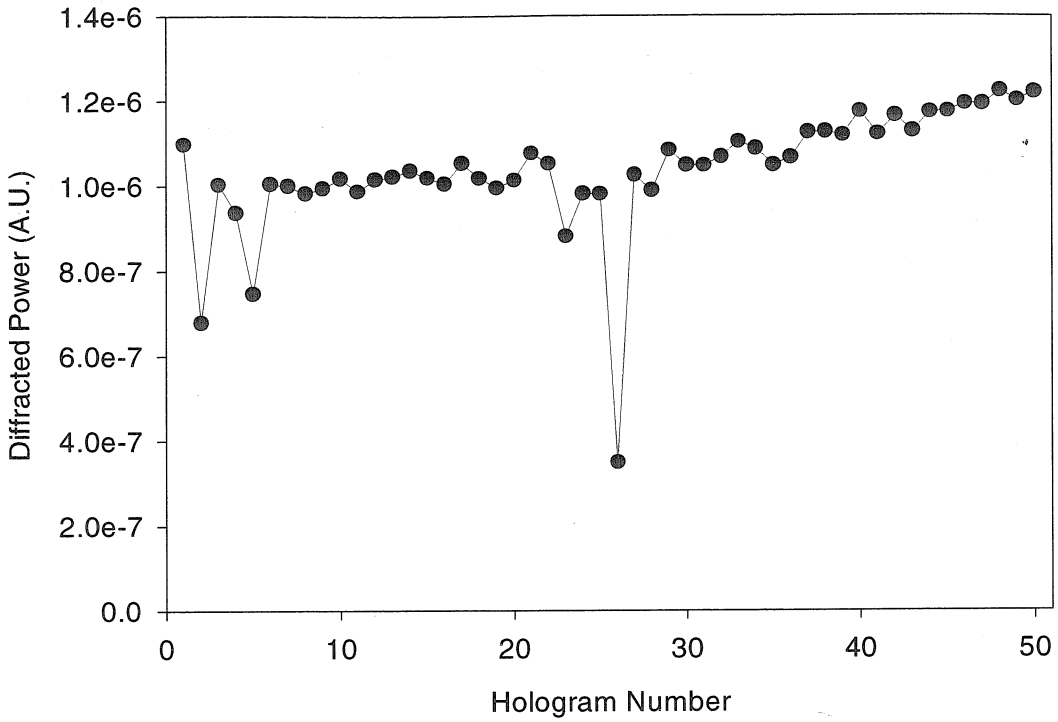

Fig. 3-12. Strength of 50 holograms recorded at a single location of 3 mm thick material.

mum of M/4.8 for a cumulative exposure energy of about 5 J/cm^2. With increased exposure energies the cumulative grating strength then begins to drop as a result of the hologram destruction process. The earlier recorded holograms are reduced in strength by the recording of subsequent holograms, and overpowers the increase gained by recording for longer exposure energies.

3.2.5 Optically induced birefringence

When illuminated with linearly polarized light the PQ:PMMA material will develop a birefringence. This behavior is not a unique attribute of PQ:PMMA and has been shown to occur in other types of materials[3-8]-[3-11] which are often used for polarization holography.[3-12] The most dramatic demonstration of this effect was made by exposing a sample with a checkerboard pattern illuminated by 488 nm polarized laser light.

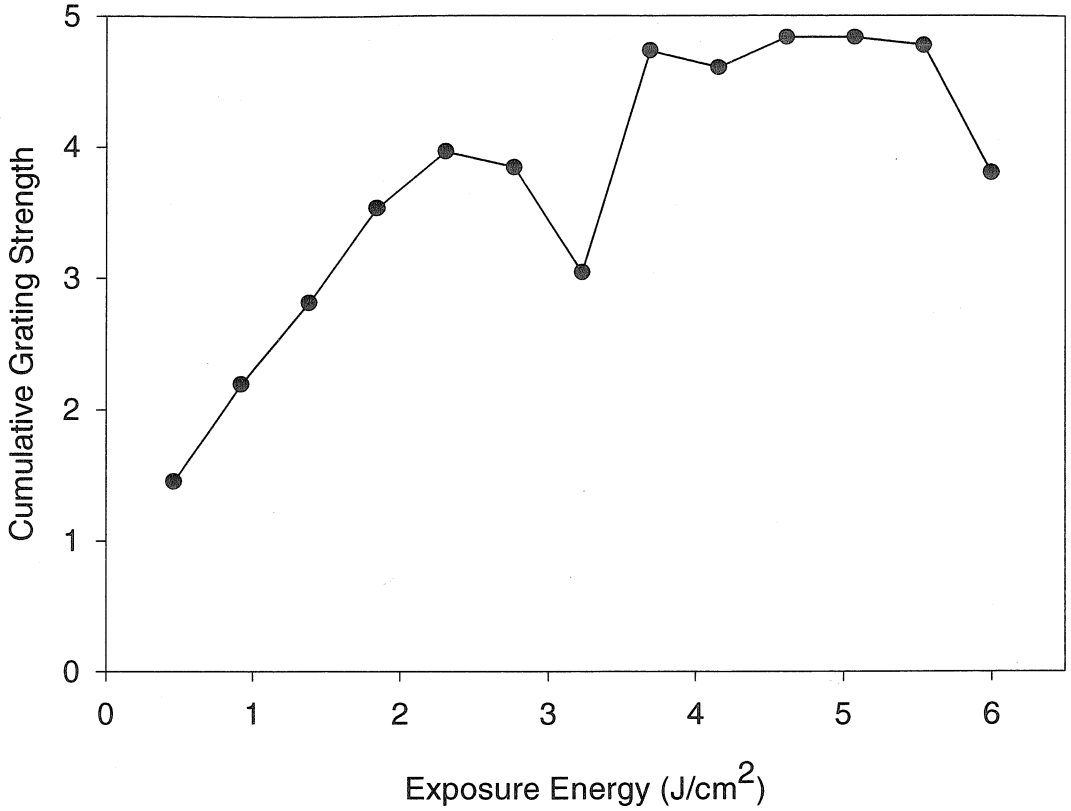

Fig. 3-13. Cumulative grating strengths for 50 holograms in 3mm thick samples with varying exposure energies.

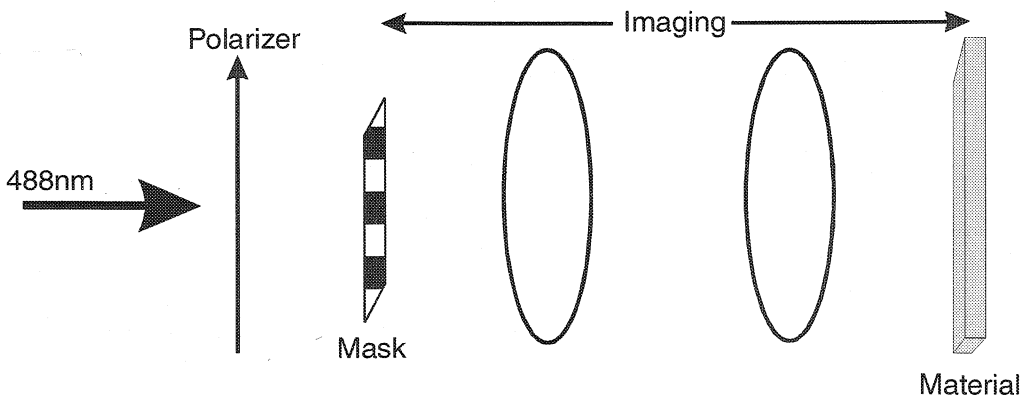

Fig. 3-14. Optical setup for creating a birefringent checkerboard pattern in the PQ:PMMA material.

Figure 3-14 shows the optical system used to record the pattern. A checkerboard mask was simply imaged to the plane of the material with two lenses. After exposing the material, the

recorded pattern can be seen in ordinary room light by rotating the material between a pair of crossed polarizers as shown in Figure 3-15. The first polarizer serves to polarize the

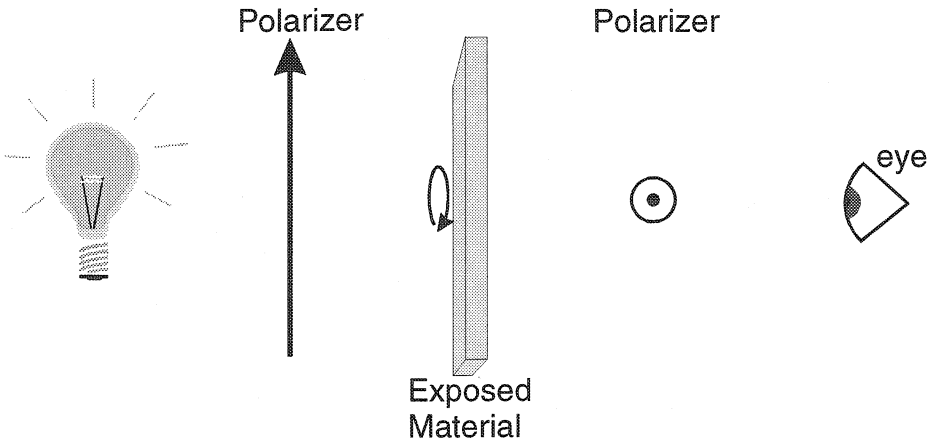

Fig. 3-15. Reading out the optically induced birefringent pattern.

unpolarized input light. The regions of the material which have become birefringent will modify the polarization of the light and allow a portion of it to pass through the second polarizer, with an intensity dependent on the angle between the primary axes of birefringence and the polarizers. Figure 3-16 shows this effect as the material is rotated. A maxi-

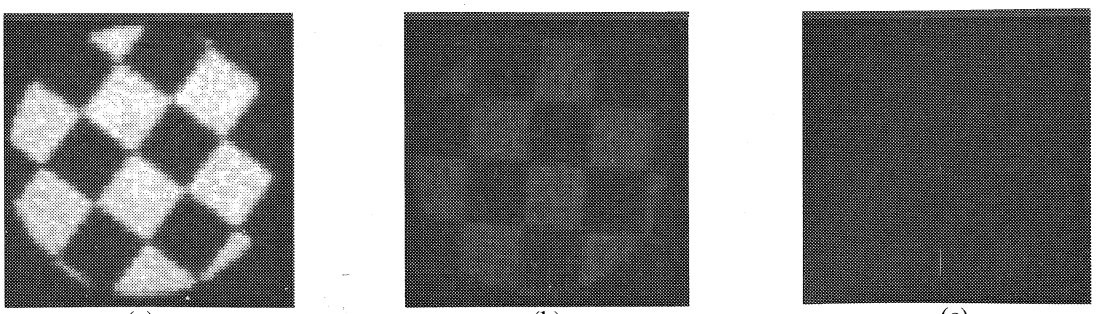

Fig. 3-16. Read-out of the recorded birefringence when the material axes are (a) at a 45-degree angle with the polarizers, (b) between 0 and 45-degrees, and (c) aligned with the polarizers.

mum contrast between exposed and unexposed regions is realized when the material axis is at a 45-degree angle to the polarizers. As the material is rotated the contrast decreases,

until vanishing when aligned with the polarizers. The effects of birefringence can also be seen in the absorption spectrum of the material when taken with polarized light. Figure 3-17 shows the absorption with light polarized parallel and perpendicular to the

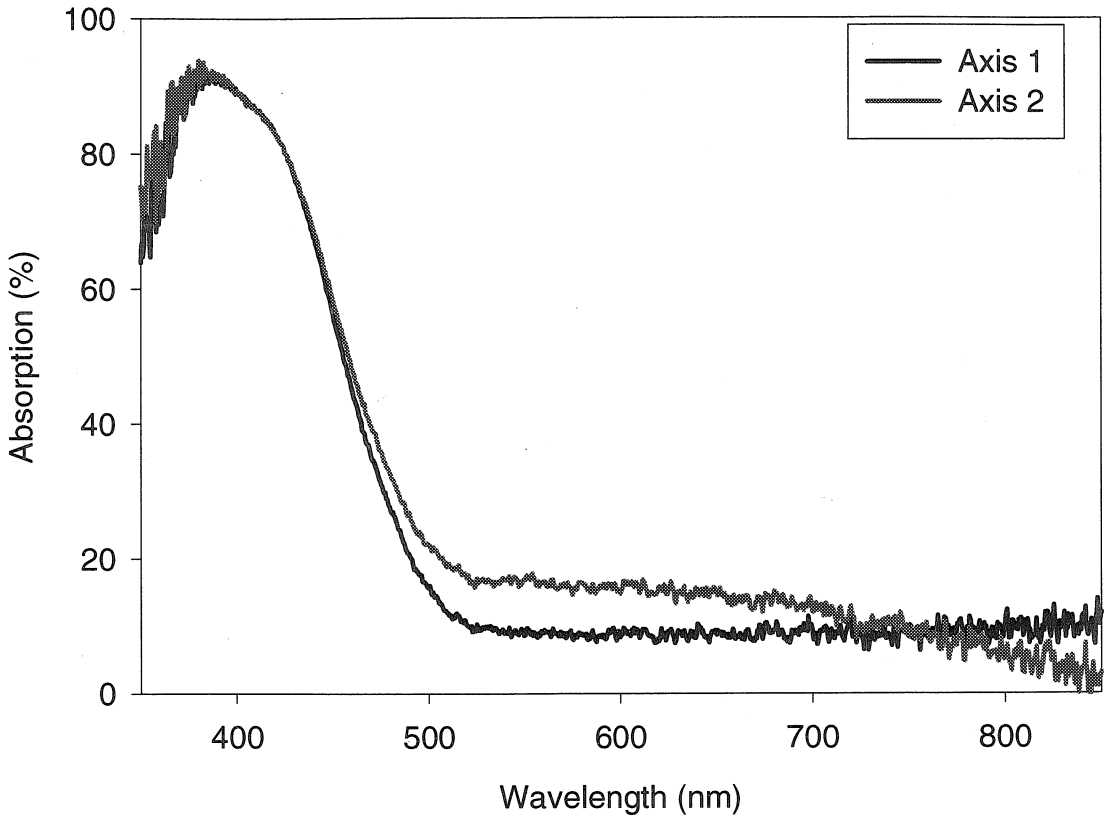

Fig. 3-17. Polarization dependent absorption in PQ:PMMA with induced birefringence.

polarization of the beam used to induce the birefringence. The different spectra for the two cases also indicates that the index of refraction is different for each polarization.

One potential application of this effect is the recording of data as patterns of birefringence. The data could then be read-out with any light source and a pair of polarizers. However, it is unlikely that a data density exceeding that of conventional DVD's could be achieved. Due to the nature of the birefringent recording, multiple pages cannot be stored at the same location of material as is the case with holographic recording. It may appear at

first that another page can be stored when the material is situated to give no contrast for the first page, such as in Figure 3-16(c). However, if another page were recorded, it would modify the birefringence of the material which composes the first page, thereby causing a considerable amount of crosstalk. The data density is limited by the spot size of each pixel, which is essentially the same physical effect limiting the density of DVD systems.

Another application for birefringent materials are waveplates used to rotate and modify the polarization of light. In order to make a waveplate to perform a desired function, such as a half-wave or quarter-wave retarder, the difference between the index of refraction for the fast and slow axes of the material must be know. To measure this as a function of exposure energy, the system shown in Figure 3-18 was used. The HeNe laser was used to

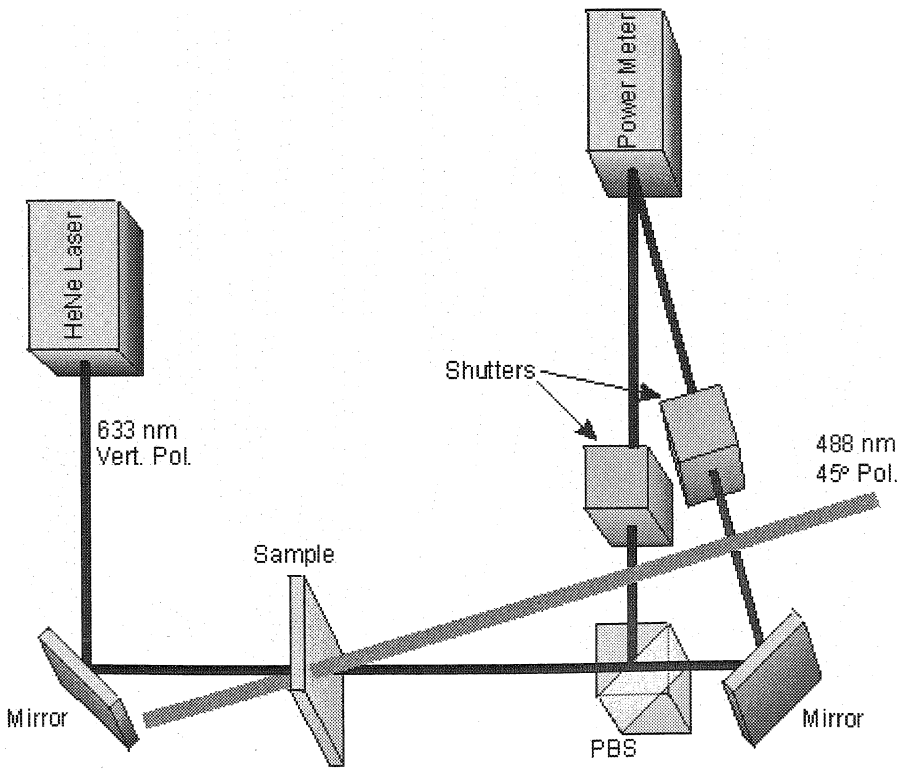

Fig. 3-18. Optical system for measuring the optically induced birefringence.

probe the birefringence of the sample and was vertically polarized. To induce the birefringence, a 488 nm beam from an Argon laser with a polarization at a 45-degree angle with respect to the probe beam was used. When the probe beam passes through the PQ:PMMA sample, its polarization will be modified due to the birefringence. A polarizing beamsplitter was used to divide the modified probe beam into its vertically and horizontally polarized components. With the assistance of two shutters, a single power meter was used to alternately measure the power of each beam.

With the use of Jones calculus,[3-13] the power in each measured beam as a function of the birefringence, Δn, is calculated as

$$\begin{aligned} P_v &= P_0 \cos^2(\Delta n \times L\pi/\lambda) \\ P_h &= P_0 \sin^2(\Delta n \times L\pi/\lambda) \end{aligned}, \tag{3-8}$$

where P_0 is the total power of the probe beam, λ is the wavelength of the probe beam, and L is the thickness of the sample. By combining the Equation 3-8 powers, the birefringence can be computed from the measurements as

$$\Delta n = \frac{\lambda}{L\pi} \operatorname{asin}\left(\sqrt{\frac{P_h}{P_h + P_v}}\right). \tag{3-9}$$

A 3-mm-thick sample of PQ:PMMA with 0.7% by weight of PQ was measured. Figure 3-19 shows plots of the measured power in vertical and horizontal polarizations. Initially, by design, 100% of the power is in the vertical component of the polarization. However, as the material is exposed with the 488 nm beam, the birefringence increases and the polarization of the probe beam is transformed to have more power in the horizontal component. Eventually the material saturates and there is no change with continued exposure.

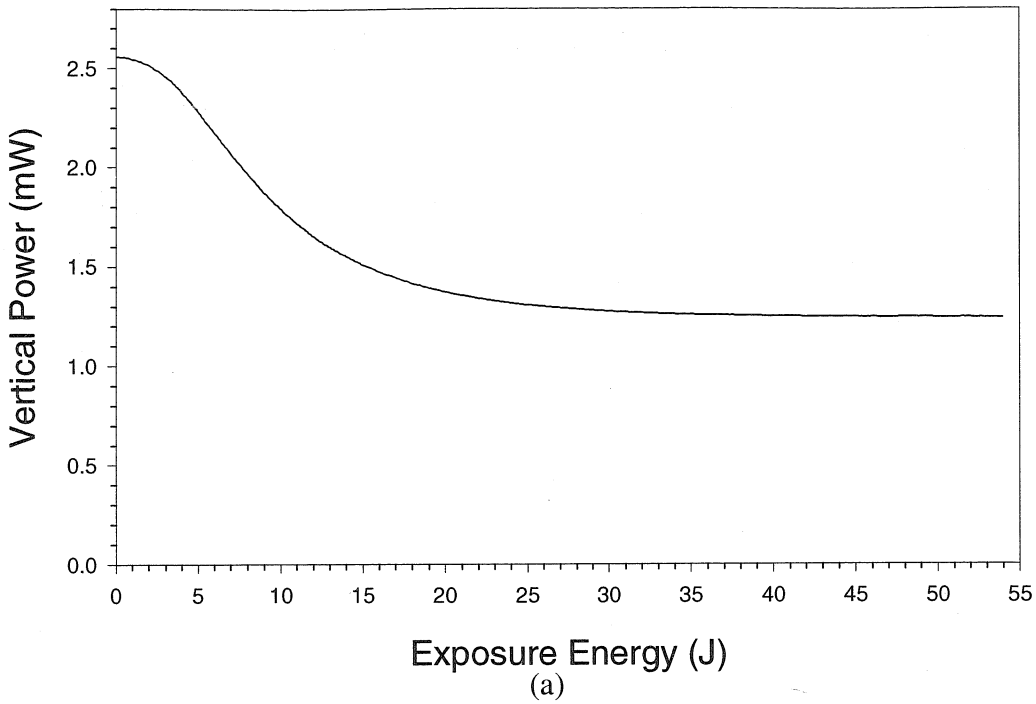

(a)

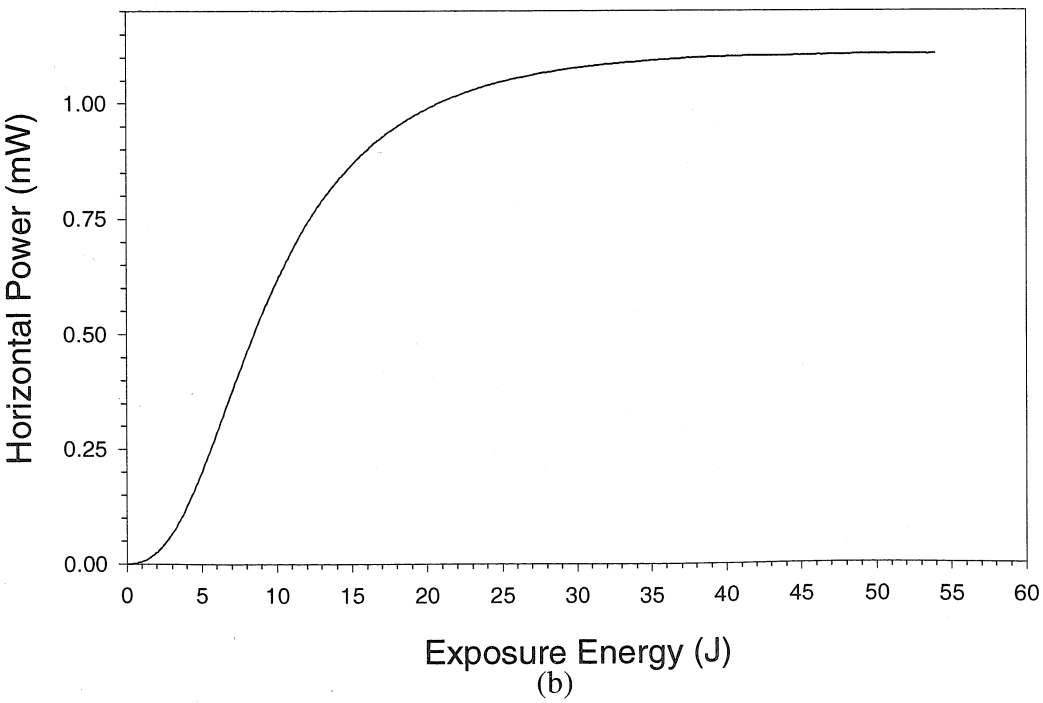

(b)

Fig. 3-19. Measured powers in vertical and horizontal polarization components of a probe beam during optical induction of birefringence.

Using Equation 3-9 the birefringence as a function of exposure energy was calculated and plotted in Figure 3-20. The maximum difference in index of refraction between the fast and

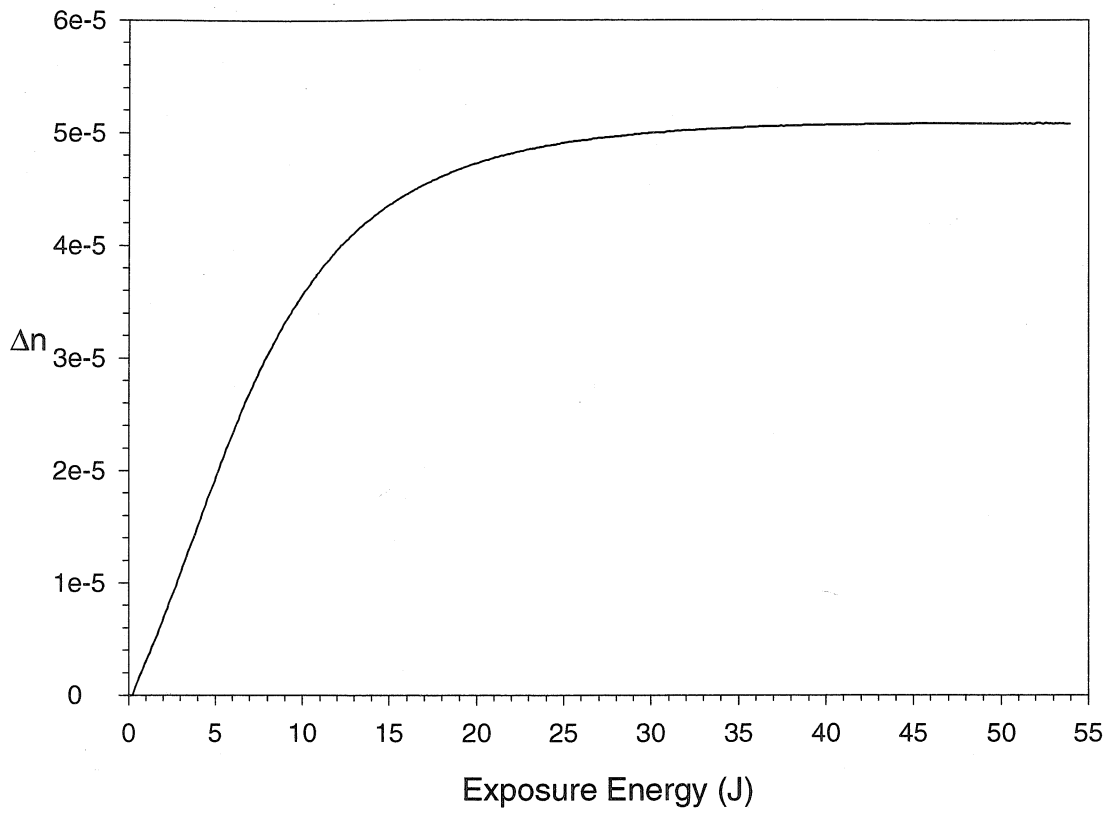

Fig. 3-20. Amount of optically induced birefringence as a function of exposure energy with a 3-mm-thick sample of PQ:PMMA.

slow axes of the material was 5×10^{-5}. With this small amount of birefringence, a sample with a thickness of almost 5 mm would be required for a half-wave retarder at 488 nm. However, by baking the material, the level of birefringence will actually decrease. The same sample used for the plots shown was baked at 55° C for 24 hours, after which time the birefringence was measured to be approximately 2.7×10^{-5}. With this decreased amount of birefringence, a half-wave plate would require a thickness of 9 mm.

3.3 Naphthoquinone-based copolymer material

In PQ:PMMA the dynamic range is limited by the amount of dopant chromophore present in the material. This is limited by the solubility of PQ in MMA when in solution. If too much PQ is added, it will ultimately lead to a recording material with poor optical quality and high scatter. The motivation behind development of the material described in this section is to increase the fraction of chromophore that can be present in the recording material, with the goal of increasing M/#.

With PQ:PMMA, upon illumination the dopant chromophore PQ undergoes a chemical reaction which causes it to attach to the host PMMA matrix. When illuminated with an interference pattern, two gratings are formed. The first consists of PQ molecules which are attached to the polymer matrix, and the second consists of unattached PQ molecules. Subsequent baking of the material causes an acceleration in the diffusion rate of the unattached PQ molecules, which causes an overall amplification of the resulting diffraction efficiency. In this new material system, chromophores are initially attached to the polymer chains. This is accomplished by a monomer containing a photo-sensitive side-chain that exhibits desired photo-chemical properties and co-polymerizing it with a monomer that forms a known high optical-quality material, such as PMMA. Upon illumination of the material, the attached chromophores undergo a photo-chemical reaction causing them to detach from the polymer backbone. When the material is illuminated with an interference pattern, a grating composed of two components, attached and detached chromophores, results, as in the case of the PQ-doped system. Heating of the material causes an amplification of the grating strength through diffusion of the detached molecules. The recorded holograms are also persistent at room temperature under continuous illumination at the

recording wavelength. Because the chromophores are part of a side chain of a monomer which participates in polymerization during fabrication of the material, in principle a much higher chromophore concentration can be achieved than is the case with PQ:PMMA.

3.3.1 Material description

Figure 3-21 shows the material components and the process of detaching the chromophore from a polymer chain. The optically active component, shown in Figure 3-21(a), is the monomer N,N'-dimethyl-N-(3-methyl-1,4-naphthoquinonyl-2)-N'-acryloyl-hexamethylenediamine. This monomer is based on the chromophore 1,4-naphthoquinone (NQ) (left in Figure 3-21(a)), attached by an alkyl chain (center) to the right section which can take part in co-polymerization with MMA. These monomers are co-polymerized with the monomer methyl methacrylate (MMA) to form a mostly PMMA based material. In this respect, the material is similar to PQ:PMMA in bulk mechanical and optical properties, although the absorption spectrum is different due to the different chromophore characteristics. The co-polymer structure is shown in Figure 3-21(b), illustrating the structure that occurs when the chromophore is present as a side chain in the polymer. When illuminated, N-naphthoquinonylamine undergoes a transformation first to a meta-stable state before transforming to its final stable form.[3-14] A portion of the chromophore detaches from the polymer and is free to diffuse as discussed previously.

3.3.2 Holographic recording

A basic holographic recording system was used to test this material. The system consisted of two 514 nm recording beams each incident at a 20 degree angle (in air) from the material's surface normal. A Bragg-matched 633 nm probe beam was used to read-out

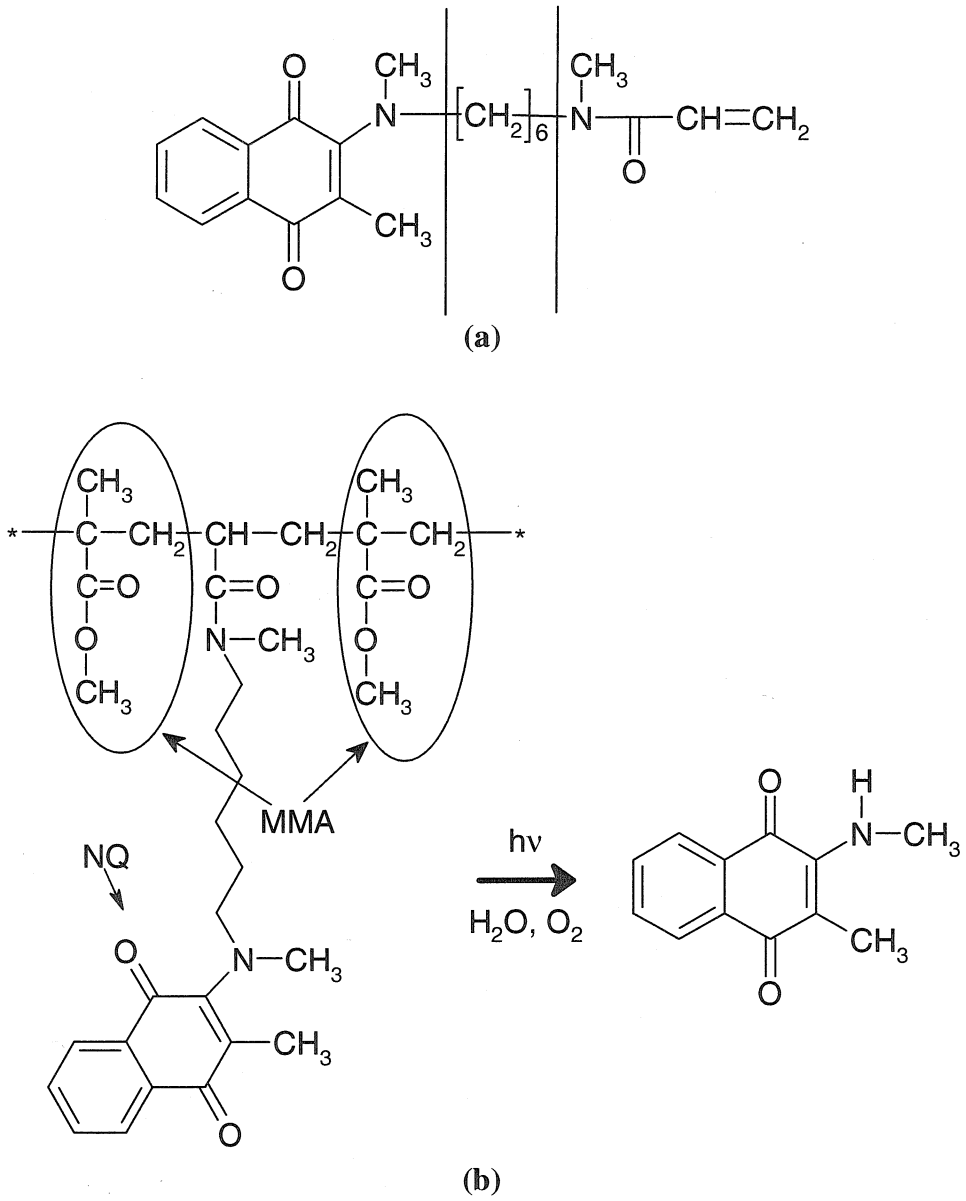

Fig. 3-21. (a) Synthesized monomer form of the NQ chromophore (b) co-polymer of the NQ chromophore with MMA and the photochemical reaction causing detachment from the polymer chain.

the holograms. The intensity of the recording beams was 20 mW/cm^2 each. The absorption spectrum of this material, with a chromophore concentration of 0.1% by weight and a thickness of 0.5 mm, Figure 3-22, shows little to no absorption at the 633 nm probe wavelength,

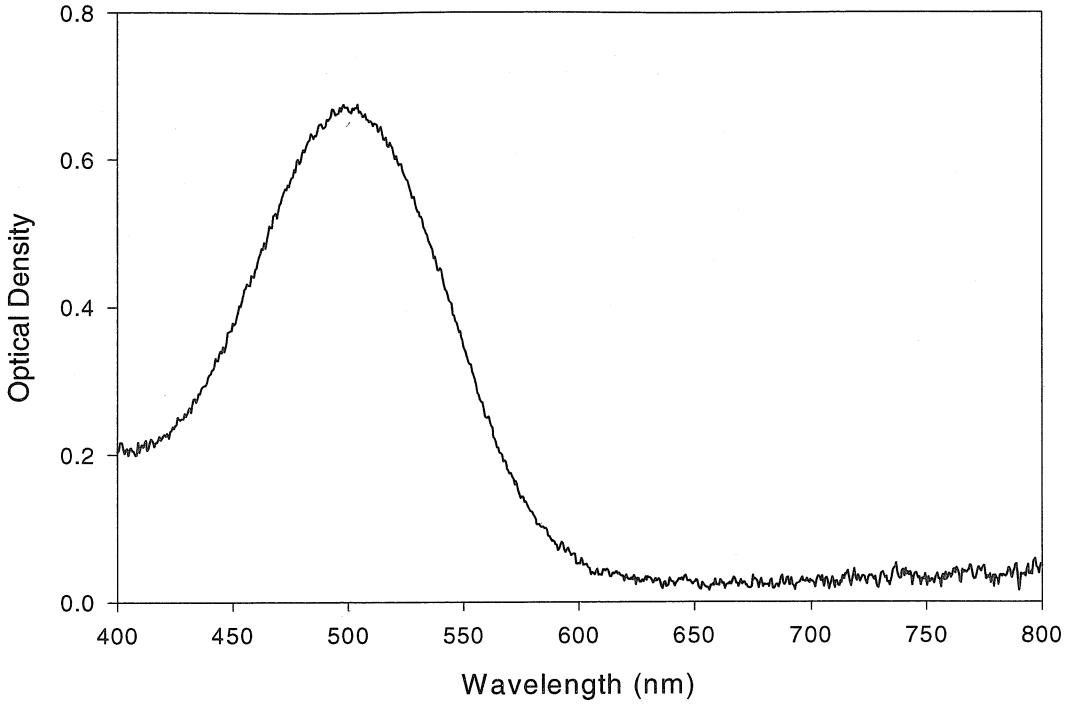

Fig. 3-22. Absorption spectrum for a 0.5 mm thick sample with a chromophore concentration of 0.1% by weight.

and significant absorption at 514 nm due to the added chromophore, compared with Figure 3-3 of pure PMMA.

Samples were tested with chromophore concentrations of 0.05%, 0.1%, 0.2%, and 0.4%, by weight. Eleven holograms were recorded in each sample, at different locations, with exposure energies varying between 0.04 J/cm^2 and 1.6 J/cm^2. Each recorded hologram was then measured after 11 days of baking at 75° C. Figure 3-23 contains a plot of the measured diffraction efficiencies before and after baking in a 0.1% by weight, 0.6 mm thick, sample. As expected, the recorded holograms were amplified after baking, supporting the assumption of hologram recording and amplification through the optical detachment of chromophore side-chains and subsequent diffusion. The eventual decrease in hologram strength with increasing exposure energy is an expected behavior of saturable recording

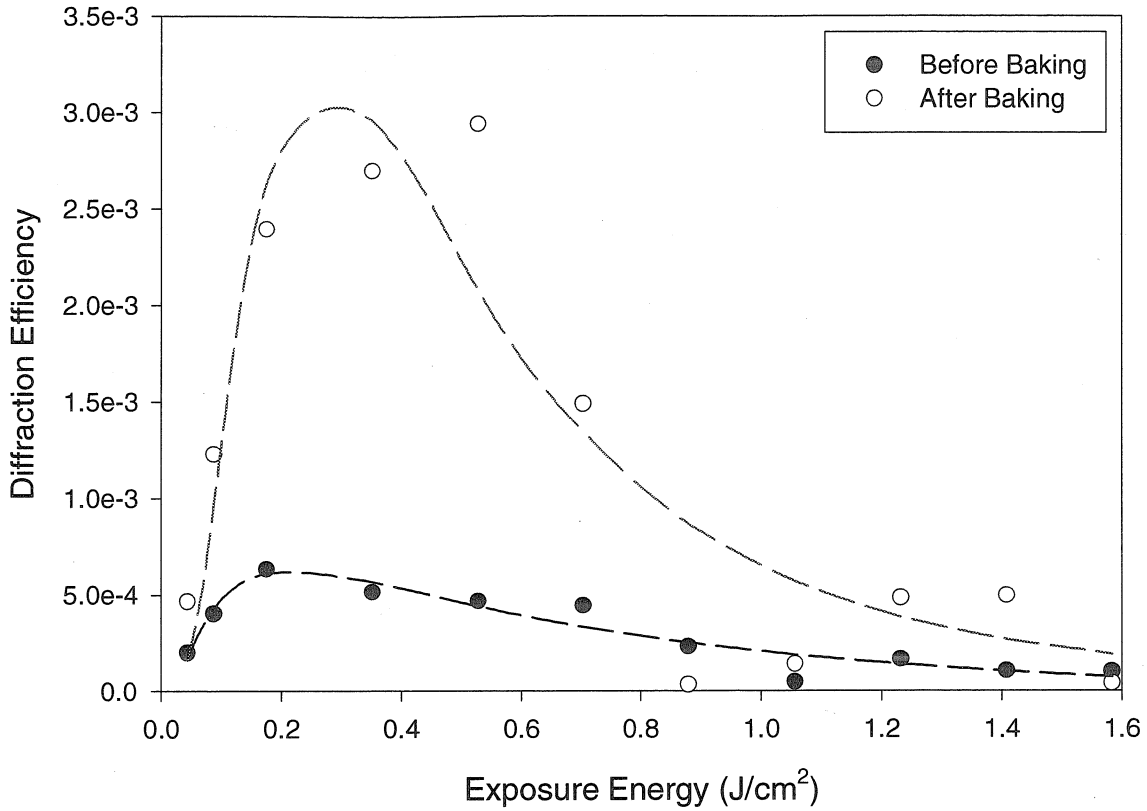

Fig. 3-23. Diffraction efficiency vs. exposure energy for 11 holograms recorded in a sample 0.6 mm thick with a chromophore concentration of 0.1% by weight, before and after baking.

materials which do not exhibit significant diffusion at room temperature, and was also seen with PQ:PMMA.

Figure 3-24 shows the diffraction efficiency as a function of exposure energy when a recorded hologram is exposed to uniform illumination at 514 nm. There is an initial drop in diffraction efficiency of approximately 40% at around 0.5 J/cm^2. Subsequently, the diffraction efficiency remains unchanged yielding non-destructive read-out.

The initial decay is due to the detachment of the remaining chromophores which causes an index change similar to the effect that results in the observed diffraction efficiency before baking. However, at room temperature, the non-uniformity of the detached

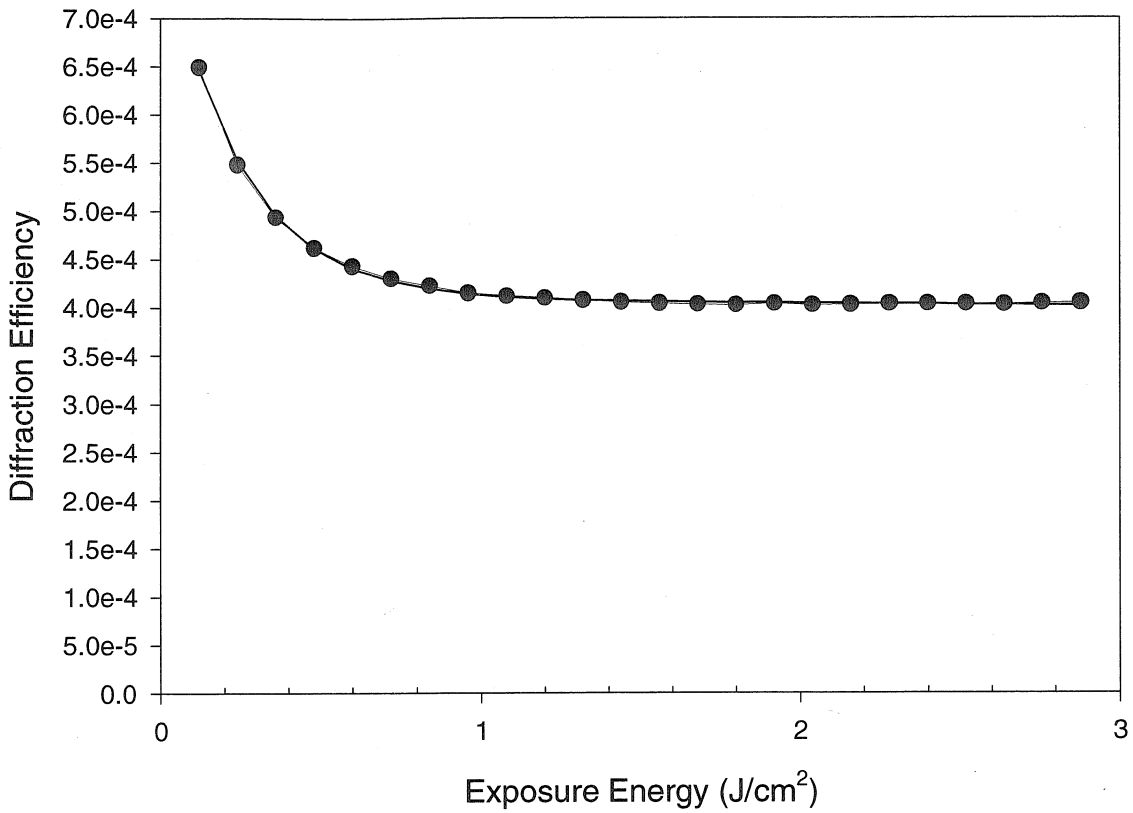

Fig. 3-24. Decay in the hologram strength when exposed after recording and thermal amplification due to the detachment of the remaining attached chromophores.

chromophores remains in place and gives persistent diffraction. Using the analysis and notation of Section 3.2.3, immediately after recording the index modulation is $\Delta n(0) = c_0(\alpha_A - \alpha_B)$. After complete diffusion of the detached molecules, however, the index modulation grows to $\Delta n(\infty) = c_0\alpha_A$. When the material is subsequently illuminated, the concentration modulation of attached chromophores is transferred to the detached form. The index of refraction can be then written as

$$n(x, \infty^+) = n_0 + c_A(x, 0)\alpha_B + c_B(x, \infty)\alpha_B . \qquad (3\text{-}10)$$

Here, the only spatial modulation of the index of refraction is in the concentration c_A, since diffusion has removed the initial concentration modulation of the chromophores detached

during recording. Using Equation 3-4 and combining terms in Equation 3-10 yields a final index modulation given by

$$\Delta n(\infty^+) = c_0 \alpha_B . \tag{3-11}$$

The final amplification,

$$\frac{\Delta n(\infty^+)}{\Delta n(0)} = \frac{\alpha_B}{\alpha_A - \alpha_B}, \tag{3-12}$$

is independent of the chromophore concentration, as was also the case with PQ:PMMA.

By noting that

$$\Delta n(0) = \Delta n(\infty) - \Delta n(\infty^+), \tag{3-13}$$

the index modulations after recording but before baking, after baking but before the final illumination, and after the final illumination, can be compared by taking the square root of the measured diffraction efficiency in each case. For the hologram used to generate Figure 3-24, the index modulation immediately after recording was 1.4×10^{-6}. After baking and after post illumination the index modulations were 5.4×10^{-6} and 4.2×10^{-6}, respectively. The decrease during the final illumination was 1.2×10^{-6}, while Equation 3-13 would predict 1.4×10^{-6} from the initial diffraction efficiency, demonstrating agreement between this model and the experimental results.

3.3.3 Effects of chromophore concentration

Samples have been tested with a chromophore concentration as high as 0.4% by weight. The total index modulation to be expected should increase roughly linearly with increased chromophore concentration. In PQ:PMMA the dynamic range is limited by the maximum doping level of the PQ chromophores. A maximum concentration of 0.7% by

weight has been achieved, resulting in M/#=4.8 for a 3-mm-thick sample. The concentration is limited by the solubility of PQ. The approach with the NQ material in principal can support a higher concentration of the active chromophore. However, for higher concentration material a longer recording wavelength must be used and the attached chromophores redesigned so that the absorption is reduced without sacrificing sensitivity. With current absorption levels, at 514 nm even 0.4% concentrations are too high, which limits the ability to record thick holograms. As a result, the overall diffraction efficiencies are reduced and the angular selectivity is broadened. Figure 3-25 is a comparison of the angle selectivity

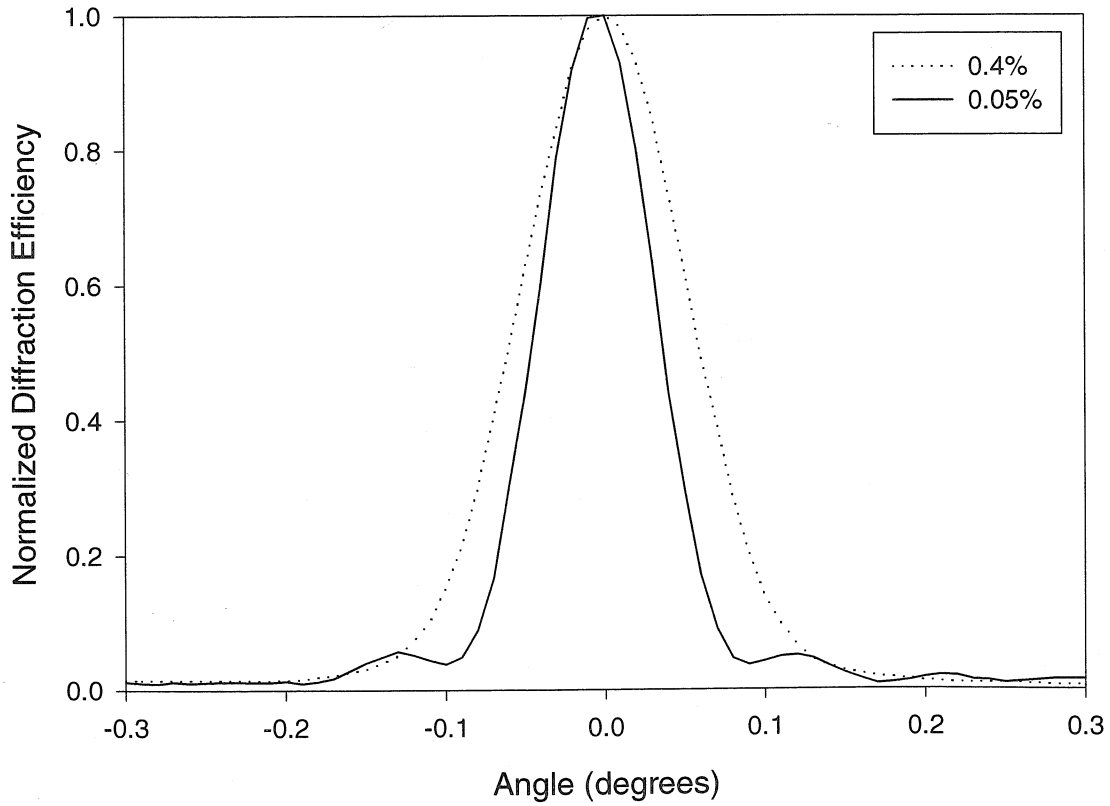

Fig. 3-25. Angle selectivity measurements of holograms recorded in materials with 0.05% and 0.4% chromophore concentrations.

curves, measured at 633 nm, obtained for a hologram recorded at 514 nm, in a sample with a chromophore concentration of 0.05% and a sample with a chromophore concentration of

0.4%, with the same thickness. The selectivity curves were normalized and centered to facilitate comparison. It is easy to see well defined nulls for the 0.05% sample. However, the selectivity curve for the 0.4% sample does not have nulls, and is also broader, indicating that the hologram is not recorded throughout the volume of the material, but rather varies in strength throughout the thickness of the material.

The grating strength of the hologram recorded with optimal exposure energy is plotted in Figure 3-26 for samples with four different NQ concentrations. A linear increase in

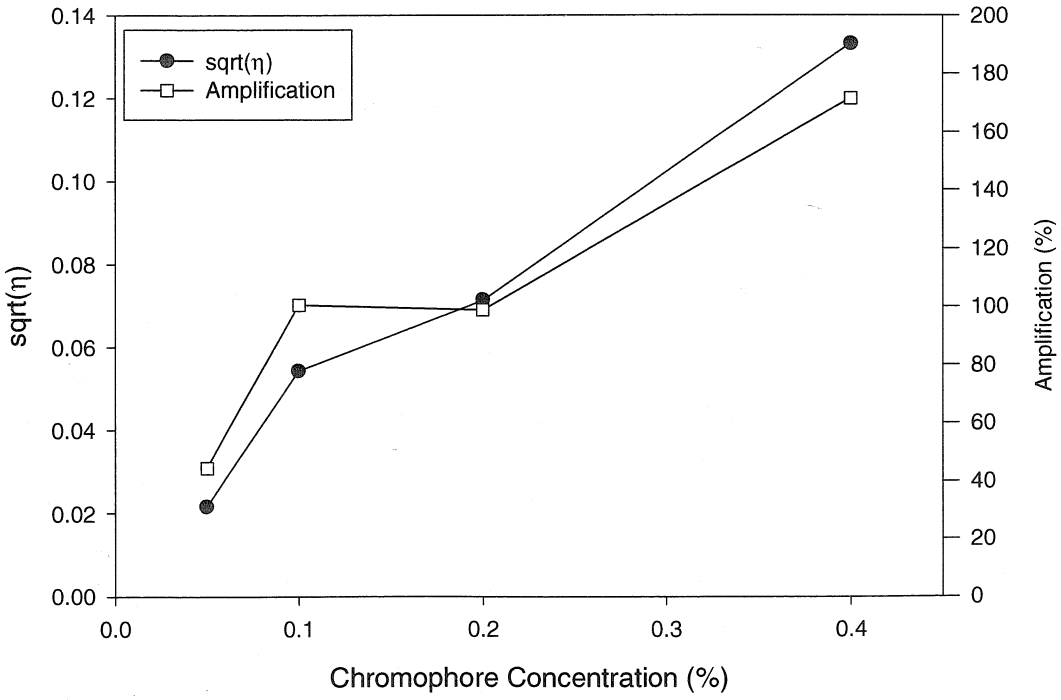

Fig. 3-26. Dependence of the maximum diffraction efficiency and amplification of the recorded holograms in the NQ-MMA co-polymer, after 11 days baking, on the chromophore concentration. The samples were 0.5 mm thick.

grating strength with concentration is observed. Also plotted in Figure 3-26 is the average amplification of the grating strengths of the 11 holograms in each sample after 11 days of baking at 75° C, as a function of chromophore concentration. Amplifications between 50% and 170% were realized. From Equation 3-7, the amplification is expected to be indepen-

dent of chromophore concentration. One possible explanation for the increase with concentration is that for higher concentrations the grating is not uniform throughout the volume of the material, resulting in detached chromophore diffusion in directions normal to the grating vector, rather than strictly parallel to it as would be the case with a uniform modulation depth.

3.4 Conclusion

When compared to other holographic recording materials, PQ:PMMA has some advantages and some disadvantages. Compared to DuPont HRF-150 films, which have been used extensively for holographic storage,[3-15] PQ:PMMA has the advantage of being able to be made in thick, high-optical quality samples. Furthermore, there is no shrinkage. However, its M/# is not as high. The HRF-150 film had M/6.5 for a 100-μm-thickness in [3-6], whereas a value of only M/4.8 was obtained for a 3-mm-thick PQ:PMMA sample. Furthermore, HRF-150 has a higher sensitivity, reaching a saturation diffraction efficiency in just 300 mJ/cm^2.

With any recording material there is a trade-off to be made between absorption, sensitivity, and wavelength. Generally, if the wavelength is changed to decrease the absorption there will be a corresponding decrease in the sensitivity. Alternatively the material can be modified to adjust its absorption to suitable levels for a desired operating wavelength, thickness, and chromophore concentration. The index modulations that can be achieved are mostly dependent on the quantity and type of chromophore present, which directly affects the amount of absorption. For a sample with 0.1% by weight of NQ, the concentration is roughly 3.4×10^{-6} mol/cm^3, with $\Delta n = 1.2 \times 10^{-5}$ and a molar extinction coefficient

$\varepsilon = 3.85 \times 10^6$ cm^2/mol. The corresponding holographic sensitivity is S = 1.83 cm/J in a 0.6 mm thick sample. By comparison, for a PQ:PMMA sample with 0.7% by weight PQ, the concentration is about 4×10^{-5} mol/cm^3, with $\Delta n = 1.1 \times 10^{-4}$ and a molar extinction coefficient $\varepsilon = 9.41 \times 10^4$ cm^2/mol. The holographic sensitivity is 14 cm/J for a 1 mm thick sample. The index modulation of the PQ:PMMA material is almost 10 times greater than that of NQ:PMMA; however, it has a chromophore concentration that is approximately 12 times higher but is doped only 7 times higher by weight. It can be concluded that per molecule the NQ chromophore yields a higher index modulation. However, it also has a much higher absorption, indicating a less efficient conversion of photons into detached chromophores, compared to the PQ:PMMA material's conversion of PQ to attached chromophores.

References

[3-1] J. T. Gallo and C. M. Verber, "Model for the effects of material shrinkage on volume holograms," Appl. Opt. **33**, 6797-6804 (1994).

[3-2] D. A. Waldman, H.-Y. S. Li, and M. G. Horner, "Volume shrinkage in slant fringe gratings of cationic ring-opening holographic recording material," J. Imaging Sci. Techn. **41**, 497-514 (1997).

[3-3] A. Yariv, *Quantum Electronics*, 3rd ed. (Wiley, New York, 1989).

[3-4] A. V. Veniaminov, V. F. Goncharov, and A. P. Popov, "Hologram amplification by diffusion destruction of out-of-phase periodic structures," Opt. Spektrosc. **70**, 864-869 (1991).

[3-5] K. Curtis, A. Pu, and D. Psaltis, "Method for holographic storage using peristrophic multiplexing," Opt. Lett. **19**, 993-994 (1994).

[3-6] A. Pu, K. Curtis, and D. Psaltis, "Exposure schedule for multiplexing holograms in photopolymer films," Opt. Eng. **35**, 2824-2829 (1996).

[3-7] D. Psaltis, D. Brady, and K. Wagner, "Adaptive optical networks using photorefractive crystals," Appl. Opt. **27**, 1752-1759 (1988).

[3-8] M. Montecchi, M. Settembre, and M. Romagnoli, "Optically induced birefringence and dichroism in rigidly held dye molecules," J. Opt. Soc. Am. B **5**, 2357-2362 (1988).

[3-9] G. E. Dovgalenko, M. Klotz, G. J. Salamo, and G. L. Wood, "Optically induced birefringence in bacteriorhodopsin as an optical limiter," Appl. Phys. Lett. **68**, 287-289 (1996).

[3-10] N. C. R. Holme, P. S. Ramanujam, and S. Hvisted, "Photoinduced anisotropy measurements in liquid-crystalline azobenzene side-chain polyester," Appl. Opt. **35**, 4622-4627 (1996).

[3-11] P.-A. Blanche, Ph. C. Lemaire, M. Dumont, and M. Fischer, "Photoinduced orientation of azo dye in various polymer matrices," Opt. Lett. **24**, 1349-1351 (1999).

[3-12] L. Nikolova, T. Todorov, M. Ivanov, F. Andruzzi, S. Hvilsted, and P. S. Ramanujam, "Polarization holographic gratings in side-chain azobenzene polyesters with linear and circular photoanisotropy," Appl. Opt. **35**, 3835-3840 (1996).

[3-13] A. Yariv, *Optical Electronics*, 4th ed. (Saunders, Philadelphia, 1991).

[3-14] R.P. Shishkina, V.N. Berezsnaya, Russian Chemical Reviews, **63**(2), 139-146 (1994).

[3-15] A. Pu and D. Psaltis, "High-density recording in photopolymer-based holographic three-dimensional disks," Appl. Opt. **35**, 2389-2398 (1996).

4 Holographic Data Storage with Diffusion Amplified Photopolymers

4.1 Introduction

One of the primary applications for thick holographic recording materials is holographic data storage. Due to the Bragg effect of volume holograms,[4-1] multiple holograms can be recorded within the same volume of material and be reconstructed with minimal crosstalk.[4-2] The idea of using volume holography as a means of storing data is not new,[4-3]-[4-4] and with the advancements of electronic detectors and spatial light modulators, is closer to commercialization than ever before. Data storage experiments with PQ:PMMA are described in Section 4.2, including an experimental comparison of the scatter from recording materials, which in this case is the limiting factor of density.

There is a large degree of flexibility in the design of a holographic storage system and it is not immediately apparent the effects changes will have on the ultimate capacity of a system. Furthermore, it is desirable to be able to simulate a system without having to actually perform an experiment. To this end, the holographic data storage process with shift multiplexing[4-5] was modeled and simulated to determine the effects of material properties and optical system design on overall data storage density. A detailed description of the modeling as well as the genetic algorithm used to simulate the system is described in Section 4.3.

PQ:PMMA is a material capable of recording holograms, but once recorded the material cannot be erased and re-used. For this reason it is suitable only as a read only

memory (ROM). Currently the most popular ROM systems widely available are CD and DVD, both optical, bit-oriented, storage systems. CD, originally used for digital audio recordings, is capable of storing up to 700 MB on a single 12 cm disk. With approximately 88 cm^2 of usable area, the data density is about 0.6 bits/μm^2. DVD, on the other hand, is a much newer technology utilizing a shorter wavelength readout laser, among other enhancements, and can store approximately 5 GB in a single layer. This increases the density to about 4.5 bits/μm^2. Future generations of DVD are planned that have two layers single-sided, and even two layers double-sided. However, the double-sided scheme would require either the disk be mechanically flipped in the player, or the use of one read head for each side. Even with the double-layer single-sided approach, the density of DVD approaches 10 bits/μm^2. For a holographic system to be commercially feasible, it must greatly exceed this density or provide some other performance enhancement that might be needed for niche markets, such as a very high readout bandwidth.

4.2 Holographic data storage with PQ:PMMA

PQ:PMMA is a recording material that can be made into arbitrary thicknesses and does not exhibit shrinkage. These properties, plus its self-supporting rigidity and ruggedness made it an attractive candidate for a holographic data storage medium. Furthermore, it is relatively inexpensive and can be easily made into the widely used disk format.

There are several techniques for multiplexing holograms in a recording material such as angle, peristrophic,[4-6] and shift.[4-5] Shift multiplexing is a convenient method for several reasons. For a disk-based application, the rotation of the disk provides the material shift required. Furthermore, the reference beam can be generated with a single lens and

does not require any moving parts. Therefore, the only motion required is the disk rotation and radial head movement, to access different tracks.

4.2.1 Holographic recording system

Figure 4-1 shows the experimental system used for recording holograms. In this

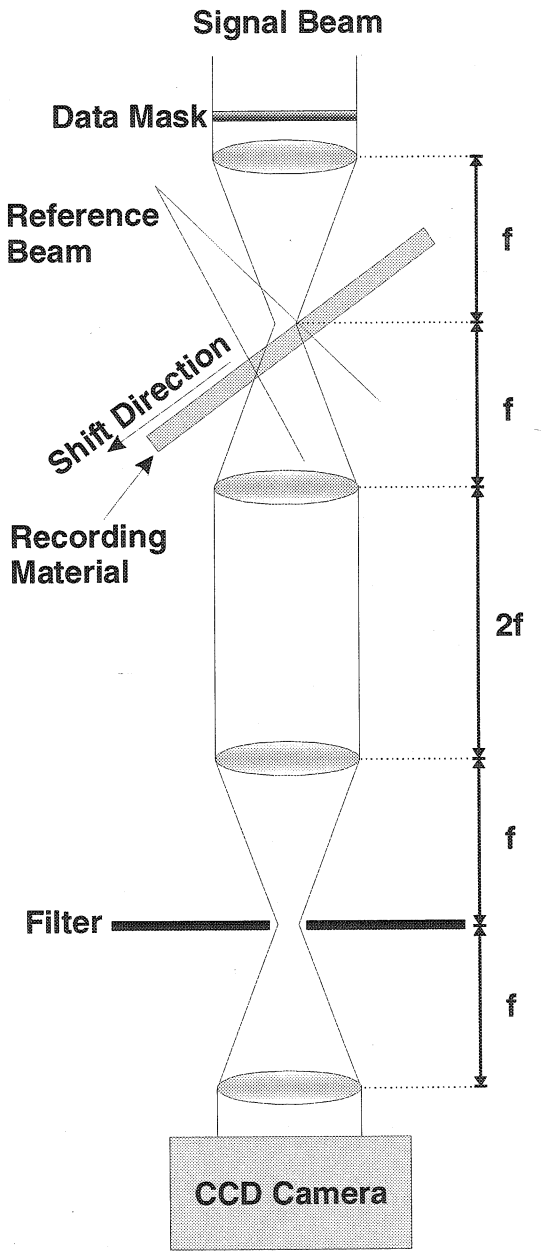

Fig. 4-1. Experimental system for recording holograms with shift multiplexing.

system a disk was not used, but rather the material was mounted on a translation stage to provide the necessary shift. With a disk it was found experimentally that without additional tracking information recorded, it was very difficult to align and Bragg-match the recorded holograms after the material was removed from the optical system, to be baked, and then reinserted.

The optical system consists of four F/1.4 Nikon lenses arranged to image a data mask to a CCD detector. The lenses had 50-mm focal lengths and 3.5 cm apertures, allowing 560,000 pixels of the 40-micron pixel data mask to be imaged. Four lenses were necessary in order to record near the Fourier plane of the first lens, and to provide a second Fourier plane for filtering. The filter consists of a simple iris designed to allow the fundamental order of the data mask to be transmitted, while blocking any light outside of it. The filter stage greatly helps in reducing the amount of scattered light that makes it to the detector. The reference beam was generated by a single lens (not shown) positioned to allow adjustment of the focal point distance relative to the material. The divergence angle of the reference beam could also be adjusted by opening an iris before the lens to control the diameter of the incident beam. The reference beam was aligned to be incident normally on the material, and with a focal point 2 cm from the material's front surface. The signal beam made an angle of 35 degrees with the surface normal. The laser wavelength used was 488 nm. With the reference beam coming to a focus 2 cm before the material in order to completely cover the signal beam on the front and back surface of the material, the numerical aperture of the reference was 0.15.

The data mask consisted of a two-dimensional array of 40-micron pixels each with a 100% fill factor. This mask was made by electron-beam lithography of chrome on glass

providing a high contrast ratio and sharp transitions between on and off pixels. The CCD was a Pulnix TM-7CN camera with its front glass cover plate removed to avoid interference fringes resulting from multiple reflections. This camera has 768×494 pixels each with a size of 8.4×9.8 microns. The NTSC output was digitized by a Data Translations framegrabber in a PC to give a 640×480 pixel image with 8 bits-per-pixel of dynamic range. This process causes the originally discrete CCD output to be converted to an analog signal and then re-sampled by the framegrabber. The result is that each pixel in the image on the PC represents a square with an edge length of approximately 10.08 microns at the camera plane. Since the data mask has 40 micron pixels, each one takes approximately a 4×4 box of pixels in the captured image. For clarity, the captured image region associated with a single data mask pixel will be referred to as a "super-pixel."

4.2.2 Experimental results

In order to measure the quality of the holographically reconstructed data pages, the signal-to-noise ratio was used as a metric. Because of the analog conversion process that occurs, as discussed in the previous section, there is not a one-to-one correspondence between the pixels returned by the framegrabber and the pixels on the detector in the optical system. Furthermore, the data mask pixels are oversampled by the detector and there is no explicit alignment to ensure that the detector pixel boundaries align with the data mask pixel boundaries. In fact, due to pixel size mismatch, this is impossible. As a result, some pixels in the final image will be on a boundary between on and off pixels in the data mask, and will therefore contain some value between 0 and 255. To compensate for this effect, the edge pixels of each super-pixel were discarded. Since the super-pixel started as a 4×4 array of pixels, by discarding the boundaries a 2×2 pixel area is left. These four pixel

values are averaged to obtain the value for that pixel. In order to determine the alignment of the super-pixels in the final image, a program was written to allow interactive adjustment of a grid of pixels overlaying the image. A screen shot of this program is shown in Figure 4-2. Beyond allowing adjustments to the grid size and location, the program could

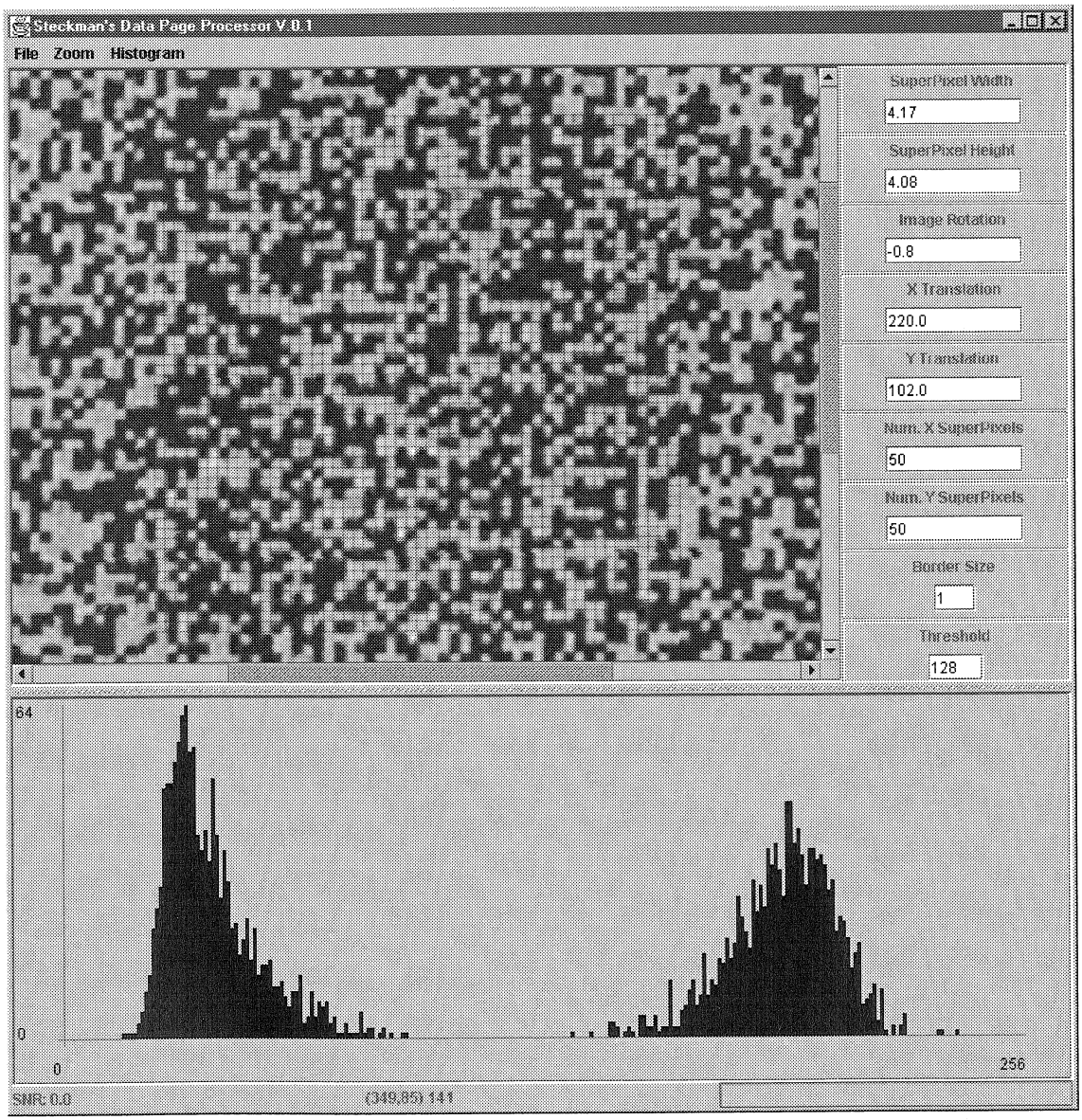

Fig. 4-2. Screenshot of the reconstructed data page processing program.

rotate the image to compensate for slight rotation errors of the actual data mask in the opti-

cal setup. It also displays a histogram of the super-pixels defined by the grid to aid in alignment.

To compute the SNR of a reconstructed data page several steps were taken. First a high-quality image of the data mask was taken through the optical system without any recording material in place. A grid was then fit to the image such that the histogram of the super-pixels showed clearly separated regions of 0 and 1 bits, as seen in Figure 4-2. A threshold was then chosen between the two separate regions of super-pixel values and a pixel map was generated indicating the correct binary value for each super-pixel. After recording holograms and reconstructing a data page, the pixel map was aligned to the new image to coincide with the same set of super-pixels as the original high quality image. Since the value of the super-pixels from the data mask are known from the process of generating the pixel map, the SNR is computed as

$$\mathrm{SNR} = \frac{\mu_1 - \mu_0}{\sqrt{\sigma_1^2 + \sigma_0^2}}. \tag{4-1}$$

Here μ_1 and μ_0 are the means of the super-pixel values for the 1 and 0 pixels, respectively, of the pixel map. σ_1 and σ_0 are the corresponding standard deviations.

There are a number of ways that the SNR can be computed with this scheme. One approach would be to use a large grid that computes the SNR of the entire image. Another approach is to use multiple smaller areas and compute the SNR of each small area individually. Then the SNR measurements from each area can be combined by averaging to obtain the final SNR for an image. For the measurements described in this thesis, the second approach was chosen for a couple of reasons. Due to the inherent Gaussian intensity distri-

bution of the laser, plus other effects causing non-uniform illumination such as low frequency interference fringes, the average intensity of the image tends to spatially vary. The result is that if a histogram of the entire image is taken, the 1's and 0's may overlap; however, if the histogram is taken over a smaller region, they may be well separated. In effect, if a global threshold were used, errors would result. However, if a local threshold is selected based on a smaller region, then the error rate would be lower. A second reason for choosing local regions over a global one is optical distortion. Essentially, optical distortion results in the super-pixel's size varying with position in the image. If a global mask is used, then the SNR is computed as if all super-pixels are the same size across the image. However, with the use of smaller regions, the pixel mask size can be adjusted with position, yielding a better fit of the mask to the actual super-pixels. For each image, a 30×30 super-pixel region was used in three of the corners and one in the center. The fourth corner was not used because the camera had a section of damaged pixels which affected the SNR measurement.

Taking an image of the data mask through the optical system is useful not only for determining the correct values of the super-pixels, but also for obtaining a measure of the quality of the optical system as an upper bound on the quality that can be expected from reconstructed holograms. Figure 4-3 shows the data mask imaged through the optical system. This image resulted in an SNR of 16.1. As a simple measure of material quality, an image of the data mask was taken through the optical system with the addition of a 3-mm-thick recording sample in place. Figure 4-4 shows the imaged mask which had an SNR of 11.4. This image had well separated histograms and sharp transitions between pixels leaving a good amount of headroom for further degradation after recording holograms.

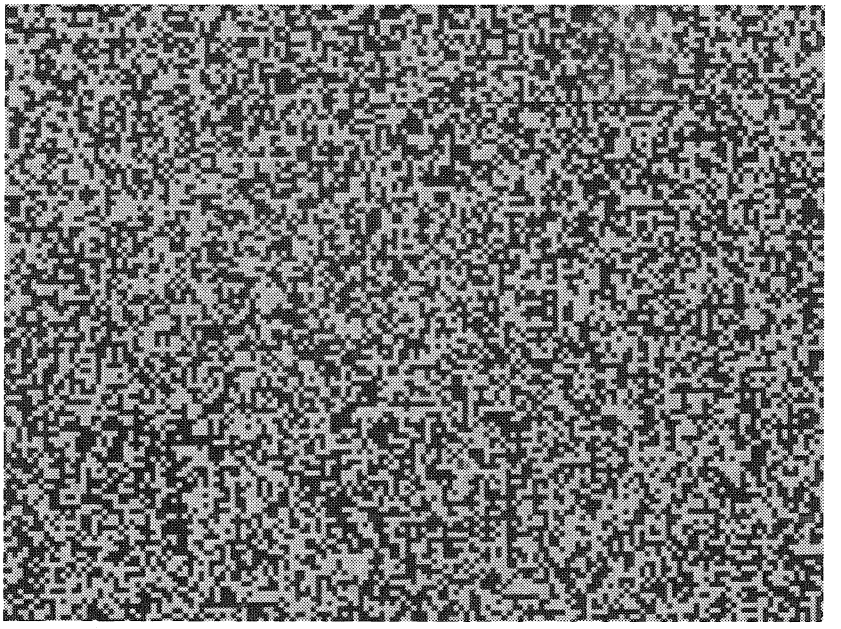

Fig. 4-3. The data mask imaged through the optical system.

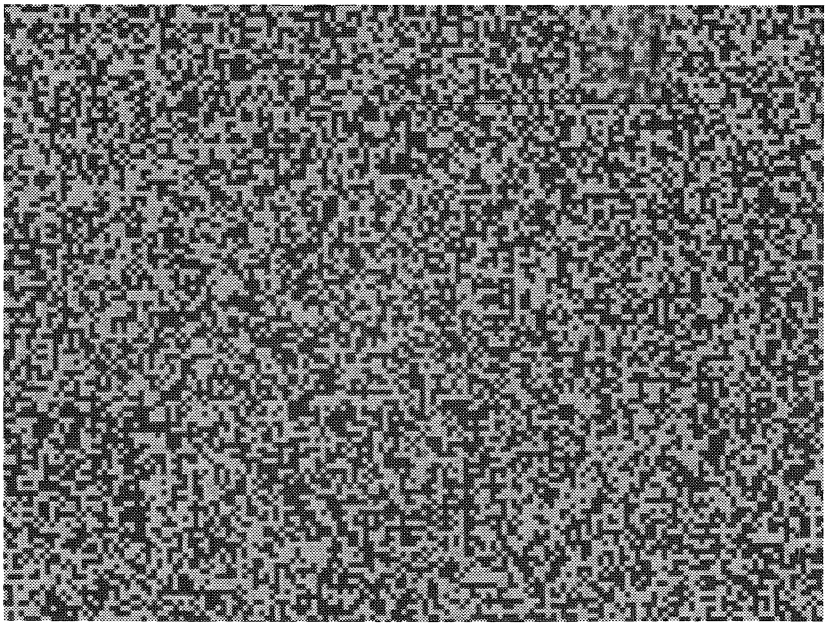

Fig. 4-4. The data mask imaged through the optical system with a sample in place.

So far the PQ:PMMA material was tested only with plane wave holograms. As an initial test, a single hologram was recorded for 500 ms in a 3-mm-thick sample. The refer-

ence beam intensity was 5 mW/cm^2 before the focusing lens and the signal beam was 830 mW/cm^2 before the data mask. These intensities were chosen to try to equalize the intensities of the two beams at the surface of the material. Figure 4-5 shows the reconstruc-

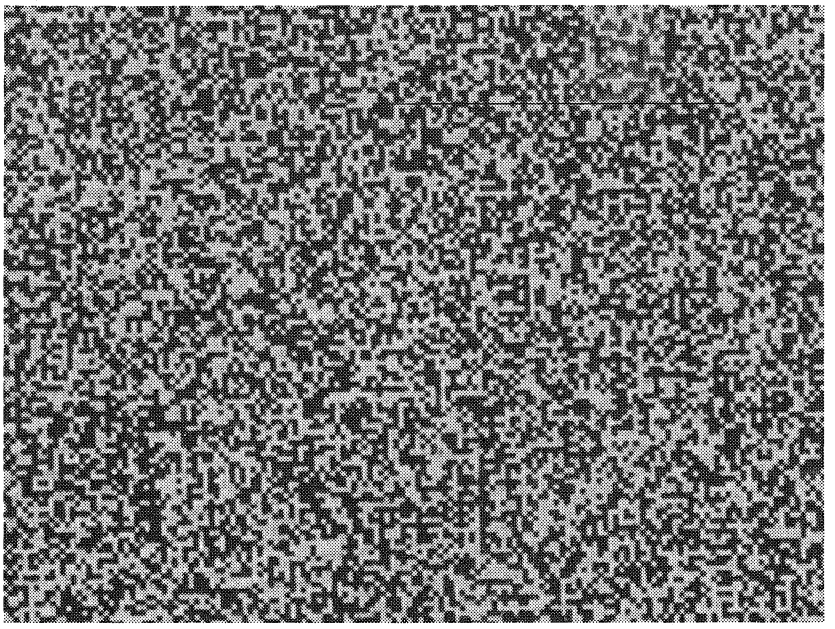

Fig. 4-5. Reconstruction of a hologram from a sample with only one hologram recorded.

tion of the recorded hologram, which has an SNR of 8.0.

The shift selectivity of the system was measured to be 25 microns with an image reconstruction. The signal beam illuminated a spot with approximately a 1.7 mm diameter. By recording with a shift distance of 50 microns, at the second null, the density would be 6.6 bits/μm^2. The density can be increased by using a reference beam that focuses closer to the material, thereby decreasing the amount of shift required between holograms. Instead of modifying the optical setup at this stage, it was decided to push this system to its limit, and then see what modifications would be required later, if any. As a first step, 60 holograms were recorded with a 100 micron shift between each, with a constant exposure time of 800 ms each. Given that the reference beam occupied a 3-mm-diameter spot, this would

cause 30 holograms to overlap at the center hologram. An image of the reconstruction of the 30th hologram is shown in Figure 4-6. The SNR of this image was 3.94.

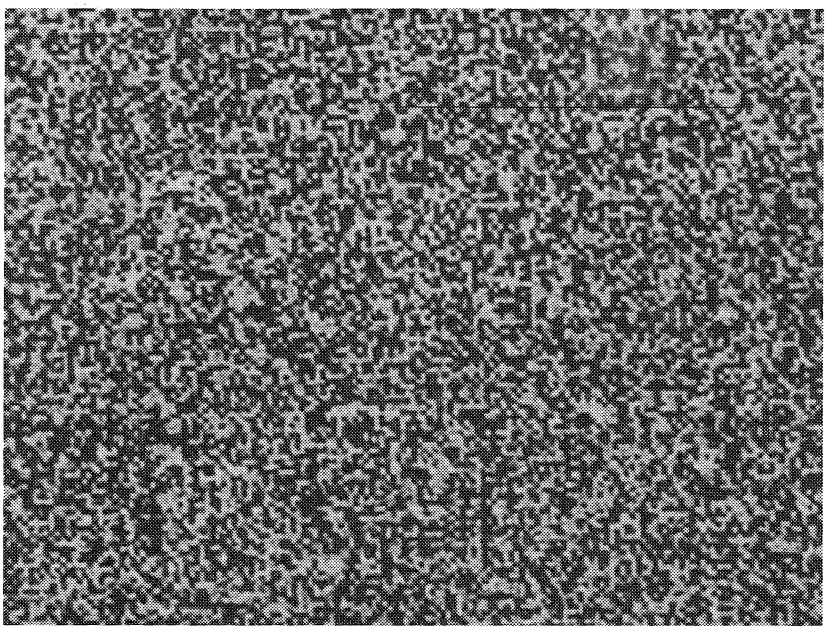

Fig. 4-6. Reconstruction of the 30th of 60 holograms.

Even though the SNR dropped significantly from the single hologram reconstruction, the reconstruction was reasonable and it was decided to push the material to the next level and record 120 holograms with a 50 micron shift between each hologram. For this experiment, the beam powers were reduced to 1.5 mW/cm^2 for the reference and 260 μW/cm^2 for the signal beam; however, the exposure time was kept at 800 ms per hologram. An image of the reconstructed 60th hologram is shown in Figure 4-7, which gave an SNR of 2.8. A plot of the shift selectivity over all 120 holograms is shown in Figure 4-8. Although the selectivity plot shows the holograms were not of equal strength, it is a bit misleading because in fact, only the center hologram was maximally overlapped by 60 holograms. The edge holograms only experience partial overlapping, resulting in a higher

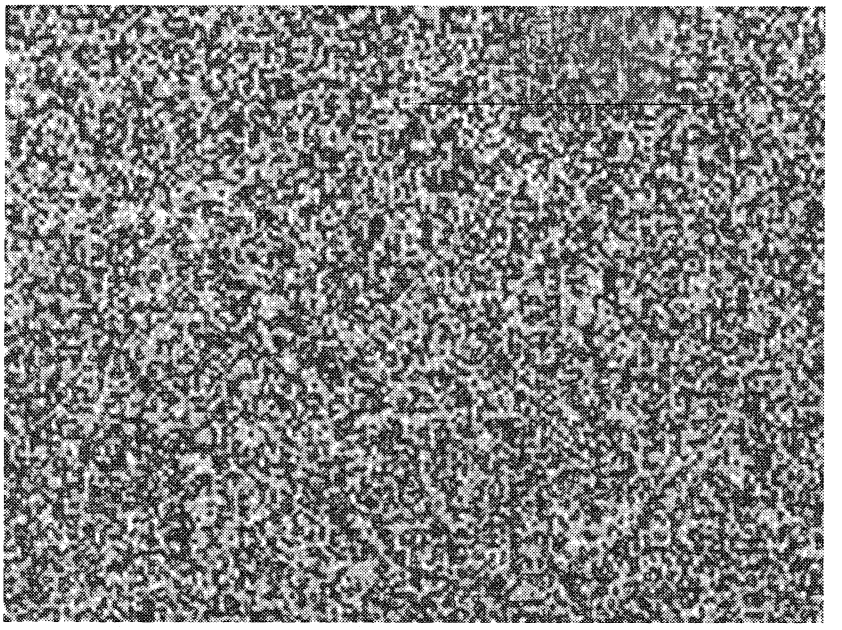

Fig. 4-7. Reconstruction of the 60th of 120 holograms.

diffraction efficiency. However, if the schedule were perfect, the strengths of the holograms would be symmetric with respect to the center. That they aren't indicates some improvement could be made by optimizing the exposure schedule. But in view of the very low SNR measured in this experiment, it is unlikely that improving the exposure schedule slightly would get the magnitude increase that is desired.

As a summary of the data storage experiments performed, Figure 4-9 contains a plot of the measured SNR as a function of the number of holograms recorded. Although there is a decrease by a factor of two from the SNR of the optical system to that of a single hologram reconstruction, the image quality is still high enough to easily detect the values of the bits in the image. This indicates that the material has a sufficient quality in terms of introducing phase front distortion that would otherwise blur the image, as well as the ability to record and reconstruct a high-bandwidth image. However, once many holograms are stored

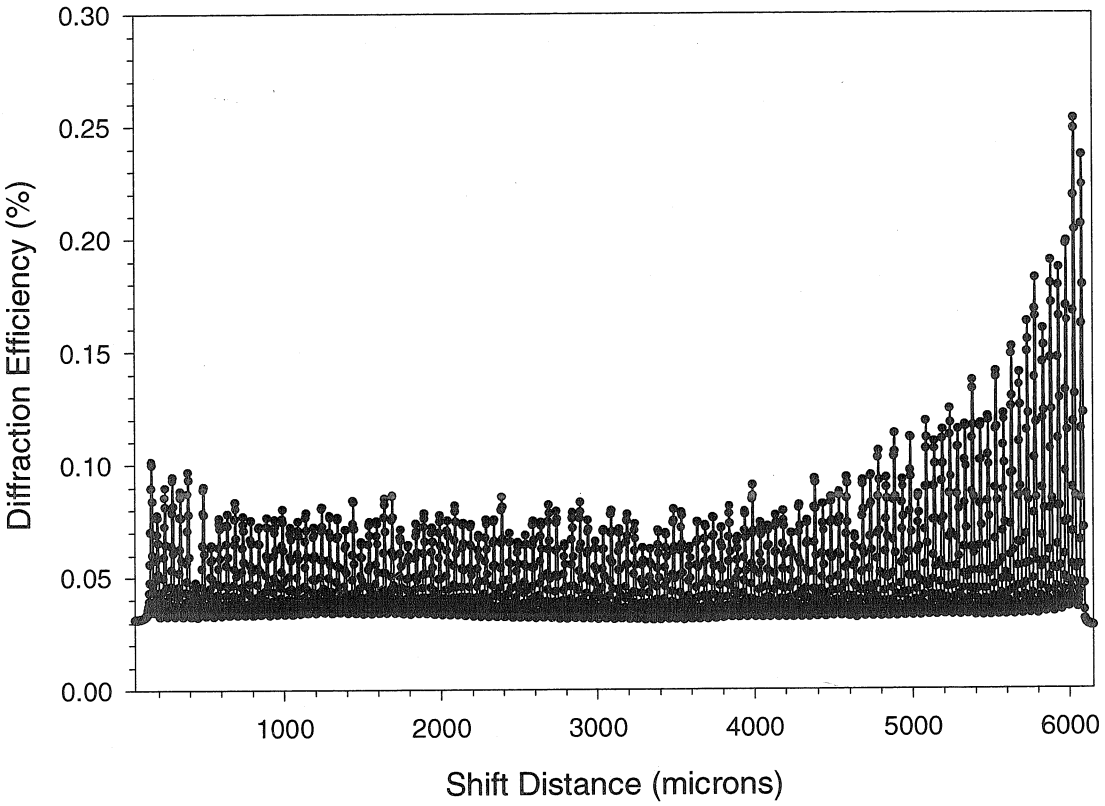

Fig. 4-8. Shift selectivity of 120 holograms recorded in 3-mm-thick PQ:PMMA.

in the material, the reconstruction quality quickly degrades. The diffraction efficiency of the holograms are not high enough to compensate for the amount of noise in the reconstruction. Even with the optical filtering stage, the main contributor to noise is scatter from the recording material itself. There are, essentially, three ways to circumvent this problem. One is to improve the fabrication of the material such that the scatter can be reduced. The second is to increase the dynamic range, or M/#, of the material to compensate for the scatter by increasing the diffraction efficiency. The third is to dramatically modify the optical system to optimize the data storage density by changing the lenses, geometry, and pixel size used.

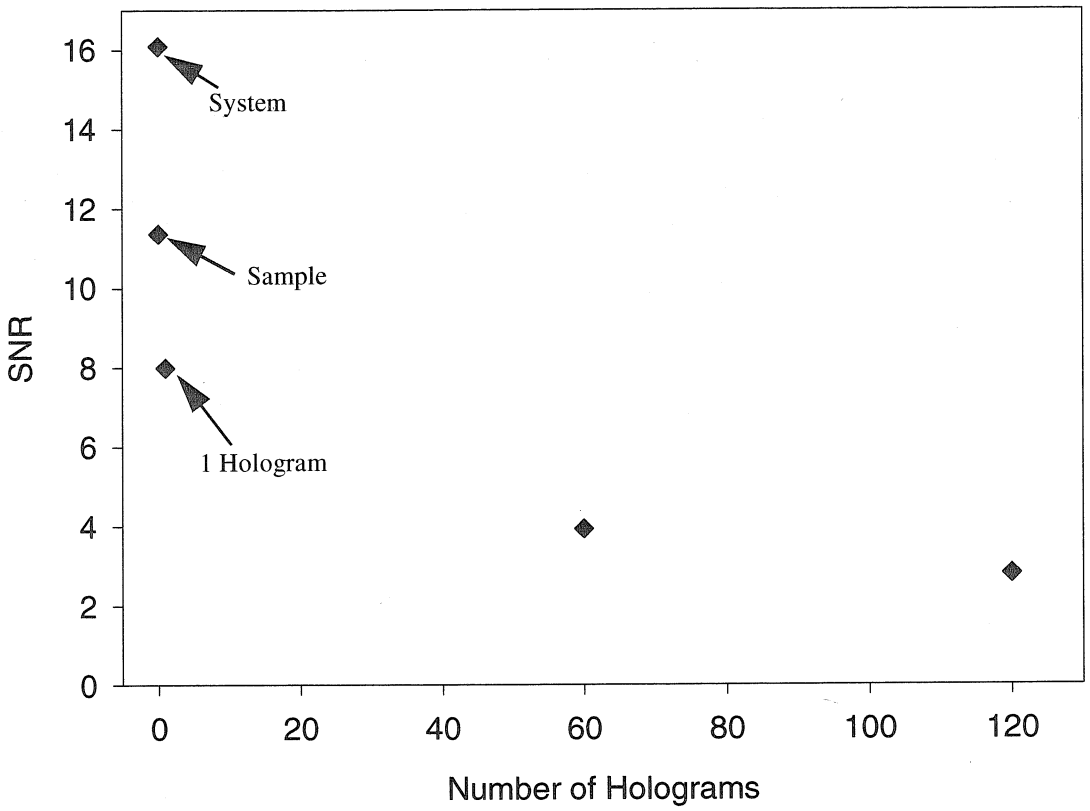

Fig. 4-9. Signal-to-noise ratios for various conditions in the data storage experiments.

4.2.3 Material scatter

From the last experiment with 120 holograms, the diffraction efficiency of the middle holograms was about 7×10^{-4} while the background noise level is approximately 2.5×10^{-4} relative to the reference beam power. Based on measurements with materials that did not have holograms recorded in them, the majority of this noise is scatter from the material rather than crosstalk. For the optical system, the scatter efficiency is measured as the power of all the scattered light that makes it through the optical system and to the back focal plane of the last lens, divided by the incident illuminating power.

A more thorough and general measurement is to determine the scatter efficiency per solid angle as a function of angle relative to the illuminating beam. To do this, the optical

setup shown in Figure 4-10 was used. A collimated laser beam is incident normally onto

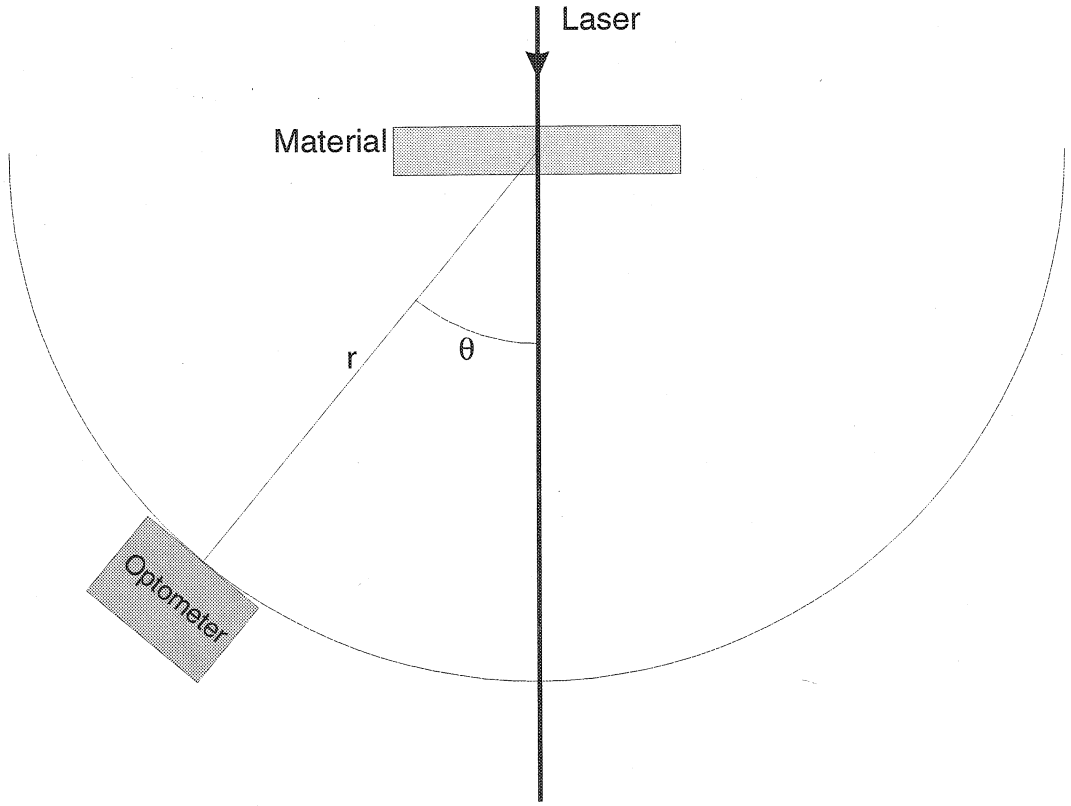

Fig. 4-10. Optical system for measuring material scatter.

the material. This beam was linearly polarized parallel to the material's surface, which is the most common situation in holographic recording. The optometer had an active area of 1 cm^2 and was positioned at various angles θ, while maintaining a distance of 38.5 cm from the center of the material being tested. At each measurement angle θ, the background noise was first measured by removing the material from the system. Then the material was replaced in the system and again a power measurement was taken. The noise was subtracted from the scatter measurement so as not to include the power from the scattered light from other optical components that were behind the sample. The scatter efficiency per steradian is calculated as

$$\eta_s(\theta) = \frac{P_i}{P_s(\theta) - P_N(\theta)} \times \frac{r^2}{1\ cm^2} \tag{4-2}$$

where P_i is the incident power, P_s is the measured scattered power and P_N is the corresponding noise power. 1 cm^2 is the detector area, and 1 cm^2/r^2 gives the number of steradians subtended by the detector.

Scatter measurements were taken for various types of holographic recording materials and modifications of the PQ:PMMA material, and at various wavelengths. Figure 4-11

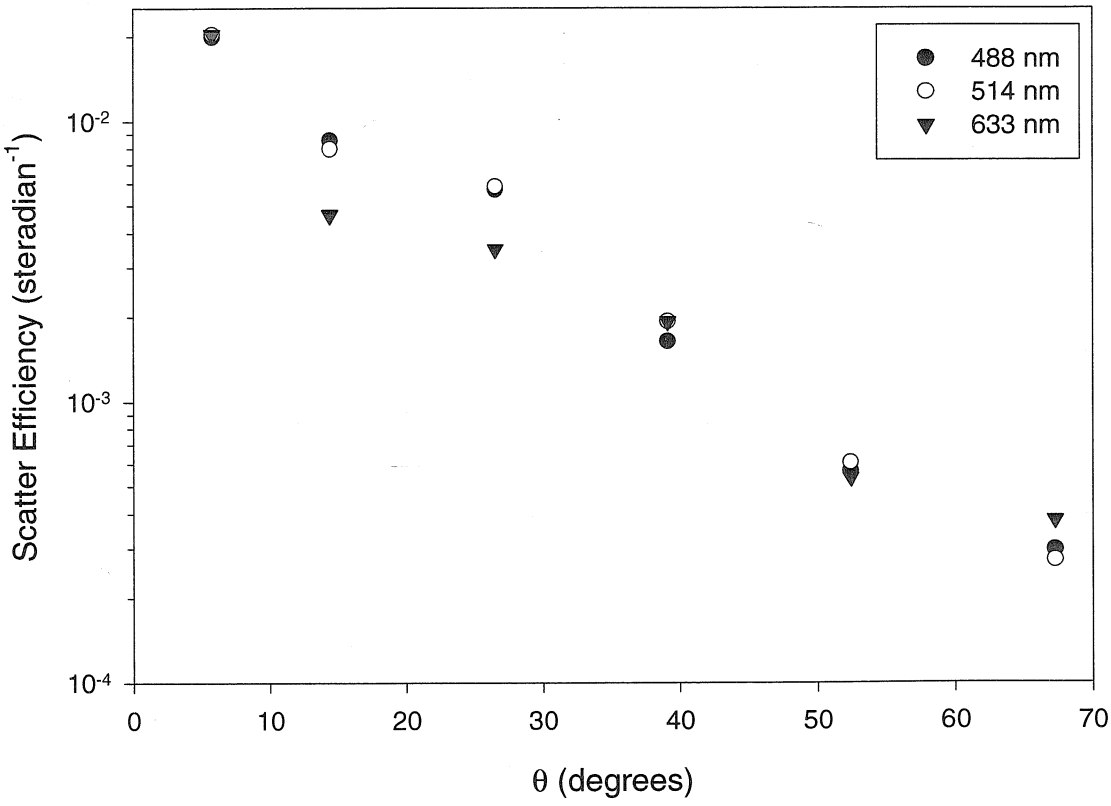

Fig. 4-11. Scatter from a 1-mm-thick sample of PQ:PMMA at 3 different wavelengths.

shows the scatter of a 1-mm-thick sample of PQ:PMMA at three different wavelengths. There is an exponential decrease in scatter with angle from the material; however, surprisingly there is little systematic difference between the three wavelengths. This indicates that

the elements contributing to scatter are predominantly very large relative to the wavelength, and a change in wavelength does not appreciably change the angle or quantity of scattered light. Figure 4-12 shows scatter measurements from several samples, all taken at 488 nm.

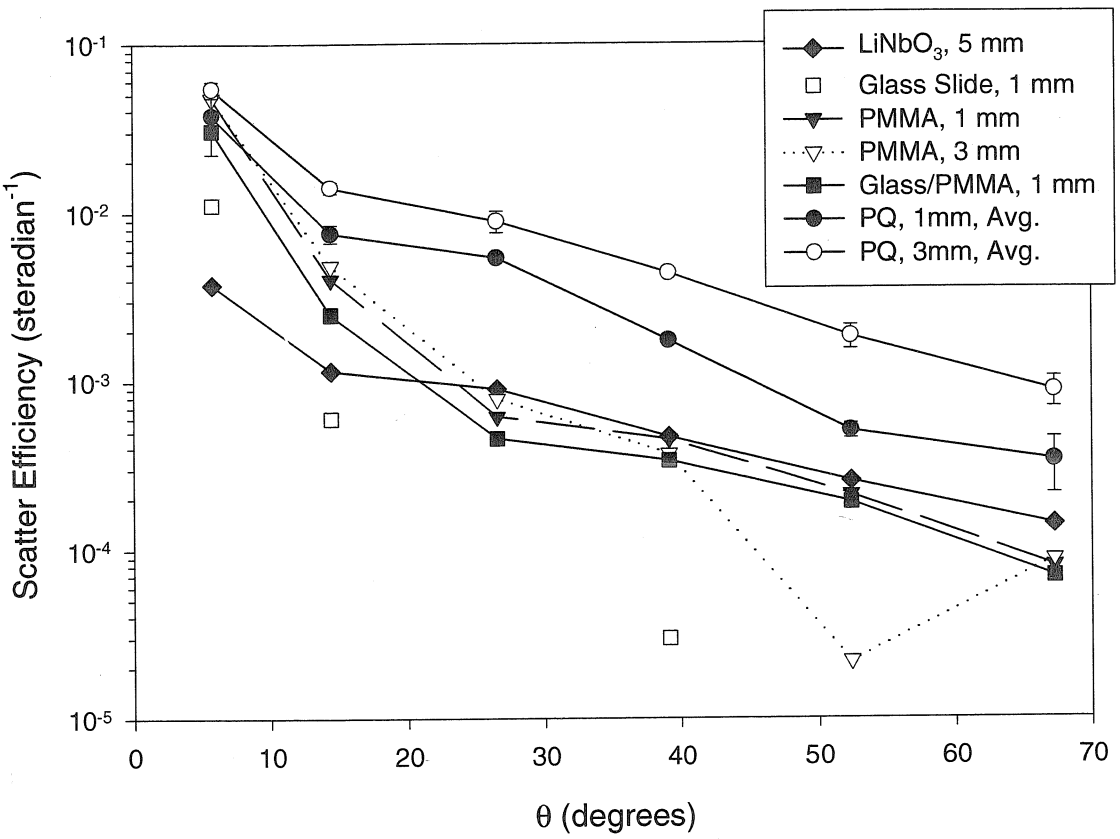

Fig. 4-12. Scatter efficiency of several samples at 488 nm.

The measurements of 1-mm-thick PQ:PMMA at 488 nm were repeated two more times to get an idea of the accuracy of the measurement system. Also, 3-mm-thick PQ:PMMA was measured three times at 488 nm. The plot shows that the standard deviation of the measurements, shown as error bars, are reasonably small. Also, the scatter from the 3-mm-thick sample is about 3 times higher than that of the 1-mm-thick sample, indicating that the volume of the material rather than the surfaces is the main contributor to scatter. To test this, a 1-mm-thick sample of PMMA was fabricated with glass microscope slides attached

to each surface. These glass slides formed part of the mold during polymerization of the material, and were bonded well to the PMMA, rather than being glued on afterwards. The curve labeled Glass/PMMA are the results with this material, and it is clearly seen that the scatter is greatly reduced. This would indicate that the surfaces were responsible for the scatter. But this sample did not have any PQ in it. As another test, PMMA samples without the PQ were also fabricated and measured. The results for both 1-mm and 3-mm-thick samples are very close to that of the 1-mm-thick PMMA with glass result. Although the sample with attached glass is better than those without, there is not a large difference, and this is a clear indication of the fact that the surfaces of the material are not the problem, but rather the addition of PQ is. However, PQ is the component responsible for hologram formation, and it cannot be removed, and decreasing the concentration will also decrease the dynamic range. For comparison purposes, the scatter of just a glass slide was measured. Here, the scatter was extremely low, and in fact for three of the measurement angles, the scatter power was essentially the same as that for the noise. Another material used for comparison was a 5-mm-thick, anti-reflection coated, 0.01% Fe doped, z-cut, $LiNbO_3$ crystal. For angles above 20-degrees, the scatter of this material was larger than that of even 3-mm thick PMMA, showing that high-quality PMMA samples can be made. However, for small angles, $LiNbO_3$ had the best scatter overall, even better than the glass microscope slide. Most likely this is due to the AR-coating on the crystal, which cut down on multiple-reflection back scattered light which is almost parallel to the incident beam.

Now that the scatter has been thoroughly measured, it must be determined if this information can be used for improving the storage density of the holographic data storage system. While increasing the angle between reference and signal beams will decrease the

scatter, it will also cause a roughly 1/cos(θ) increase in area taken by the beams on the material, tending to decrease density. It is not clear that increasing the angles will have any net gain for the system. But what if, for the sake of argument, a PQ:PMMA sample could be made with the same amount of scatter as the pure PMMA samples? This means the scatter would be reduced by an order of magnitude, so for the optical system discussed in the previous section the scatter noise would decrease to about 2×10^{-5}. Also, the diffraction efficiency of the holograms was about 3 times greater than the scatter efficiency, so the required hologram diffraction efficiency would be 6×10^{-5} to maintain the same level of SNR. From the experiment of the last section, the effective M/# was approximately 2. This is considerably lower than the value measured in the previous chapter, but is to be expected due to the modulation depth with actual images being lower than the ideal case of unity in the M/# measurement experiment. Also, with the optical system of the previous section, to obtain a density of 100 bits/μm^2 would require approximately 860 overlapping holograms. From the formula $\eta = (M/\#/M)^2$, 860 holograms each with a diffraction efficiency of 6×10^{-5} would require M/6.7. This material cannot support such a high M/#, and it would be even worse if such a drastic measure as decreasing the PQ concentration were taken for the sake of decreasing the amount of scatter. Clearly, decreasing the amount of scatter noise generated by this material is not a feasible technique for increasing the data storage density.

4.3 Data storage modeling and simulation

The purpose of this section is to address specifically the influences of material thickness and dynamic range on the storage density achievable with shift-multiplexed holographic disk systems. Past analyses on the storage capacity of holographic storage sys-

tems[4-7][4-8] have considered only the influence of material thickness on storage densities, without fully taking into account the limits imposed by the material's dynamic range. By including both geometrical and dynamic range factors, a more accurate prediction of potential storage densities can be made. Furthermore, these predictions will act as a guide for materials, which need to obtain a minimum level of performance before they can be used as the storage medium in high-density holographic storage systems.

In Section 4.3.1 a description of the optical system considered in the model will be described followed by the mathematical calculations necessary for computing the holographic data storage density of such a system. Variations of the calculation for use with both photorefractive, or re-writable, and write-once materials will be presented. Because the derived formulas are in general transcendental, and optimizations over many parameters are required, numerical techniques have been used for solving the calculation problem, specifically a genetic algorithm. The genetic algorithm used for finding the global density maximum will be described in Section 4.3.2. In Section 4.3.3 calculated values for storage density are compared with experimentally obtained densities from shift multiplexing experiments with both lithium niobate, described in reference [4-9], and the experiments presented previously in this chapter with PQ:PMMA. Finally, calculations of possible data storage densities possible with shift-multiplexed holographic memories are made relative to the performance and thickness of the storage material and the wavelength of light used.

4.3.1 Calculation of storage density

A typical configuration for a shift-multiplexed holographic storage system is shown in Figure 4-13. Lenses L1 and L2 form a 4-f imaging system between the data signal

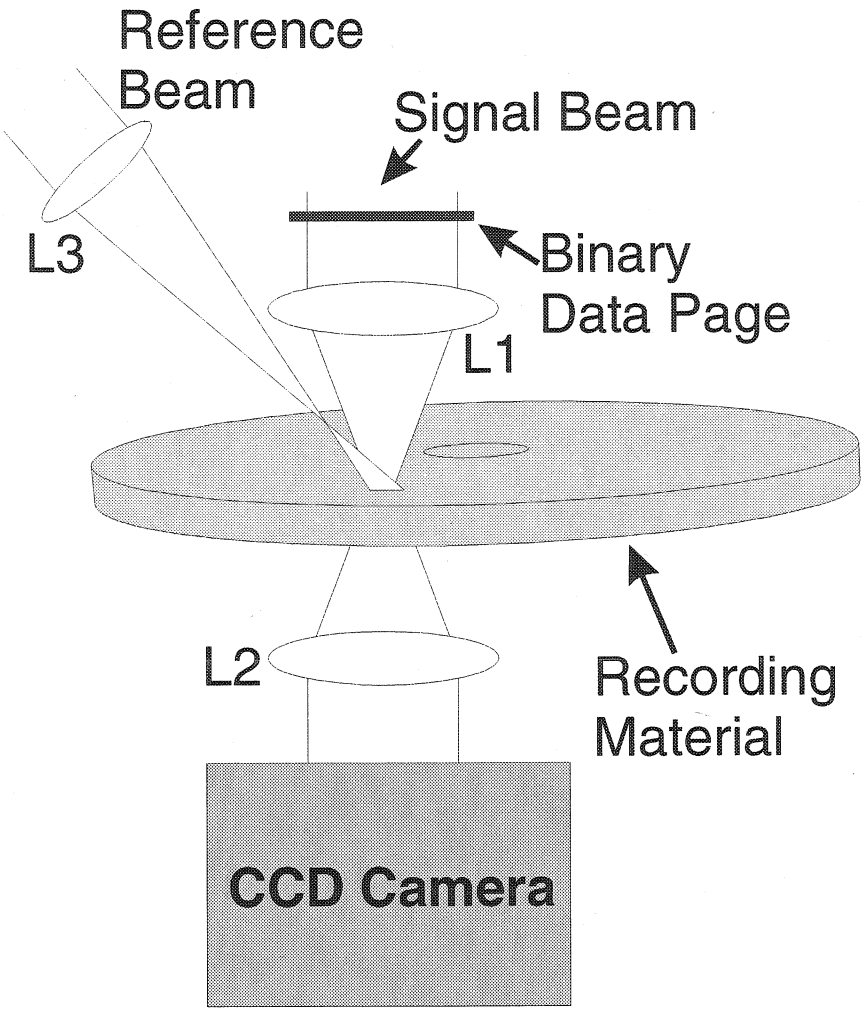

Fig. 4-13. Typical configuration for a shift-multiplexed holographic storage system.

imprinted onto the signal beam and a CCD detector used for detecting the reconstructed holograms. The recording material is placed near the Fourier plane of the signal. A spherical reference beam is created with lens L3, positioned such that the reference beam completely overlaps the signal beam throughout the material. Rotation of the disk serves as the in-plane shift mechanism, while radial translations of the optical system serves to access different tracks.

The storage density for a holographic disk using shift multiplexing can be computed by the relation $D = N_p/(\delta \cdot \delta_r)$, where N_p is the number of bits stored per hologram, δ is the shift-distance required between holograms in order to reconstruct them without substantial crosstalk and with sufficient diffraction efficiency, and δ_r is the radial shift distance required between tracks of holograms. N_p and δ_r are determined by the optical system and material thickness, while δ is predominantly determined from shift-selectivity and dynamic range limitations.

A requirement of the optical system is to have the reference beam completely overlap the signal beam throughout the volume of the material. Each beam will form an ellipse on the top and bottom surfaces of the material. The sizes and positions of the four ellipses are first determined in Section 4.3.1.1 and Section 4.3.1.2. The beam ellipses are used for two purposes. First, by comparing the sizes and position of the ellipses it can be ensured that the signal and reference beams will completely overlap each other on both the first and second surfaces of the recording material. If complete overlapping is not obtained, the density is computed as zero. Second, the sizes of the beams are needed in order to determine the shift distances required between adjacent holograms when taking into account the material's dynamic range.

4.3.1.1 Reference beam geometry

Geometrical optics is used for determining the area of recording material illuminated by the reference beam. Referring to Figure 4-14, the reference beam is completely specified by the position of its focus, given by x_f and z_f, the divergence angle, given by ϕ, and its angle relative to the material's surface normal, θ. z_f is specified as the distance of the reference beam focus from the material along a line normal to the materials surface. x_f

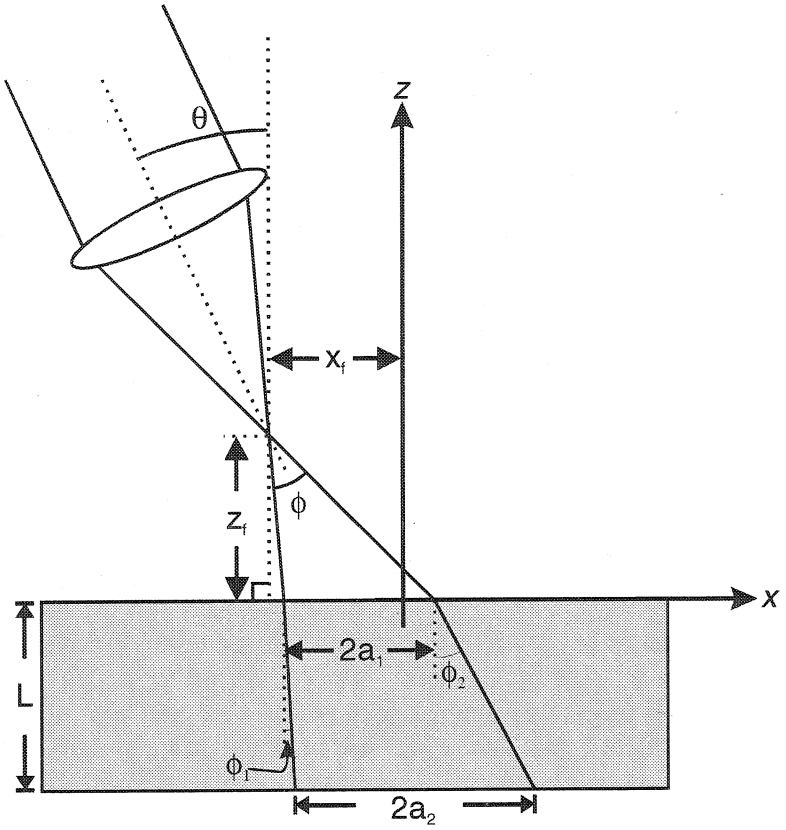

Fig. 4-14. Reference beam geometry for computing the area occupied on a recording material's surface.

is defined relative to the origin, defined by the intersection of the signal beam (not shown) with the first surface of the material. *L* is the thickness of the recording material, and *n* its index of refraction. The beam forms an ellipse on the top and bottom surfaces of the material, given by

$$\frac{(x - x_i)^2}{a_i^2} + \frac{y^2}{b_i^2} = 1 \qquad (4\text{-}3)$$

where the index *i* is 1 for the surface closer to the focus and 2 is for the surface further from the focus.

For the top surface of the material, the reference beam can be specified with the parameters calculated as

$$\begin{aligned} a_1^r &= \frac{z_f}{2}[\tan(\theta+\phi/2)-\tan(\theta-\phi/2)] \\ b_1^r &= z_f\frac{\tan(\phi/2)}{\cos(\theta)} \\ x_1^r &= x_f + a_1^r + z_r\tan(\theta-\phi/2) \end{aligned} \quad , \tag{4-4}$$

which is a straightforward application of trigonometry to the angles of the beam and its divergence together with its position. In this model, the reference beam is only allowed to tilt at an angle in the plane of the signal and normal to the surface, accounting for the lack of an angular term in the equation for *b*. Before writing the formula for the parameters of the ellipse on the 2nd surface, it is convenient to first introduce notation for the beam angles inside of the material. The divergence of the reference beam inside the material can be divided into two angles, one corresponding to each edge of the beam. Each edge is diffracted differently according to Snell's law giving the angles:

$$\begin{aligned} \phi_1 &= \operatorname{asin}\left(\frac{\sin(\theta-\phi/2)}{n}\right) \\ \phi_2 &= \operatorname{asin}\left(\frac{\sin(\theta+\phi/2)}{n}\right) \end{aligned} \quad . \tag{4-5}$$

The parameters of the ellipse on the surface further from the focal point are now easily written in terms of the parameters on the first surface as

$$\begin{aligned} a_2^r &= a_1^r + \frac{L}{2}[\tan(\phi_2)+\tan(\phi_1)] \\ b_2^r &= b_1^r + L\tan\left[\operatorname{asin}\left(\frac{\sin(\phi/2)}{n}\right)\right] \\ x_2^r &= x_1^r + \frac{L}{2}[\tan(\phi_1)+\tan(\phi_2)] \end{aligned} \quad . \tag{4-6}$$

4.3.1.2 Signal beam geometry

In the system under consideration a signal is modulated onto a laser beam with a spatial light modulator (SLM) and focused with a lens. The recording material is placed just after the Fourier plane of the incident signal. Referring to Figure 4-15, under the paraxial

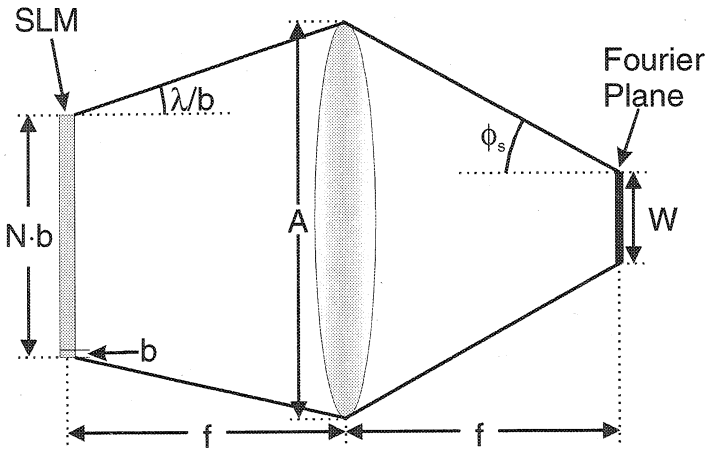

Fig. 4-15. Diffraction from a spatial light modulator forming the Fourier plane of the signal beam.

approximation the properties of a focusing signal beam can be computed based on the pixel size, b, the number of pixels across the SLM, N, the diameter of the lens, A, and the focal length of the lens, f. However, not all of these parameters are independent. From the figure it is easy to see that there is a relationship between the lens focal length and aperture size relative to the number of pixels used and the size of each pixel. The incident beam is diffracted at an angle given by λ/b, allowing N to be computed, given a fixed A and f, as

$$N = \frac{A}{b} - \frac{2\lambda f}{b^2}. \tag{4-7}$$

If more pixels than this are used, then the light diffracted from those pixels at the edge of the SLM will not be sufficiently collected by the lens, and ultimately distortion will occur in the imaging system. N·b is therefore the effective diameter of a circle of pixels which

will be adequately imaged by the optical system. The total number of square pixels with edge of length b fitting in this circle is given by

$$N_p = \frac{\pi\left(\frac{N \cdot b}{2}\right)^2}{b^2} = \frac{\pi}{4}N^2. \tag{4-8}$$

After the lens, the signal forms a converging beam with an angle given by

$$\phi_s = \frac{Nb}{2f}. \tag{4-9}$$

The size of the Fourier plane, considering only the fundamental order, is given by

$$W = \frac{2\lambda f}{b}. \tag{4-10}$$

In order to compute the area of the recording material illuminated by the signal beam, the signal beam tilt angle θ_s must also be accounted for. The derivation of the ellipse parameters for the area illuminated by the signal beam is made much simpler by realizing that the diverging signal beam after the Fourier plane can be treated as an effective point source, as shown in Figure 4-16. The parameters of the equivalent point source can be computed in terms of the other signal beam properties as

$$\begin{aligned} \phi_{se} &= \frac{Nb}{f} \\ x_s &= \frac{\lambda f}{b} \cdot \frac{\sin(\theta_s - \phi_{se}/2)}{\sin(\phi_{se}/2)} \\ z_s &= \frac{\lambda f}{b} \cdot \frac{\cos(\theta_s - \phi_{se}/2)}{\sin(\phi_{se}/2)} \end{aligned} \tag{4-11}$$

Similarly to the case with the reference beam, the parameters of the signal beam ellipse for the first surface are readily calculated as

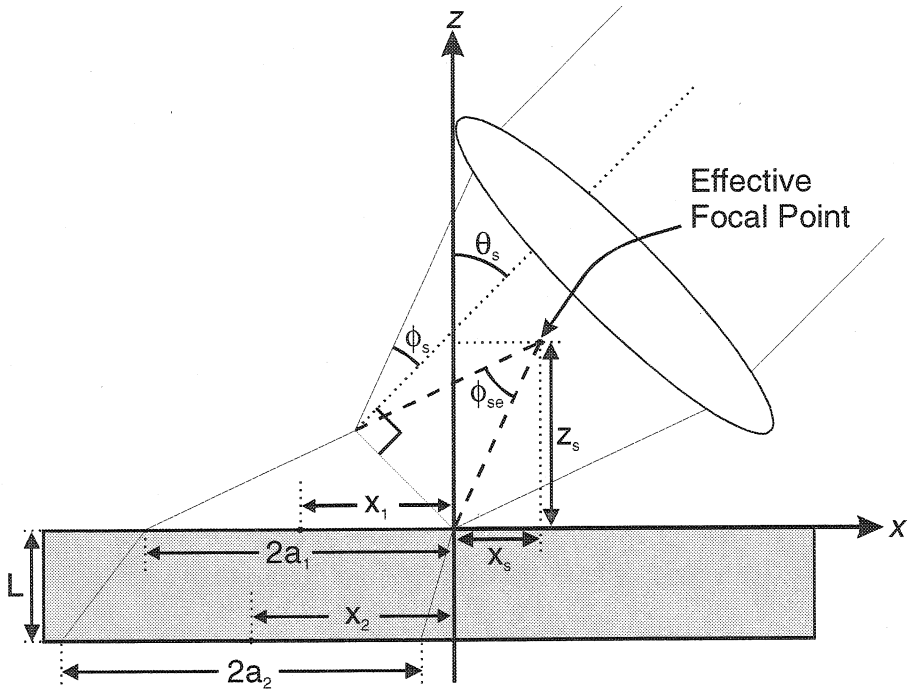

Fig. 4-16. Geometry of the signal beam for computing the area covered on a recording material's surface.

$$a_1^s = \frac{z_s}{2}[\tan(\theta_s + \phi_{se}/2) - \tan(\theta_s - \phi_{se}/2)]$$

$$b_1^s = z_s \frac{\tan(\phi_{se}/2)}{\cos(\theta_s)} \qquad (4\text{-}12)$$

$$x_1^s = x_s - a_1^s - z_s \tan(\theta_s - \phi_{se}/2)$$

The internal angles of the diverging signal beam can be written as:

$$\phi_1^s = \text{asin}\left(\frac{\sin(\theta_s - \phi_{se}/2)}{n}\right)$$

$$\phi_2^s = \text{asin}\left(\frac{\sin(\theta_s + \phi_{se}/2)}{n}\right) \qquad (4\text{-}13)$$

Written in terms of the ellipse parameters for the first surface, the ellipse of the signal beam on the second surface of the material are given by the parameters:

$$a_2^s = a_1^s + \frac{L}{2}[\tan(\phi_2^s) + \tan(\phi_1^s)]$$
$$b_2^s = b_1^s + L\tan\left[\operatorname{asin}\left(\frac{\sin(\phi_{se}/2)}{n}\right)\right]. \quad (4\text{-}14)$$
$$x_2^s = x_1^s + \frac{L}{2}[\tan(\phi_1^s) + \tan(\phi_2^s)]$$

4.3.1.3 Density for read-only and re-writable materials

For write-once materials, the width of each hologram in the in-track direction is given by the size of the reference beam:

$$W_{ip} = 2a_2^r. \quad (4\text{-}15)$$

For re-writable materials, the portion of the reference beam incident on unrecorded material does not need to be considered. Therefore, the shift distance which would be required to record two completely non-overlapping holograms is less than the total length of the beams on the material during recording. This distance may be different depending on the shift direction, but should be taken as the minimum since that will allow higher storage densities. The in-track shift distance can be computed from

$$W_{ip} = \min(\left|x_2^r + a_2^r - (x_2^s - a_2^s)\right|, \left|x_2^r - a_2^r - (x_2^s + a_2^s)\right|). \quad (4\text{-}16)$$

For the beam width in the radial direction, that portion of the reference beam which would not overlap the signal beam can be blocked with an aperture. In this case the effective width is the same as that of the signal beam

$$W_{op} = 2b_2^s. \quad (4\text{-}17)$$

The shift distance between adjacent holograms is determined by taking the maximum of two different constraints: the shift selectivity and the dynamic range limitation.

According to reference [4-5], after taking into account the tilt of the reference beam, the shift required between adjacent holograms in order to satisfy the selectivity constraint is

$$\delta_s = P \cdot \left(\frac{\lambda \cos(\theta_{si}) \left(z_f + \frac{L}{2n} \right)}{L \cos^2(\theta_{ri}) \sin(\theta_{si} + \theta_{ri})} + \frac{\lambda}{2 \sin(\phi_r / 2)} \right), \tag{4-18}$$

where P is a number greater than 1 used to indicate the number of null distances to shift between holograms. Increasing P will reduce noise associated with crosstalk, but will decrease the storage density. It is assumed here that P is chosen such that crosstalk noise can be ignored compared to other noise sources, predominantly scatter noise. θ_{si} and θ_{ri} are the center angles of the signal and reference beam, respectively, after being corrected for refraction. Equation 4-18 must be modified slightly since for the situation being considered the signal beam is not a plane wave but rather has a bandwidth. The shift selectivity will therefore become worse because some components of the signal beam have angles which are less than θ_{si}. If the shift distance is not large enough to satisfy the selectivity constraint for all signal beam angles, crosstalk will result at one edge of the reconstructed signal beam, since angles at the Fourier plane correspond to spatial position in the image plane. In order to avoid using a shift distance which is too small, the minimum internal signal beam angle should be used, yielding for the shift selectivity the formula

$$\delta_s = P \cdot \left\{ \frac{\lambda \cos(\phi_1^s) \left(z_f + \frac{L}{2n} \right)}{L \cos^2(\theta_{ri}) \sin(\phi_1^s + \theta_{ri})} + \frac{\lambda}{2 \sin(\phi_r / 2)} \right\}. \tag{4-19}$$

With a suitable choice for P, Equation 4-19 will ensure crosstalk noise is not a problem. However, the shift selectivity does not take into account the limitation of the material's

dynamic range, measured as the M/#. The relationship between a material's M/# and the diffraction efficiency of M stored holograms is given by [4-10]

$$\eta = \left(\frac{M/\#}{M}\right)^2, \tag{4-20}$$

where the diffraction efficiency is assumed to be equal for each of the stored holograms. In order to have sufficient signal-to-noise ratio of the reconstructed holograms, a minimum diffraction efficiency must be achieved. Therefore, by fixing the diffraction efficiency required, the absolute maximum number of holograms which can overlap can be computed. Given M, the shift distance between holograms required to avoid overlapping too many holograms at the same location is given by:

$$\delta_M = \frac{W_{ip}}{M/2}, \tag{4-21}$$

where W_{ip} is taken from either Equation 4-15 for write-once materials or Equation 4-16 for re-writable materials. The value M/2 is used because it is assumed that half of the holograms will be multiplexed by shifts in the plane of the reference and signal beam, while the other half are to be multiplexed through an out-of-plane, or radial, shift.

Finally, the storage density can be calculated by combining Equations 4-8, 4-17, 4-19, and 4-21. The final computed density is

$$D = \frac{N_p^{\,2}}{\max(\delta_M, \delta_s) \cdot W_{op}/2}. \tag{4-22}$$

Simply put, this is the number of bits per holographic data page divided by the effective area for each hologram. The effective area of each hologram is half the width in the radial direction multiplied by the in-track shift required; the maximum required by

either selectivity or the M/# limit. Half the radial width is used because that is the shift required to cause a reconstructed hologram to rotate completely off of the detector,[4-9] and will allow twice as many holograms to be recorded in the same area, compensating for the M/2 used in Equation 4-20.

4.3.2 Genetic algorithm for finding optimal densities

While Equation 4-22 for computing the surface storage density appears simple, embedded in it are several parameters which may or may not need to be optimized depending on the particular situation to be modeled. Typically these are the reference beam angle (θ_r), the signal beam angle (θ_s), the reference beam divergence (ϕ) and position (x_r, z_r), the pixel size (b), the imaging lens (f, A), and material thickness (L). Other parameters are typically fixed, such as the material's M/# and index of refraction (n). Also, for a given system the amount of noise will dictate the required diffraction efficiency (η) needed in order to obtain an acceptable SNR. While attempting to numerically solve for the parameters that maximize the storage density, it was discovered that there exists local extrema in the function. Typically, when the number of parameters to be optimized exceeded two, using gradient-descent approaches for maximizing the density function resulted in solutions depending on the initial parameter values. In order to circumvent this limitation, a genetic algorithm[4-11] approach was employed for optimizations.

In the genetic algorithm, each gene corresponds to a parameter, for example the signal beam angle, θ_s. A chromosome is composed of all the genes, i.e., one gene for each parameter to be optimized. Therefore, the chromosome length differs depending on the number of parameters to be optimized and results in a vector of length n, $\langle \alpha_1, \alpha_2, \ldots, \alpha_n \rangle$,

with each element representing the value of a specific gene. An initial population of chromosomes is generated by randomly selecting gene values within a range of allowed values. It makes little sense, for example, to allow the algorithm to compute the density of a system with 1 micron pixels and F/0.1 optics, since from a practical viewpoint they are not realizable. Each parameter is therefore constrained by an upper and lower bound. The size of the population was chosen between 200 and 1000 chromosomes, depending on the length of the chromosome. As more parameters need to be optimized, a larger population is needed in order to obtain satisfactory convergence. The fitness of each chromosome was computed by using its parameter (gene) values in the calculations discussed in the previous section. The chromosomes are then mutated to generate a new population the same size as the original, which is then again tested on the fitness function (computation of the storage density). This process is repeated a predetermined number of times in order to obtain the optimal solution.

The mutation at each cycle of the process was carried out by first retaining the chromosomes which had a fitness in the top 10% of the current population. This ensured that if a close to optimal solution was found, it would be retained throughout all the iterations of the algorithm, as well as being able to create additional mutations of the most fit chromosomes in subsequent iterations. The remaining 90% of the new population was filled with new chromosomes generated from mutations of chromosomes from the top 10%. Each new chromosome was generated as shown in the chart of Figure 4-17. Two different chromosomes from the top 10% were selected at random; for each gene a value was randomly selected from either of the two selected chromosomes; this value was modified by a small random perturbation within +/- 10% of the original value; the resulting value is used for the

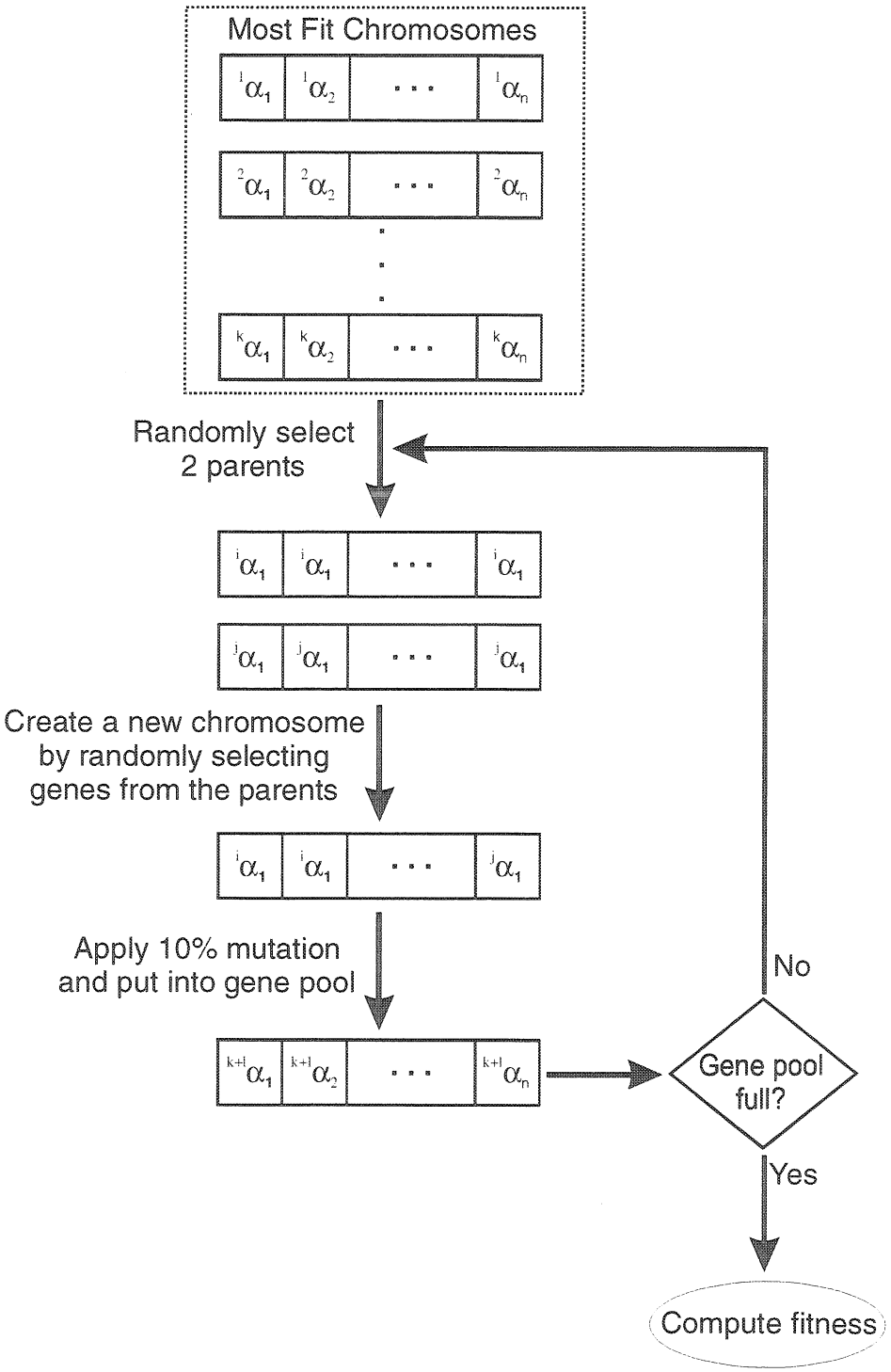

Fig. 4-17. The process used to repopulate the gene pool with new chromosomes derived from those which yielded the highest storage density on the previous iteration.

current gene of the new chromosome. If the new value is outside of the constraints, a new random modifier is selected until the value falls within the allowed range.

When all gene values have been selected, the completed chromosome is added to the gene pool. The fitness is then computed for the new genes, and the whole process is repeated. The number of iterations required depends on the number of parameters to be optimized and the size of the gene pool. This value was experimentally determined for each case by observing the behavior of the optimal values with respect to those found for incrementally varied parameters. For example, if a simulation of the density as a function of material thickness is to be performed, it is expected that the plot of density versus material thickness will be a smooth function. If the results of the simulation results in an extreme number of large jumps in random directions, then it can be concluded that the genetic algorithm was not run for enough iterations to reliably converge to the optimal solution.

4.3.3 Comparison with experimental results

To confirm the accuracy of the density calculations comparisons were made with experiments performed with both the photorefractive crystal $LiNbO_3$:Fe and PQ:PMMA. In the case of $LiNbO_3$, the comparison is with experiments performed in [4-9] for which sufficient information of the system was available to perform a reasonable simulation. In the case of PQ:PMMA, the system used for the experiments described in Section 4.2 was simulated. For both cases, the experimental system was similar to that used in Figure 4-1, utilizing Nikon F/1.4 camera lenses, a 488 nm laser, and the material mounted on translation stages.

4.3.3.1 Storage density with $LiNbO_3$:Fe

In this experiment the optical system was configured to have the signal and reference beam angles each at 35-degrees from the normal to the material's surface. A chrome-on-glass mask was used as the data page with a rectangular array of 45 micron square pixels. The reference beam was created with an F/1.1 lens giving a divergence angle ϕ_r=48 degrees. Finally, each hologram was recorded at the 2nd null, a shift distance of 7.8 microns, to avoid crosstalk. Multiple tracks were recorded with a separation of 0.75 mm. At 590,000 pixels per hologram, and a hologram area of 0.75 mm x 7.8 microns, the storage density was 100 bits/μm^2. The scatter noise at the detector in the system was measured as 3.4×10^{-7}, relative to the incident reference beam power, with an average diffraction efficiency of the recorded holograms of 4.4×10^{-6}.

This system was modeled using the genetic algorithm, optimizing the density over the focal point position of the reference beam since for this experiment the exact position of the reference beam focal point is not known. The recording material's M/# was reported to be 1. A slight variation of the calculations described previously had to be made to allow the reference beam to come to a focus behind the material, which was the case for the actual experiment. The optimal storage density was found to be 71 bits/μm^2 whereas the experimentally achieved density was 100 bits/μm^2. A careful inspection of the calculations being made showed that according to Equations 4-7 and 4-8 only 446,000 pixels are imaged adequately by the F/1.4 lenses. However, these formulas were derived under the typical thin lens assumption, which isn't completely accurate for the 7-element 6-group lenses which were being used. Furthermore, it had been experimentally verified that these lenses are

capable of imaging 590,000 pixels. Adjusting the calculations to take this into consideration increases the calculated density to 94 bits/μm^2.

There are a few discrepancies between the experimental system and the modeled system. The first lies in the size of the signal beam on the material. The experimentally measured signal beam was 1.5 mm in diameter on the entrance surface of the material. However, Equations 4-12 predict the signal beam will occupy 1.76 mm on the entrance surface. The calculated size of the signal beam is 17% larger than what was measured however, in absolute terms amounts to only 0.26 mm, which is within measurement error. Another cause for the error is again the questionable applicability of the thin lens assumption. The second difference between the experiment and the calculation is the fact that in the experiment the reference beam did not overlap the signal beam on both the entrance and exit surfaces, but rather complete coverage was only obtained on the entrance surface. However, even with these differences, the calculated density is 94 bits/μm^2 compared with an experimentally achieved value of 100 bits/μm^2, demonstrating that the calculations are a good predictor of storage densities in re-writable materials.

Figure 4-18 shows a plot of the calculated storage density as a function of material thickness for this system, where the M/# was modeled as increasing linearly with thickness, with a value of one at 1 mm. The storage density increases with thickness, saturating at a value near 410 bits/μm. The density tends to increase with thickness because of an increased M/# and better selectivity. However, counteracting these tendencies is the increased area required for the signal and reference beam due to diffraction. There is one caveat to this simulation, however: the assumption that M/# increases linearly with thickness. For small deviations in thickness from the thickness at which the M/# was measured,

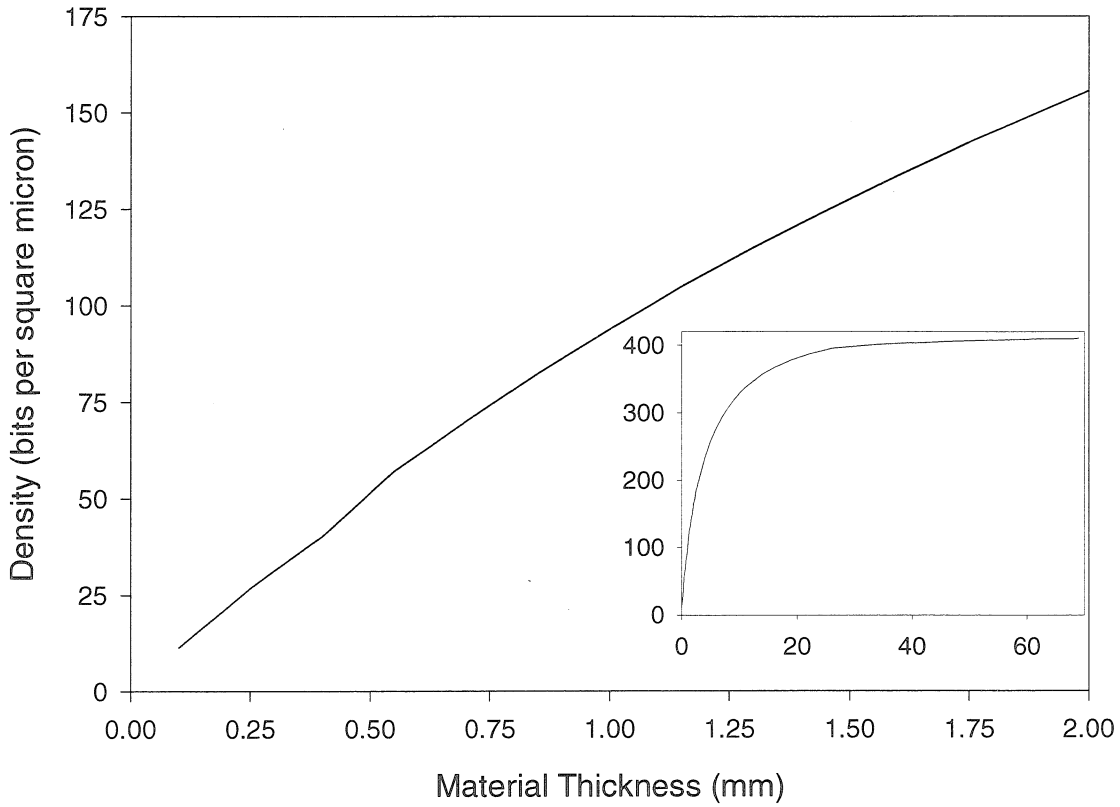

Fig. 4-18. Storage density in LiNbO3 computed as a function of the material thickness with the following parameters: θ_s=35 deg., θ_r=35 deg., ϕ=48 deg., M/#=1/mm, λ=488 nm, f=50 mm, A=35 mm, b=45 μm, P=2, and $\eta=4.4 \times 10^{-6}$. The inset shows the same result over an extended range of material thicknesses, in mm.

this is a valid approximation. However, certainly over the long range plotted in the figure it is not. In order to maintain a linear increase in M/#, the absorption coefficient of the material would have to stay constant, which would effectively decrease the usable thickness of the material due to the lack of beam penetration, and correspondingly decrease the measured M/# and decrease the hologram selectivity. A detailed study of the trade-offs between M/#, absorption, and material thickness in the context of data storage can be found in reference [4-12].

4.3.3.2 Storage density with PQ:PMMA

The simulation of this system was made using actual values for all parameters except for the position of the focal point of the reference beam. Optimization over these two parameters (x_f and z_f) was made because measurement of the exact position relative to the incidence of the signal beam on the material could not be made accurately enough for use in the simulation. For example, using the above quoted focal point distance of 2 cm and optimizing the lateral location of the focal point, x_f, the calculations show that it is not possible for the reference beam to completely overlap the signal beam on both surfaces of the material. The simulation was performed for material thicknesses between 100 microns and 4.8 mm, with the M/# of the material modeled as a linear function of the thickness, with the measured value of 4.8 at 3 mm. The required diffraction efficiency was 4×10^{-4}, which was obtained experimentally. Figure 4-19 contains a plot of the results of the simulation. The density computed for a 3 mm thick material is 7.8 bits/μm^2, with a focal point position of z_f=2.5 cm and x_f=-1.9 mm.

The calculated density is close to the experimentally achieved value, and the optimal focal point position is close to what was measured experimentally. Some factors that cause differences include the exact reference beam positioning as well as the positioning of the signal relative to the material, which both act to decrease the actual storage density achieved. One shortcoming of the simulation causes the predicted values to be somewhat lower than what should be achievable if the exact optical system required could be realized. The shortcoming is the assumption that, for the write-once materials only, the area of the hologram is taken to be the entire area of the reference beam. However, for the location where only the reference beam is incident, and the signal is not, the illumination intensity

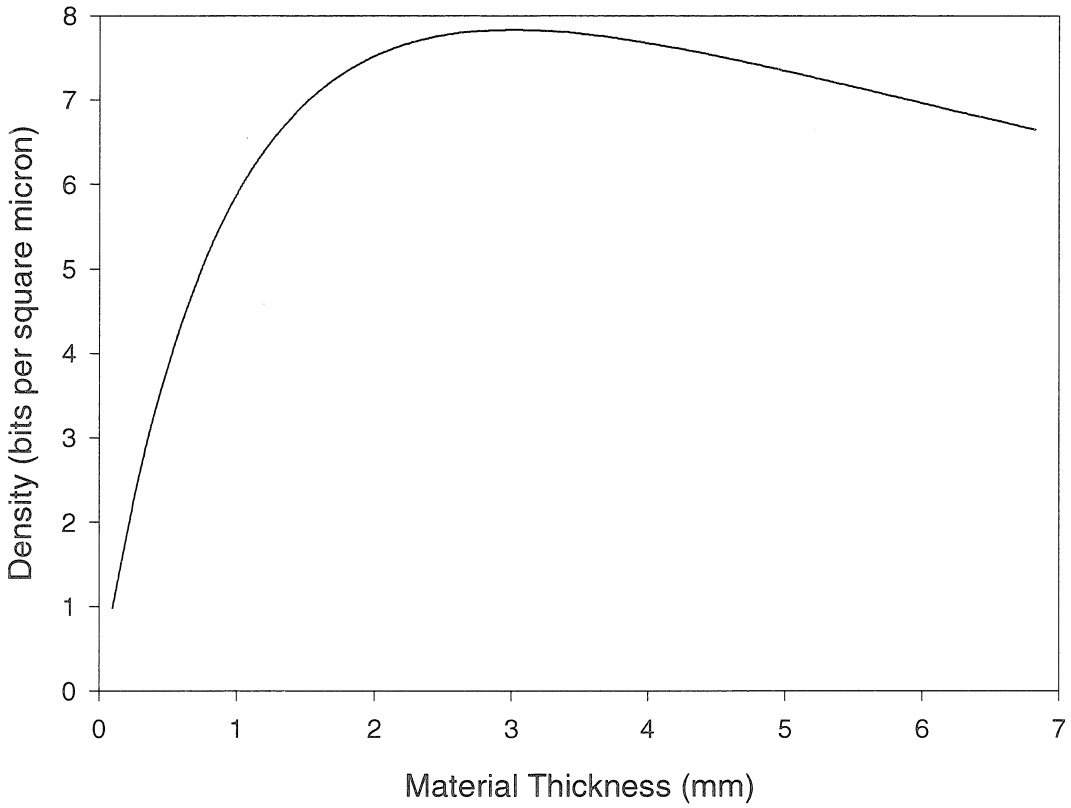

Fig. 4-19. Simulation of the storage density of phenanthrenequinone-doped PMMA as a function of thickness.

is half of that where both beams overlap. Therefore, the dynamic range of the material is not consumed as quickly as in the areas where both beams overlap, and more holograms should be able to be overlapped than is computed, which would increase the computed storage density slightly. However, in practice, the M/# realized with images is slightly less than what is measured with plane waves, explaining the lower density obtained experimentally. Furthermore, as was pointed out in Section 4.2.2, the storage density could have been increased slightly by utilizing a more efficient exposure schedule. With these differences taken under consideration, the simulation is seen to also give reasonably accurate numbers

for write-once materials. As a result, the simulation can be used to predict the storage density of holographic systems under various conditions.

4.3.4 Effects of M/#, wavelength, and thickness on storage density

As a final exercise, the storage density model has been applied to calculating the density obtainable with a fixed optical system as a function of the storage material's M/#. One application for holographic data storage is the read-only disk, where it would be desirable to have a 12 cm diameter disk used for storing approximately 100 gigabytes of information, or a density of about 85 bits/μm^2. One fundamental obstacle to the realization of such a system is the availability of an adequate holographic recording material. Therefore, it is helpful to know how high of an M/# is required of a recording material before a high-density holographic disk can be successfully implemented. In order to model such a system, the material's index of refraction was fixed at 1.5, a typical value for polymer materials. The system was simulated assuming lenses of focal length 13 mm and diameter 11.8 mm. The density was then maximized by the parameters of pixel size, b, focal point position, x_r and z_r, signal beam angle, θ_s, reference beam angle, θ_r, and divergence angle, ϕ_r. For practical reasons, the pixel size was limited to a minimum of 1 micron and the reference beam divergence angle was limited to a maximum of 90 degrees. Furthermore, the required diffraction efficiency of the holograms was 4×10^{-4}, separated by 2 null spacings.

Figure 4-20 shows the results of six simulation runs with various material thicknesses and two different wavelengths. It is interesting to note that for a given M/# and wavelength, a thinner material will yield a higher storage density until the M/# gets large enough that selectivity becomes the primary constraint. A comparison between the density

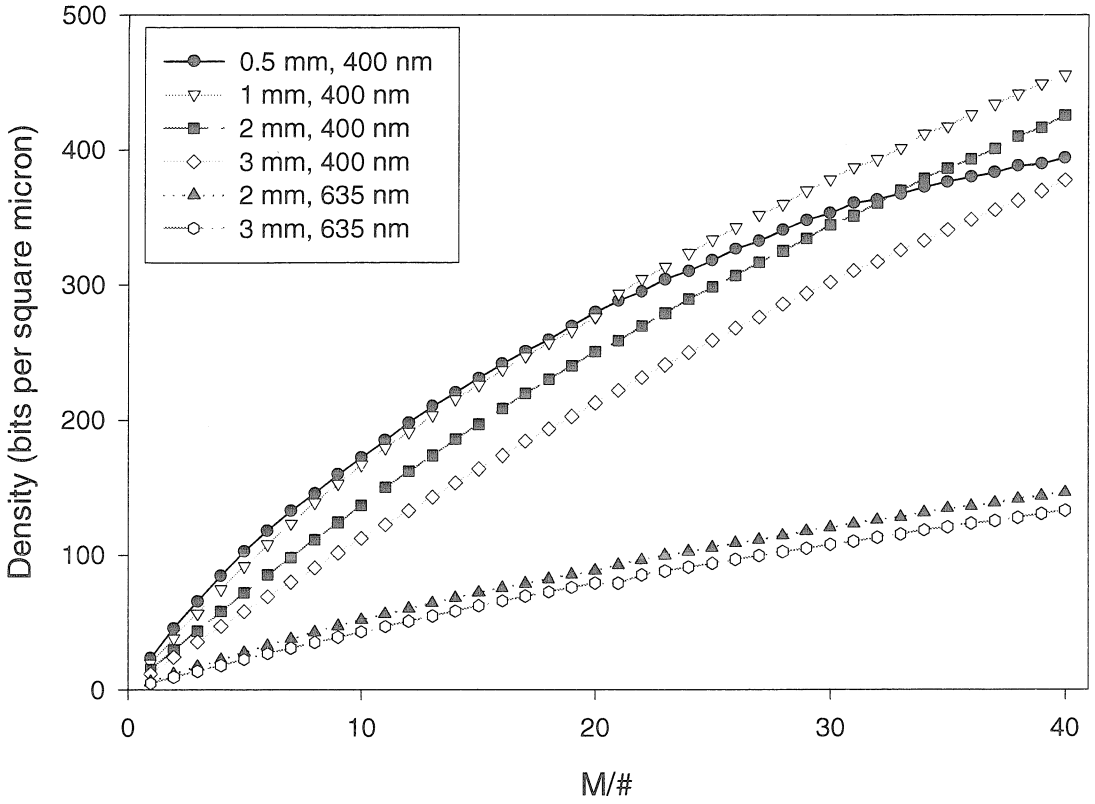

Fig. 4-20. Theoretical storage density for various wavelengths and material thicknesses as a function of M/#.

curves for a system using 400 nm light shows that a 0.5 mm thick material will yield the highest density until the M/# reaches about 20, at which point a 1 mm thick material, with its better selectivity, will allow higher storage densities. An important result is the revelation that a large thickness is not an absolute requirement for achieving very high densities, since a 0.5 mm thick material should be able to achieve storage densities well in excess of 100 bits/μm^2. For many materials, M/# is roughly linear with thickness within a small range, and if a comparison is made between the storage density of a thicker material with a thinner material with a correspondingly reduced M/#, the thicker material will have a higher potential storage density. For example, if a recording material were 3 mm thick with

M/20, then the system using 400 nm light could be expected to achieve a storage density of roughly 200 bits/μm^2. However, if the same material is used to make a 2 mm thick recording media, then it will have approximately M/13 and the corresponding density would be about 175 bits/μm^2. The other important result of these simulations is the dramatic density improvement that results from using shorter wavelengths. Once the M/# exceeds a value of 10, there is at least a factor of two increase in density even when comparing a 2 mm to a 3 mm thick material. The performance gained for thinner materials is even greater. At the extreme end of the plot with M/40, the increase in density with wavelength scales with the rough $1/\lambda^3$ approximation commonly used.

4.4 Conclusion

Initially, due to the thickness with which the PQ:PMMA material could be made, it was thought that very high data storage densities could be achieved with this material. However, after performing actual data storage experiments, it was seen to be a difficult task. An analysis of the situation revealed that between noise, M/#, and diffraction efficiency, many holograms could not be overlapped. One proposed solution to the problem was to decrease the scatter noise generated by the material. After performing measurements of the scatter from various materials, it was determined that PQ:PMMA had very good performance in this respect, and it was unlikely that the scatter noise could be reduced to such extremes as to allow the desired increase in storage density.

An alternative approach is to modify the optical system to improve the efficiency with which the material is used in terms of the trade-off between selectivity and area per hologram. Since it is impractical to carry out experiments with multiple sets of optical

equipment and recording geometries to find an optimal solution, a method for computing the storage density was developed. This model addresses the issues of geometry as well as the recording material's M/#. Furthermore, crosstalk noise can be accounted for in the calculations by requiring that shifts between holograms be a predetermined number of null spacings of the hologram selectivity function. The result is a powerful simulation capable of optimizing the optical recording system given constraints on the material and optical components. The analysis presented here can be of assistance in the design and optimization of future holographic memory systems whose performance is limited by the capabilities of the recording material. Furthermore, the simulations can provide an indication of the requirements for a recording material in order to achieve a desired storage density. With respect to the PQ:PMMA material, Figure 4-20 indicates that even with an optimized system it is unlikely a density above 50 bits/μm^2 can be achieved in a 3-mm-thick sample with a 400 nm wavelength laser. In order to build a system capable of posing a serious challenge to conventional optical storage systems, a higher performance material is needed.

References

[4-1] H. Kogelnik, "Coupled wave theory for thick hologram gratings," Bell Sys. Tech. J. 48, 2909-2945 (1969).

[4-2] X. Yi, S. Campbell, P. Yeh, and C. Gu, "Statistical analysis of cross-talk noise and storage capacity in volume holographic memory: image plane holograms," Opt. Lett. **20**, 779-781 (1995).

[4-3] P. J. van Heerden, "Theory of optical information storage in solids," Appl. Opt. **2**, 393 (1963).

[4-4] Collier, Burckhardt, and Lin, *Optical Holography*, 454-493 (Academic Press, New York, 1971).

[4-5] G. Barbastathis, M. Levene, and D. Psaltis, "Shift multiplexing with spherical reference waves," Appl. Opt. **35**, 2403-2417 (1996).

[4-6] K. Curtis, A. Pu, and D. Psaltis, "Method for holographic storage using peristrophic multiplexing," Opt. Lett. **19**, 993-994 (1994).

[4-7] H.-Y. S. Li and D. Psaltis, "Three-dimensional holographic disks," Appl. Opt. **33**, 3764-3774 (1994).

[4-8] J. R. Wullert II and Y. Lu, "Limits of the capacity and density of holographic storage," Appl. Opt. **33**, 2192-2196, (1994).

[4-9] A. Pu, *Holographic 3D-disks and optical correlators using photopolymer materials*, Ph.D. thesis, California Institute of Technology, 1997.

[4-10] F. H. Mok, G. W. Burr, and D. Psaltis, "System metric for holographic memory systems," Opt. Lett. **21**, 896-898 (1996).

[4-11] Coley, *An Introduction to Genetic Algorithms for Scientists and Engineers* (World Scientific, London, 1999).

[4-12] G. Burr, *Volume holographic storage using the 90-degree geometry*, Ph.D. thesis, California Institute of Technology, 1997.

5 Optical Holographic Correlators

5.1 Introduction

This chapter describes experiments performed with optical holographic correlator systems.[5-1] First, a system that was designed and built for the automated real-time tracking of targets is described. The experimental characterization of this system when used with simple and complex targets is presented. The second part of the chapter deals with a technique which can be used to control the shift-invariance of optical correlators. The theory behind its operation is developed, and experiments confirming the expected behavior are described.

5.2 Target tracking system

Target recognition is an application particularly well suited for an optical processing system because of the inherent ease with which 2-D linear transformations can be performed. The correlator compares the input image with a database of stored template images. In the case of the angle-multiplexed hologram based correlator system, the stored template images are correlated with the input in parallel, providing for a powerful recognition engine. An added benefit of the holographic based system is the effective storage capacity of the hologram. There is no need for an external memory system to provide for the long-term storage of template images. Consequently, there is no need to be concerned about the data transfer rate between a long-term memory system and optical components, such as is the case with the joint transform correlator.[5-2]

The system used is actually an optical-electronic hybrid. The optical correlator provides correlations of the input, displayed on a liquid crystal spatial light modulator, with all of the holographically stored template holograms. Then a CCD camera and framegrabber digitize the correlation output plane. A digital computer then makes the final object classification and position determination. Since the optical system performs a vast majority of the required computation in a time limited by the frame rates of the SLM and camera, it is trivial to obtain real-time performance with modest electronic computing equipment.

Section 5.2.1 describes the experimental apparatus used for the real-time recognition and tracking system, including the electronic hardware and processing. In Section 5.2.2, the performance of the system with simple 2-d and 3-d geometrical objects is presented. The purpose of these tests was to get a better understanding of the rotational invariance of the correlation algorithm in an actual optical setup. Section 5.2.3 details the performance of the system in both recognizing and tracking models of vehicles under a variety of conditions of obscurity, resolution, and contrast. A real-time recognition and tracking system capable of tracking multiple targets simultaneously is described in Section 5.2.4.

5.2.1 Experimental apparatus

The elements involved in the real-time recognition and tracking system can be divided into two groups: (i) the optical system and opto-electronic components and (ii) the digital electronic hardware and software. Section 5.2.1.1 describes the optical system and the interfacing with the electronic components. Section 5.2.1.2 describes the software and algorithms used to generate recognition results and tracking information.

5.2.1.1 Optical system

The optical setup is shown in Figure 5-1. It is a Vander Lugt[5-1] correlator with

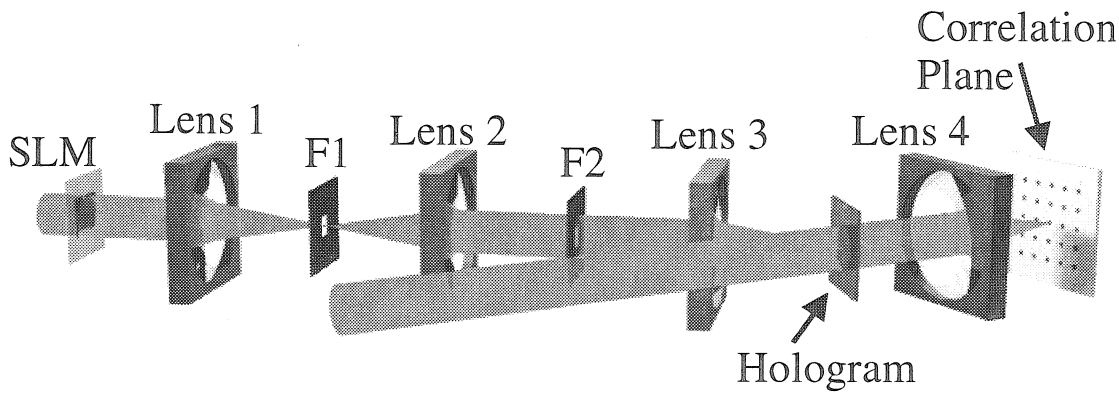

Fig. 5-1. Optical correlator system.

two layers of optical image processing for edge enhancement and removal. The input device is a liquid crystal display with a resolution of 640 pixels horizontally by 480 vertically, a 24 μm pixel pitch, and an active area of 15.36×11.52 mm. It is driven by the VGA output of a PC and is capable of displaying 256 gray levels. The SLM is illuminated with 532 nm collimated light from a solid-state laser.

Lenses 1 and 2 combined with spatial filters F1 and F2 perform elementary filtering tasks. Lens 1 takes the Fourier transform of the input image presented on the SLM. The filter F1 consists of a DC blocking element contained within a square aperture. The DC block removes low frequency image components acting to edge enhance the input image. This edge enhancement dramatically improves the system's ability to discriminate between objects to be recognized. The square aperture blocks the higher diffracted orders of the SLM, results of a non-unity pixel fill factor. After passing through Lens 2, a filtered version of the input image appears at the plane of the filter F2. This filter removes the outline of the

edge of the SLM produced by the edge-enhancement operation. Without this step, all scenes would automatically have a biased correlation strength corresponding to the static SLM edges. Removing them improves the signal-to-noise ratio of the correlation signal.

Lens 3 takes the Fourier transform of the filtered image, appearing at the plane of the holographic recording material. Angle multiplexing is used to store multiple holograms at one location of the recording material (DuPont HRF-150 photopolymer[5-3], with a thickness of 38 μm). Lens 4 performs the Fourier transform of the hologram reconstruction. The output plane thus contains an array of correlations between the input signal and the templates stored as Fourier transform holograms. The spatial position of each correlation at the output plane relates to the reference beam angle that was used to record the corresponding template. This output plane is recorded by a CCD camera.

5.2.1.2 Digital processing system

Once the correlation output plane has been recorded by the CCD camera, it is digitized by a framegrabber board in a computer. From the information contained in this digitized correlation plane, computer software extracts tracking information and determines the identity of the input target object.

The first step for the digital system is to obtain a mechanism for counteracting optical pattern noise in the correlation plane. To achieve this goal, a completely white (in intensity) image is displayed on the SLM and an image of the correlation plane is stored. This "noise frame" is subtracted from all subsequently digitized correlation plane images.

The next step is to obtain normalization values for all template images stored in the holographic database. Referring to Figure 5-2 as an example case, consider k simple shapes

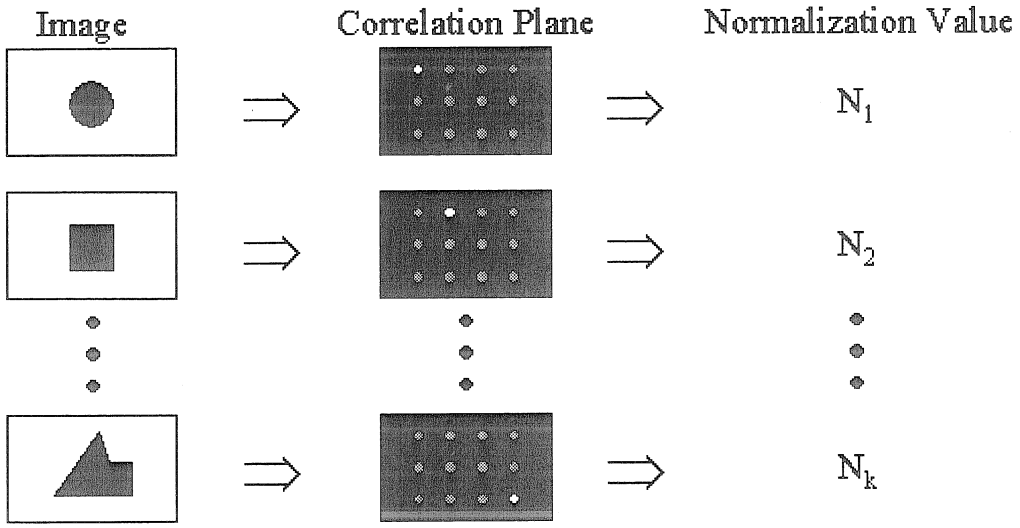

Fig. 5-2. Determining normalization values.

stored as template images. Each template is displayed on the SLM in sequence, which causes its corresponding area of the correlation plane to have a bright spot, while the other areas are dimmer blurred areas of light. The value of the correlation peak corresponding to the displayed template image is recorded and saved as a normalization value.

During system operation, whenever a frame is digitized, the areas corresponding to each template correlation are analyzed in sequence, as shown in Figure 5-3. The first task is to find the center of the correlation peak for each region, and the second is to find its position relative to the center of the correlation region. Due to the shift-invariant nature of the correlation operation, the relative peak position is an indication of the input object displacement in the frame relative to the location of the template object in its frame. Each peak value, P_i, is divided by its normalization factor, N_i, to form a set S of normalized peak values,

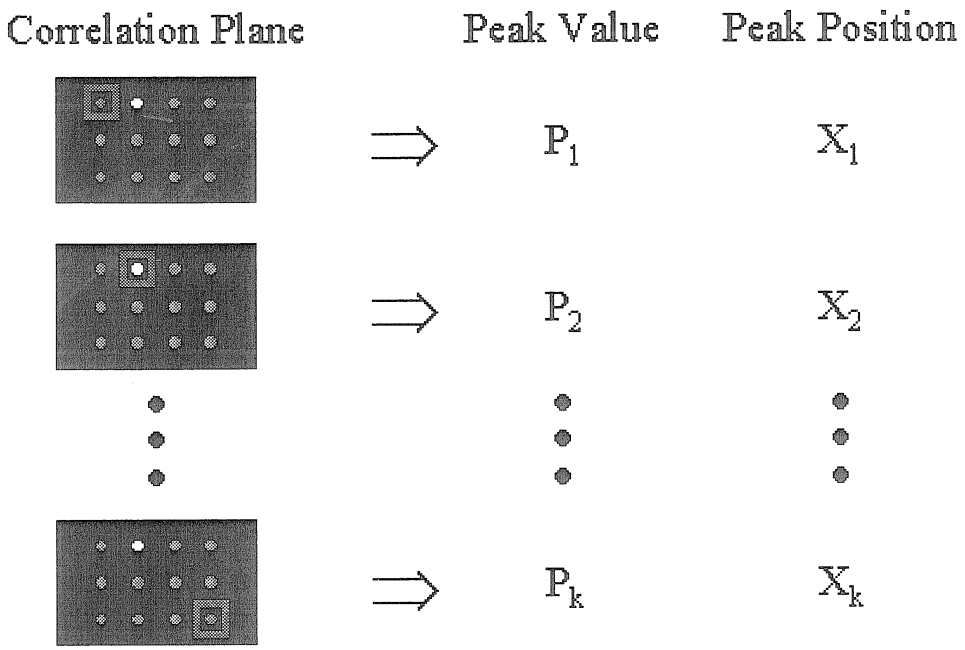

Fig. 5-3. Analyzing the correlation plane.

$$S = \left\{ \frac{P_1}{N_1}, \frac{P_2}{N_2}, \ldots, \frac{P_k}{N_k} \right\}. \tag{5-1}$$

If object recognition is to be performed, each element of the set S is compared with a corresponding threshold, T_i. If an element is above threshold, then it is assumed that the object corresponding to what was in the template image is present in the input scene. The value, x, of its peak position is an indication of its relative position in the input scene.

5.2.2 Geometric object recognition

To better understand the discrimination capabilities of the optical correlator system, tests were run with a variety of two-dimensional and three-dimensional geometrical objects. The tolerance of the system to the rotation of objects and to the degradation of the input resolution was investigated.

5.2.2.1 Two-Dimensional objects

The 16 two-dimensional objects shown in Figure 5-4 were recorded as templates in

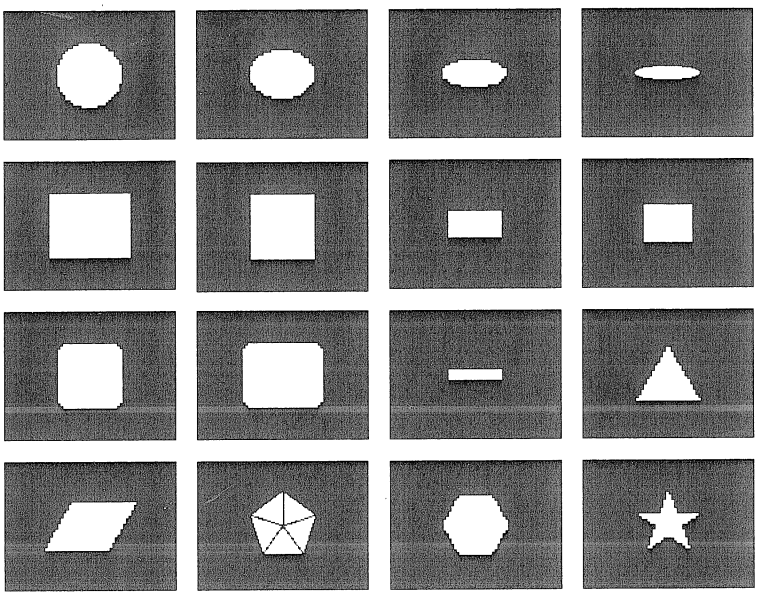

Fig. 5-4. Objects stored as templates.

the optical correlator system. The correlation between each image and each template stored in the database was measured and normalized as described previously. Figure 5-5 graphically portrays the result of these measurements as a grid of cross-correlation strength indicators.

Each square in the grid has a side length proportional to the value of the normalized correlation strength. Hence, the maximum side length has a value of 1. The horizontal and vertical spacing between grid locations is one unit. From this figure, it is seen that the auto-correlations yield the largest values. It is also easy to see which objects have a strong cross-correlation, such as those between squares and squares with rounded edges. The asymmetry of the correlation values is a result of the normalization process, which is based on auto-correlation values only.

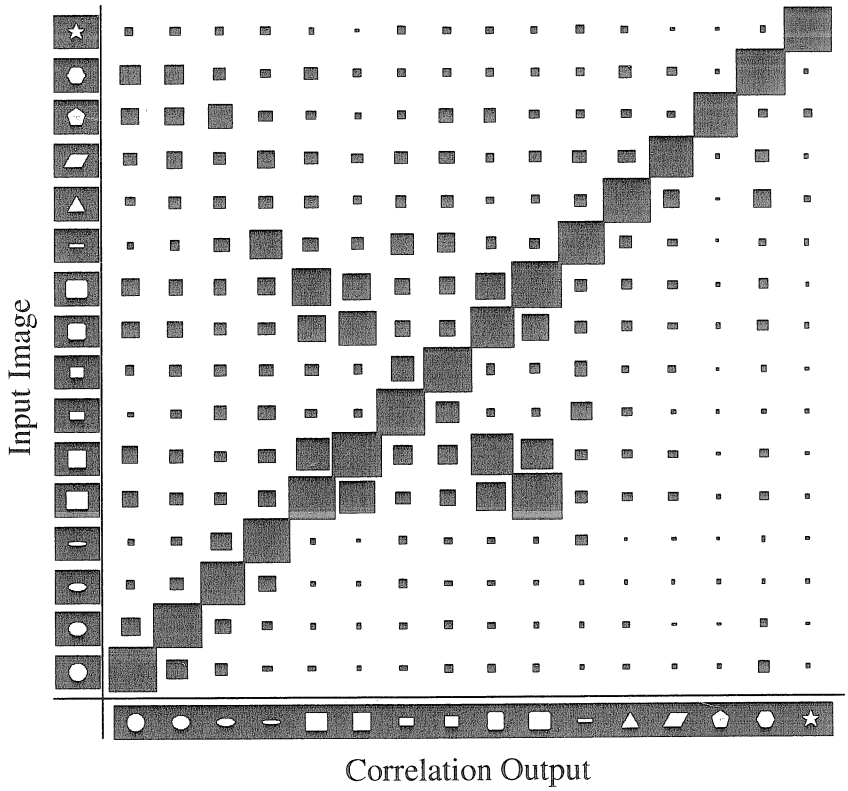

Fig. 5-5. 2-D object cross-correlation matrix.

Several objects were rotated through 180 degrees about their centers with correlation strengths measured after each degree of rotation. Figure 5-6 shows how the measured correlation varies with rotation for four different objects. Each plot is the normalized autocorrelation strength as a function of rotation of the input template object. The plots for the rotation of the square and hexagon show significant peaking at the points of rotational symmetry for each of these objects. The three non-primary peaks for the triangle correspond to when one of the triangle edges is horizontal, thus correlating with the horizontal edge of the stored template triangle.

These curves can be used to determine the rotational separation needed between images of template holograms if an object is to be recognized regardless of orientation.

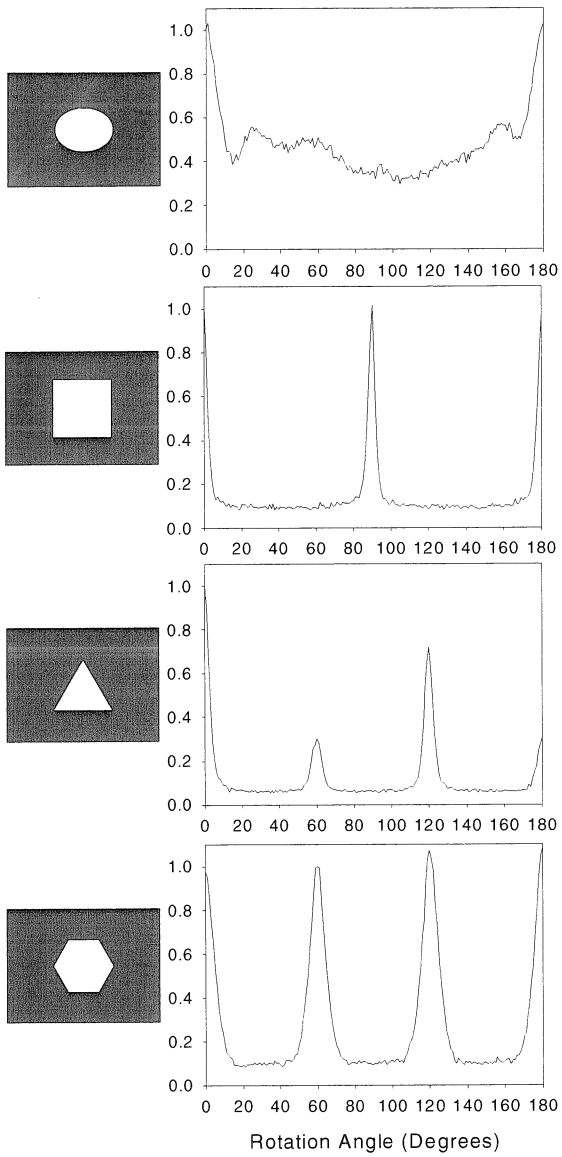

Fig. 5-6. Auto-correlation of rotated template objects.

Such a recognition scheme would also provide orientation information. For example, if it were desirable to recognize a square regardless of orientation, then a template hologram of a square rotated every 5 degrees between 0 and 90 degrees could provide not only detection, but determination of the squares orientation within 5 degrees of accuracy.

5.2.2.2 Three-Dimensional objects

The nine three-dimensional geometrical objects shown in Figure 5-7 were stored as

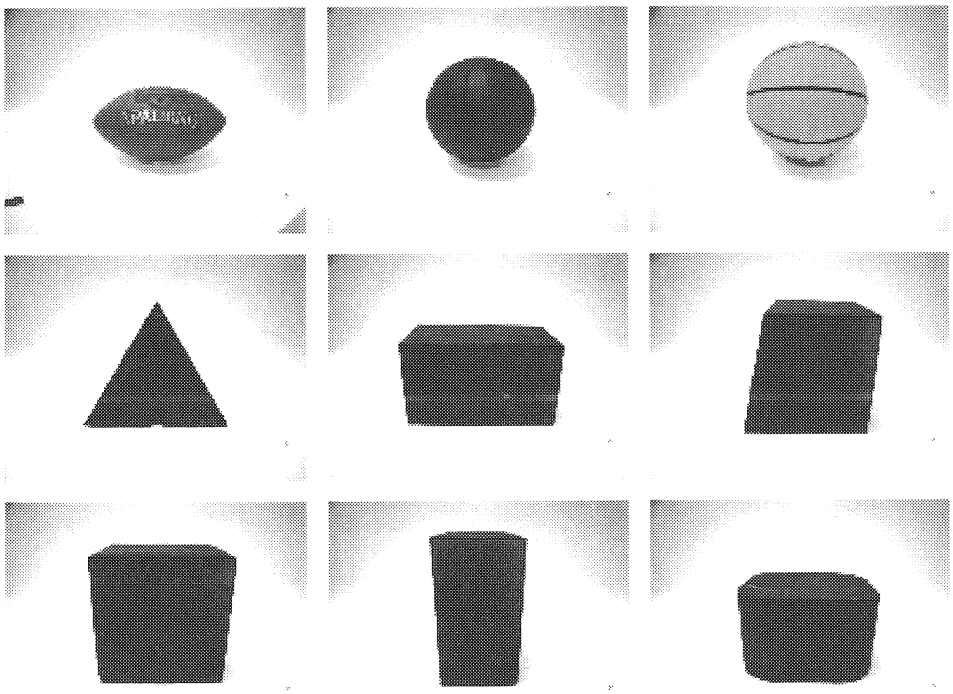

Fig. 5-7. 3-D objects stored as templates.

templates in the optical correlator system. The correlation between each image and each template stored in the database was measured and normalized as described previously. Figure 5-8 graphically portrays the result of these measurements as a grid of cross-correlation strength indicators as was done in the previous section for the 2-d objects. Unlike the case with the 2-d shapes, here there is little room for confusion between objects. The largest cross-correlation is between the basketball and the black volleyball; however, the values are far below the auto-correlation for each of these objects, allowing for easy discrimination between them.

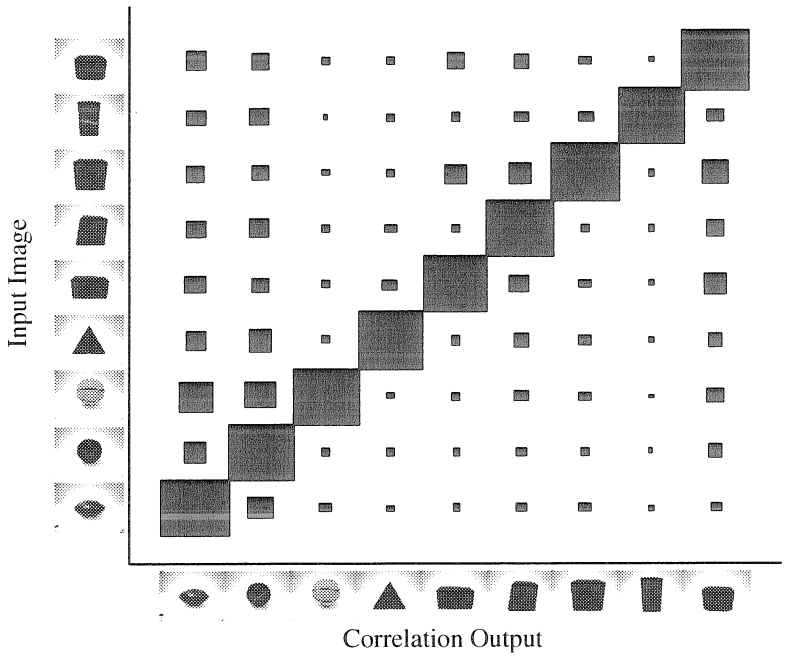

Fig. 5-8. 3-D object cross-correlation matrix.

Four of the objects were rotated about an axis vertical to the horizontal and passing roughly through the object centers. Figure 5-9 shows the correlation between each object with its rotated version, in one-degree increments. The amount of symmetry of an object can again be seen by the cyclical nature of the curves. The rotation of the cube object produces distinct peaks at 0, 90, and 180 degrees of rotation, as expected.

5.2.3 Target recognition

The six models of vehicles pictured in Figure 5-10 were stored in the optical correlator system. The cross-correlation matrix of these six models is shown in Figure 5-11.The cross-correlation matrix is asymmetrical. The cross-correlation values are in general greatest for the output of a relatively small object when the input is relatively larger. Hence, the third and fourth columns of the matrix tend to have cross-term entries much larger than those for the other models. This asymmetry is entirely a result of the normalization proce-

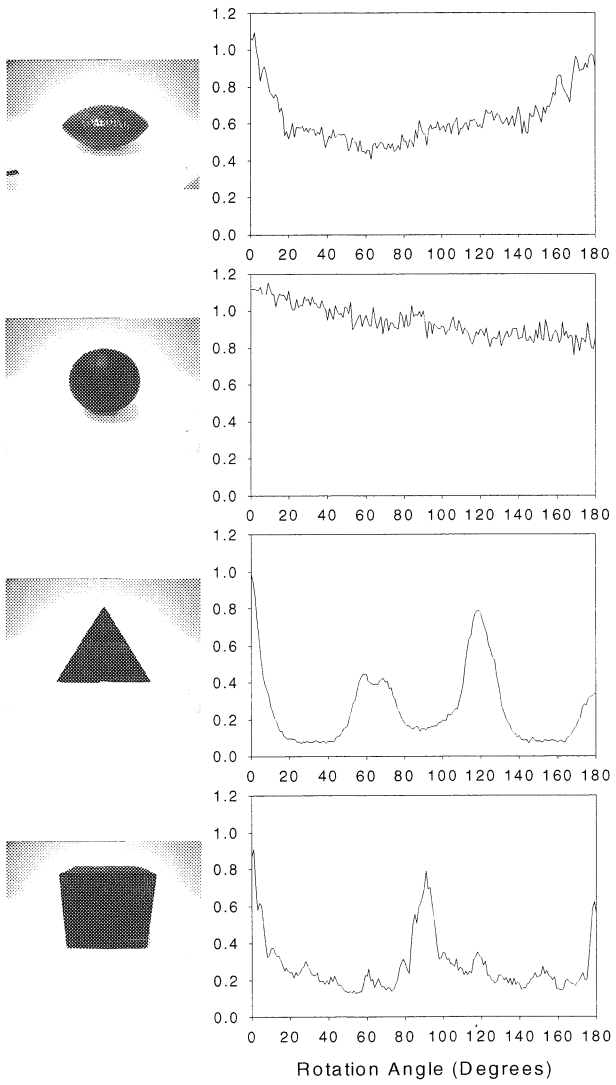

Fig. 5-9. Auto-correlation of rotated template objects.

dure. Larger objects have larger features, which results in a bright correlation peak, yielding a large normalization value. The auto-correlation of smaller objects results in smaller normalization values. The correlation between two objects should be symmetrical, but when a larger object is the output, the result is divided by a larger normalization value. When a small object is the output, the result is divided by a relatively small normalization value. An asymmetrical normalized cross-correlation matrix results from this process.

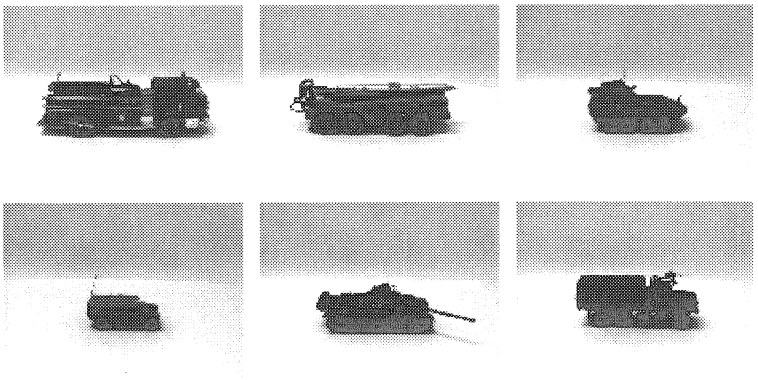

Fig. 5-10. Models used in the target recognition system.

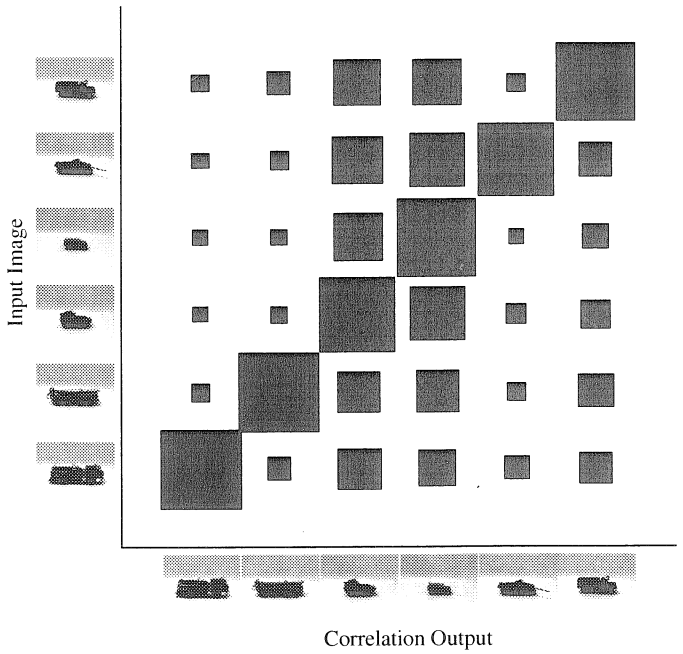

Fig. 5-11. Cross-correlation matrix for the 6 models.

5.2.3.1 Rotation

The correlations between each model and rotated versions of the models as a function of rotation angle have been measured, and are plotted in Figure 5-12. For realistic targets, this measurement is of prime importance because it gives an indication of how many templates of each target are required for rotation invariant detection of the target. After

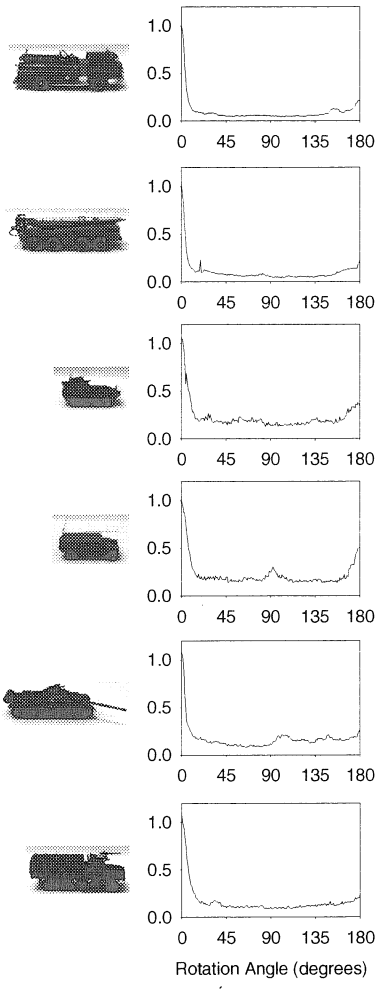

Fig. 5-12. Correlation with rotated models.

about three or four degrees the correlation for most models dropped by about 10%. This indicates that approximately 120 templates per vehicle would be required for rotation invariant detection around all 360 degrees. In many cases the rotational sensitivity is not uniform for all views of the target object. In such cases more or less templates would be required.

5.2.3.2 Reduced resolution

The performance of the recognition system in relation to the resolution of the images is of practical importance. If sufficient performance were obtained with a low resolution image, then it would make little sense to incur the additional cost of high resolution image sensors. To test the performance degradation with reduced resolution, the original 640×480 images were digitally reduced in resolution, and correlated with the original templates recorded from the 640×480 images. Figure 5-13 shows the reduction in correlation

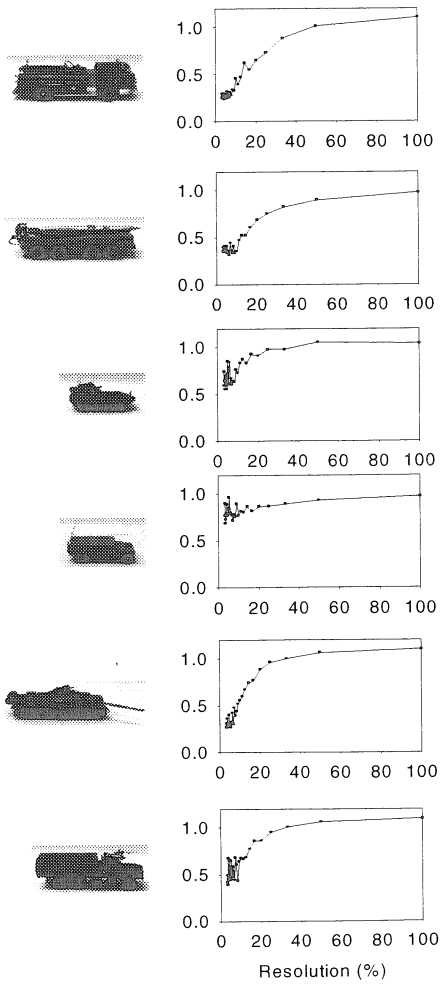

Fig. 5-13. Correlation with reduced resolution.

strength as each image's resolution is reduced. There is little drop in performance until the

resolution is reduced to about 30-40% of its original, corresponding to a resolution of approximately 213 × 160 pixels. In a typical usage scenario, templates would be recorded with a high-resolution camera beforehand and multiple holograms made. These template database holograms would then be placed into multiple field units with less expensive low-resolution image sensors, which could perform their recognition task with little performance degradation.

5.2.3.3 Magnification

Object magnification is a transformation for which the correlation operation is not invariant. If templates are stored with several different scales for each object, then recognition can be performed for the object throughout a range of magnification. Once a target is found, the differential between the correlations with two templates of slightly differing scale can be used to control a zoom lens of the camera, which acts to always keep the target at a constant size.

For this technique to work, the templates must be such that for the magnifications of interest there is a noticeable difference in correlation strength. However, the strength should not be allowed to drop too far or else the system may be tricked into thinking the target has changed to a different object. Figure 5-14 shows the dependence on magnification for the six models used. For most models, the correlation strength dropped by 25% with between two to four percent magnification changes. If two templates of an object were recorded with four percent of difference in scale, a system could be built to control a zoom lens to keep the magnification of the object relatively constant.

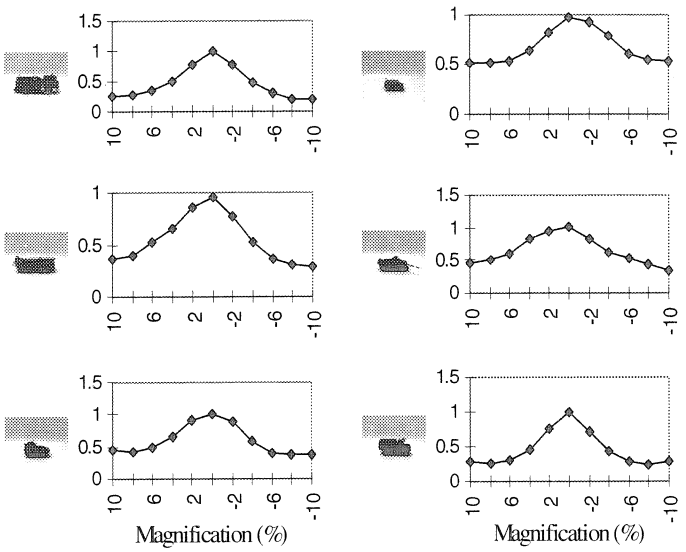

Fig. 5-14. Correlation with magnification.

5.2.3.4 Reduced contrast

The issue of contrast between an object and its background is an important one for recognition either in poor lighting conditions or when the target takes on a color similar to the terrain in which it is located. To simulate these conditions, the backgrounds of each model were darkened, using digital image editing software, between gray levels of 0% to 100%, where 0% is white and 100% is black. The results of the auto-correlations are shown in Figure 5-15.

For most objects, with a 20% gray background the correlation dropped by about 25%. When the gray level was increased to 40%, most correlation strengths dropped by almost 50% of their original values. This indicates that the outline edges of the models provided a large amount of the correlation. Little can be done to compensate for the reduced contrast since the correlator uses the edges of objects to perform recognition.

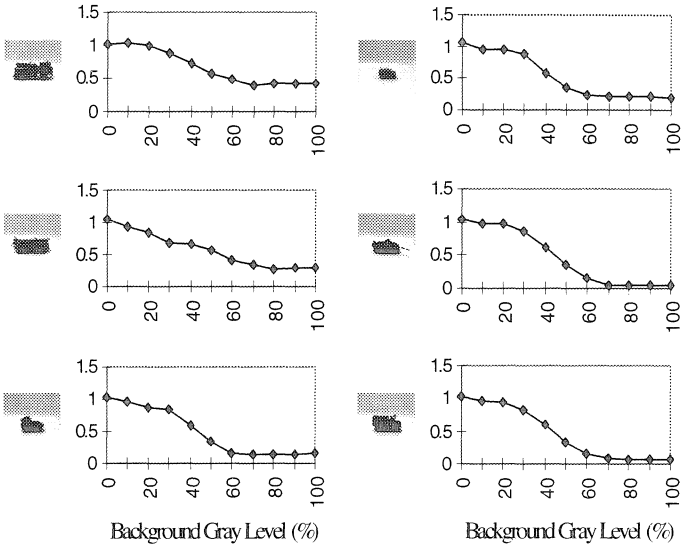

Fig. 5-15. Correlation with reduced contrast.

5.2.3.5 Obscured recognition

Another obstacle to target recognition is obscuring of the target itself. With increasing amounts of obscuring it becomes increasingly difficult to find and track a target. A robust system would be able to tolerate some obscuring before failing to recognize a target.

Each of the 6 models were partially obscured from both the left and right sides, ranging from 10 to 90 percent. This was performed by digitally altering pictures of the models by placing a black region over increasing areas of the model, and then using these images as the input to the optical correlator. Figure 5-16 shows how the correlation strength of the models drops with increasing amounts of obscuring from the left and right sides. For the most part there is a linear drop in correlation with obscuring, which is not surprising since the correlation algorithm considers features from the entire target template. In some cases the drop in correlation strength is faster than linear, indicating important features of

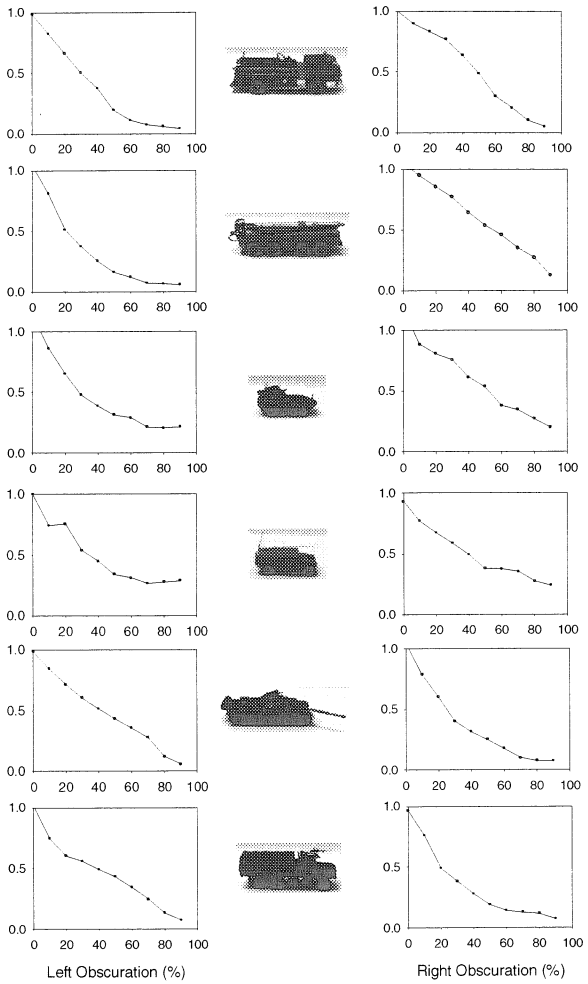

Fig. 5-16. Correlation with partial obscuring.

the object. Such cases occur for the turret of the tank and the left side of the SCUD launcher where object features create distinct edges with the background.

5.2.4 Tracking

The shift-invariant nature of the correlation algorithm allows the optical correlator to be used to track the objects stored in its holographic database. Because of the parallel nature of the system, all the targets can be recognized and tracked simultaneously and without interference. Four of the models were selected for testing of a real-time target recogni-

tion and tracking system. Computer software was written to present a real-time display showing the recognition status and relative position of the possible targets. Figure 5-17

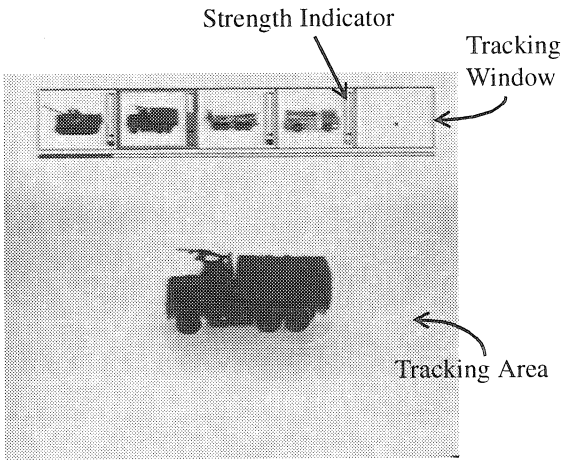

Fig. 5-17. Real-time tracking system.

shows a screen-shot of the software running on a 120MHz Pentium computer. The correlation strength of each object stored in the holographic database is tracked and compared with a pre-defined threshold set a small amount above the cross-correlation strength between the object and the others in the database. When the correlation strength for an object is above its threshold, its location is determined by measuring the distance of the correlation peak from the center of its domain, and an icon representing the object and its location is placed in the tracking window.

The digital computation requirements are the same regardless of what is present in the input scene, namely searching for and measuring the correlation peaks from each object in the template database. As a result, with modest computer resources the system can track in real-time regardless of how many objects are in the input scene and whether or not those objects are targets. Figure 5-18 shows the system recognizing and tracking multiple targets

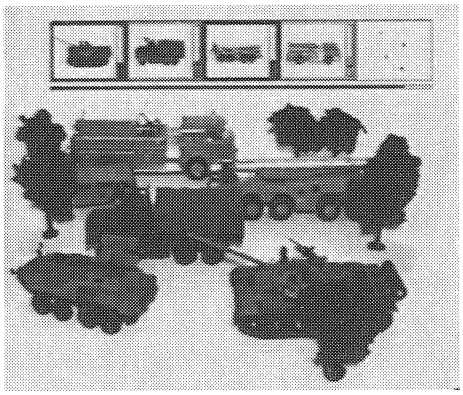

Fig. 5-18. Real-time tracking of multiple targets with noise.

in the presence of foreground and background clutter (trees) as well as false targets (vehicles not programmed into the holographic database).

5.3 Shift-invariance controlled correlator

Pattern recognition systems built from large numbers of correlation templates can be a powerful tool for many applications, including security, navigation, and human-computer interfaces.[5-4] The robustness and effectiveness of such systems improves if a larger number of templates is used. If templates are sequentially entered into the correlator, as the number of templates increases, the system speed decreases. However, holographic correlators are capable of performing multiple correlations simultaneously, displaying the results on the same detector at the output. We can distinguish the responses from different templates by dividing the output plane into individual domains, one for each template. If an input image shifts too much, the corresponding correlation peak will move into a domain designated for another template, leading to a false identification. Limiting the shift invariance of the system prevents this error from occurring. The less shift-invariance a system has, the smaller the individual domains can be and therefore more templates can be used in

parallel. However, some amount of shift-invariance is necessary for robust recognition. The trade-off between shift-invariance and the number of templates used is an important design parameter for pattern recognition systems.

The use of volume holograms is one method through which the shift invariance can be reduced.[5-5][5-6] In this case, Bragg selectivity can cause the correlation peak to disappear for shifts of the input image. Bragg selectivity in the plane defined by the reference and signal beams is much greater than that for the out-of-plane direction, leading to a very asymmetric correlation domain. This is a problem since most applications require symmetric correlation domains. The relatively weak control over the size of the domain in the out-of-plane direction also prevents the storage of more templates in this direction.

In this section a new method[5-7] is presented for controlling the shift invariance by shifting the hologram away from the Fourier plane, into the Fresnel region.

5.3.1 Theory

When the input image shifts in the optical correlator, the plane wave components at the Fourier plane all experience the same phase shift. This property results in shift-invariance for thin holographic correlators stored in the Fourier plane. If the hologram is recorded away from the Fourier plane, however, the phase shift is not uniform across all plane wave components. As a result, the various components of a shifted input image begin to add destructively and the correlation peak eventually disappears. The further the holographic material is from the Fourier plane, the bigger the phase difference between the various component plane waves and the more shift invariance is reduced.

Figure 5-19 shows the basic correlator system with the holographic material shifted

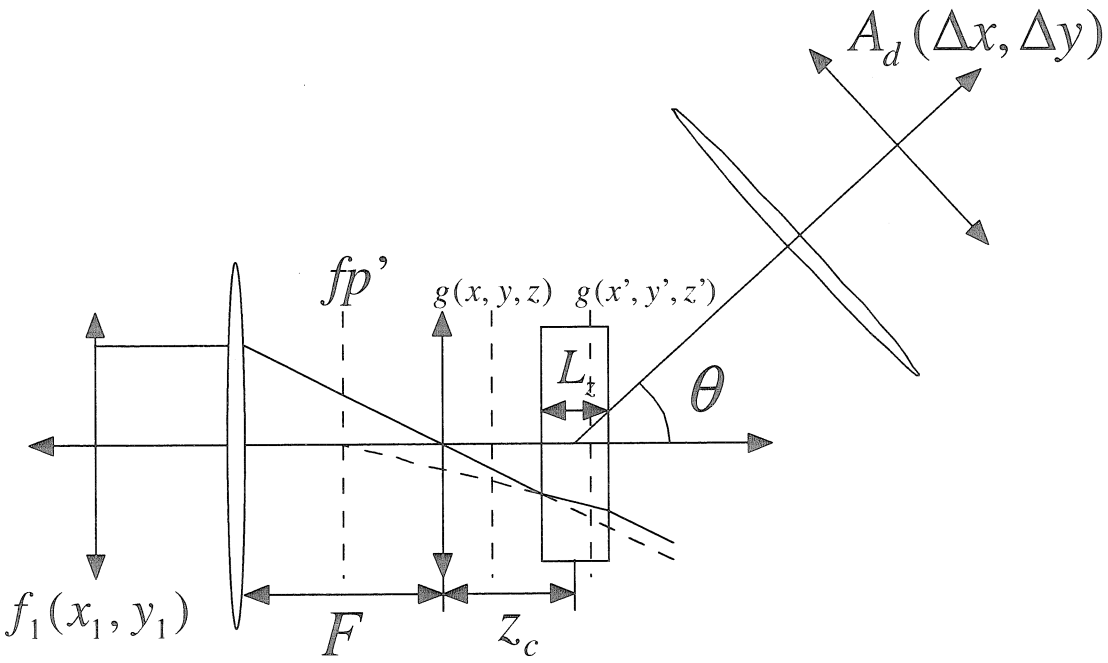

Fig. 5-19. Basic holographic correlator.

a distance z_c from the Fourier plane. A transparency $f_1(x_1,y_1)$, illuminated by monochromatic light of wavelength λ, produces the disturbance $g(x,y,z)$ in the Fresnel zone given (within the paraxial approximation and assuming z_c is small relative to F) by

$$g(x, y, z) = \int_{-\infty}^{\infty}\int_{-\infty}^{\infty} f_1(x_1, y_1)\exp\left(-j\frac{k}{F}(x_1x + y_1y)\right)\exp\left(j\frac{k}{2F^2}(x_1^2 + y_1^2)z\right)dx_1dy_1 \tag{5-2}$$

where $k = 2\pi/\lambda$, F is the focal length of the lens, and z is the distance from the Fourier plane. The refractive index, however, makes the Fourier plane appear to be shifted from its actual position. The field inside the material is then

$$\begin{aligned} g(x', y', z') = \int_{-\infty}^{\infty}\int_{-\infty}^{\infty} f_1(x_1, y_1)\exp\left(-j\frac{k}{F}(x_1x + y_1y)\right) \\ \times \exp\left(j\frac{k}{2nF^2}(x_1^2 + y_1^2)(z' + (z_c - L_z/2)(n-1))\right)dx_1dy_1 \end{aligned} \tag{5-3}$$

where z_c is the distance from the Fourier plane to the center of the recording material.

A plane wave reference incident at an angle θ interacts with the signal beam to record a hologram given by

$$|\exp(jk(x'\sin\theta' + z'\cos\theta')) + g(x', y', z')|^2 \tag{5-4}$$

where θ' is the angle of the reference beam inside the medium.

Illuminating the hologram with a new input image, $f_2(x_2,y_2)$, produces the diffracted field amplitude A_d along the wave-vector $\boldsymbol{k}_d$ given (within the Born approximation[5-8]) by

$$\begin{aligned} A_d(\hat{k}_d) = {} & \iint dx_1 dy_1 \iint dx_2 dy_2\, f_1(x_1, y_1) f_2(x_2, y_2) \\ & \times \iiint_{\text{volume}} \exp\left(-j\frac{k}{2nF^2}(x_1^2 - x_2^2 + y_1^2 - y_2^2)(z' + (z_c - L_z/2)(n-1))\right) \\ & \times \exp\left(j\frac{k}{F}(x_1 - x_2)x'\right)\exp\left(j\frac{k}{F}(y_1 - y_2)y'\right)\exp(jn(k\sin\theta' - k_{dx})x')\exp(-jnk_{dy}y') \\ & \times \exp(jn(k\cos\theta' - k_{dz})(z' + (z_c - L_z/2)(n-1)))dx'dy'dz' \end{aligned} \tag{5-5}$$

where k_{dx}, k_{dy}, and k_{dz} are the x, y, and z components of the diffracted wave-vector such that $|\hat{k}_d|^2 = k_{dx}^2 + k_{dy}^2 + k_{dz}^2$.

Performing the integral over the volume of the material with the change of variables $z = z' - z_c$ yields

$$\begin{aligned} A_d(\hat{k}_d) = {} & \iint dx_1 dy_1 \iint dx_2 dy_2\, f_1(x_1, y_1) f_2(x_2, y_2) \\ & \times \exp\left(-j\frac{k}{2nF^2}(x_1^2 - x_2^2 + y_1^2 - y_2^2)(z_c + (z_c - L_z/2)(n-1))\right) \\ & \times \exp(jn(k\cos\theta' - k_{dz})(z_c + (z_c - L_z/2)(n-1))) \\ & \times \operatorname{sinc}\left[\frac{L_z}{2\pi}\left(\frac{k}{2nF^2}(x_1^2 - x_2^2 + y_1^2 - y_2^2) + kn\cos\theta' - nk_{dz}\right)\right] \\ & \times \operatorname{sinc}\left[\frac{L_x}{2\pi}\left(\frac{k}{F}(x_1 - x_2) + kn\sin\theta' - nk_{dx}\right)\right] \\ & \times \operatorname{sinc}\left[\frac{L_y}{2\pi}\left(\frac{k}{F}(y_1 - y_2) - nk_{dy}\right)\right] \end{aligned} \tag{5-6}$$

with $\mathrm{sinc}(x) = \frac{\sin \pi x}{\pi x}$. The transverse dimensions L_x and L_y are large enough to approximate the last two sinc functions as delta functions. Integrating over x_2, and y_2 yields

$$\begin{aligned} A_d(\Delta x, \Delta y) = \iint & f_1(x_1, y_1) f_2(x_1 + \Delta x, y_1 + \Delta y) \\ & \times \exp(j(z_c + (z_c - L_c/2)(n-1))\alpha) \mathrm{sinc}\left(\frac{L_z}{2\pi}\alpha\right) dx_1 dy_1 \end{aligned} \tag{5-7}$$

where

$$\begin{aligned} \alpha &= \frac{k}{2nF^2}(x_1^2 - (x_1 + \Delta x)^2 + y_1^2 - (y_1 + \Delta y)^2) + kn\cos\theta' - nk_{dz} \\ \Delta x &= nF(\sin\theta' - k_{dx}/k) \\ \Delta y &= -nFk_{dy}/k \end{aligned} \tag{5-8}$$

Equation (5-7) is the cross-correlation between f_1 and f_2, with a sinc term from the Bragg-selectivity and an exponential term involving the position of the hologram, z_c. Both the exponential and the sinc term act as a window function on the correlation, attenuating the signal for non-zero values of Δx and Δy, i.e., for deviations from the center of the correlation domain. For volume holograms recorded at the Fourier plane, the exponential term becomes identically equal to one, and only the sinc term acts to limit shift invariance. Likewise, for thin holograms recorded away from the Fourier plane the sinc term becomes negligible and the exponential term becomes the limiting factor. The presence of this window function within the integral also acts to sharpen the correlation peaks by suppressing the sidelobes, since they occur at non-zero values of Δx and Δy even when the input is centered. Issues concerning shift invariance aside, the sidelobes of the correlations place an upper limit on how tightly the correlations can be packed in a conventional correlator. Attempting to store correlators too closely together results in the sidelobes from one template interfering with the neighboring template, reducing both outputs to noise.

5.3.2 Experiment

The experimental setup for the correlator is shown in Figure 5-20. An image of

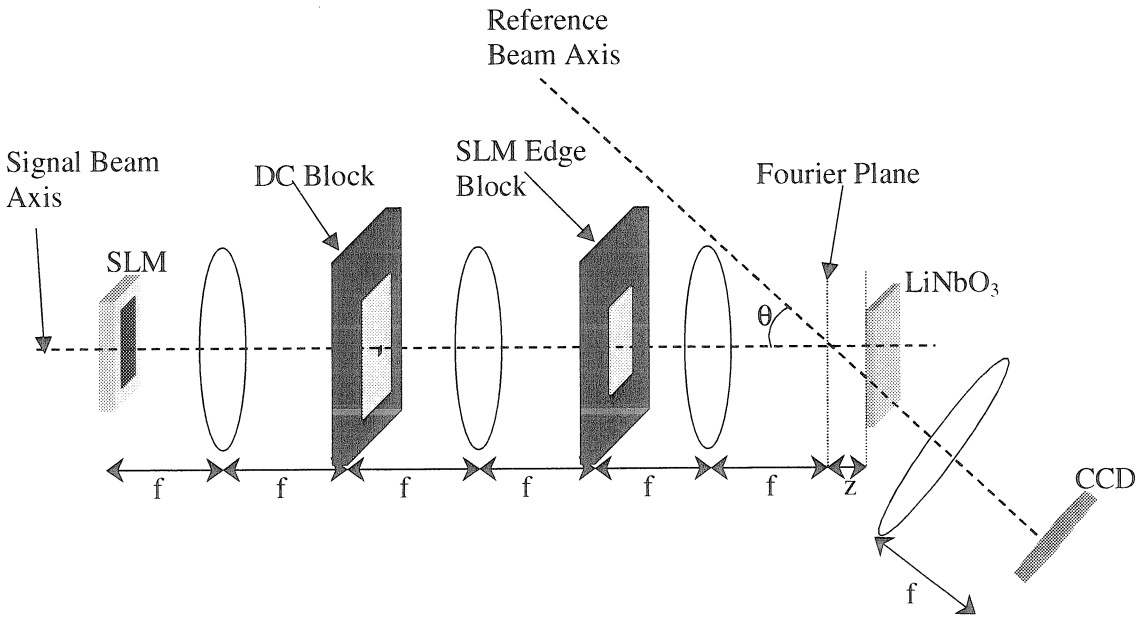

Fig. 5-20. Experimental correlator setup.

random white and black rectangles, shown in Figure 5-21, was displayed on a portion of

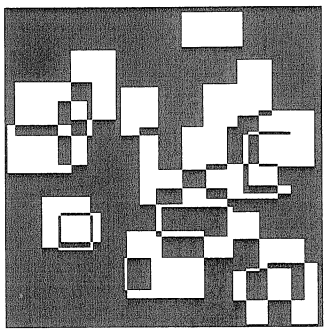

Fig. 5-21. Randomly generated image 120 by 120 pixels in size.

the liquid crystal spatial light modulator, which has a resolution of 640 by 480 pixels and a 24 μm pixel pitch. A DC block in the Fourier plane of the first lens edge enhances the image before correlation. The filter behind the second lens blocks the edges of the SLM, created

by the edge-enhancement process of the DC-block. If not blocked, the SLM creates an undesirable constant DC offset to the strength of the correlation regardless of what image is presented on the SLM. The holographic material (a 250 μm thick $LiNbO_3$ crystal) is mounted on a motorized translation stage so as to enable computerized control of the location relative to the Fourier plane. The signal beam is coincident with, and the reference beam at a 25° angle to, the recording material's surface normal. A lens is placed along the path of the reference beam and in its back focal plane a CCD camera is used to capture the intensity and position of the correlation peak. The video signal from the CCD camera is digitized and analyzed by a computer.

For each hologram displacement distance z_c, a hologram of the input pattern centered on the SLM is recorded. After recording, the reference beam is turned off and the image on the SLM is correlated with the stored hologram. The input image is shifted, electronically, on the SLM. The image is first shifted horizontally (the in-plane direction) while centered vertically. For each horizontal location, the intensity of the correlation peak and its location on the CCD is measured. The image is then shifted vertically (the out-of-plane direction) while centered horizontally, and again the peak intensity and position are measured. The correlation measurements are taken under very weak illumination to both prevent saturation of the CCD and erasure of the hologram.

Figure 5-22 shows typical curves of peak intensity versus image location for both horizontal and vertical displacements. The shift-selectivity is measured as the width of such curves when they attain half of their maximum values. Plots of the shift-selectivity for both the in-plane and out-of-plane directions together with the theoretical predictions are shown in Figure 5-23 as functions of the recording material location relative to the Fourier plane.

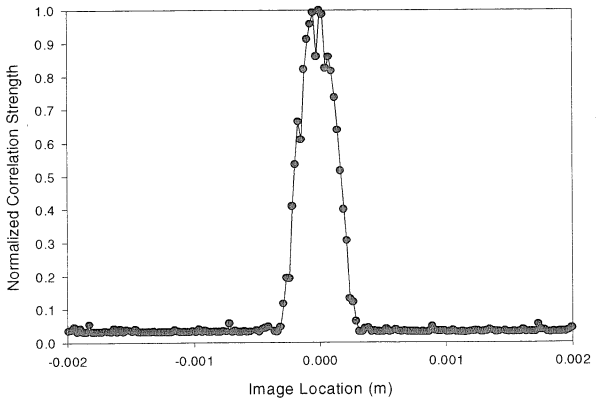

(a)

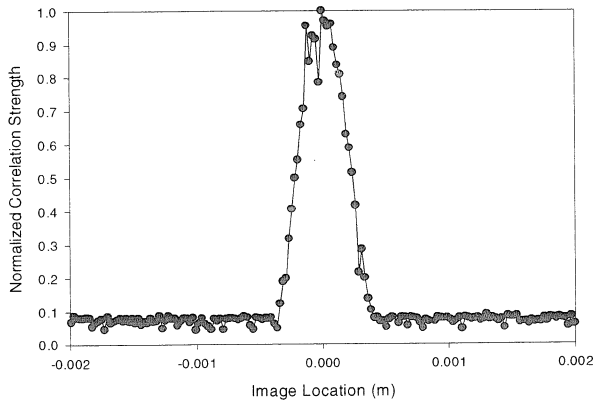

(b)

Fig. 5-22. Correlation strength versus image displacement for both (a) in-plane and (b) out-of-plane shifts.

The correlation integral derived in the previous section was computed with a Monte Carlo technique with experimental values for beam angle (25°), material thickness (250 μm), and index of refraction (2.24).

The experiment agrees well with the theoretical calculations over a large range of material displacements. Theory and experiment deviate most for out-of-plane shifts close to and at the Fourier plane, where the predicted value of the shift-invariance shoots up to 25 degrees. The figure shown does not contain the full vertical range of the theoretical curve so that the details of the wings would be evident.

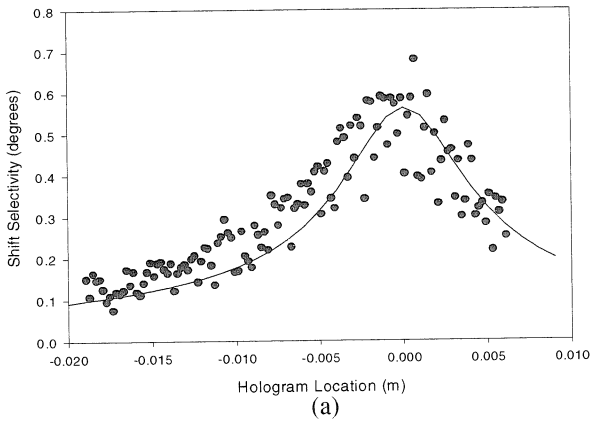

(a)

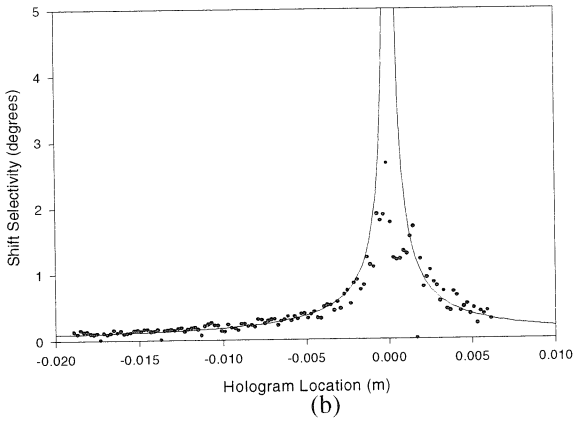

(b)

Fig. 5-23. (a) In-plane and (b) out-of-plane shift selectivity with the recording material displaced from the Fourier plane.

5.4 Conclusion

Overall, the optical holographic correlator system works well at recognizing and tracking multiple targets in real time. Issues concerning orientation-invariant recognition and scale problems were addressed. Because of the high capacity of holographic systems, multiple views can be used for orientation-invariant recognition. Dynamic lens control can be implemented for tracking objects of varying scale, once they are recognized, with a slight increase in the number of required templates. Furthermore, system costs can be greatly reduced due to the tolerance of the system to low resolution image input devices.

A method to control the shift-invariance was addressed through the simple modification of moving the recording material away from the Fourier plane. While it is possible to rely on Bragg-selectivity alone to control the shift invariance of holographic correlator systems, simply recording the holograms in the Fresnel zone allows for convenient control without the need to have material of the precise thickness necessary for a given application.

References

[5-1] A. VanderLugt. "Signal detection by complex spatial filtering," *IEEE Trans. Inf. Theory.* **IT-10**:139-145, 1964.

[5-2] C. S. Weaver and J. W. Goodman. "Technique for optically convolving two functions," *Appl. Opt.* **5**:1248-1249, 1966.

[5-3] K. Curtis and D. Psaltis. "Recording of multiple holograms in photopolymer films," *Appl. Opt.* **31**:7425-7428, 1992.

[5-4] *Optoelectronic Information Processing*. B. Javidi and P. Refregier, Editors. SPIE Press, November 1997. ISBN: 081942675X.

[5-5] C. Gu, J. Hong, and S. Campbell. "2-D Shift-invariant volume holographic correlator." *Optics Communications*. **88**:309-314, 1992.

[5-6] J. Yu, F. Mok, and D. Psaltis. Spatial Light Modulators and Applications II, U. Efron, ed. "Capacity of optical correlators." *Proc. SPIE* **825-22**: 128-135, 1987.

[5-7] D. Psaltis and M. Levene. "Optical Neural Networks," in *Critical Reviews of Optical Science and Technology*. S-S. Chen and H.J. Caulfield, eds. SPIE Press, Bellingham, WA. Volume CR55, pp. 141-149, April, 1994.

[5-8] J.D. Jackson. *Classical Electrodynamics*. Wiley, New York, 1975.

6 The High Frame-rate Holographic Movie Camera

6.1 Introduction

Everyone is familiar with the results of strobe-photography, which have provided such memorable pictures as bullets piercing apples and water drops falling into a glass. For certain investigations, there is also a need for high-frame rate video cameras (as opposed to still photography). One example is in the study of crack propagation velocity, in which a film based camera capable of capturing 80 frames at up to 2 million frames per second was used.[6-1] An alternative approach is to use cameras consisting of multiple CCD imagers, which are capable of very high frame rates (100 Mfps), but are limited in the number of frames that can be captured to about ten.[6-2]

Holographic interferometry[6-3] is an approach that has been used for many years to measure displacements or index variations in materials. The advantage of holography over ordinary photographic approaches is that with holography the phase associated with an object is recorded, in addition to its amplitude. Through interference, an original object recorded holographically can be compared with a new, stressed or otherwise perturbed, object. This is an elegant approach which has also been applied to high-speed events through double-exposure interferometry.[6-4] With this technique a pulse laser is used to first record a reference hologram. Then another pulse is used to record an additional hologram with an identical reference beam. Upon reconstruction, both holograms are reconstructed by a single reference beam, and will interfere with each other, allowing the analysis

of the fringes produced from this high-speed event. Essentially, this is an extension of strobe-photography, with the benefit of the recording of phase information that is possible with holography. In another application, holography was used not for its interferometric capabilities, but rather for the ability to record and reproduce three-dimensional scenes produced by hypervelocity impacts.[6-5] A Q-switched Nd:YAG pulse of 5 ns duration was used to holographically record the debris field from a steel ball impacting a steel sheet. From the holographic reconstruction, the researchers were able to extract three-dimensional position information as well as the size and shape of the debris particles. By repeating the experiment with different delays between time of impact and the pulse used to record the hologram, an idea of the time-evolution of the trajectory of the debris projectiles could be constructed.

Holography has proven to be very useful for single image applications where its interferometric and depth-information capabilities allow analyses not possible with photographic, CCD, or other intensity sensitive camera systems. However, there have been few investigations into multi-frame holographic systems for recording high-speed events. In one system, a rotating mirror was used[6-6] to provide a time-varying reference beam for angle multiplexing. However, due to the use of mechanical motion the frame-rate was limited to 20 kHz and the system suffered from smearing effects. A similarly performing system[6-7] overcame the smear effect by having multiple fixed reference beams, each of which passed through an electro-optic shutter. The shutters were opened in turn to record successive holograms with a different reference beam angle. Other attempts at multi-frame recording have utilized multiple lasers, each firing a pulse at a different point in time.[6-8] The output of each laser was split to generate unique reference beam angles for each frame

to be recorded. The frame-rate was 1 MHz, but the cost and space requirements of multiple lasers severely limits the number of frames that can be recorded with this technique. In another system, up to 4000 holograms with a 300 kHz frame rate were recorded[6-9] by combining an acousto-optic deflector and rotation of the recording material to provide spatial multiplexing. While the number of holograms recorded with this system is impressive, the frame-rate is not fast enough for many applications. For very high frame-rates, non-mechanical techniques for the generation of multiple pulses must be utilized. A holographic system using a cavity formed by parabolic mirrors has been used to study several high-speed events.[6-10]-[6-12] This system was capable of recording ten holograms with a minimum separation of 28.3 ns. One advantage of the technique used was the ability to vary the frame rate. However, the system required a custom-made graded-reflectivity beamsplitter, and like many other systems, utilized signal beams which passed through the test object at a different angle for each frame. Such a technique eliminates the possibility of performing holographic interferometry with the recorded frames.

This chapter describes the development of a high-speed, multi-frame, holographic camera system made possible by the high performance of modern polymer recording materials. The goals of the system were to have frame rates comparable to that of CCD camera systems, while having a potentially larger number of frames that could be recorded. The system was designed to allow the use of interferometric analysis techniques enabled by holographic recording. Furthermore, holography enables a large depth of focus to be achieved, depending on the reconstructing optics, which is not available with 2-D recording techniques. The system utilizes a Q-switched Nd:YAG laser capable of 300 mJ, 5.9 ns pulses at a wavelength of 532 nm. The development of the system began with a search for

a suitable recording material and its characterization, detailed in Section 6.2. The design and development of the optical system is described in Section 6.3. Section 6.4 describes experiments using the system for the recording of a 5-frame holographic movie with a 12 ns frame period.

6.2 Recording Material

Most experiments in holographic interferometry and double-pulse holography have been performed with thin film, plate-based, materials.[6-3],[6-5] Besides requiring messy and time consuming wet-development processing, these materials yield poor Bragg selectivity and exhibit shrinkage. It would be much more desirable to use a polymer material that alleviates these problems. However, so far in this thesis all recording has been performed with CW lasers, and it was not obvious whether or not the materials will record well with pulsed exposures. Furthermore, the system to be developed places strict demands on the material. Because frame periods on the order of ten's of nanoseconds are needed, all holograms must be recorded from the energy available in a single output pulse from the laser. Also, the M/# should be high enough to allow the reconstruction of the holograms with sufficient efficiency to not be affected by noise.

The system requires use of a doubled Nd:YAG laser at 532 nm. This immediately rules out the use of PQ:PMMA, which is extremely insensitive to this wavelength, and would require much more energy than could be provided by a single pulse from the laser. Photorefractive polymers are not suitable due to dark decay, and other problems discussed in Chapter 2. The next potential candidate is the DuPont HRF-150 material used for the optical correlator system described in the previous chapter. It has been reported[6-13] that

another DuPont photopolymer, HRF-800X001-20, is capable of recording with 25 ns pulse exposure in the reflection geometry. However, this film is only 20 microns thick, which is not sufficient for recording 100 holograms with angle multiplexing. My own experiments performed with HRF-150 to record transmission holograms with 6 ns pulses at 532 nm did not prove fruitful. In some cases with the right pre-exposure conditions, very weak holograms could be seen. But overall the performance was not satisfactory.

The final candidate is a new polymer material manufactured by Aprilis, Inc. Their line of recording materials are designed for holographic data storage applications, and are claimed to be capable of recording holograms with 20 ns pulses as well as in CW. The remainder of this section details the testing of the Aprilis ULSH500-7A material, which is 200 microns thick and is sensitized for both 514 nm and 532 nm recording. This material utilizes a cationic ring-opening polymerization as the mechanism for recording.[6-14] It begins in a viscous liquid state and is sandwiched between two glass slides and sealed at the edges. A pre-exposure is required to increase the viscosity of the material before a stable hologram can be recorded.

6.2.1 CW Recording in Aprilis ULSH500-7A

CW recording experiments were performed at 514 nm with an Argon laser. For pre-exposure, a white light lamp with a green filter, to narrow the emission spectrum, was used. A recording setup was built with the recording beams each 20-degrees (in air) from the normal to the material's surface, in the transmission geometry.

To see the effects of pre-exposure on hologram quality, single holograms were recorded with two different amounts of pre-exposure, while using an intensity of

15 mW/cm^2 for each recording beam and a pre-exposure intensity of 1 mW/cm^2. In the first experiment, a pre-exposure energy of 100 mJ/cm^2 was used, with a recording time of 33 seconds. Measurement of the angle selectivity of this hologram shows quite a bit of distortion, as seen in Figure 6-1. In this plot, the solid line is the theoretical Bragg selectivity

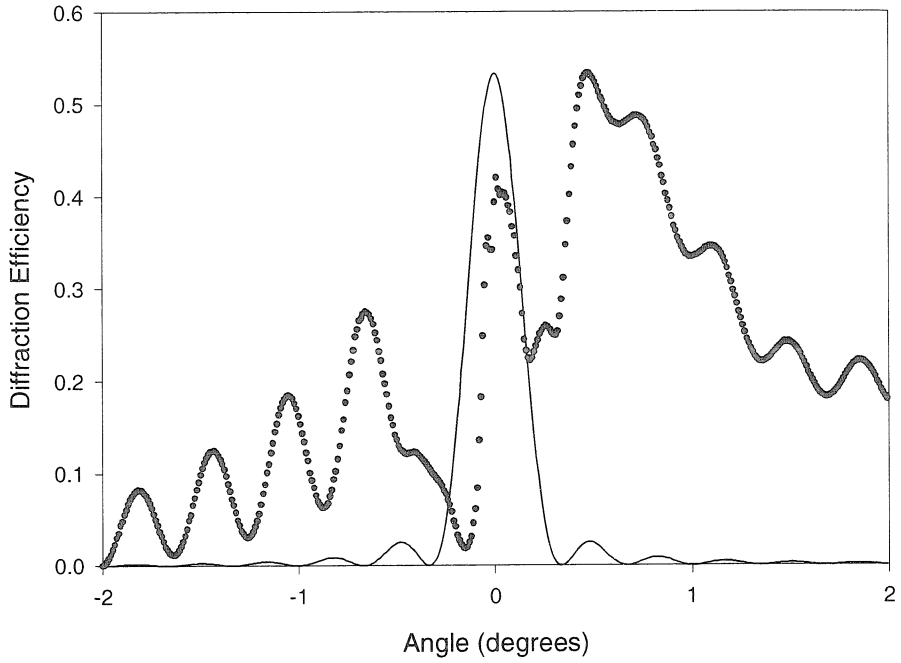

Fig. 6-1. Angle selectivity of a hologram recorded with 100 mJ/cm^2 of pre-exposure.

curve of a 200 μm thick hologram. When the pre-exposure is increased to 150 mJ/cm^2, however, the selectivity improves greatly, as shown in Figure 6-2. Again the recording time was 33 seconds. Insufficient pre-exposure causes hologram distortion due to the material not being structurally stable. Too much pre-exposure will not cause the holograms to distort however, it will decrease the dynamic range of the material.

For the high-speed movie system, multiple holograms need to be recorded on a single spot of the material. Therefore, multiplexing experiments were first performed under

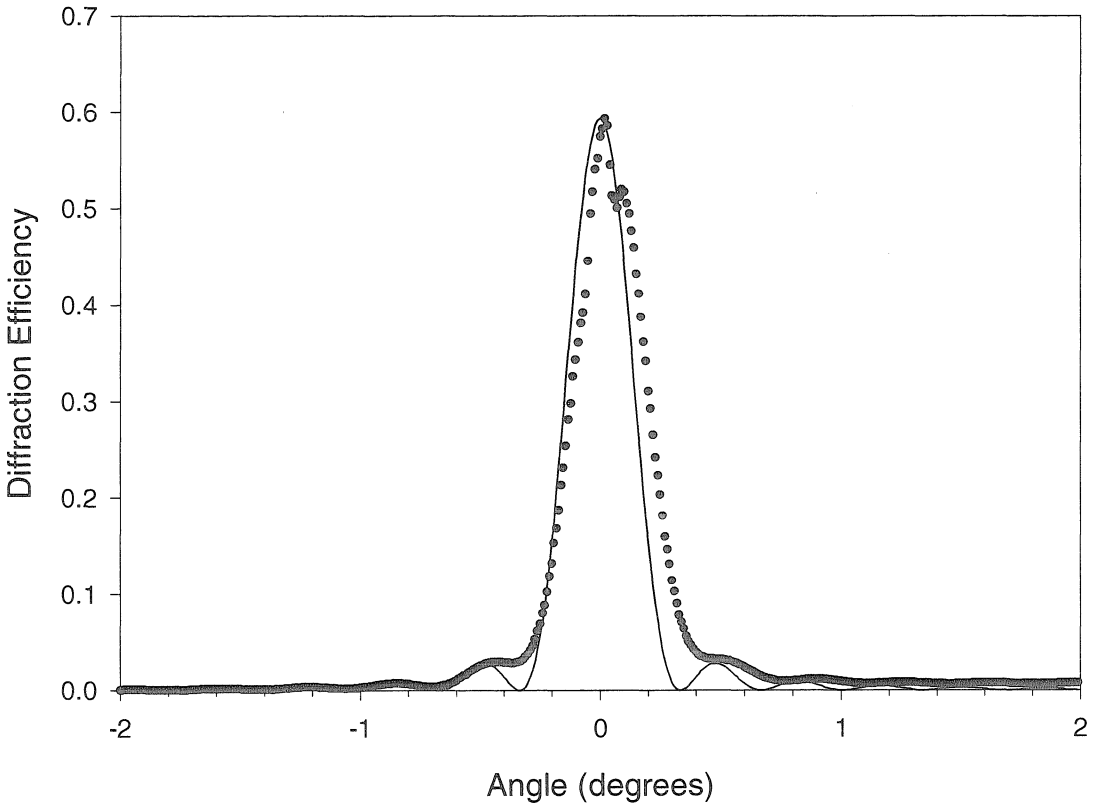

Fig. 6-2. Angle selectivity of a hologram recorded with 150 mJ/cm^2 of pre-exposure.

CW exposure. The material was mounted on a rotation stage to provide peristrophic multiplexing, while a mirror mounted on a rotation stage together with a 4-f system was used to provide angle multiplexing. Combined, 720 holograms were recorded, with 120 holograms 1.5 degrees apart peristrophically, and at 6 different angles separated by 1 degree. The recording beams were each 2.5 mW/cm^2. A pre-exposure of 120 mJ/cm^2 was used. Figure 6-3 contains the results of this multiplexing experiment, where each hologram was recorded with an exposure of 150 ms (750 μJ/cm^2). The cumulative grating strength is approximately 4.2, but the holograms decay in strength exponentially due to the lack of a recording schedule. This data was used to generate an exposure schedule as described in [6-15]. By keeping all other conditions constant and using the exposure schedule, 720 holo-

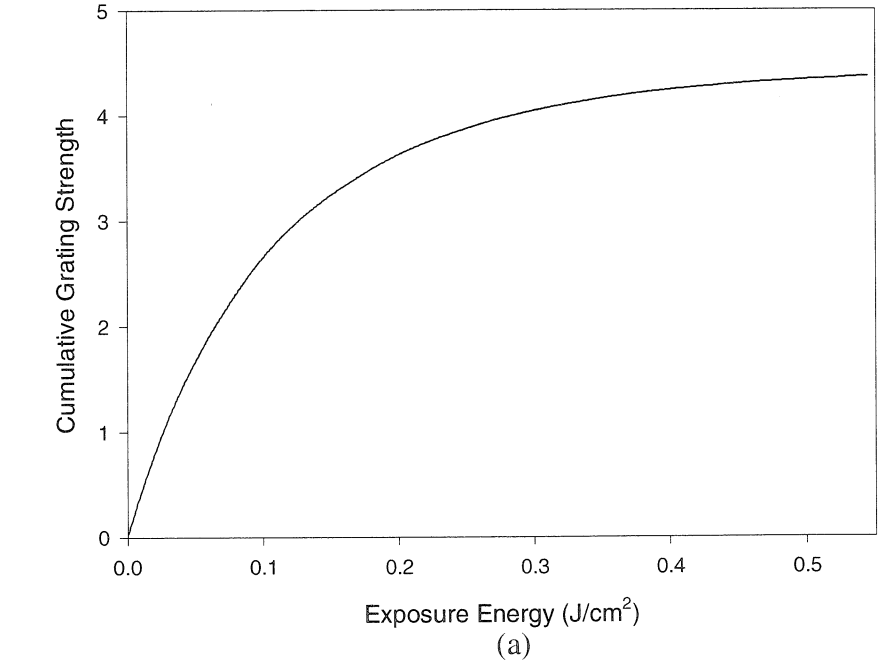

(a)

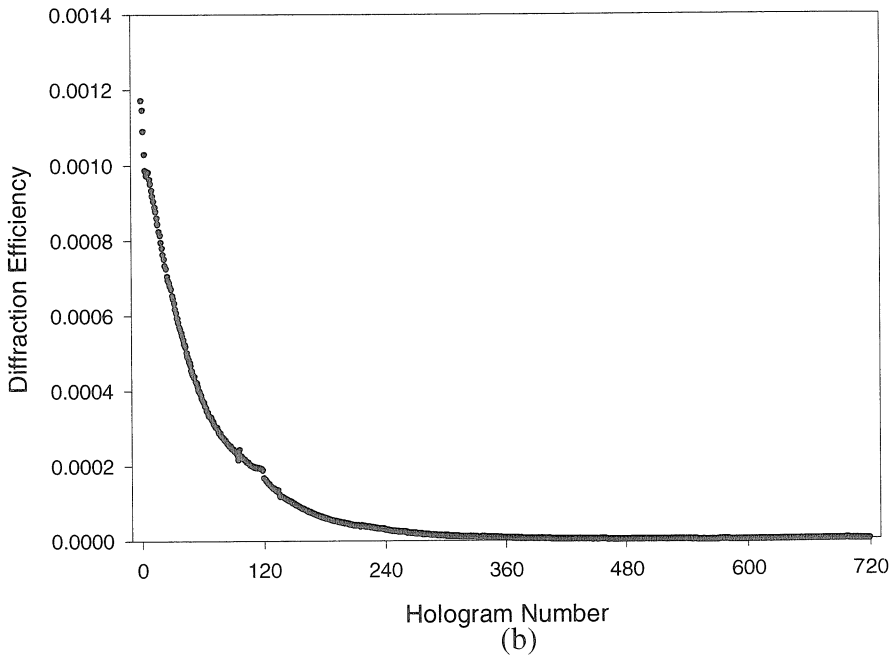

(b)

Fig. 6-3. (a) Cumulative grating strength of 720 holograms and (b) individual hologram strengths with equal exposures for each hologram.

grams were multiplexed in a new sample. The results are plotted in Figure 6-4. With the

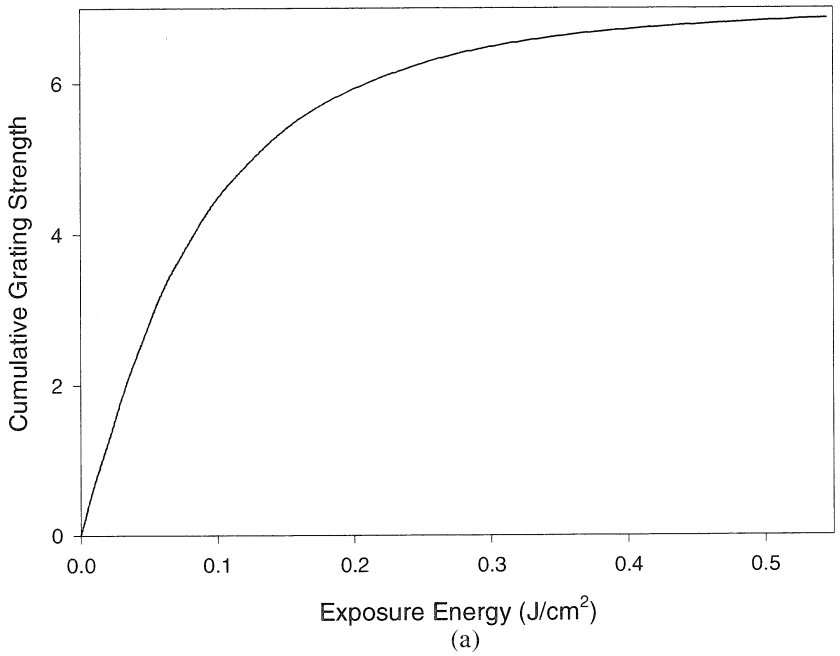

(a)

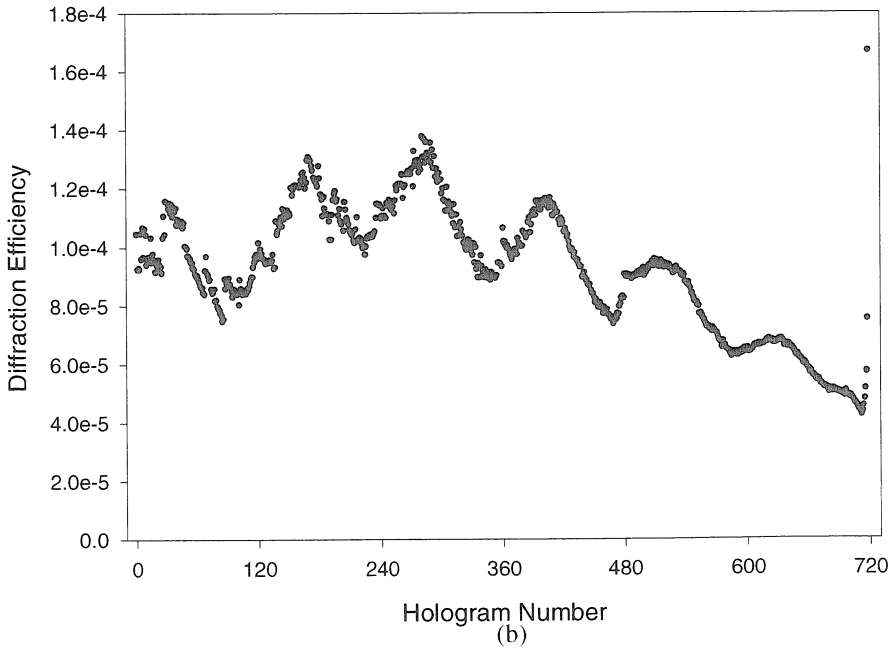

(b)

Fig. 6-4. (a) Cumulative grating strength of 720 holograms and (b) individual hologram strengths with an exposure schedule.

schedule, the holograms are much more equal, and the M/# approaches 7 with just 500 mJ/cm^2 of exposure.

For the actual movie recording system, real images and not just plain waves have to be stored. Therefore, it is also necessary to examine the ability of the material to record images with acceptable quality. To get a quantitative measure, the 40-micron pixel mask used in the data storage experiments of Chapter 3 was employed. Figure 6-5 is a schematic

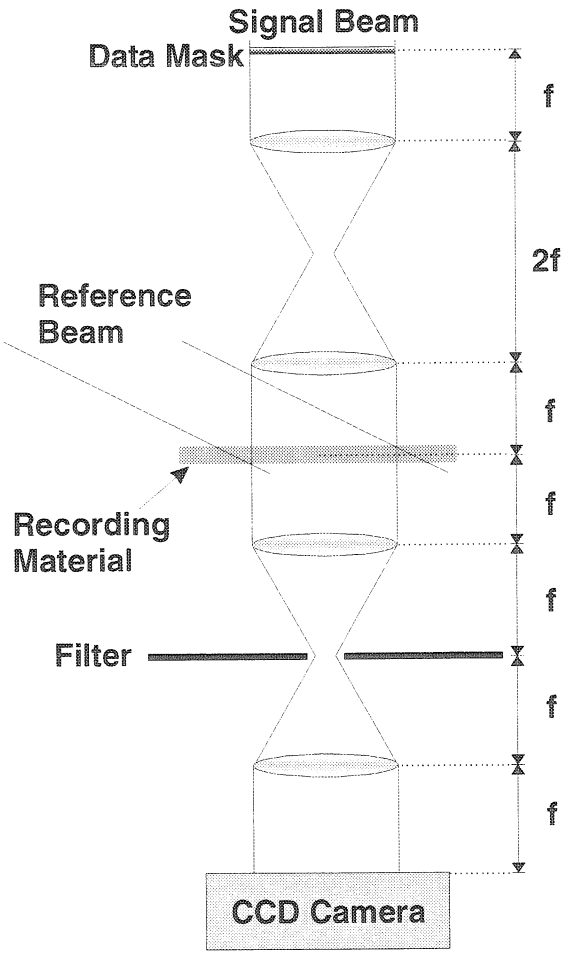

Fig. 6-5. Optical system used to record images in the Aprilis material.

of the optical system constructed for the holographic storage of images. The lenses had 8 cm focal lengths and were arranged to record the holograms at the first image plane of the

mask. For this experiment, the material was placed on two rotation stages to allow peristrophic and angle multiplexing to be combined, while keeping the two recording beams fixed. There was a 32.5 degree angle between the reference beam and the signal beam, with the material placed symmetrically between the two when at the zero position. SNR measurements were taken identically to that described in Chapter 3 with the holographic data storage experiments. First, the SNR of the mask imaged through the optical system was measured. Its value was 8.2. Since the recording material is sandwiched between glass, the next step was to determine the SNR of the mask imaged through the optical system with the glass slides in place. This value was 8.1. As a final measurement before recording holograms, a uniformly exposed sample was placed in the optical system. The SNR of the imaged mask was then 8.65. These measurements clearly show that the material itself does not cause image distortion, within the margin of error in computing the SNR.

A single hologram was recorded with 2.5 mW/cm^2 in each beam for a total exposure of 1.5 mJ/cm^2. The SNR of the reconstruction was measured as 6.5. An image of the reconstructed page is in Figure 6-6. For multiplexing, 45 holograms were recorded 4 degrees apart in the peristrophic orientation, and 6 sets were recorded each 2 degrees apart in angle, for a total of 270 holograms. Again the beam intensities were 2.5 mW/cm^2, but each hologram was recorded for 0.75 mJ/cm^2. The reconstruction of three of the holograms is shown in Figure 6-7. The average SNR of these images was 5.3. Since no exposure schedule was used, the holograms were not of similar diffraction efficiency. A schedule was made from the measured hologram strengths, again using the method from [6-15]. Using the schedule, 270 holograms were recording, keeping all other conditions the same. Figure 6-8 are pictures of the 1st, 135th, and 270th hologram reconstructions, which had an

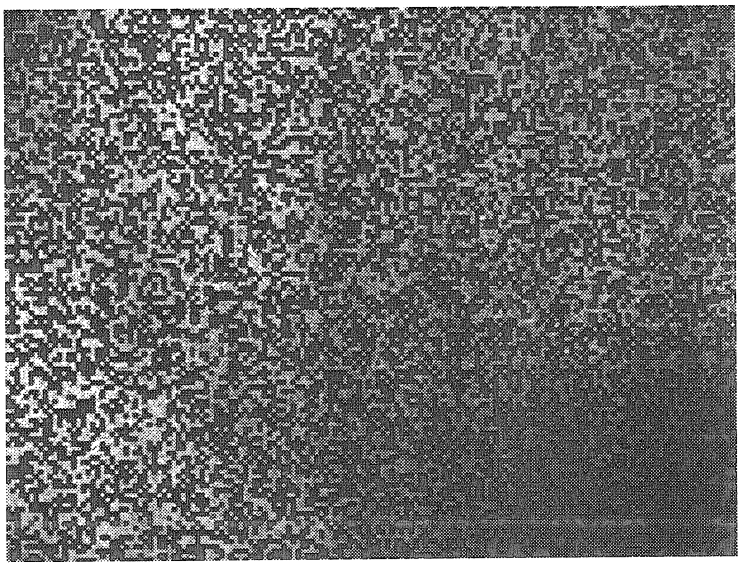

Fig. 6-6. Reconstruction of a single hologram.

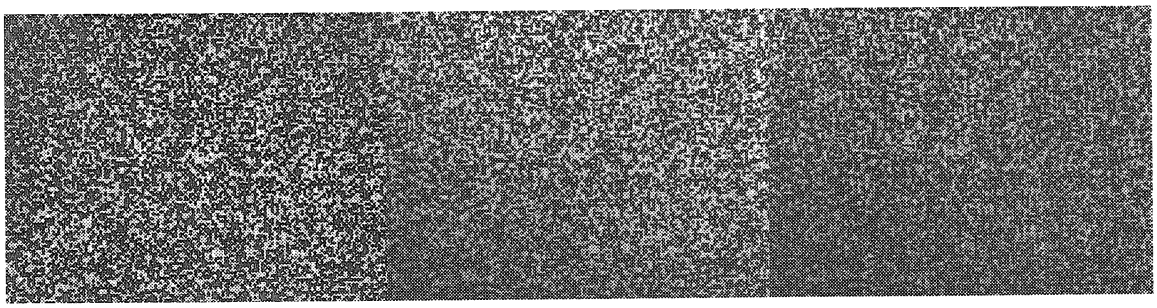

(a) (b) (c)

Fig. 6-7. Reconstruction of the (a) 1st, (b) 135th, and (c) 270th hologram from an unscheduled set of holograms.

average SNR of 5.1, similar to the unscheduled case. Figure 6-9 shows the cumulative grating strength of this set of holograms. The maximum reaches almost 3. Due to the binary nature of the holograms, a 50% reduction in M/# from plane-wave holograms is expected. Furthermore, it can be seen that the cumulative grating strength curve is still growing even at the last hologram. This indicates that all of the dynamic range was not consumed, and the M/# is actually higher. Nevertheless, this experiment proves that the Aprilis material is

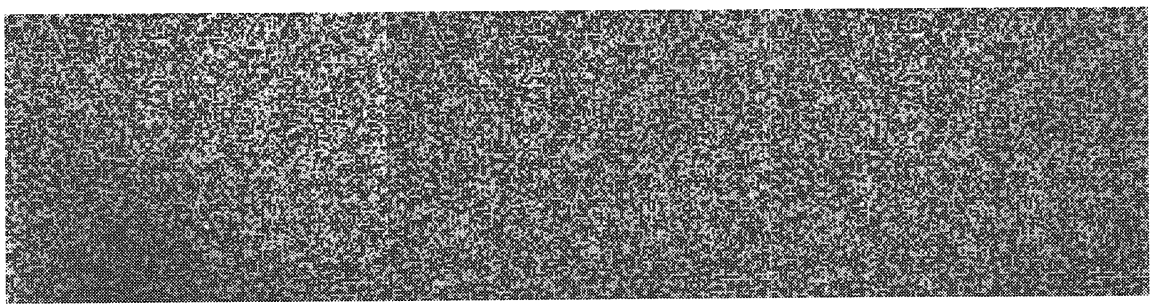

(a) (b) (c)

Fig. 6-8. Reconstruction of the (a) 1st, (b) 135th, and (c) 270th hologram from a scheduled set of holograms.

capable of recording holograms with high fidelity and without sacrificing M/# due to the bandwidth of the holograms.

6.2.2 Pulsed Recording in Aprilis ULSH500-7A

Section 6.2.1 showed that under CW illumination conditions the Aprilis material had enough dynamic range and sufficient imaging quality to be a viable candidate for the holographic movie system. The next step is the determination of the material's response under pulsed illumination. The laser source used was a Q-switched Nd:YAG which was frequency doubled to 532 nm. The beam diameter was 9 mm at the $1/e^2$ width, and the pulse duration was 5.9 ns. For these experiments a white-light lamp without a color filter was used for pre-exposure in order to increase the intensity of the available light and decrease the required pre-exposure times. As a result, the pre-exposure energies required are different than those for the color-filtered lamp used previously.

For the first experiment, an optical system was constructed to record in the symmetric transmission geometry with beam angles of 12.5 degrees from the material's surface normal. Using a pre-exposure of approximately 2 J/cm^2, holograms were recorded with

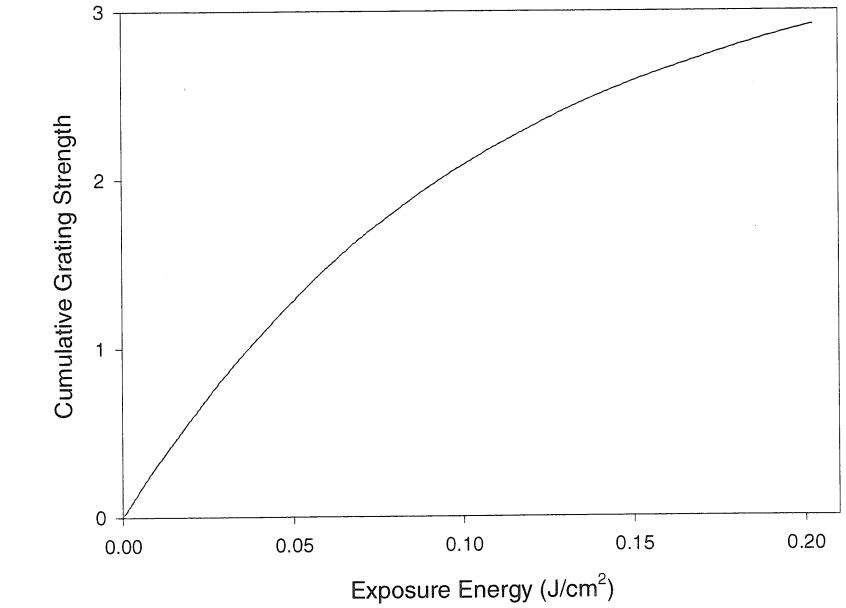

(a)

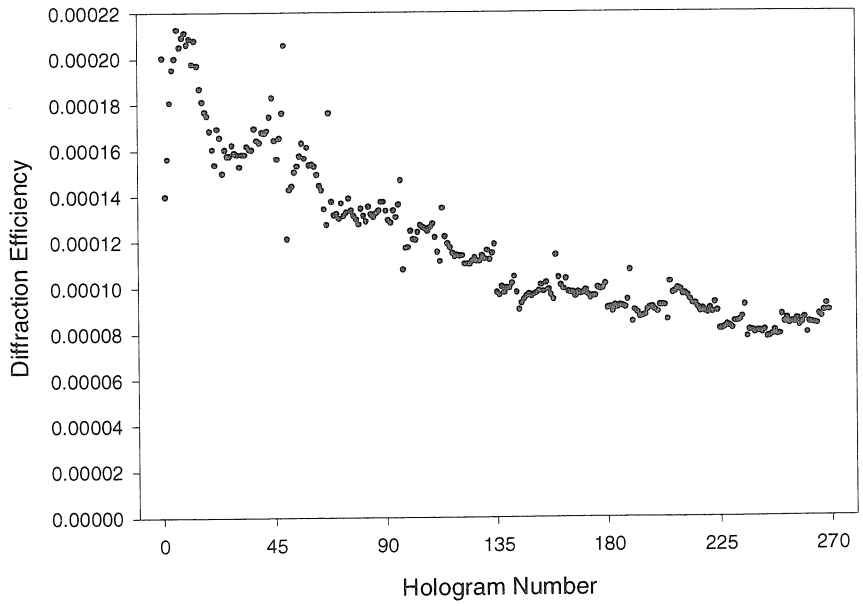

(b)

Fig. 6-9. (a) Cumulative grating strength of 270 image-plane holograms and (b) individual hologram strengths with an exposure schedule.

various pulse energies, with each recording beam having an approximately equal fraction of the total pulse energy. Each hologram was recorded in an unexposed sample, so no multiplexing was performed. Figure 6-10 is a plot of the diffraction efficiencies measured for

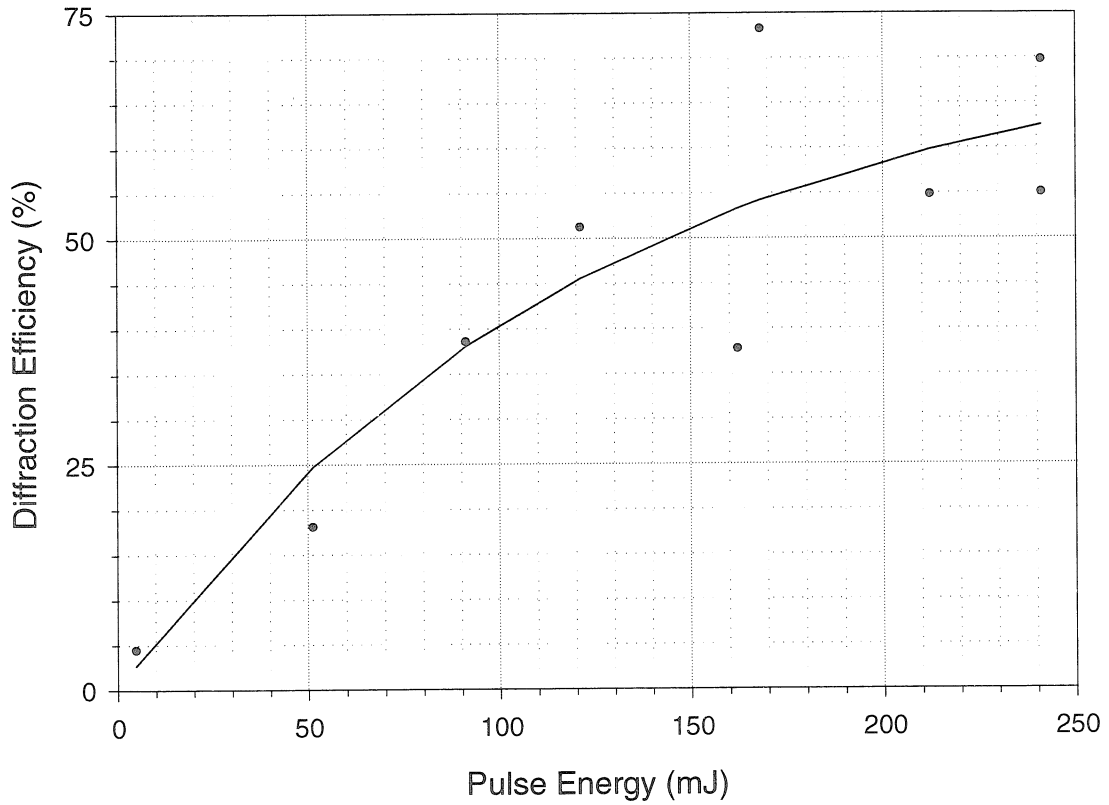

Fig. 6-10. Diffraction efficiencies of holograms recorded with various single pulse energies.

each hologram. This experiment confirms that the material is capable of recording holograms with high energy, 5.9 ns, pulses. Between the high sensitivity of this material, and the ability to record strong holograms with small single pulse energies (5 mJ yields a hologram with 5% diffraction efficiency), this material is a good candidate for the holographic movie recorder. Ideally, assuming a lossless optical system and a linear recording material, with a maximum pulse energy of 250 mJ/cm^2 and a required diffraction efficiency of 1% per hologram, 250 holograms could be recorded.

6.3 Optical System

High-speed film based cameras are available commercially that provide approximately 25 million frames per second and up to about 100 frames. These systems use either a rotating drum or rotating mirror design. Mechanical motion limits their frame-rate. Their electronic counterpart, cameras with multiple CCD's, can take up to about 10 frames with a 100 million frame per second rate. In this case, cost, packaging, and light efficiency limit the system's total frame count. To obtain very high frame-rates, mechanical motion must be avoided. However, to record multiple frames holographically, a multiplexing method must be used. Also, with a Q-switched Nd:YAG laser with 5.9 ns pulses and a 5 Hz repetition rate, one pulse must be used to record all of the holograms.

An optical system meeting the above requirements has been designed, and is schematically illustrated in Figure 6-11. The general idea of the system is to take a single pulse from the laser and to split it into multiple, time-delayed, pulses. Since light travels 3 m in 10 ns, an optical delay path is a convenient way to delay a pulse by this amount of time. One set of pulses become the signal beam, and the other the reference beams. The generation of the reference beams will be described first.

A single pulse from the laser is divided in power by PBS1. The ratio is adjusted by the waveplate just before the beamsplitter. The part of the pulse traveling down in the figure will generate the reference beams. Mirrors M1, M2, and M3 form an optical delay line for adjusting the reference beam's total path length from the laser to the recording material. The beam is inserted into a cavity formed by a 100% reflecting mirror (M5) and a partially reflecting mirror (M6). Two lenses, L1 and L2, are positioned in the cavity to produce a 4-f system such that the mirrors are at the image planes. The lenses are used to counteract dif-

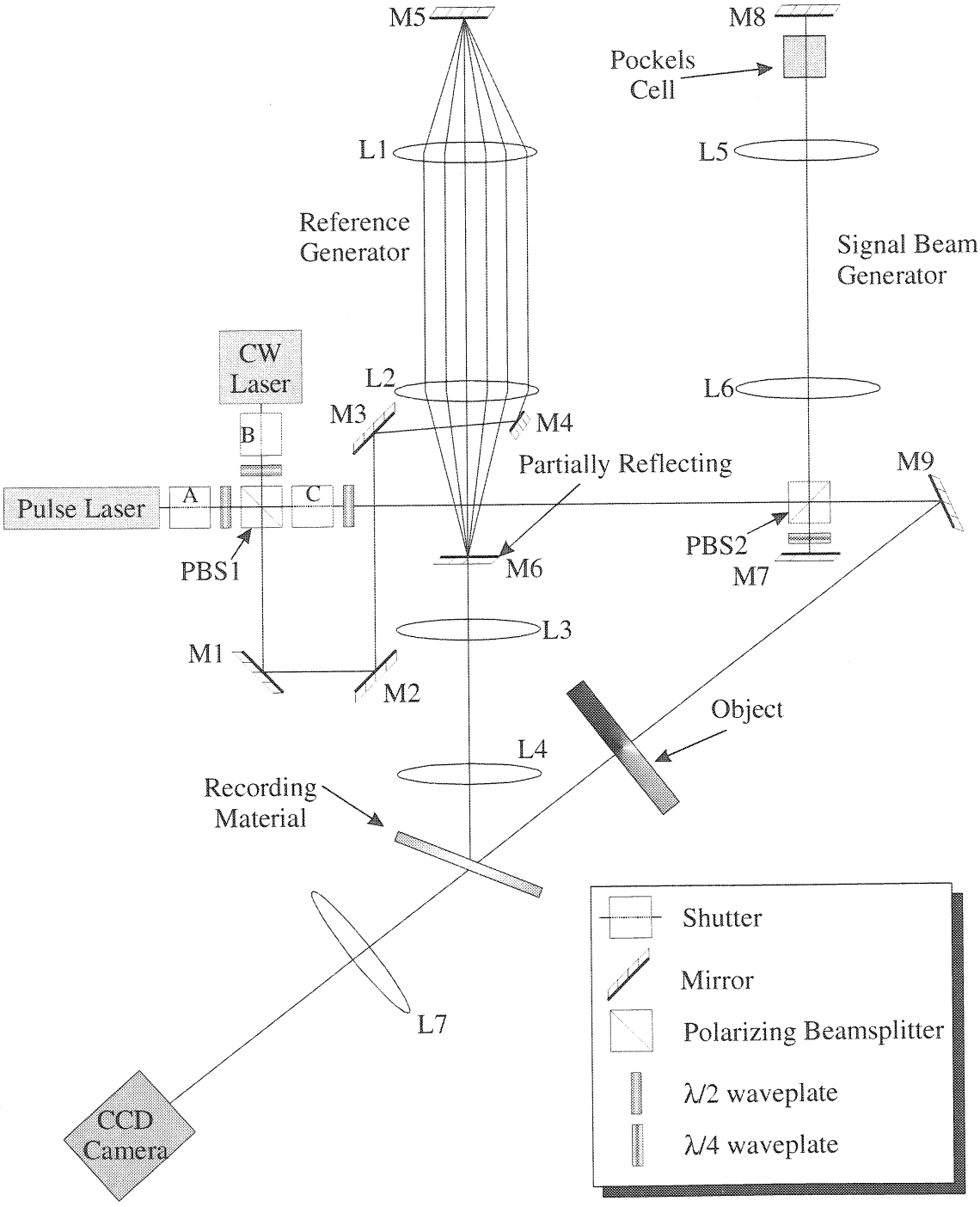

Fig. 6-11. Schematic illustration of the optical system for the high frame-rate holographic movie camera.

fraction of the beam as well as to generate multiple reference beam angles. The pulse is inserted into the cavity by mirror M4 positioned such that the beam appears to be originat-

ing from the center of the partially reflecting mirror. This beam will therefore be imaged to the plane of mirror M5. Assuming the cavity is perfectly aligned, the pulse will then travel back through the two lenses, reflect off mirror M6, and then hit the back of mirror M4. This would produce a single pulse output from the partially reflecting mirror M6. To generate multiple pulses, mirror M5 is tilted so that when the pulse reflects off the mirror it intersects the lens L1 closer to the optical axis than the pulse was when it was traveling towards the mirror. The angle of the beam is relayed by the 4-f system to M6, where part of the pulse energy escapes. M5 is tilted enough so that the returning pulse misses mirror M4 and remains in the cavity. On the next pass through the cavity the beam is again reflected off of M5, and is consequently moved closer to the optical axis. The pulse will now be incident on M6 with a different angle than it had the first time through the cavity, therefore generating a second pulse with a different angle than the first. The pulse will continue through the cavity until it propagates directly down the optical axis. At this point the pulse will retrace its path, but in the opposite direction, generating more pulses with different angles, and eventually exiting the cavity via the pulse-insertion mirror, M4. After the cavity, a 4-f system comprised of lenses L3 and L4 is used to relay the pulses to the plane of the recording material.

The lenses L1 and L2 were chosen to have a 45 cm focal length. The total cavity length is therefore 180 cm, and the pulse-to-pulse delay time is 12 ns. A slight variation in time between each pulse is created due to the beam traveling at different distances from the optical axis for each trip through the cavity. If the maximum distance from the optical axis is 5 cm, then the round trip distance through the cavity is 361.1 cm. This amounts to a time variation of approximately 37 ps, or 0.6% of the total pulse length. Relative to the error in

adjusting the path length difference between the reference and signal beams, this amount is insignificant.

The generation of the signal beam pulses requires a different cavity design since they all need to be aligned in order to pass through the object to be observed at the same location and angle. The pulse after PBS1 will be polarized in the plane of the page, and is passed through a half-waveplate to reorient the polarization such that the pulse is completely reflected by PBS2. A cavity is formed by two mirrors, M7 and M8. Again two lenses are used to counteract beam diffraction in the cavity. Each lens had a focal length of 45 cm in order to achieve the same overall cavity length, and hence pulse delay time, as the reference beam generator. Assume for the moment that the pockels cell and the waveplate are not present in the cavity. The pulse would then reflect off M8, and on the way back reflect off PBS2 and head back towards the laser. This is not the desired behavior, as multiple pulses need to be generated for the signal beam. Now consider what happens if the Pockels cell is inserted into the cavity. The Pockels cell is switched on to provide quarter-wave retardation for the duration of the initial pulse. It is then switched off. In this way, upon the first pass through the cavity the polarization of the pulse is rotated to be in the plane of the page. The pulse will therefore pass through PBS2 without any portion being reflected out of the cavity. From then on the pulse will remain in the cavity while losses cause it to decay. Next, consider what occurs if the waveplate is inserted into the cavity. When the pulse passes through the waveplate, its polarization vector is rotated by an amount determined by the orientation of the $\lambda/4$ waveplate. If this rotation is by 45-degrees, then half of the pulse energy will be transmitted out of the cavity by PBS2, and half will remain inside. With each successive pass through the loop, half of the pulse energy is trans-

mitted out of the cavity. Figure 6-12 is a plot of the energy in each pulse emitted from this

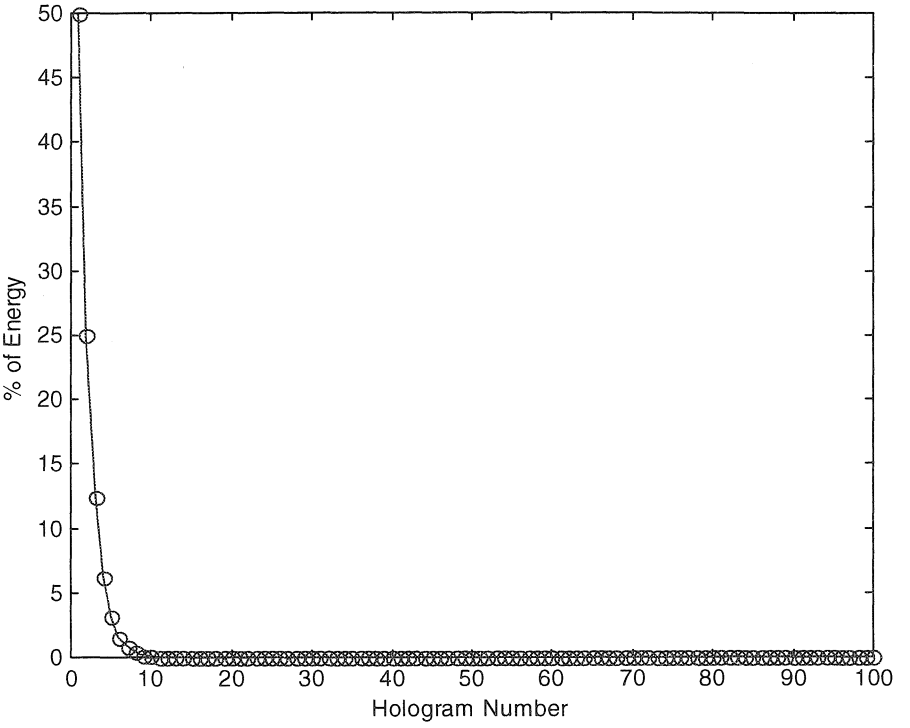

Fig. 6-12. Percent of total pulse energy in each pulse generated for the signal beam when 50% of the energy in the cavity is transmitted at each iteration.

cavity. The fast exponential decay in energy would make it difficult to record more than just a few holograms with this pulse energy distribution. Figure 6-13 is a plot of the fractional energy in each pulse when 2% of the cavity pulse energy escapes at each pass. If more energy is coupled out at each pass the decay is faster, but if less is coupled out, then more of the original pulse energy is wasted by staying in the cavity and being consumed by losses.

In order for this scheme to work properly, there must be a synchronizing of the switching off of the pockels cell after the pulse has passed through the first time, and before it makes it back through the cavity. For a 12 ns delay, this leaves about 6 ns to switch off due to the 6 ns pulse width. Ideally, the voltage on the pockels cell could be varied in real-

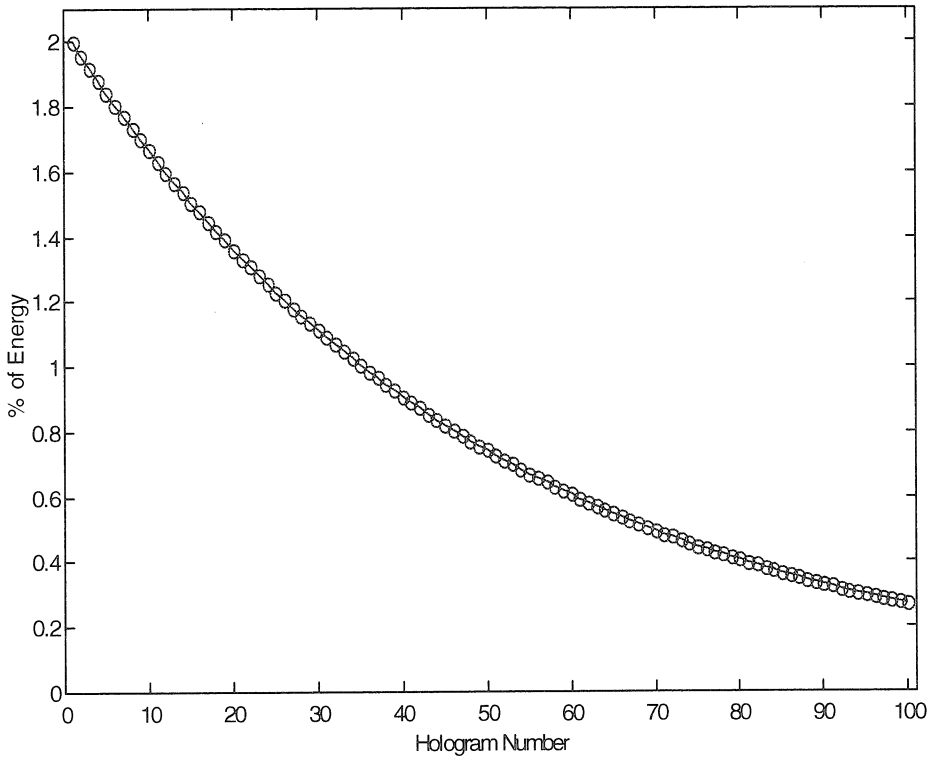

Fig. 6-13. Percent of total pulse energy in each pulse generated for the signal beam when 2% of the energy in the cavity is transmitted at each iteration.

time to allow a pre-determined percentage of energy out of the cavity with each cycle. However, due to the high voltages required to drive the pockels cell this would require very high power electronic amplifiers to drive the load. Another difficulty is in the exposure of the recording material. Typically for a scheduled recording, the recording energy of successive holograms grows exponentially larger. But in this case, the available energy will be exponentially smaller with each hologram. The result is an inefficient use of the dynamic range of the material and holograms that become weaker the later they are recorded. After the signal beam pulse generator, mirror M9 deflects the beam through an object to be recorded, and then through the recording material, where it will interfere with the reference beams.

During recording, shutters A and C are opened while shutter B is closed. After recording, the holograms need to be read out with a CW beam in order for the reconstruction to be captured by the CCD camera. Therefore, shutters A and C are closed and shutter B is opened. With a CW laser, all reference beams are simultaneously created by the reference beam generator cavity. Depending on which holograms are to be reconstructed, individual reference beams can be blocked at the plane half-way between the two lenses L3 and L4 of the 4-f relay system. At this plane, each reference beam is spatially separated from the others, and forms a focused spot. Therefore, one or more reference beams can be blocked simultaneously. If multiple references are used, then multiple images will be reconstructed and will interfere. This allows holographic interferometry to be performed between any pair of holograms that were recorded. If the first hologram is taken of the object before being modified, then interferometry can be performed between the original object and the object from any time interval during the recording period. Lens L7 is used to image the reconstruction to the standard frame-rate CCD camera.

6.3.1 Pockels Cell Timing

Before holograms can be recorded with the optical system, the Pockels cell voltage and timing must be set. The pockels cell drive electronics had a knob for adjusting the applied voltage, as well as one input for turning on the voltage, and a second for turning off the voltage. To time the pockels cell switching, a digital delay generator was used that had picosecond resolution. The q-switched laser provides an electronic "advanced sync" output which pulses a predetermined time before the q-switch in the laser fires, with a jitter of less than 1 ns. In other words, the advanced sync gives an electronic warning of when the laser pulse is going to come out of the laser. This advanced sync was used to trigger the delay

generator and start its timing. The delay generator was set to turn on the pockels cell as soon as the advanced sync signal arrived. To determine the quarter-wave voltage needed to drive the Pockels cell, the delay generator was set to turn off the pockels cell several microseconds after the arrival of the advanced sync signal. This was sufficient time to ensure the laser pulse would completely pass through the pockels cell while it was in the on state. The polarization of the beam after passing through the pockels cell could then be determined by monitoring the intensity of the beam at the location of M7 as well as that portion reflected back towards the laser, which was separated from the incoming beam by a partially reflecting mirror. The Pockels cell's quarter-wave voltage was adjusted to minimize the intensity of the back-reflected pulse and maximize the intensity at the position of M7.

The next step in the adjustment of the pockels cell was its turn-off timing. The pockels cell must be on for the duration of the first pass through the cavity, and then off by the time the pulse reflects off M7 and gets back to the pockels cell. To determine the correct timing, the turn-off delay time was decreased while the pulse shape after the signal beam generator was monitored with a fast photodiode and oscilloscope. When the pockels cell is turned off too soon, the output pulse intensity decreased, as seen in Figure 6-14 for the curve labeled "1044 ns," corresponding to a turn off delay of 1044 ns after the triggering of the delay generator. Once a reduced pulse output was seen, the turn-off time was increased in increments of 1 ns until no change in pulse intensity was observed. This corresponded to a time of 1050 ns. At this point, the pockels cell switches off just after the first pulse passes through it, and will be off by the time the pulse returns for its next trip through the cavity. Although the photodiode had a 1.5 GHz bandwidth, the 200 MHz digital oscilloscope that was available did not have enough bandwidth to be able to see changes in the

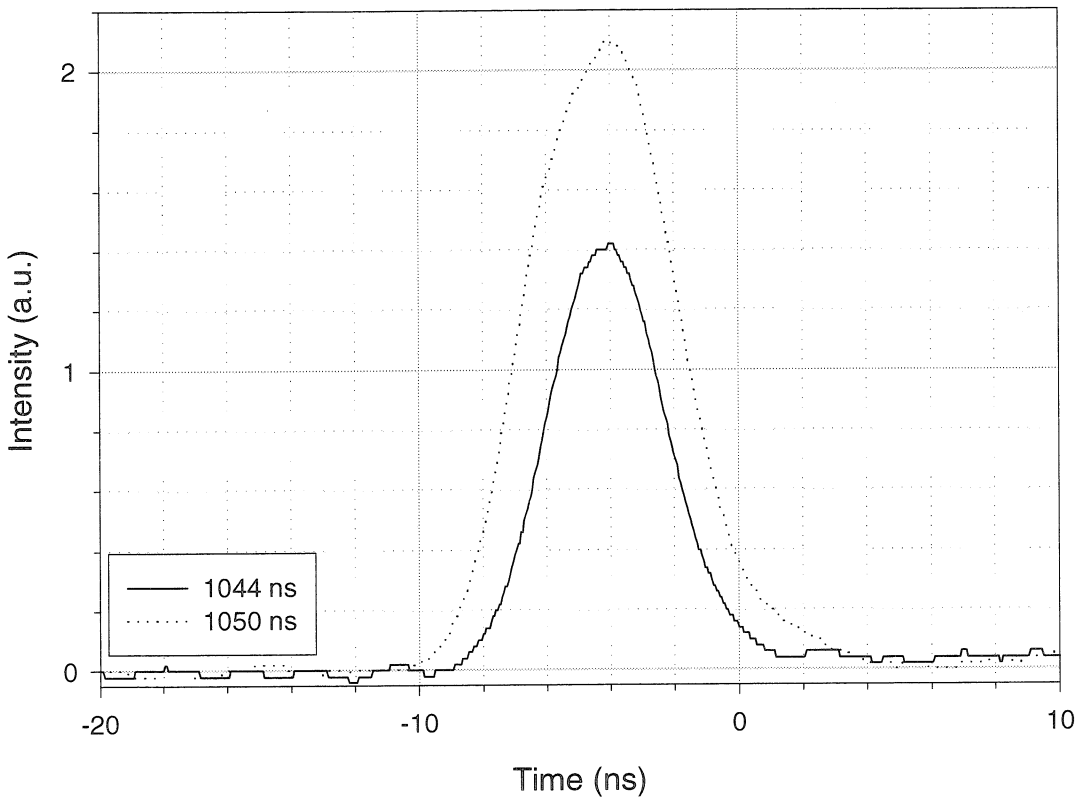

Fig. 6-14. Signal beam pulse when the pockels cell is turned off too soon (1044 ns), and when the pockels cell is turned off just after the pulse passes through it (1050 ns).

pulse shape itself, although it was still sufficient to set the timing of the pockels cell. The final proof that the signal beam generator actually works is the detection of multiple output pulses. Figure 6-15 shows the output of the cavity with more than 8 pulses being generated. The number and relative intensity of the pulses could be varied by adjusting the quarter waveplate.

6.4 Experimental Results

Due to aberrations of lenses L1 and L2 limiting the performance of the reference beam generator, 5 separate pulses could be generated. Due to the high peak intensity of the pulses, standard cemented doublet lenses cannot be used. Therefore, lenses L1 and L2 were

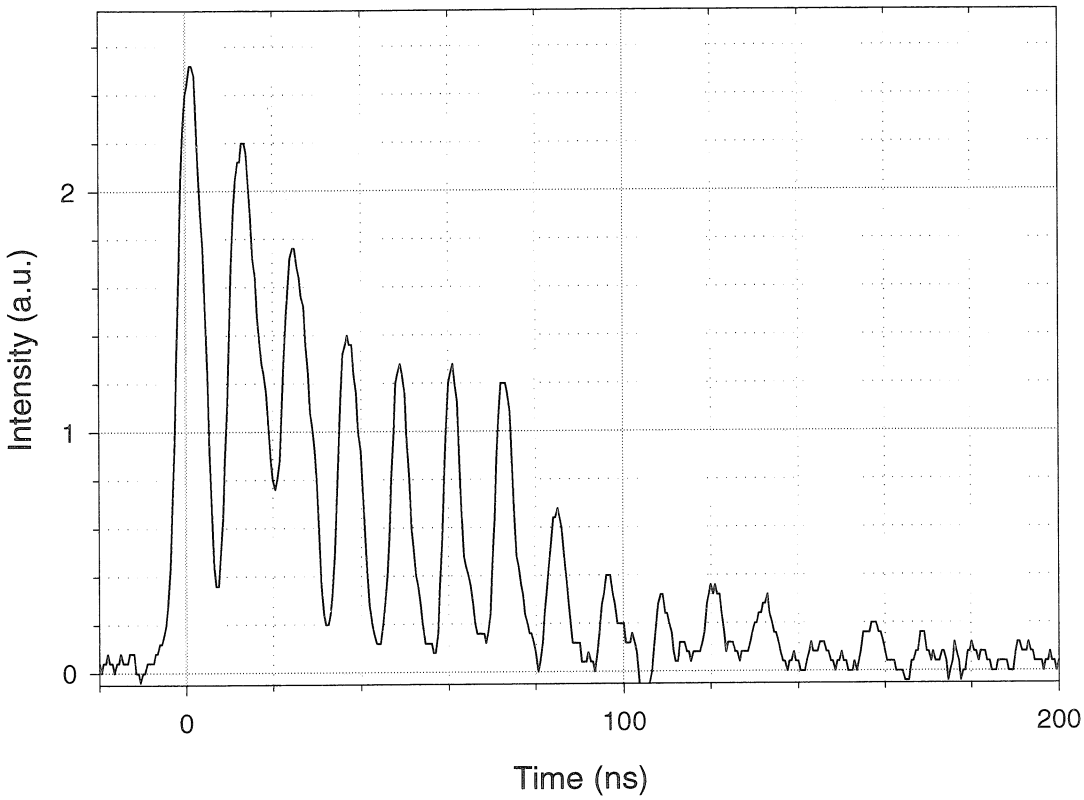

Fig. 6-15. Pulses generated by the signal beam generator cavity.

singlets whose focal length varied with distance from the center of the lens (spherical aberration). If too large an aperture were used, eventually the beam would focus near one of the lenses which could damage the anti-reflection coating, or perhaps with high-enough intensity, the glass itself. With this cavity design the usable aperture of the lenses directly limits the number of round trips the beam can make. One reference beam is generated for each round trip in the cavity.

The signal beam generator's quarter-waveplate was set to give 5 pulses of reasonable strength, which are shown in Figure 6-16. Ultimately, it is desired to determine the energy that is in each pulse. This can be accomplished by measuring the relative intensities of the pulses with the fast photodiode and oscilloscope, and then measuring the total power

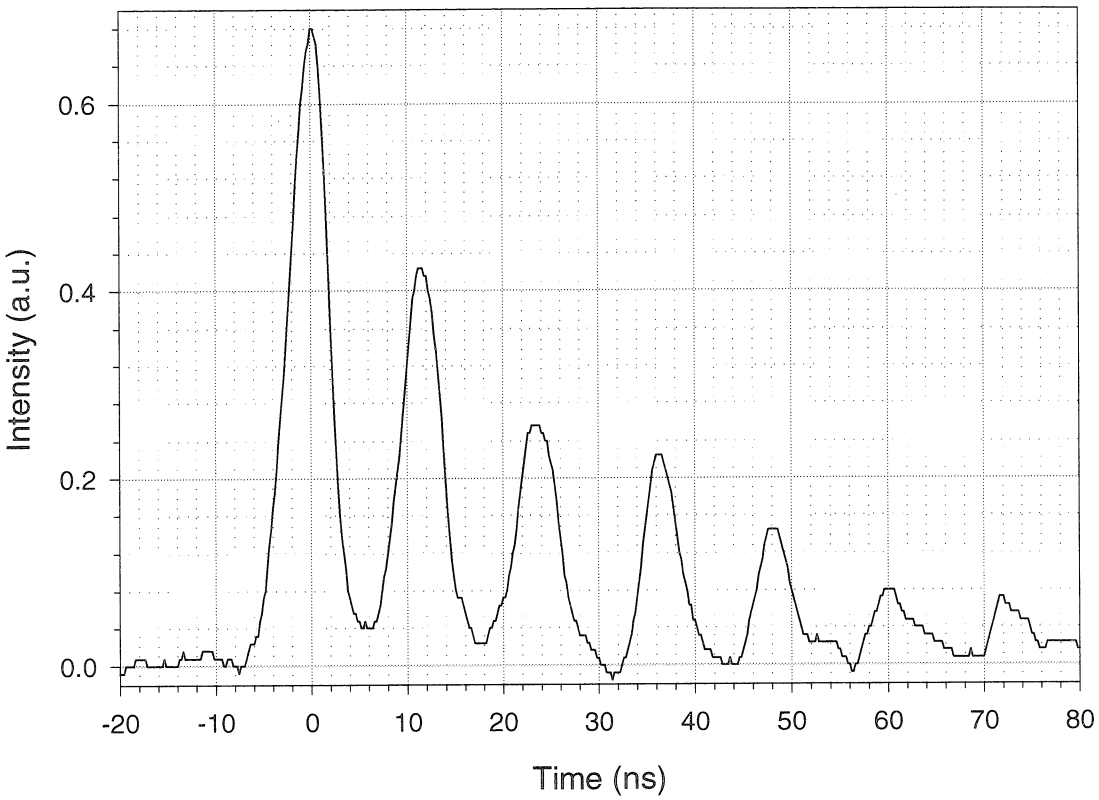

Fig. 6-16. Five signal beam pulses used for recording holograms.

in all the pulses with a standard high-intensity laser thermal power meter. Figure 6-17 actually shows the peak intensities of the first 6 pulses, which allows the relative energies to be approximated assuming a negligible amount of energy exists after the 6th pulse. The plot also includes the expected distribution of pulse intensities with 15% output coupling for each cycle through the cavity and a 20% round trip loss. The 20% loss figure was measured from the sum of the losses of each element in the cavity, while the output coupling was used to approximately fit the solid curve to the actual measured pulse intensities.

For the reference beam generator a partially reflecting mirror was used which was measured as reflecting 82% of the incident light. Each pulse from the reference beam generator was measured separately by blocking all but one pulse at the focal plane of lens L3

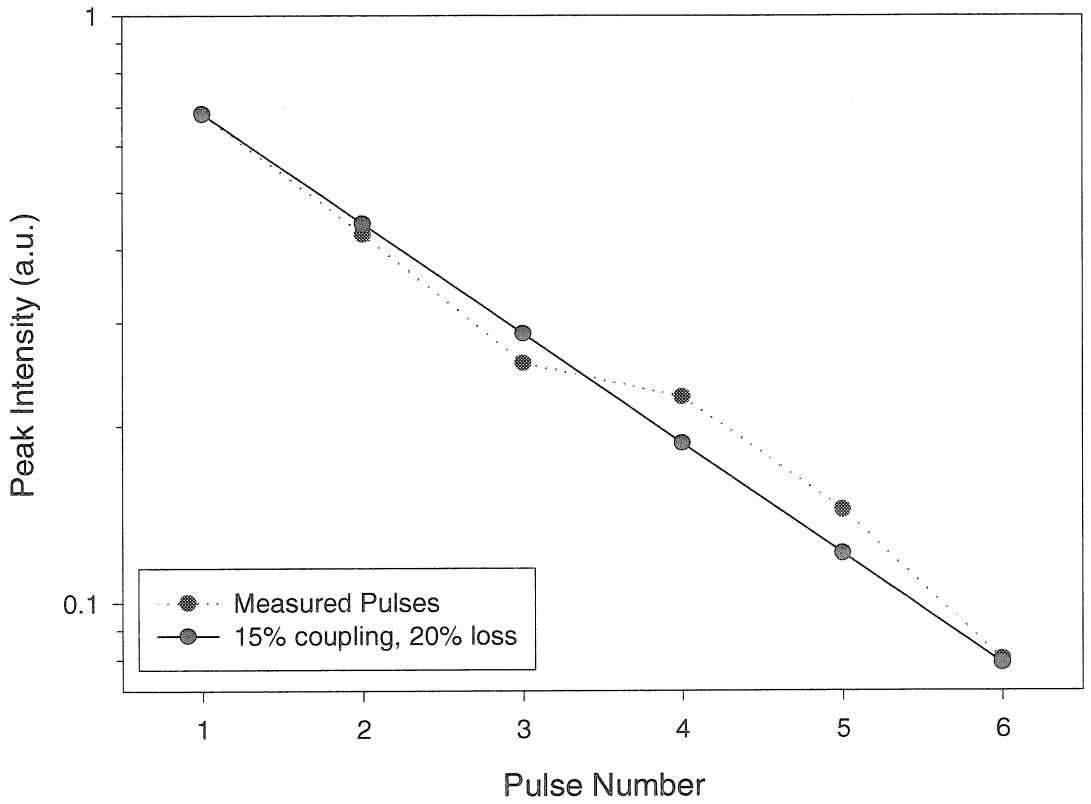

Fig. 6-17. Relative peak intensities of the signal beam pulses.

and then measuring the remaining pulse. Figure 6-18 shows the measurement of each of the five generated reference beam pulses. From this figure an artifact of the electronics can be seen in the form of a secondary spike approximately 37 ns after the peak of the pulse. Because each pulse was measured separately, this artifact does not affect the measurement; however, it is something that cannot be taken into account when measuring the signal beam pulses due to the inability to isolate and measure only a single pulse. The peak intensities of these five pulses are plotted in Figure 6-19 with a calculated curve taking into account the 82% reflectivity of the mirror and a measured round trip cavity loss of 12%. The measured and calculated values are in excellent agreement.

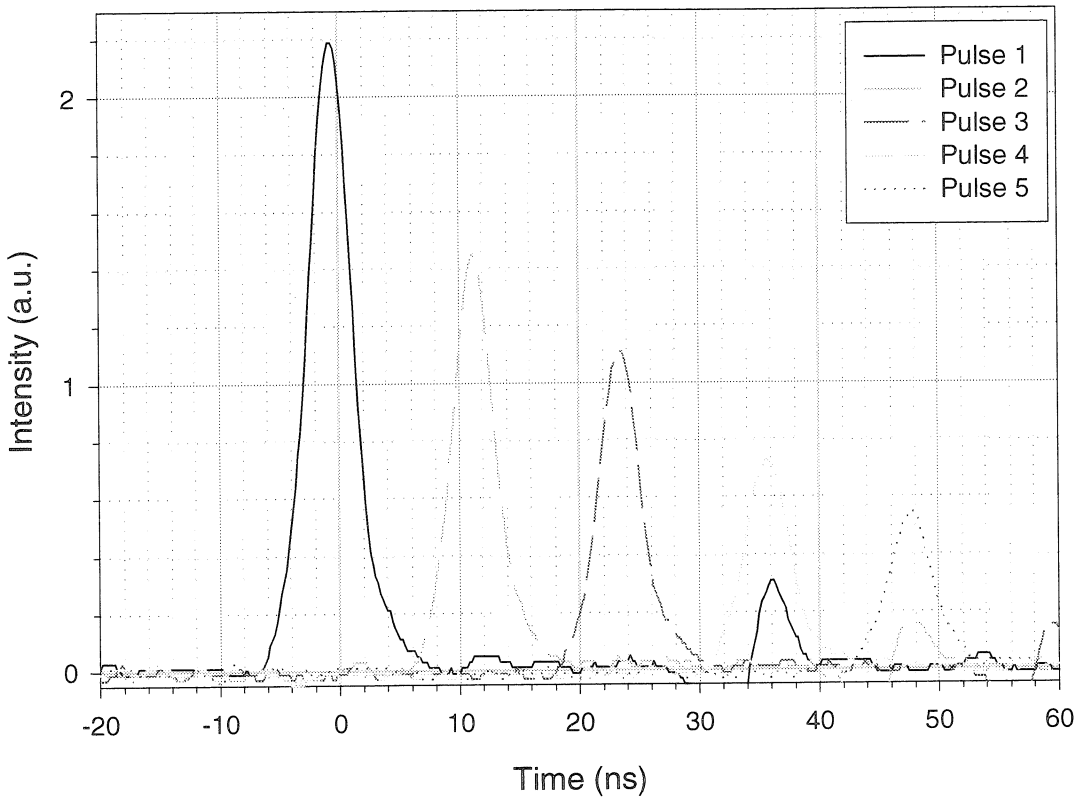

Fig. 6-18. Measurement of the five generated reference beam pulses.

Before recording a holographic movie, the beam energy was adjusted between the signal and reference arms. The system was set to maximize the amount of pulse energy entering the reference beam generator before dielectric breakdown of the air occurred in the focal plane of lens L3, which had a focal length of 10 cm. After passing through their respective pulse generators, the reference beam pulses had a cumulative energy of 50 mJ, while the signal beam pulses had a cumulative energy of 67 mJ. By using the relative pulse intensities measured by the fast photodiode and oscilloscope, the individual pulse energies could be approximated. They are plotted in Figure 6-20 together with a plot of the relative signal to reference beam pulse energy ratio. The cumulative energy used to record each successive hologram decays exponentially; however, the ratio of the two beams remains

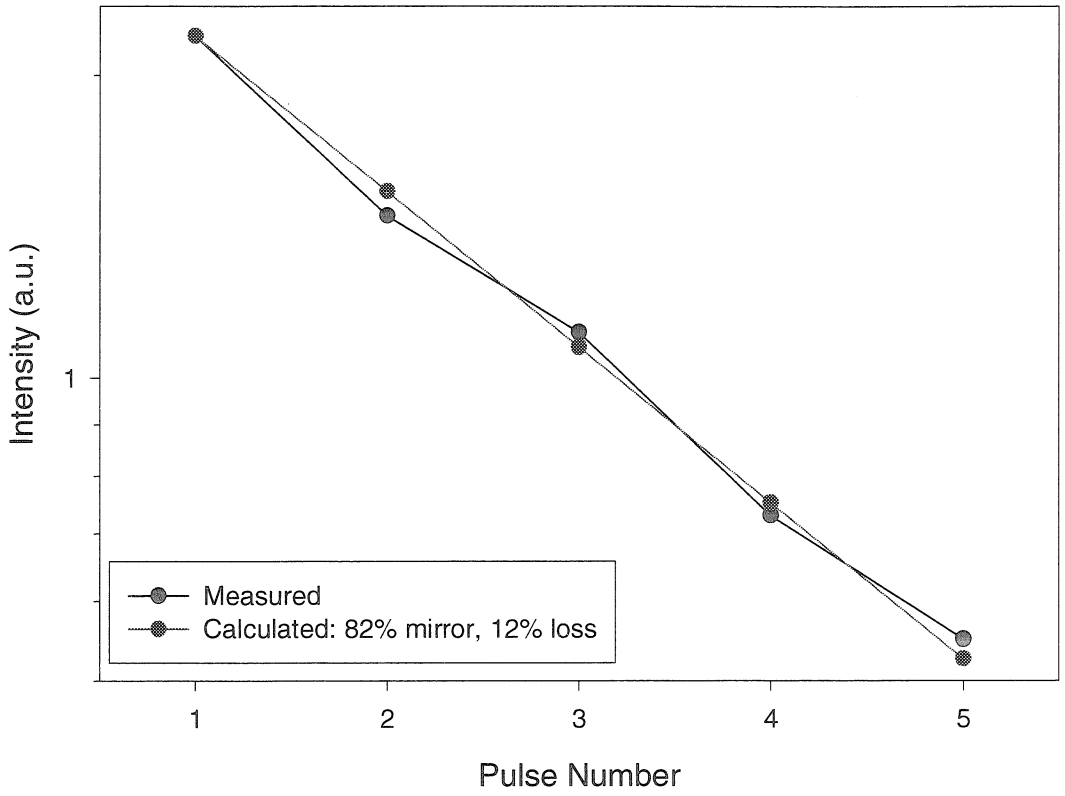

Fig. 6-19. Peak intensities of the five reference beam pulses with a calculation of the expected relative intensities given the known mirror reflectivity and cavity losses.

between 1 and 1.4 for all holograms. A slight improvement to this ratio could be made if more power could be diverted to the reference beams. However, this was not possible with the current optical system due to the 10 cm focal length lenses used as part of the reference beam path. Five holograms were recorded and read with the CW YAG laser. Each hologram was read individually by blocking all but one of the reference beams at the focal plane of lens L3. The plot in Figure 6-21 shows the diffraction efficiency of each hologram. The maximum diffraction efficiency, occurring for the first hologram, was 25%. As expected, each successive hologram is exponentially weaker, with the fifth hologram diffracting only 0.07% of the light. Comparing with the diffraction efficiencies of the holograms in

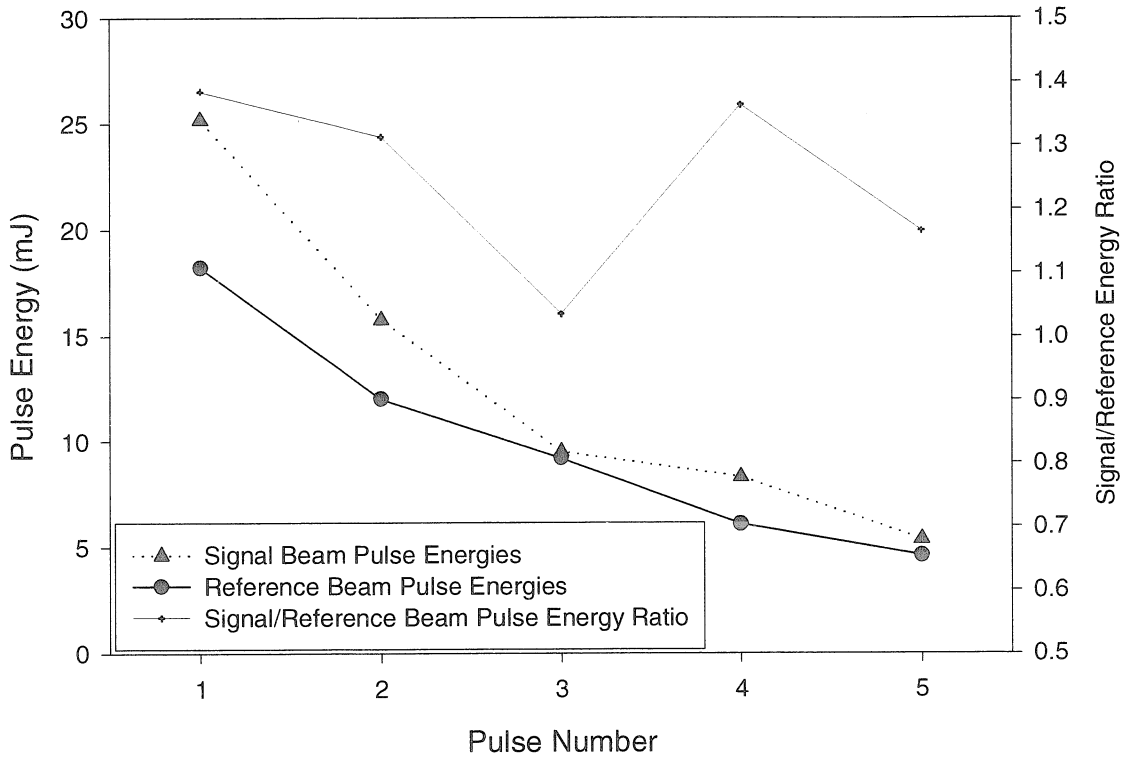

Fig. 6-20. Signal and reference beam pulse energies used to record a 5 hologram movie. The right axis is for the beam ratio that occurred for each pulse.

Section 6.2.1 carrying random bit patterns, these are very strong holograms. Therefore, good image reconstruction quality can be expected from this system.

6.5 Conclusion

The holographic system described in this chapter was developed to take advantage of the high sensitivity, high dynamic range, and large thicknesses of modern polymer recording materials. A high-speed, multi-frame, holographic recording system has all the advantages of holographic interferometry, with the added benefit of being able to capture the motion of fast events. The goal in the development of the system was to provide an instrument capable of recording faster than 2 million frames per second, while providing a comparable number of frames as the current generation of CCD array cameras. Through

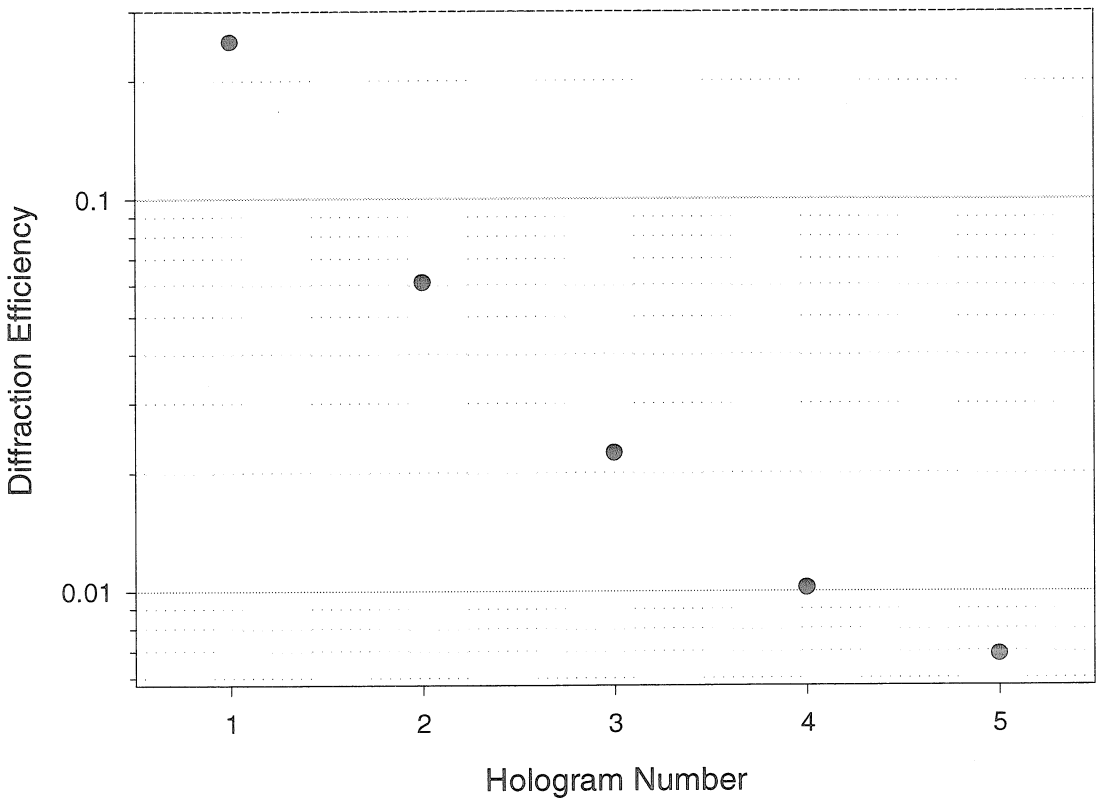

Fig. 6-21. Diffraction efficiencies of each hologram of a five hologram movie with 12 ns between holograms.

holographic interferometry and the simultaneous reconstruction of multiple holograms, any two frames in the sequence can be interfered for comparison purposes.

There are a number of steps that can be taken to improve the performance of the system. The reference beam generator was severely limited by the aberrations of the imaging lenses. As a beam propagates further from the center of the lenses, the focal length changes, which changes the imaging condition and eventually causes the beam to focus where it isn't supposed to. With the high-energy pulses being used, this is potentially catastrophic because if a focused spot occurs on the lens, damage will occur. One potential solution to the problem is to use air-spaced doublets instead of the singlets in the current design. In this

way more of the aperture of the lenses will be usable, allowing more round-trips to occur in the reference beam generator. Cemented contact doublets cannot be used due to the low damage threshold of the cement and the high intensity of the laser. Another step that can be taken to increase the number of reference beams would be to use an optical isolator at the input to the reference beam generating cavity. After the pulse makes its passes through the cavity it will be reflected out of the cavity by the original mirror used to reflect it into the cavity. At this point the circulator can be used to redirect this returning pulse into yet another reference beam generation cavity, with perhaps a stage of optical amplification to boost the beam power.

The signal beam generator with a pockels cell is a compact way to generate multiple pulses with identical propagation direction and position. The current implementation was limited by the approximately 8% loss occurring through the pockels cell. With the use of appropriate anti-reflection coatings on all surfaces, this loss can be reduced to less than 1%. A simple way to increase the number of pulses generated is to place an optical amplifier somewhere in the cavity. In this way after each round trip the pulse will get amplified to compensate for the losses and the fraction of light emitted to be used for recording. With enough gain, it should even be possible to increase the energy of each successive output pulse, thereby partially satisfying the scheduling requirements when multiplexing holograms in the polymer recording material, rather than having an exponentially decreasing recording energy for each successive hologram.

References

[6-1] A. J. Rosakis, O. Samudrala, and D. Coker, "Cracks Faster than the Shear Wave Speed," Science **284**, 1337-1340 (1999).

[6-2] For example, the Cordin Model 240-N, http://www.cordin.com.

[6-3] R. J. Collier, C. B. Burckhardt, and L. H. Lin, *Optical Holography*, Academic Press, New York, 1971, Chapter 15.

[6-4] L. O. Heflinger, R. F. Wuerker, and R. E. brooks, "Holographic interferometry," J. Appl. Phys. **37**, 642 (1966).

[6-5] J. A. Ang, B. D. Hansche, C. H. Konrad, W. C. Sweatt, S. M. Gosling, and R. J. Hickman, "Pulsed holography for hypervelocity impact diagnostics," Int. J. Impact. Engng. **14**, 13-24 (1993).

[6-6] R. G. Racca and J. M. Dewey, "Time smear effects in spatial frequency multiplexed holography," Appl. Opt. **28**, 3652-3656 (1989).

[6-7] R. G. Racca and J. M. Dewey, "High speed time-resolved holographic interferometer using solid-state shutters," Opt. & Laser Tech. **22**, 199-204 (1990).

[6-8] S. Suzuki, Y. Nozaki, and H. Kimura, "High-speed holographic microscopy for fast-propagating cracks in transparent materials," Appl. Opt. **36**, 7224-7233 (1997).

[6-9] W. Hentschel and W. Lauterborn, "High speed holographic movie camera," Opt. Eng. **24**, 687-691 (1985).

[6-10] M. J. Ehrlich, J. S. Steckenrider, and J. W. Wagner, "System for high-speed time-resolved holography of transient events," Appl. Opt. **31**, 5947-5951 (1992).

[6-11] J. S. Steckenrider and J. W. Wagner, "Study of crack-tip motion in dynamic fracture by microscopic time-resolved holography," Int. J. of Fracture **73**, 213-222 (1995).

[6-12] J. Diaci, D. hurley, J. W. Wagner, and J. Mozina, "Simultaneous monitoring of ablative shocks in air by high-speed cineholography and multiple-pass beam deflection probe," Appl. Surf. Sci. 96-98, 154-158 (1996).

[6-13] K. T. Weitzel, U. P. Wild, V. N. Mikhailov, and V. N. Krylov, "Hologram recording in DuPont photopolymer films by use of pulse exposure," Opt. Lett. **22**, 1899-1901 (1997).

[6-14] D. A. Waldman, H.-Y. S. Li, and M. G. Horner, "Volume shrinkage in slant fringe gratings of cationic ring-opening holographic recording material," J. of Imaging Science and Technology **41**, 497-514 (1997).

[6-15] A. Pu, K. Curtis, and D. Psaltis, "Exposure schedule for multiplexing holograms in photopolymer films," Opt. Eng. **35**, 2824-2829 (1996).